Deformation processes during the last stages of the continental collision: the brittle-ductile fault systems in the Bergell and Insubric areas (Eastern Central Alps, Switzerland – Italy)

Thèse présentée à la Faculté des sciences
Institut de Géologie
Université de Neuchâtel

Pour l'obtention du grade de docteur en sciences

Par

Laurent Ciancaleoni

Acceptée sur proposition du Jury:

Prof. M. Burkhard, Faculté des sciences de l'Université de Neuchâtel, directeur de thèse
Prof. D. Marquer, Faculté des sciences de l'Université de Besançon, directeur de thèse
Prof. A. Kalt, Faculté des sciences de l'Université de Neuchâtel, rapporteur interne
Prof. S. Schmid, Faculté des sciences de l'Université de Bâle, rapporteur externe
Dr C. Sue, Faculté des sciences de l'Université de Neuchâtel, rapporteur interne
Dr. B. Fügenschuh, Faculté des sciences de l'Université de Bâle, rapporteur externe

Soutenue le 12 mai 2005

Université de Neuchâtel
2006

Université
de Neuchâtel unine

IMPRIMATUR POUR LA THESE

Deformation processes during the last stages of the continental collision : the brittle-ductile fault systems in the Bergell and Insubric areas (Eastern Central Alps, Switzerland - Italy)

Laurent CIANCALEONI

UNIVERSITE DE NEUCHATEL

FACULTE DES SCIENCES

La Faculté des sciences de l'Université de Neuchâtel,
sur le rapport des membres du jury

Mme A. Kalt,
MM. M. Burkhard (directeur de thèse),
C. Sue,
D. Marquer (Besançon F)
S. Schmid (Bâle) et B. Fügenschuh (Bâle)

autorise l'impression de la présente thèse.

Neuchâtel, le 21 novembre 2005

Le doyen :

J.-P. Derendinger

Faculté des Sciences
■ Rue Emile-Argand 11 ■ CP 2 ■ CH-2007 Neuchâtel
■ Téléphone : +41 32 718 21 00 ■ Fax : +41 32 718 21 03 ■ E-mail : secretariat.sciences@unine.ch ■ www.unine.ch

Mots clés en français:

Alpes Centrales orientales, intrusion du Bergell, système de failles Périadriatique, faille, zone de cisaillement, fragile-ductile, granite de Novate, extension, décrochement, extrusion, paléocontrainte, analyse cinématique, traces de fission, exhumation, Néogène

Mots clés en anglais:

Eastern Central Alps, Bergell intrusion, Periadriatic Fault System, fault, shear zone, brittle-ductile, Novate granite, extension, strike-slip, extrusion, paleostress, kinematic analysis, fission track, exhumation, Neogene

Abstract:

The brittle and brittle-ductile fault and shear zone patterns are investigated in the Oligo-Miocene intrusions of the Bergell and Insubric regions in the Eastern Central Alps. In the study area, the late deformation pattern encompasses, from the regional scale up to the microtectonic scale, normal, oblique-slip and strike-slip faults. Much lesser reverse faults occur only at the microtectonic scale. The tectonic regime associated with these faults is distributed in space and time into extensional and transcurrent displacements. Fault data from 120 measurements stations, which altogether represent ca. 3500 fault planes, have been collected in this study. The fault-slip data analysis of the minor fault populations is coherent for both the extensive and strike-slip tectonic regimes and yields a very consistent ENE-WSW directed orientation of the extension axis, *i.e.* parallel to the Alpine belt direction.

Widespread normal faulting is a major long-lived event which led to orogen-parallel extension. This extension is materialized by a dominant set of NW-SE striking normal faults (transversal faults to the alpine belt direction). A minor part of this extensional deformation is also accommodated by oblique-normal slip on sets of E-W striking (longitudinal) faults.

Amongst the former ones, the Forcola fault is a major late Alpine normal fault located at the contact between the middle and upper Penninic units. The brittle-ductile fault consists of mylonites and cataclasites accommodating early Miocene NE-SW extension at the eastern border of the Lepontine dome. This E-dipping extensional structure is a prominent regional feature that:
(1) relatively displaces the wall rocks by a significant vertical minimum amount of approximately 3000m. The fault is proposed to be a conjugate fault with respect to the extensional Simplon fault system in the western Central Alps.
(2) promoted the space available for emplacement of the 25 Ma old Novate leucogranite. The extensional deformation within the syn-tectonic intrusion is heterogeneous and characterized by conjugated shear zones surrounding lens-shaped domains of weakly deformed granite. These structures developed during fast cooling of the intrusion.

This first evidence for orogen-parallel syn-extensional leucogranite emplacement during Oligocene convergence in the Alps brings new insights into the lower timing activity of the Forcola fault. Conversely, new zircon and apatite fission track ages across

the Forcola fault give an upper age limit (Langhian) for the cessation of significant vertical movement on the fault.

The strike-slip shearing event commonly but non systematically over imposed on the earlier extensional structures. The transcurrent paleostress field is calculated from conjugated sets of strike-slip faults that define triangular wedges associated with an orogen-parallel orientation of the extension axis. The transcurrent displacements are materialized by:
(1) right-lateral slip along reactivated and/or neoformed longitudinal faults and reactivated transversal faults
(2) left-lateral slip along N-S to NE-SW oriented faults.

The available zircon and apatite fission-track ages in the Eastern Central Alps depict a horizontal steady gradient of decreasing cooling ages from S to N and from E to W, regardless of sampling elevation. This late cooling pattern is actually part of a cross and along-strike broader gradient associated with migration of the time of enhanced cooling and exhumation toward the north (external crystalline massifs) and west (Lepontine dome). Regarding the Tonale fault, the fission track data suggest the likelihood of vertical displacements and block rotation along the fault from the Middle Miocene onwards.

On the basis of these observations, the following Neogene tectonic evolution of the Alpine collision belt in the Eastern Central Alps is proposed. In response to the northwestward motion and anticlockwise rotation of the Apulian microplate, the internal domain of the belt in the Bergell region reacted by E-directed lateral extrusion by the late Oligocene onwards. This lateral escape was typically accommodated by a combination of normal and transcurrent displacements. The onset of orogen-parallel extension at the Forcola fault is kinematically and temporally compatible with the late Oligocene dextral slip at the E-W oriented Tonale Line and sinistral strike-slip at the NE-SW oriented Engadine Line. These prominent regional shear zones define a first order tectonic block that accommodated the E-directed extrusion of the Bergell area. Within the extruding block, the tectonic regime evolved from a major extensive to transtensive tectonic regime to a more transcurrent one.

Because of strong lateral confinement due to indentation along the Giudicarie-Pustertal indenter at the end of the Burdigalian, orogen-parallel extension and lateral escape loosed efficiency. With on-going convergence, lateral extrusion was then primarily relocated sideways in the Western and Eastern Alps by the early Miocene onwards, according to free boundary availabilities.

Lateral extrusion in the core of the Alpine belt during the last stages of the continental collision is therefore an outstanding deformation process that predominates along the western, central and eastern segments of the belt. Lateral extrusion must therefore be definitely considered as a tectonic process characteristic of the late Alpine geodynamics since the Neogene.

A mes parents

A toi maman, qui n'a pas eu le temps

"*Avec le temps va tout s'en va. [...] Avec le temps tout s'évanouit. [...] Avec le temps tout va bien.*"
Léo Ferré

Summary

Chapter 1

Deformation processes during the last stages of the continental collision: the brittle-ductile fault systems in the Bergell and Insubric areas (Eastern Central Alps)

Introduction

Introduction

This thesis aims primarily to a better understanding of the deformation processes during the last stages of the continental collision, through the example of the brittle-ductile deformations in the Bergell and Insubric areas of the Eastern Central Alps. While numerous structural studies place emphasis on the tectonic importance of ductile deformations during nappe emplacement, fewer studies have been carried out on the brittle and brittle-ductile deformation in the internal part of a collision belt. Over the last decades however, the importance of such deformations and their relation to the present day geometry of the Alpine belt has been clearly established. One important aspect related to the late tectonic history is the partitioning of deformation between late extension and strike-slip faulting at the scale of the internal domain of the belt. In other words, the bulk kinematics of faulting mainly lead to the vertical and lateral extrusion of the previously thickened domain. Such processes have been extensively described not only in various segments of the Alpine belt (Eastern Alps, Western Alps) and in other modern collisional orogens such as the Himalayas, but also in old mountains ranges such as the Hercynian belt. In that sense extensional and transcurrent processes appear to be very characteristics of the late stages of a belt history.

The reason to live of this research project can be addressed by three questions.

(1) Why the Bergell and Insubric areas?

Simply because the Oligo-Miocene brittle tectonics in this region have not been studied in details. This region is particular in that it is the site of a close spatial relationship between late Alpine plutons and major faults. The plutons belong to the so-called late Oligocene Periadriatic intrusions in the eastern Central Alps: the Bergell pluton, the Sondrio intrusion and the Novate granite, and provide important timing constraints on the deformation. The major faults are the Insubric Line, the Engadine Line, the Forcola Line, and the Muretto Line and have well-known kinematics encompassing the characteristic late strike-slip and normal displacements in mountain belts. Therefore this region appears to be a key area for understanding the late deformation processes in the eastern Central Alps. In particular the comparison of the deformation field within the Bergell pluton (32-30 Ma) and the Novate pluton (25 Ma), and their tectonic relation with the main discontinuities will bring new insights on the late deformation and tectonic history in this Alpine region.

(2) Why granitic rocks?

Because the study of the brittle and brittle-ductile deformations within the Tertiary plutonic rocks of the Bergell area permits to avoid perturbations due to previous deformations and strong mechanical anisotropies. Granitic rocks are considered, indeed, as mechanically isotropic in their initial state. Finally, the widespread distribution of granites in the different parts of the crust make them good analogues for the study of the rheological behavior of the continental crust.

(3) Why brittle and brittle-ductile deformation?

The study of the heterogeneous deformation at the brittle-ductile transition offers a general view of the geometry and evolution of the deformation mechanisms in locally deformed zones. On one hand, shear-zone pattern analyses in granites provide useful paleostrain indications to constrain the bulk kinematics from ductile deformations. On the other hand, classical methods of fault slip analysis permit the analysis of brittle deformation via fault populations, but they are not well developed at the brittle-ductile transition. In this project, the different advanced methods of fault-slip analysis will be applied to brittle-ductile deformation fields. The resolved principal axes of deformation will be compared to those deduced from a classical strain analysis, using schistosity-stretching lineation couples where they exist. With this approach, the bulk kinematics at the brittle-ductile transition during the last stages of the continental collision may be adressed.

This manuscript is organized into six chapters, addressing particular aspects of the brittle-ductile deformations in the Bergell area. *Chapter two* is a publication that investigates the geometry and kinematics of orogen-parallel brittle-ductile extension at the Forcola normal fault. This fault is a major greenschist facies mylonite zone situated at the contact between the Lower and Upper Penninic units. It contributes to the last stages of unroofing of the Lepontine structural dome. An introduction to the regional geology and tectonics is summarized in this paper.

Chapter three is devoted to the analysis of brittle and brittle-ductile tectonics in the Tertiary intrusions. The first part of this chapter deals with a comparative analysis of the methods of fault slip analysis. In that sense it proposes to be an introduction to methods of fault-slip analysis. Several methods currently available are applied to a natural measurement site located in the Bergell pluton, and the results are critically assessed. The site was chosen because the local deformation is representative of the regional brittle deformation. A detailed geological setting of the Bergell area is also given in this chapter.

The regional brittle deformation is investigated in part two of chapter 3. The brittle deformation is analysed at the regional scale via the recognition of the map-scale fault patterns and kinematics, and at the outcrop scale via the paleostress and strain analysis of minor fault populations. The bulk deformation field is discussed in relation to the late denudation and lateral extrusion in the Eastern Central Alps.

In *chapter four*, the heterogeneous deformation in the Novate granite is studied via the analysis of shear zone patterns and the study of deformation mechanisms of minerals in mylonites. Additionally, the estimated conditions of deformation in the mylonites permit to better document the deformation history recorded in the Novate granite. This chapter provides new constraints on the activity of the Forcola Line, and proposes a simple model for late leucogranite emplacement in the Eastern Central Alps.

While the bulk kinematics of deformation and upper timing constraints in the Bergell area have been discussed in the previous chapters, *chapter five* proposes absolute timing constraints on the main discontinuities activity via fission track dating. The lower age limit for displacements along the major faults is discussed in relation to new apatite and zircon fission track ages. The late exhumation history in the Eastern Central Alps is evaluated by incorporating these new ages within the regional pattern of available ages.

Finally, *chapter six* summarizes the main results of this thesis. The new results are integrated in a large scale orogen-parallel extension and eastward lateral extrusion model of the Eastern Central Alps by the late Oligocene onwards.

Chapter 2

Syn-orogenic extension along the Forcola fault: Correlation of Alpine deformations in the Tambo and Adula nappes (Eastern Penninic Alps)

CHRISTIAN MEYRE, DIDIER MARQUER, STEFAN M. SCHMID, LAURENT CIANCALEONI

PUBLISHED IN ECLOGAE GEOLOGICAE HELVETIAE

0012-9402/98/030409-12 $1.50 + 0.20/0
Birkhäuser Verlag, Basel, 1998

Eclogae geol. Helv. 91 (1998) 409–420

Syn-orogenic extension along the Forcola fault: Correlation of Alpine deformations in the Tambo and Adula nappes (Eastern Penninic Alps)

CHRISTIAN MEYRE[1], DIDIER MARQUER[2], STEFAN M. SCHMID[3] & LAURENT CIANCALEONI[2]

Key words: Normal faulting, kinematics, extension, collision belts, Penninic domain, Alps

ABSTRACT

The Adula and Tambo nappes both experienced the Tertiary tectonics leading to the closure of the Valais ocean, however, their deformation and metamorphic histories show certain differences: the Adula nappe underwent a complex subduction evolution that culminated under eclogite facies conditions (Sorreda-Trescolmen). In contrast, the Tambo nappe recorded lower pressure conditions during nappe stacking (D1). Moreover, E-W syn-orogenic extension took place in the Tambo nappe (D2) while the south-directed subduction was still active in the Adula nappe (Zapport). Since the Eocene, these nappes underwent the same tectonic evolution.

The contact between the Adula nappe and the Tambo nappe is marked by a major Alpine normal fault. This Forcola normal fault consists of mylonites and cataclasites exposed between Mesocco in the Valle Mesolcina (Grisons, Switzerland) and Gordona in the Val Mera (Italy). This ductile-brittle normal fault offsets the two nappes by a vertical amount of approximately 3000 m. In map view the Forcola normal fault cuts out part of the Tambo nappe, the entire Misox zone and parts of the structurally higher the Adula nappe.

The Forcola normal fault reflects Early Miocene NE-SW extension responsible pro-parte for the dome-like structure of the Eastern Penninic domain. This extensional structure could be a conjugate fault with respect to the Simplon fault system. It contributes to the late stages of unroofing of the Lepontine structural dome.

ZUSAMMENFASSUNG

Die Adula-Decke und die Tambo-Decke erfuhren beide die tektonischen Vorgänge im Tertiär, die zur Schliessung des Valais-Ozeans führten, obwohl wesentliche Unterschiede in deren strukturellen und metamorphen Entwicklung festgestellt werden können: Die Adula-Decke durchlief eine komplexe Subduktionsphase, die unter eklogitfaziellen Bedingungen kulminierte (Sorreda-Trescolmen Phase). Im Gegensatz dazu sind in der Tambo-Decke wesentlich tiefere Drucke während der Deckenstapelung (D1) festzustellen. Ausserdem fand eine E-W Extension in der Tambo-Decke statt (D2), während in der Adula-Decke gleichzeitig die süd-gerichtete Subduktion noch immer aktiv war. Seit diesen Ereignissen im Eozän ist die tektonische Entwicklung beider Decken identisch.

Der Kontakt zwischen der Adula-Decke im Liegenden und der Tambo-Decke im Hangenden stellt eine bedeutende Abschiebung (Forcola-Abschiebung) dar. Entlang dieser Abschiebung werden Mylonite sowie Kataklasite beobachtet. Die Forcola-Linie, die zwischen Mesocco im Valle Mesolcina (Graubünden, Schweiz) und Gordona im Val Mera (Italien) aufgeschlossen ist, versetzt die zwei Decken um einen Vertikalbetrag von ca. 3000 m. Im Kartenbild ist ersichtlich, dass die Forcola-Linie Teile der Tambo-Decke, die gesamte Misoxer Zone, sowie geringe Teile der Adula-Decke herausschneidet.

Die Forcola Abschiebung reflektiert eine NE-SW gerichtete frühmiozäne Extension, die mitverantwortlich für die Dom-Struktur der östlichen Penninischen Einheiten ist. Diese Extensions-Struktur stellt möglicherweise ein konjugiertes System zur Simplon Abschiebung dar. Die Forcola Linie trägt einen wesentlichen Teil zur späten Heraushebung des Lepontins bei.

Introduction

The Mesozoic sediments of the Misox zone, situated in the eastern Lepontine dome, separate the Adula nappe from the Tambo nappe. These sediments represent the southern extremity of the North Penninic Bündnerschiefer (Fig. 1). While the Adula nappe paleogeographically belongs to the south European margin, the Tambo nappe represents a part of the Briançonnais domain (Schmid et al. 1990). Hence, the Misox zone represents the suture between the European margin and the Briançonnais paleogeographic domain (Tambo, Suretta and Schams nappes) that resulted from the closure of the Valais trough during Middle to Late Eocene (Stampfli et al. 1998). It was suggested that in the southern part of the area, a normal fault might be responsible for the disappearance of this suture, caused by a major displacement of the Tambo nappe

---

[1] Mineralogisch-Petrographisches Institut der Universität Basel, Bernoullistrasse 30, CH–4056 Basel
Tel/Fax: 061 302 01 43; email: christian.meyre@hmc.ch

[2] Institut de Géologie, Université de Neuchâtel, Rue Emile Argand 11, CH–2007 Neuchâtel

[3] Geologisch-Paläontologisches Institut der Universität Basel, Bernoullistrasse 32, CH–4056 Basel

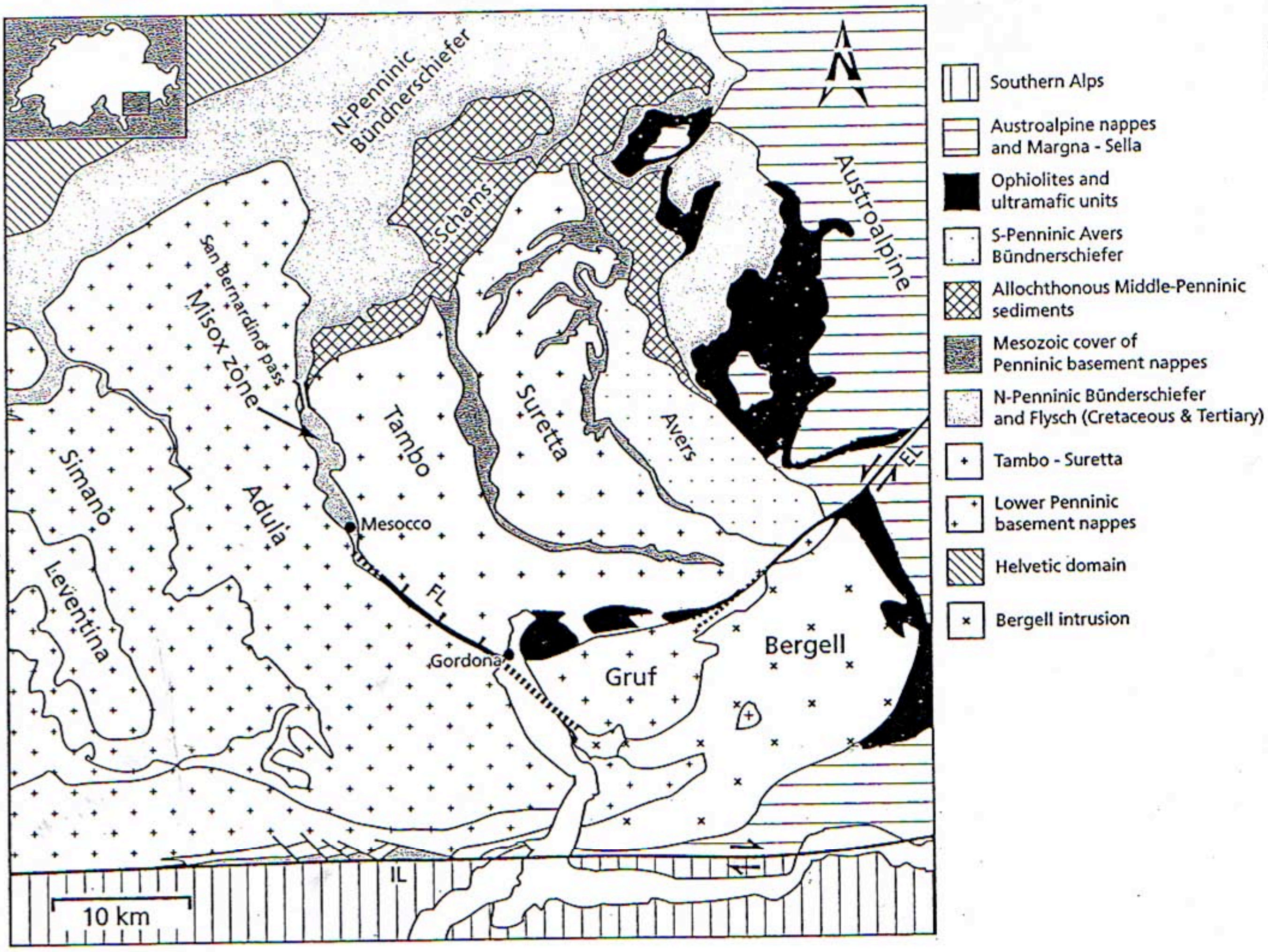

Fig. 1. Simplified tectonic map of the eastern Central Alps (after Schmid et al., 1990). – EL = Engadine line, IL = Insubric line, FL = Forcola line.

relative to the Adula nappe (Marquer, 1991; 'Forcola phase' of Schmid et al., 1997a; Fig. 2). Previous field investigations clearly pointed out that the Forcola normal fault, amongst other faults mapped within the Tambo nappe, is associated with substantial omissions of structural levels and that these normal faults formed late during the tectonic history of the Eastern part of the Penninic domain (phase D4 of Marquer, 1991). It is the aim of this study (i) to provide a correlation of Alpine structures between Adula and Tambo nappe, and (ii) to describe the geometry and the kinematics of deformation along this major normal fault in more detail.

Geological setting

The Misox zone includes strongly attenuated units at the southern extremity of the N-Penninic 'Bündnerschiefer', namely the Ucello units and the Gadriol mélange (see Steinmann, 1994, for a correlation with tectonic units further to north). The Misox zone does not exceed a thickness of 800 m in its middle part and consists mainly of calcareous schists with some extremely stretched lenses of gneisses (e.g. Gadriol gneiss of Gansser, 1937) and mafic rocks. Southward, this zone progressively thins out and finally disappears near the Passo della Forcola. This leads to a direct contact between the Tambo and Adula nappes (Fig. 1).

The Adula nappe largely consists of well-foliated quartz-rich ortho- and para-gneisses of pre-Alpine age (Jäger et al. 1967; Hänny et al. 1975). Interlayered with these quartzofeldspatic rocks are metapelites and mafic lenses of unknown age, occuring as slices of different length (several meters to kilometers). The mafic lenses often show assemblages of Tertiary eclogite facies metamorphism (Heinrich 1986; Meyre et al. 1997). Dolomitic marls and quartzites are rare and are referred to as 'Internal Mesozoic' due to their probable Triassic age (Jenny et al. 1923). In the southern part of the Adula nappe migmatic rocks are abundant, some of them are of Variscan age (Hänny et al. 1975). The Adula nappe is characterized by a well developed main schistosity. Because of this

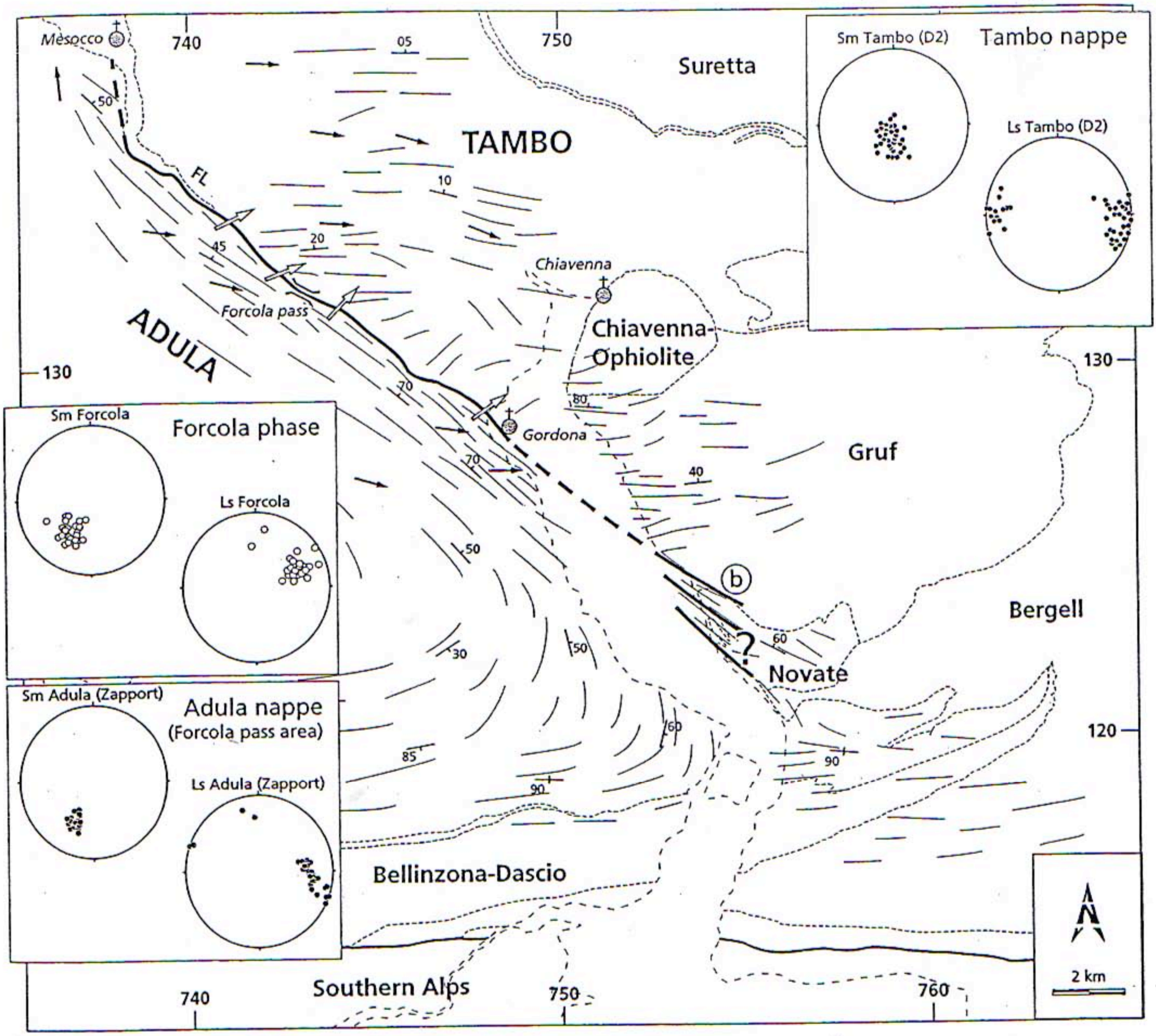

Fig. 2. Foliation trajectory map of the southeastern 'Lepontine'. FL = Forcola Line. Open arrows indicate the direction of faulting (top to NE) according to the Forcola stretching lineation; solid arrows indicate direction of the 'Zapport' stretching lineation. Data are compiled from Wenk (1973), Moticska (1970), Weber (1966), Marquer (1991), Hänny (1972), Rosenberg (1996), A. Berger (pers. comm.), and this study. b = only brittle features. Insets (stereograms): Sm = main foliation, Ls = stretching lineation.

dominant Alpine schistosity, relics of primary contacts of intrusive rocks are only preserved in the less deformed northern part of the nappe (e.g. Zervreila gneiss; Jäger et al. 1967; Löw 1987).

The Tambo basement mainly consists of pre-Alpine ('polycyclic') basement which is intruded by the Truzzo granite in the southern part. The Truzzo granite underwent only Alpine deformation and metamorphism. The 'polycyclic' lithologies are characterized by signs of strong pre-Alpine deformation and metamorphism and mostly consist of metapsammites or metagreywackes. Some metapelites (micaschists) are also present, containing pre-Alpine minerals such as staurolite, kyanite, andalusite, garnet, muscovite and biotite. Some migmatitic rocks are found in the southern part of the nappe. In the northern part of the nappe aligned lenses of mafic and ultramafic rocks are especially well developed. These are amphibolites with few preserved pyroxene-garnet assemblages (pre-Alpine eclogites; Biino et al. 1997). In other parts of the nappe, these mafic rocks underwent a complete Alpine retrograde metamorphism producing amphibolites and prasinites. A pre-Permian orthogneiss crosscuts the entire nappe body and may have been emplaced under anatectic conditions. The 'monocyclic' basement of the Tambo nappe is mainly represented by the Truzzo granite, exposed in the southern part of the nappe (Blanc 1965; Weber 1966; Gulson 1973; Marquer 1991). This early Permian granitic complex (268 ± 0.4 Ma, 206Pb/238U zircons, Marquer et al., in press) experienced only Alpine deformations. Accordingly, it appears as an originally isotropic and homogeneous body of porphyritic granite (with centimetric K-feldspars porphyroclasts), crossed by many Alpine shear zones (Marquer 1991).

Tectonic setting

The stacking of the Adula, Tambo and Suretta nappes results from middle Tertiary accretion of crustal slices (Schmid et al. 1990, 1997a, 1997b; Marquer et al. 1994). By the end of the Eocene, the entire width of the Briançonnais domain had been subducted, together with large parts of the North Penninic 'Bündnerschiefer' (Schmid et al. 1996). The Tambo and Suretta nappes reached peak pressure conditions (10–13 kbar; Baudin & Marquer 1993) by this time. Peak temperatures (500–550 °C) prevailed until 40–35 Ma ago (Hurford et al. 1989; Marquer et al., 1994; Schmid et al., 1996). The subduction of the Adula nappe, representing the southern tip of Europe at that time, is due to the collision of stable Europe with the Briançonnais and the Adriatic plate/microcontinent in late Eocene times, culminating under eclogite facies conditions. Subduction was followed by rapid exhumation and the formation of the Adula nappe, associated with the establishment of the complete nappe pile of the higher Penninic units by the end of the Eocene (35 Ma). In the following we summarize and compare the structural evolution of Adula and Tambo nappes.

Adula nappe

The structural evolution of the Adula nappe has recently been examined in detail (Löw 1987; Meyre & Puschnig 1993; Partzsch et al. 1994; Partzsch 1998). According to these authors, the Adula nappe experienced the following five deformation phases during its Alpine evolution:

Sorreda phase

The Sorreda phase (Löw 1987) represents the imbrication of Mesozoic sediments with basement rocks during subduction of the continental margin of the European plate. However, contacts between these lithologies are totally overprinted by later structures. Although the direction of the Sorreda deformation cannot be reconstructed, a southward directed subduction is most probable, based on the large scale geometry of basement-cover relationships.

Trescolmen phase

The Trescolmen phase operates under eclogite facies conditions, after peak pressure along the retrograde path. Pressure and temperature estimations for this event are in the range of 19–21 kbar and c. 650–700 °C for the middle Adula nappe (Trescolmen locality; Meyre et al. 1997). Elongated garnet aggregates and recrystallized omphacite define a distinct foliation as well as a stretching lineation only apparent in the core of mafic lenses that preserved eclogite facies assemblages. During the following Zapport deformation phase substantial rotations of the mafic lenses do occur. The kinematics of the Trescolmen deformation phase remain therefore unknown. The eclogite facies conditions have no equivalence in the other Penninic units (Simano, Tambo, Suretta).

Zapport phase

Schistosity and lineation formed during the Zapport deformation phase are the dominant fabrics in the Adula nappe (Löw 1987; Meyre & Puschnig 1993; Partzsch et al. 1994; Partzsch 1998). In the central part of the nappe the main foliation dips with about 20° to the ENE and represents the axial plane of isoclinal folds. The fold axes strike subhorizontally N-S to NNW-SSE, the stretching lineation being parallel to the fold axes. Shear sense indicators reveal a top to the North movement during this deformation phase.

In the Forcola pass area the stretching lineations of the Zapport deformation phase progressively curve into an E-W strike while the main foliation constantly dips towards the Northeast.

Leis phase

The Leis phase is characterized by open folds overprinting the Zapport folds and foliation. In sheet-silicate rich lithologies a crenulation develops. The fold axes of the Leis phase strike E-W, the fold axial plane is steeply south dipping, the folds being constantly north-vergent within the entire nappe.

Carassino phase

The Carassino phase mainly affected the frontal part of the Adula nappe and is responsible for an undulation and kinking of the leucocratic lithologies of the Adula nappe. Possibly, the Carassino phase is a time-equivalent to the Forcola phase (Schmid et al. 1996), but no direct correlations exist.

Tambo nappe

D1 deformation

The D1 ductile Alpine deformation (Marquer 1991) is linked to the progressive Eocene stacking of the Suretta, Tambo and Adula nappes towards the NNW (Ferrera phase of Schmid et al. 1997a). D1 is associated with a strong SSE-NNW oriented stretching lineation and a top to the NNW shearing (Baudin et

Table 1: Correlation of Alpine deformation phases of the Adula nappe and the Tambo nappe

Time interval	Deformation phases				Tectonic events (Central Alps)
	Adula nappe	*Ref.	Tambo nappe	*Ref.	
Middle to Late Eocene (c. 45–40 Ma)	Sorreda subduction (S-directed) imbrication	(1)	D1 (Ferrera) nappe stacking; thrusting and isoclinal folding LS: SSE–NNW; S: subhorizontal	(2, 3, 4)	subduction of and peak-P in Briançonnais domain, followed by subduction of European margin (Adula), leading to eclogite facies conditions
Late Eocene – Early Oligocene (c. 40–30 Ma)	Trescolmen eclogite facies conditions after peak-pressure Zapport top-N shearing, isoclinal folds LS/FA: NNW–SSE; S: dipping 40° to ENE	(5) (1, 6, 7)	D2 (Niemet-Beverin) E-W Extension LS: E–W; S: subhorizontal	(2, 3, 4)	ongoing N-S compression in Central Alps, combined with E-W stretching in the Tambo and Suretta nappes intrusion of Bergell granodiorite (30 Ma)
Middle Oligocene (c. 30–25 Ma)	Leis crenulation; open folds ENE dipping fold axes (dipping 35°), north vergent fold axes	(1, 6, 7)	D3 (Domleschg) staircase geometry folds E–W fold axis, north vergence fold axial plane: steeply south dipping	(2, 3, 4)	back-thrusting along the Insubric Line
Oligocene–Miocene (c. 25–21 Ma)	Forcola (Carassino?) top-NNE normal fault kinking and undulation in frontal part of Adula nappe brittle-ductile deformation	(1, 8)	D4 (Forcola) NNW–SSE normal faults brittle-ductile deformation	(2, 3, 4, 8)	dextral brittle slip along Insubric Line block rotation along sinistral Engadine Line

*References:
(1) Löw (1987), (2) Marquer (1991), (3) Baudin et al. (1993), (4) Schmid et al. (1996), (5) Meyre et al. (1997), (6) Meyre & Puschnig (1993), (7)Partzsch et al. (1994), (8) this study.
LS = stretching lineation, FA = fold axe, S = foliation

al., 1993). Estimates of the P-T conditions are based on phengitic substitution (Massonne & Schreyer 1987) in D1 mylonitic foliations and systematically show HP-LT metamorphic conditions (Baudin & Marquer 1993). For example, metamorphic conditions of about 12 kbar and 500 °C are attained at the bottom of the Tambo nappe. Ahead of the Tambo and Suretta basement, the pile of crystalline and sedimentary slabs (Ucello, Areua, Schams, Vignone) represents an accretionnary wedge particularly well-developed in the northern Penninic 'Bünderschiefer' and flysch (Steinmann 1994). The overall geometry of the frontal slices is related to the closure of the Valais trough.

D2 deformation

Deformation D2 is a ductile and heterogeneous deformation linked with a gentle east-dipping schistosity and an E-W stretching lineation. Most of the D2 mylonitic zones cross-cut previous contacts and indicate top to the East shearing. D2 is responsible for large scale structure on the top of the Suretta nappe, developing recumbent SE vergent folds F2 with very low angles between fold axes and mainly N70 to E-W oriented stretching lineations (Marquer et al., 1996). The phengitic substitution values measured in the D2 mylonites or in the D2 shear bands indicate pressures, which progressively decrease with time, associated with a slight decrease in temperature. For example, a progressive decrease of pressure and temperature from 11 down to 5 kbar and 550 down to 500 °C is recorded at the bottom of the Tambo nappe (Baudin & Marquer 1993) and from 10–5 kbar at 400–450 °C in the Roffna granite (Challandes, 1996). This tectono-metamorphic evolution of the D2 deformation is interpreted in terms of strong vertical shortening associated with preferentially top to the East shearing, which occurred synchronously with substantial decompression (Baudin & Marquer 1993). This progressive deformation induces crustal thinning with a stretch parallel to the Alpine chain during Late Eocene to Early Oligocene (Marquer et al. 1994), simultaneous with refolding of the Schams nappes (Niemet-Beverin phase of Schmid et al., 1996) and ongoing N-S convergence in the Adula nappe.

D3 deformation

This deformation event occurred under lower greenschist facies conditions and became much more localized. D3 deformation results in local staircase shaped folding, with steeply south dipping axial planes and E-W fold axes, preferentially developed in the southern part of the nappes (Baudin et al. 1993). This D3 deformation was generated by differential uplift of the southern part of the nappe and could be associ-

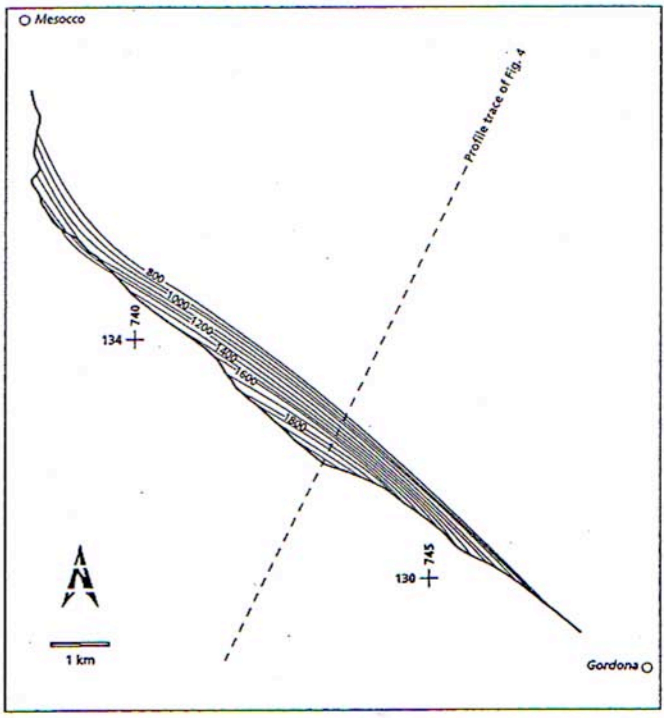

Fig. 3. Contour map of the fault plane of the Forcola normal fault. The contours are mainly constrained by data from Weber (1966) and our own field observations. Contour lines are given in 100 m interval. Profile trace refers to the cross-section in Figure 4.

ated with the Oligo-Miocene vertical movements along the Insubric Line (Hurford 1986; Heitzmann 1987; Schmid et al., 1989).

D4 deformation

The last extensional D4 deformation consists of several NNW-SSE brittle-ductile normal faults, steeply dipping towards the ENE and systematically lowering the eastern compartments with hectometric fault throws. The geometry and the kinematics of this deformation is contemporaneous with activity along the Forcola normal fault.

Tectono-metamorphic evolution

The tectono-metamorphic evolution of the Adula and the Tambo nappe is described in detail in Löw (1987), Meyre & Puschnig (1993), Partzsch et al. (1994), Partzsch (1998), Meyre et al. (1997) concerning the Adula nappe and in Baudin & Marquer (1993), Marquer et al. (1994) concerning the Tambo nappe. A comprehensive description of the tectonic evolution of the entire Penninic domain can be found in Schmid et al. (1996; 1997a; 1997b). The structurally higher part of the Adula nappe experienced a clockwise Alpine PT-loop culminating under eclogite facies conditions. The temperatures and pressures of this event range from 450–550 °C and 11–13 kbar in the northern part (locality Vals) to 750–900 °C and 18–35 kbar in the southern part (localities Alpe Arami, Cima di Gagnone) (Heinrich 1983; Heinrich 1986; Risold et al. 1996). The retrograde path is characterized by isothermal decompression during the Zapport phase. The tectono-metamorphic Alpine evolution of the Tambo nappe is characterized by peak metamorphic conditions at c. 500 °C and 13 kbar in its southern part. Like in the Adula nappe it is also followed by isothermal decompression. For the further retrograde evolution the pressure- and the temperature-path coincide (cf. Marquer et al. 1994).

Correlation of deformation phases in the Adula and Tambo nappes

Concluding from the above sections, we can correlate the deformation phases in the footwall (Adula nappe) and in the hangingwall (Tambo nappe) of the Forcola fault (Tab. 1). The 'Trescolmen' deformation phase, associated with eclogite facies conditions in the Adula nappe (Meyre & Puschnig 1993, Meyre et al. 1997), corresponds to the early stages of the Zapport phase of Löw (1987) and Schmid (1996).

The subsequent decompression of the Penninic units is accompanied by E-W extension restricted to the hangingwall (D2 in Tambo nappe) and N-S compression in the footwall ('Zapport' deformation phase in the Adula nappe).This D2 deformation is correlated with the Niemet-Beverin phase described in the Suretta and the Schams nappes by previous authors (Milnes & Schmutz 1978; Schmid et al. 1990; Schreurs 1993) and the Zapport phase in the Adula nappe. This correlation is based on the observation of a continuous transition of the Zapport foliation into the Niemet-Beverin axial planar foliation in the San Bernardino pass area. In the same area the stretching lineation continuously turns from a N-S direction ('Zapport') into an E-W direction (D2). The latest stages of the 'Zapport' phase were contemporaneous with the Niemet-Beverin phase in the Schams nappes and in parts of the North Penninic 'Bündnerschiefer' (Schmid et al. 1996). This equivalence gives an important time constraint for this deformation event because structures related to the Niemet-Beverin phase are cut by the Turba normal fault (Nievergelt et al. 1996), which is itself truncated by the intrusion of the Bergell granodiorite (30 Ma, after von Blanckenburg, 1992). It is important to note that D2 E-W stretching was active in the upper Penninic nappes (i.e. the Tambo and Suretta nappes) while the lower Penninic nappes (i.e. the Adula nappe) were progressively stacked towards the north ('Zapport'). Moreover D2 thinning could also explain part of the exhumation of the eastern part of the high grade Ticino dome (Bradbury & Nolen-Hoeksema 1985; Hurford 1986; Hurford et al. 1989; Merle 1994).

The Leis phase can be correlated with the Domleschg phase that has been described in the N-Penninic Bündnerschiefer and flysch by Pfiffner (1977). The Domleschg phase is equivalent with the D3 deformation phase in the Tambo nappe (Steinmann 1994; Schmid et al. 1996).

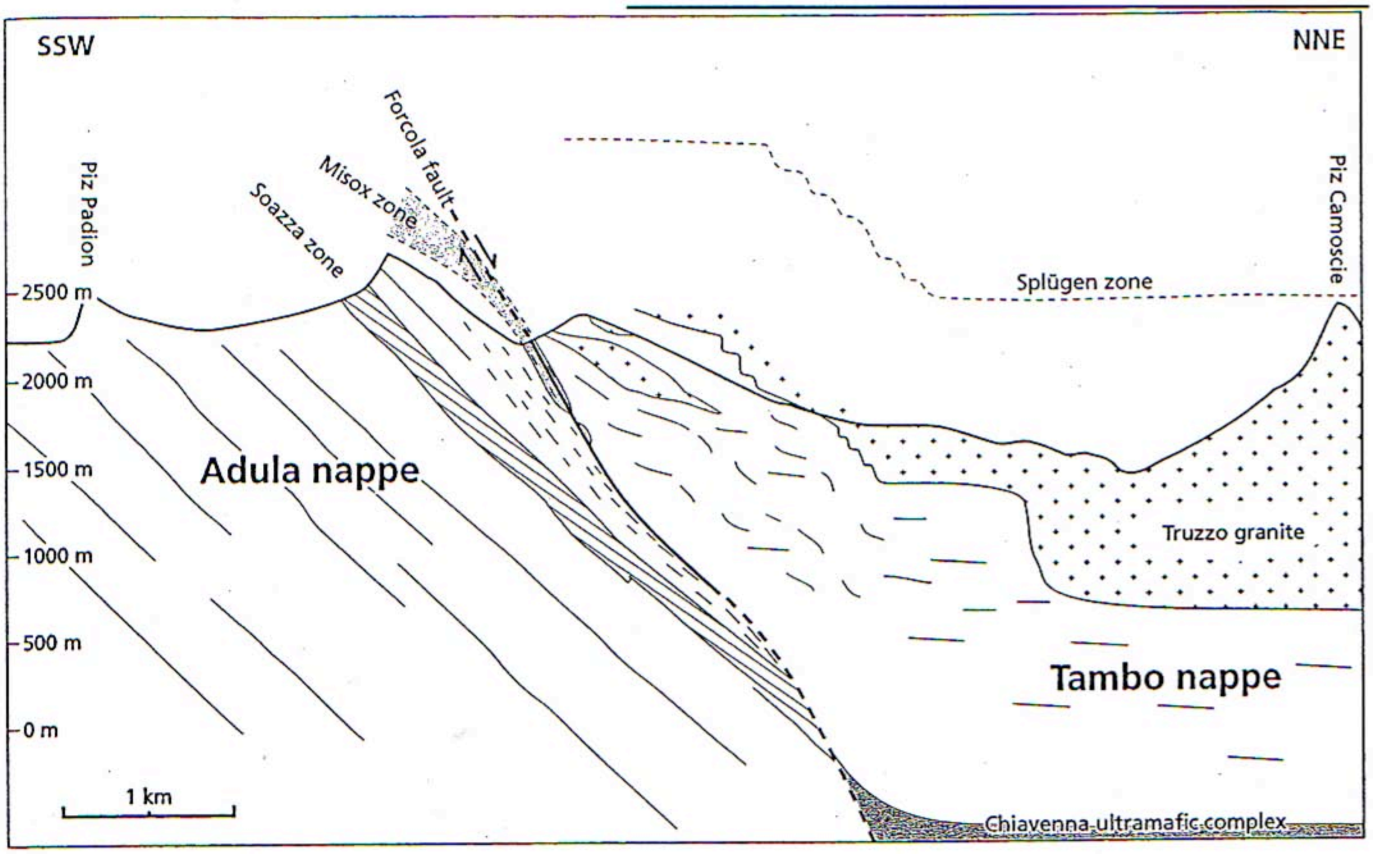

Fig. 4. Tectonic cross-section at the Forcola pass area, perpendicular to the fault orientation. Minor relics of the Misox zone can be observed at the Forcola pass area. The Soazza zone is truncated by the Forcola Line because of a high angle between the main foliation in the footwall and the fault.

Forcola phase

Field geometry

In map view the trace of the Forcola Line forms a slight arc concave towards the northeast. The construction of a contour map of the fault surface reveals a more or less constant inclination of the fault between 40° and 50° towards northeast (Fig. 3).

The flat lying foliation of the hangingwall is clearly discordant to the fault zone, whereas in the footwall a discrimination between the pre-existing 'Zapport' foliation and the subparallel Forcola mylonitic schistosity is not always clear because of the small angle between the two foliations. Towards the southeast, the Forcola normal fault cuts off the 'Soazza' zone (Weber 1966), which is a zone of metasedimentary rocks (paragneisses and metapelites) within the leucocratic gneisses of the structurally higher Adula nappe. The Misox zone is entirely thinned out due to Forcola phase movements. The last small slices of the Misox zone are preserved in the Forcola pass area.

The vertical component of displacement, induced by normal faulting may be estimated from a cross section in the Forcola pass area (Fig. 4) and amounts to 3000m at least.

The continuation of the Forcola line towards the southeast, as well as towards the northwest is still unclear. In the northwest (the Valle Mesolcina) the fault possibly continues at the base of the Misox zone, although north of Mesocco no relics of this normal fault could be detected so far. In the southeast the trace of the normal fault is covered by the alluvial plain of the Valle Mera, the last outcrop being found near the village of Gordona. However, inspection of the foliation trajectory map of the southeastern part of the Lepontine area (Fig. 2), reveals a significant change in the orientation of the foliation across Valle Mera: The E-W striking foliation on the east side of Valle Mera (Gruf unit) contrasts with the NW-SE strike of the west side (Adula nappe). This prominent change could indicate a continuation of this line across the alluvial plain of Valle Mera, as indicated in Figure 2. This hypothesis is supported by the occurrence of brittle fractures and faults in the region north of Novate (work in progress, L. Ciancaleoni). However, the exact localization of the major fault zone in the Novate intrusion is still unknown. Furthermore, mylonites clearly related to the Forcola phase are not apparent on the east side of the Valle Mera. The continuation of the Forcola normal fault across the Valle della Mera south of Gordona, such as suggested by Fig. 2 has two important consequences:

]]>

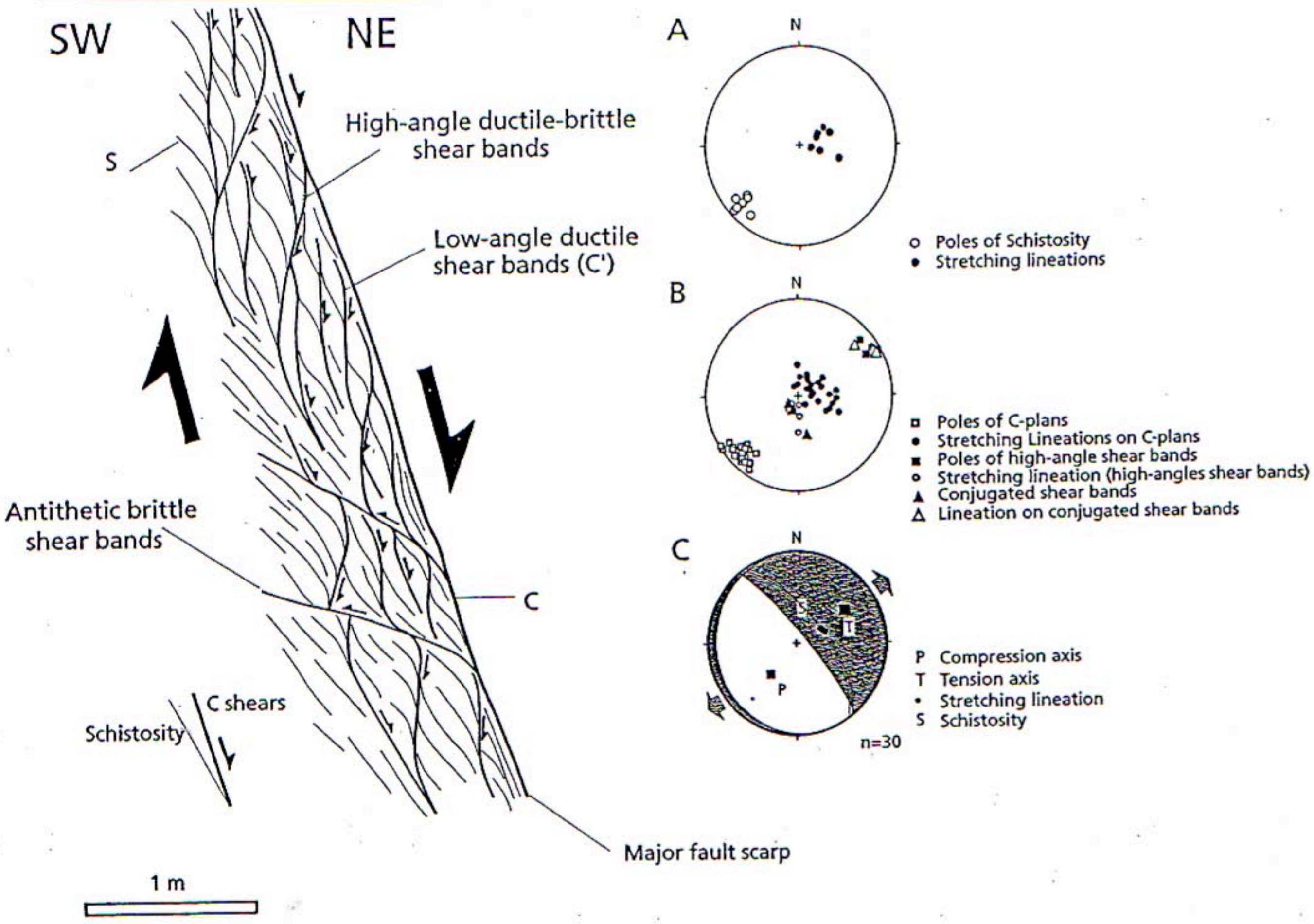

Fig. 5. Kinematic analysis in the footwall of the Forcola fault. (location: west of village of Gordona). Lower hemisphere stereograms. S: schistosity, C: shear plane after Berthé et al. (1979).

(i) the Chiavenna ultramafic complex appears as the lateral equivalent of the Misox zone, both units being situated in the hangingwall of the Forcola normal fault and structurally below the Tambo nappe, and

(ii) the Gruf unit is separated from the Adula nappe by the Forcola normal fault, causing the same angular difference between the foliation trajectories east and west of the normal fault also observed north of Gordona (NW-SE vs. EW). This supports the view that the Gruf unit represents the lateral equivalent of the Adula nappe as proposed by Berger et al. (1996).

Deformation

The Forcola phase is characterized by three dominant structures: a schistosity S_F, a lineation L_F and shearbands, which are especially well established in the hangingwall (Tambo nappe). The Forcola phase overprints the Zapport and Leis structures in the Adula nappe with increasing intensity towards the Forcola Line. In the footwall, the strain due to the Forcola deformation is restricted to a zone that is at most 200 m wide. Within the Tambo nappe, however, shear bands and small normal faults related to the Forcola phase can be observed within the entire nappe. Brittle features are abundant in the hangingwall but can also be observed in the footwall.

Schistosity S_F

In average the Forcola schistosity S_F is dipping with about 42° towards NNE (032/42; cf. inset in Fig. 2). Within the Tambo nappe, the Forcola schistosity is oblique with respect to the older flat-lying predominant schistosities. In the Adula nappe, however, the Forcola schistosity is subparallel to the older 'Zapport' foliation. Here, it is therefore difficult to differentiate between the two schistosities or even between two parageneses. No folds related to the Forcola phase can be observed.

First isoclinal folds in the footwall clearly belong to the Zapport deformation phase and occur about 150 meters below the normal fault zone. Only a few open folds of the Leis phase have been detected in the footwall of the Forcola pass area.

Lineation L_F

The Forcola lineation L_F dips with about 40° to the ENE (067/39). This stretching lineation is mainly built up by chlorite and elongated quartz aggregates. The orientation of the lineation L_F is interpreted to be oriented subparallel to the displacement vector on the normal fault. The Forcola lineation makes a small angle with respect to the pre-existing lineation in the footwall (Zapport lineation of the Adula nappe) as well as in the hangingwall (D2 lineation in the Tambo nappe; Fig. 2).

Shear bands

Shear bands related to the Forcola phase are very abundant and sporadically develop within the non-mylonitic rocks of the hangingwall (Tambo nappe). Deformation is much more pervasive and homogenous in the footwall (Adula nappe) than in the hangingwall. These shearbands are prominent within the first 50 m of Adula-derived mylonites. Further below, shear bands die out as the Forcola phase deformation becomes less intense. A strong deformation gradient within the top 200 m of the Adula nappe is also apparent with respect to fold geometry: Older 'Zapport'-phase folds are not present within the mylonites of the fault zone, while dismembered folds can be observed in the structurally lower 200m. In the Soazza zone isoclinal folds, clearly related to the Zapport phase, are apparent.

Although no quantitative determinations of pressure and temperature are possible, a qualitative statement with respect to the difference between hangingwall and footwall of the fault zone can be deduced. The observed microstructures imply colder temperatures in the hangingwall and warmer conditions in the footwall: Brown biotite has grown within shear bands in the mylonites of the Adula nappe and green biotite and chlorite found in comparable lithologies from the Tambo nappe support this assumption. Therefore, shearbands as well as the other structural elements clearly developed under greenschist facies conditions. Although brittle as well as ductile features can be observed, it is not possible to map out a systematic distribution of brittle and ductile phenomenas due to insufficient displacement across the Forcola normal fault.

Kinematics

In the footwall of the Forcola fault (300m west of Gordona), extensional structures developed under gradually decreasing temperatures (Fig. 5). On the outcrop, C/S relationships, asymmetric clasts, foliation boudinage, and shear bands are the typical structures of the ductile deformation (Hanmer and Passchier, 1991). Low-angle ductile shear bands (C' of Berthé at al. 1979) are better expressed in phyllosilicate-rich lithologies and have shallow angles to the main mylonitic schistosity. In more competent layers, like gneisses, brittle-ductile shear bands develop at higher angles (up to about 60°) to the main mylonitic schistosity (high-angle ductile-brittle shear bands of Fig. 5). These high-angle shear bands gradually evolved into brittle faults, bearing quartz-chlorite striae. They are in the orientation of synthetic Riedel shears with respect to the C-surfaces (Fig. 5). The down-dip chlorite stretching lineation on the major fault scarp, parallel to the C-planes is associated with sense of shear criteria indicating a consistent top-down to the NE-directed relative offset. Antithetic brittle shear bands developed during the last increments of the progressive deformation, conjugate to the main C-surfaces and cross-cutting earlier formed high-angle ductile-brittle shear bands (Fig. 5). All these ductile-brittle shear bands did not offset the main C-planes. On the basis of these field relationships, these microstructures are interpreted as coeval progressive sets of shear bands associated with ongoing Forcola deformation under cooling conditions and across the ductile-brittle transition.

In ductile shear zones, the shear plane and stretching lineation may be considered in first approximation to reflect the displacement-plane and vector, respectively. The inversion programs, often used to deduce stress axes in brittle deformation, can give indications about the incremental strain axes and the bulk kinematics of ductile deformation (Marquer et al., 1996). The program 'Fault kinematics' (Allmendinger et al., 1989), which is based on the P-T axes and the right dihedral graphical methods, was used to determine principal strain axes from striated faults and brittle-ductile shear zones. Fault-slip data from these brittle-ductile normal faults indicate NE-SW oriented extension (Fig. 5C) which is compatible with the extension direction deduced from schistosity-stretching lineations pairs of the ductile deformation (Fig. 5A). The bulk asymmetry between the resolved T axis comprise in the T-intermediate axes plane and the average of schistosity-stretching lineation couple give an indication for a normal faulting with a lowering of the north-eastern block (Fig. 5C).

The results of the kinematic analysis of the brittle and brittle-ductile deformations in the Forcola area are coherent in the footwall and the hangingwall. In the latter, particularly well-developed shear bands are found in the Truzzo granite, north of the Forcola pass (Fig. 6). Brittle faults with the same direction and sense of shear occur further northeast in the Tambo nappe, far away from the main Forcola fault. These results are consistent with an NE-SW directed extension affecting the entire area. This extension was active during decreasing temperatures conditions, as shown by the ductile to brittle transition.

This latter observation indicates that the Forcola normal fault must have been active at a time when the southern Tambo nappe cooled down to below about 300 °C, that is between about 18 and 25 Ma according to biotite Rb-Sr and K-Ar ages (Jäger et al. 1967; Purdy and Jäger 1976; Marquer et

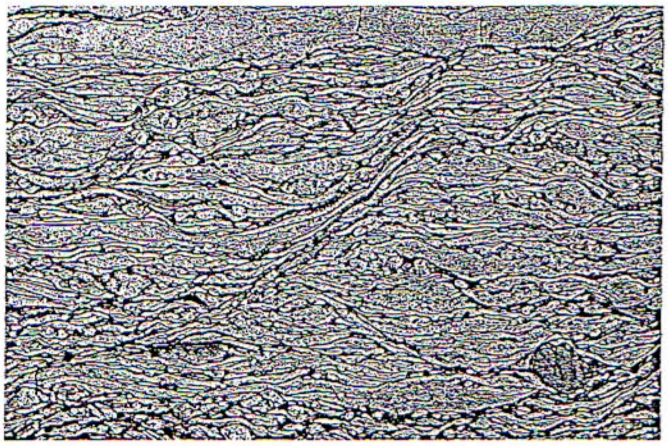

Fig. 6. Micrograph of shear band in deformed 'Truzzo' granite (sample T34, southern Tambo nappe). Sinistral sense of shear indicates top to NE shearing. Field of view is 2.7 mm.

al., 1994). The beginning of the Forcola fault activity cannot be placed before 25Ma because the 25Ma old Novate granite was also deformed by this normal faulting phase. During its last stage (i.e. at around 18Ma), the Forcola phase seems to be coeval with the beginning of displacement on the Simplon normal fault, its symmetrical equivalent structure starting around 20Ma at the western part of the structural Lepontine dome (Steck 1984, Mancktelow 1985; Steck 1990). From its age and kinematics the Forcola normal fault has to be seen in the context of Late Oligocene-Early Miocene transpression, associated with an orogen-parallel stretch and coeval with conjugate dextral and sinistral strike slip along the Insubric and Engadine Lines (Periadriatic fault system), respectively (Schmid & Froitzheim 1993).

Hence, this normal faulting substantially post-dates normal faulting along another prominent E-dipping normal fault in a higher tectonic level, the Turba mylonite (Zapport-D2) (Nievergelt et al. 1996), which predates the intrusion of the Bergell granodiorite (30 Ma; von Blanckenburg 1992). The Early Miocene NE-SW directed extension, well-expressed by the Forcola fault, could be interpreted as the continuation of the Oligocene ductile deformation phase in the Upper Penninic nappes (E-W extension during D2 within the Tambo nappe and Turba normal fault), but with a slightly different stretching direction. It appears that normal faulting on the eastern side of the Lepontine dome corresponds to a main process of stretching oriented parallel to the orogen belt from Late Eocene to Early Miocene time. While the late Eocene-Oligocene E-W extension (D2) is associated with a large isothermal decompression and Oligo-Miocene extension (D4) acts during typical Barrovian cooling, this last event does not necessarily imply a strong crustal thinning or extensional collapse. Hence E-W to NE-SW extensions are not incompatible with the simultaneous N-S to NW-SE bulk compression which is documented in the northern and southern foreland of the Alps for the same interval of time. These two events of stretching parallel to the Alpine belt correspond to different deformation processes during the tectonic evolution of the internal domain of the Alpine belt. These different tectono-metamorphic evolutions reflect a strong exhumation during the main European subduction and lateral extrusion during the evolution of the Periadriatic system, respectively.

Conclusions

Being both due to the Tertiary closure of the Valais ocean, the deformation phases of the Adula and the Tambo nappes can be correlated. However, there are some differences in their tectonic and metamorphic histories: the Adula nappe underwent a complex subduction process that culminated under eclogite facies conditions (Sorreda-Trescolmen), in contrast the Tambo nappe reached lower pressure conditions (D1). Furthermore, deformation related to the south-directed subduction was recorded in the Adula nappe (Zapport), while E-W syn-orogenic extension D2 took place in the Tambo nappe during Eocene time. After these early deformations, the two nappes followed the same Oligo-Miocene tectonic history.

From the observations discussed in the previous chapter, it is evident that the Forcola normal fault greatly contributes to the late stages of unroofing in the Central Alps and plays an important role for the dome-like structure in the SE-Lepontine zone. The main tectonic implications concerning the Forcola deformation are the followings:

(1) The Forcola normal fault offsets the Tambo nappe in the hangingwall relative to the Adula nappe in the footwall with an amount of approximately 3000 m. The direction of faulting is top to ENE.
(2) Due to the observation of ductile and brittle structures, the Forcola fault was active under progressive retrograde conditions. 'Cold' structures are apparent in the hangingwall, 'warmer' structures are apparent in the footwall. An offset of the mineral isograds cannot be determined because of the lack of critical assemblages in the different lithologies as well as a insufficient resolution of the petrologic data.
(3) The continuation of the fault towards the southeast is not clear. However, from trajectory maps of the southeastern 'Lepontine', from contour maps of the fault surface and from recent field work we can suggest that the fault continues into the northern end of the Novate intrusion.
(4) Timing constraints of the Forcola Line are given indirectly by cooling ages from this well-studied part of Central Alps. A realistic age interval is between 25 and 18 Ma.
(5) The Forcola fault might be an equivalent structure to the Simplon fault in the western Central Alps. The Forcola fault was active before the normal faulting in the Simplon area. This time-discrepency could be related to the time-space evolution of the Periadriatic fault system during the late Oligocene-early Miocene transpressive displacement of the Adria plate.

Acknowledgements

We would like to thank M. Frey, N. Froitzheim, R. Hänny, R. Huber, T. Nagel, and J. H. Partzsch for fruitful discussions about the tectonics of the Central Alps. The constructive and helpful reviews by T. Baudin and G. Stampfli are gratefully acknowledged. This study is part of the Ph.D. thesis of C. Meyre that was financially supported by the Swiss National Science Foundation, grants 20–39130.93 and 20–45270.95. D. Marquer was supported by the SNSF grant 20–26313.89. L. Ciancaleoni is supported by the SNSF grant 20–45405.95.

REFERENCES

Allmendiger, R.W., Marrett, R.A. & Cladouhos, T. 1989: Fault kinematics: a program for analysing fault slip data for the Macintosh computer. Cornell university, Ithaca, 34p.

Baudin, T. & Marquer, D. 1993: Métamorphisme et déformation dans la nappe de Tambo (Alpes centrales suisses): évolution de la substitution phengitique au cours de la déformation alpine. Schweiz. mineral. petrogr. Mitt. 73, 285–299.

Baudin, T., Marquer, D. & Persoz, F. 1993: Basement-cover relationships in the Tambo nappe (Central Alps, Switzerland): geometry, structure and kinematics. J. Struct. Geol. 15, 543–553.

Berger, A., Rosenberg, C., Schmid, S. M. 1996: Ascent, emplacement and exhumation of the Bergell pluton within the Southern Steep Belt of the Central Alps. Schweiz. mineral. petrogr. Mitt. 76, 357–382

Berthé, D., Choukroune, P. & Jégouzo, P. 1979: Orthogneiss, mylonite and non coaxial deformation of granites: example of the south armorican shear zone. J. Struct. Geol. 1, 31–42.

Biino, G. G., Marquer, D. & Nussbaum, C. 1997: Alpine and pre-Alpine subduction events in polycyclic basements of the Swiss Alps. Geology 25, 751–754.

Blanc, B. L. 1965: Zur Geologie zwischen Madesimo und Chiavenna (Provinz Sondrio Italien). Mitt. Geol. Inst. ETH Univ. Zürich 37,

Bradbury, H. J. & Nolen-Hoeksema 1985: The Lepontine Alps as an evolving metamorphic core complex during A-Type subduction: Evidence from heat flow, mineral cooling ages, and tectonic modeling. Tectonophysics 4, 187–211.

Challandes N. 1996: Déformation hétérogène et transferts de matière dans les zones de cisaillement des Roffna porphyres de la nappe de Suretta (Col du Splügen, Grisons). Diploma work, Neuchâtel.

Gansser, A. 1937: Der Nordrand der Tambodecke. Schweiz. mineral. petrogr. Mitt. 17, 291–522.

Gulson, B. L. 1973: Age relations in the Bergell region of the Sout-East swiss Alps: With some geochemical comparisons. Eclogae geol. Helv. 66/2, 293–313.

Hanmer, S. & Passchier, C. 1991: Shear-sense indicators: a review. Geol. Soc. Canada, 90–17, 72p.

Hänny, R. 1972: Das Migmatitgebiet des Valle Bodengo. Beitr. geol. Karte Schweiz NF 145, 109.

Hänny, R., Grauert, B. & Soptrajanova, G. 1975: Paleozoic Migmatites Affected by High-Grade Tertiary Metamorphism in the Central Alps (Valle Bodegno, Italy). Contrib. Mineral. Petrol. 51, 173–196.

Heinrich, C. A. 1983: Die regionale Hochdruckmetamorphose der Aduladecke, Zentralalpen, Schweiz. Unpub. Ph. D. Thesis, ETH Zürich.

– 1986: Eclogite Facies Regional Metamorphism of Hydrous Mafic Rocks in the Central Alpine Adula Nappe. J. Petrol. 27, 123–154.

Heitzmann, P. 1987: Evidence of late oligocene/early miocene backthrusting in the central alpine 'root zone'. Geodinimica Acta 1, 183–192.

Hurford, A. J. 1986: Cooling and uplift patterns in the lepontine alps south central Switzerland and an age of vertical movement on the insubric fault line. Contrib. Mineral. Petrol. 92, 413–427.

Hurford, A. J., Flisch, M. & Jäger, E. 1989: Unravelling the thermo-tectonic evolution of the Alps: a contribution from fission track analysis and mica dating. In: Alpine Tectonics (Ed. by Coward, M. P., Dietrich, D. & Park, R. G.). The Geological Society of London, Oxford, 45, 369–398.

Jäger, E., Niggli, E. & Wenk, E. 1967: Rb-Sr Altersbestimmungen an Glimmern der Zentralalpen. Beitr. geol. Karte Schweiz NF 134,

Jenny, H., Frischknecht, G. & Kopp, J. 1923: Geologie der Adula. Beitr. geol. Karte Schweiz NF 51, p. 123.

Löw, S. 1987: Die tektono-metamorphe Entwicklung der Nördlichen Adula-Decke (Zentralalpen, Schweiz). Beitr. geol. Karte Schweiz NF 161,

Mancktelow, N. 1985: The Simplon Line: a major displacement zone in the western Lepontine Alps. Eclogae geol. Helv. 78, 73–96.

Marquer, D. 1991: Structures et cinématique des déformations alpines dans la granite de Truzzo (Nappe de Tambo: Alpes centrales suisses). Eclogae geol. Helv. 84, 107–123.

Marquer, D., Baudin, T., Peucat, J.-J. & Persoz, F. 1994: Rb-Sr mica ages in the Alpine shear zones of the Truzzo granite: Timing of the Tertiary alpine P-T-deformations in the Tambo nappe (Central Alps, Switzerland). Eclogae geol. Helv. 87, 225–239.

Marquer, D., Challandes, N. & Baudin, T. 1996: Shear zone patterns and strain partitioning at the scale of a Pennine nappe: the Suretta nappe (eastern Swiss Alps). J. Struct. Geol., 18/6, 753–764.

Marquer, D. , Challandes, N. & Schaltegger, U. (in press): Early Permian magmatism in Briançonnais terranes: Truzzo granite and Roffna rhyolite (Eastern pennine nappes, Swiss and Italian Alps). Schweiz. mineral. petrogr. Mitt.

Massonne, H.-J. & Schreyer, W. 1987: Phengite geobarometry based on the limiting assemblage with K-feldspar, phlogopite, and quartz. Contrib. Mineral. Petrol. 96, 212–224.

Merle, O. 1994: Syn-convergence exhumation of the Central Alps. Geodinimica Acta 7, 129–138.

Meyre, C. & Puschnig, A. R. 1993: High-pressure metamorphism and deformation at Trescolmen, Adula nappe, Central Alps. Schweiz. mineral. petrogr. Mitt. 73, 277–283.

Meyre, C., de Capitani, C. & Partzsch, J. H. 1997: A ternary solid solution model for omphacite and its application to geothermobarometry of eclogites from the Middle Adula nappe (Central Alps, Switzerland). J. metamorphic Geol. 15, 687–700.

Milnes, A. G. & Schmutz, H. U. 1978: Structure and history of the Suretta nappe (Pennine zone, Central Alps): A field study. Eclogae geol. Helv. 71, 19–33.

Moticska, P. 1970: Petrographie und Strukturanalyse des westlichen Bergeller Massivs und seines Rahmens. Schweiz. mineral. petrogr. Mitt. 50, 355–443.

Nievergelt, P., Liniger, M., Froitzheim, N. & Ferreiro Mählmann, R. 1996: Early to mid Tertiary crustal extension in the Central Alps: The Turba Mylonite Zone (Eastern Switzerland). Tectonics 15, 329–340.

Partzsch, J. 1998: The tectono-metamorphic evolution of the middle Adula nappe, Central Alps, Switzerland. Unpub. Ph.D. Thesis, University of Basel.

Partzsch, J. H., Frey, M., Kruspan, P., Meyre, C. & Schmid, S. M. 1994: Die tektono-metamorphe Entwicklung der mittleren Adula-Decke (Zentralalpen, Schweiz) In: 5. Symposium Tektonik-Strukturgeologie-Kristallingeologie. Göttinger Arb. Geol. und Paläont., 124–126).

Pfiffner, O. A. 1977: Tektonische Untersuchungen im Infrahelvetikum der Ostschweiz. Mitt. Geol. Inst. ETH Univ. Zürich 217, 432.

Purdy, J. W. & Jäger, E. 1976: K-Ar ages on rock-forming minerals from the Central Alps. Mem. Ist. Geol. Min. Univ. Padova v. 30, p. 32.

Risold, A. C., Trommsdorff, V., Reusser, E. & Ulmer, P. 1996: Alpe Arami and Cima di Gagnone garnet peridotites: observations contradicting the hypothesis of ultra deep origin. Eos Trans. AGU, Fall Meet. Suppl. 77, F761.

Rosenberg, C. 1996: Magmatic and solid-state flow during the syntectonic emplacement of the western Bergell pluton: field studies and microstructural analysis. Ph. D. Thesis Geol.-Paläont. Institut Univ. Basel, Nr. 8.

Schmid, S. M. & Froitzheim, N. 1993: Oblique slip and block rotation along the Engadine line. Eclogae geol. Helv. 86, 569–593.

Schmid, S. M., Aebli, H. R., Heller, F. & Zingg, A. 1989: The role of Periadriatic line in the tectonic evolution of the Alps. In: Alpine Tectonics, (Ed. by Coward, M.P., Dietrich, D. & Park, R.G.), Geol. Soc. Spec. Publ. 45, 153–171.

Schmid, S. M., Rück, P. & Schreurs, G. 1990: The significance of the Schams nappes for the reconstruction of the paleotectonic and orogenic evolution of the Penninic zone along the NFP-20 East traverse (Grisons, eastern Switzerland). Mém. Soc. géol. France 156, 263–287.

Schmid, S. M., Pfiffner, O. A., Froitzheim, N., Schönborn, G. & Kissling, E. 1996: Geophysical-geological transect and tectonic evolution of the Swiss-Italian Alps. Tectonics 15, 1036–1064.

Schmid, S. M., Pfiffner, O. A. & Schreurs, G. 1997a: Rifting and collision in the Penninic zone of eastern Switzerland. In: Deep structure of the Swiss Alps. Results of NRP 20 (Ed. by Pfiffner, O.A., Lehner, P., Heitzmann, P., Müller, S. & Steck, A.). Birkhäuser, Basel, 160–185.

Schmid, S. M., Pfiffner, O. A., Schönborn, G., Froitzheim, N. & Kissling, E. 1997b: Integrated cross section and tectonic evolution of the Alps along the eastern traverse. In: Deep structure of the Swiss Alps. Results of NRP 20. (Ed. by Pfiffner, O. A., Lehner, P., Heitzmann, P., Müller, S. & Steck, A.). Birkhäuser, Basel, 289–304.

Schreurs, G. 1993: Structural analysis of the Schams nappes and adjacent tectonic units: implications for the orogenic evolution of the Penninic zone in the Eastern Switzerland. Bull. Soc. géol. France 164, 425–435.

Stampfli, G. M., Mosar, J., Marquer, D., Marchant, R., Baudin, Th. & Borel, G. 1998: Subduction and obduction processes in the Swiss Alps. Tectonophysics, in press.

Steck, A. 1984: Structures de déformations Tertiaires dans les Alpes Centrales (transversale Aar-Simplon-Ossola). Eclogae geol. Helv. 77, 55–100.

– 1990: Une carte des zones de cisaillement ductile des Alpes Centrales. Eclogae geol. Helv. 83, 603–627.

Steinmann, M. 1994: Ein Beckenmodell für das Nordpenninikum der Ostschweiz. Jb. Geol.B.-A., 137/4, 675.721.

von Blanckenburg, F. 1992: Combined high-precision chronometry and geochemical tracing using accessory minerals: applied to the Central-Alpine Bergell intrusion (central Europe). Chemical Geology 100, 19–40.

Weber, W. 1966: Zur Geologie zwischen Chiavenna und Mesocco. Mitt. Geol. Inst. ETH Univ. Zürich 57,

Wenk, H. R. 1973: The structure of the Bergell Alps. Eclogae geol. Helv. 66, 255–291.

Manuscript received June 3, 1998
Revision accepted November 3, 1998

Chapter 3

Part I

Paleostress inversions: some outlooks from methodological comparisons (example from the Bergell area, Central Alps, Switzerland)

LAURENT CIANCALEONI, CHRISTIAN SUE, CÉCILE ALLANIC, DIDIER MARQUER

IN PREPARATION FOR: ECLOGAE GEOLOGICAE HELVETIAE

Paleostress inversions: some outlooks from methodological comparisons (example from the Bergell area, Central Alps, Switzerland)

LAURENT CIANCALEONI, CHRISTIAN SUE, CÉCILE ALLANIC, DIDIER MARQUER

1. Introduction

The response of the upper crust to continental collision and huge horizontal tectonic forces is partly by displacements localized along sets of faults. Therefore fault-slip data must be analyzed to quantify stress and strain magnitudes and orientations. The orientations, slip directions, and shear-senses of faults, which collectively form a fault-slip datum, record information on applied stress and strain. Accordingly, over the past decade, a plethora of dynamic and kinematic methods have been developed for extracting stress and strain from faults (e.g. Carey and Brunier, 1974; Angelier and Mechler, 1977; Angelier, 1979; Etchecopar et al., 1981; Gephart and Forsyth, 1984; Simon-Gomez, 1986; Lisle, 1988; Marrett and Allmendinger, 1990; Fleischmann and Nemcok, 1991; Will and Powell, 1991; Nemcok et al., 1999). The basic assumption to all these methods is that all faults slip independently in a homogeneous stress field (Wallace, 1951; Bott 1959). It is implicit in that model that the slip direction on a fault plane is determined by a single stress deviator and that all faults slipped in a way consistent with that stress deviator. Common field observations of contradictory shear senses on sets of faults with similar orientation and/or evidences of fault surfaces reactivation such as superposed stria are not compatible with a single stress tensor. In such circumstances, superimposed stress states (or heterogeneous stress states) result e.g. in a complex geometrical distribution of faults. Accordingly, several methods have been developed in order to separate stresses from heterogeneous fault-slip data (e.g. Angelier, 1979; Etchecopar et al., 1981; Armijo et al., 1982; Angelier, 1984; Huang, 1988; Hardcastle and Hills, 1991; Yin and Ranalli, 1993; Fry, 1999; Nemcok et al., 1999; Yamaji, 2000; Shan et al., 2003). Faced with the variety of methods and software packages based on different assumptions, approximations or algorithms to analayse faults and separate tensors, one can have half a mind to put into question the reliability of results from the different methods. Studies of this kind are actually few (Angelier, 1975; Casas and Simon, 1992; Arlegui-Crespo and Simon-Gomez, 1998; Tomljenovic and Csontos, 2001; Liesa and Lisle, 2004).

In this paper, we adress the analysis of one natural heterogeneous data set via the use of different methods and/or softwares. The aim of this paper is to expose a comparative analysis of these various methods on a well-constrained natural site for relative reactivation chronology and quality of fault slip measurements. The computation runs with the various methods are tested for validity against the consistent relative chronology criteria observed in the field.

2. Methodology and data analysis

The measurement site is located in the internal domain of the Alpine collision belt, within the Tertiary Bergell pluton of the eastern Central Alps (fig. 1). Brittle faulting there occured during the last stages of the continental collision, in the context of lateral eastward extrusion of the Central Alps by the late Oligocene onwards (Ciancaleoni, 2005). This site has been chosen because relative chronology criteria are well established (fig.2) and the quality of the measurements is generally good to very good. We propose a multi-method analysis of this large fault-stria set, made of 69 measurements (fig. 3a). This site has been chosen as it is representative of the regional deformation state, as exposed in chapter 3, part II: the geometric and kinematic distributions of faults are representative of the overall regional deformation. So we refer to this chapter (Chapter 3, Part II) for a regional analysis, and we only deal here with the methodological approach of paleostress inversion. This database could be actually divided into two subsets corresponding to two brittle deformation stages, on the basis of consistent relative chronology criteria such as two striae bearing fault planes and cross-cutting relationships between faults (Figure 3b, 3c and 3d). These relative slip age criteria indicate that normal faulting acted before striike-slip displacement. The faults are thus a priori attributed to different relative age data sets and each homogeneous subset of faults is assumed to correspond to a single stress tensor (figure 3c and 3d). Note that there is no relative dominance of the subgroups, since they consist of 31 faults and 38 faults, respectively. If interpreted as conjugate Andersonian systems the faults in each subset indicate roughly a shallow $\sigma 3$ direction to NE for both sets of faults, with a vertical $\sigma 1$ for normal faults and $\sigma 1$ direction to NW for transcurrent faults.

We applied here nine different methods and/or softwares to reconstruct the paleostress state, for the global dataset, and for of each subset of faults, in order to test the global reliability and stability of stress inversion/reconstruction on one given natural example. The present methods of faulting analysis fall into two groups of procedures: manual and semi-automatic ones. The former analyse data in a graphical representation form, the latter are numerical methods that automatically minimize some parameters to resolve the best fit tensor to the analysed faults. Another category of procedure, the automatic separation of homogeneous datasets from heterogeneous ones, are based on attributes of faults (e.g. Nemcok et al., 1999). This latter category was not inplemented in this study. The inversion schemes as applied to the natural site investigated are described in the following sections. These methods are the graphical P-B-T axes (Turner, 1953) and Right Dihedra (Angelier and Mechler,

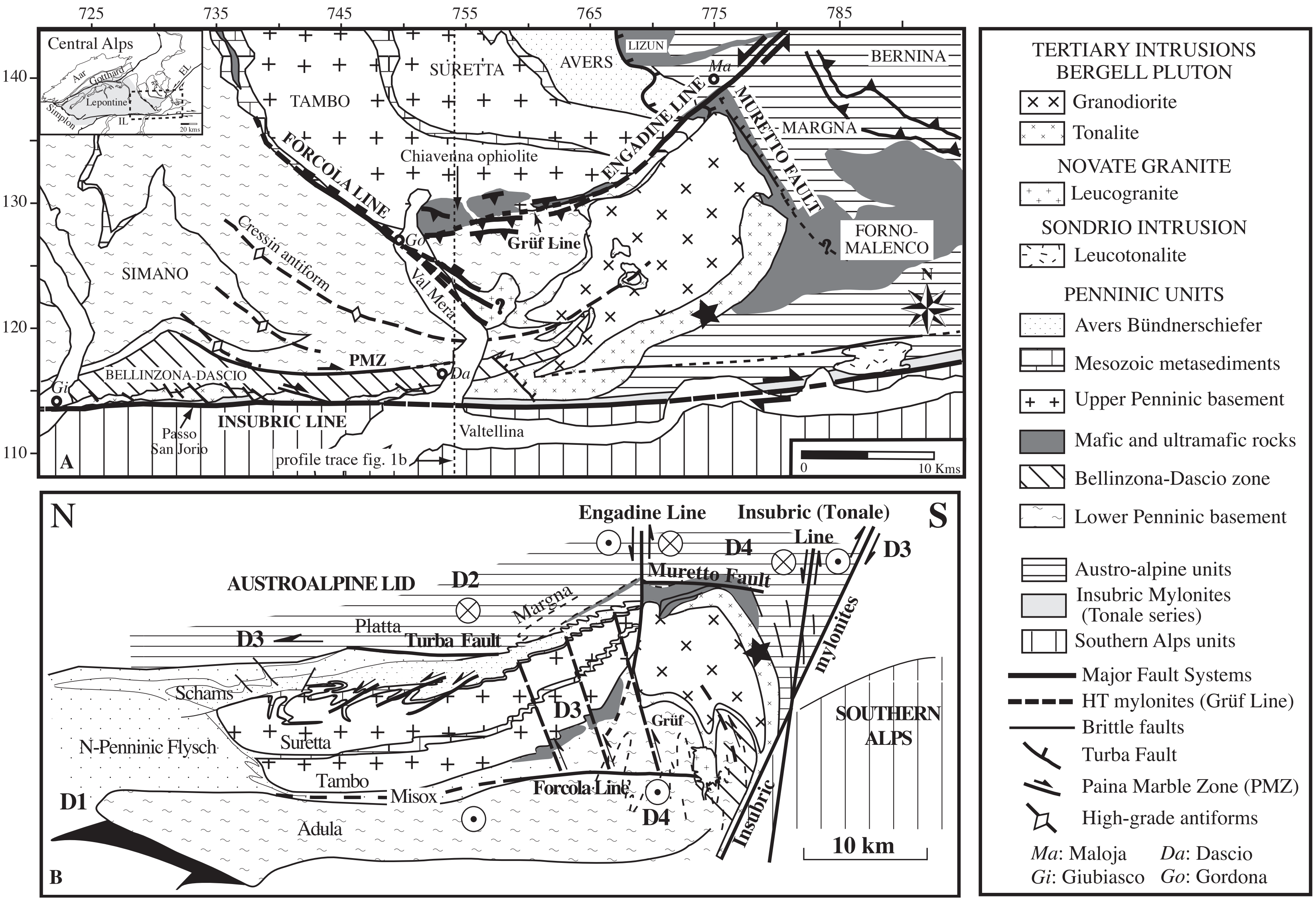

Fig. 1. (A) Geologic and tectonic setting of the Bergell and Insubric areas in the Eastern Central Alps. Question marks when the lateral prolongation of faults is uncertain. Modified from Rosenberg et al. (1995), Huber and Marquer (1996) and Meyre et al. (1998). The solid star represents the location of the site chosen for the study.(B) N-S geological profile along the Eastern Traverse. Modified from Schmid et al. (1996a) and Huber and Marquer (1996). Regional deformation phases (D1-D4) are discussed in Huber and Marquer (1996) and Meyre et al. (1998).

Fig. 2. Cross-cutting relationships of striations on a fault surface of the natural site investigated. Both the down-dip (older) and shallow dip (younger) stria are epidote-chlorite bearing and mineral steps indicate a normal and dextralkl offset, respectively.

1977) methods. Numerical methods implemented therein are the Numerical Dynamic Analysis (Sperner et al., 1993), the Direct Inversion Method (Angelier, 1979) and the Stress inversion method of Reches (1987). The software packages Faultkin (Allmendinger et al., 1989), TectonicVB (Ortner et al., 2002), and Stress (Villemin and Charlesworth, 1992) have been used to graphically and numerically analyse our fault-slip data. The global results are extensively detailed in table 1. Note that these methods are also generally applicable to earthquake focal mechanism solutions, as the problems of fault/stria and focal mechanism inversion are very similar.

Fig. 3. (A) The heterogeneous natural measurement site investigated is made of a database of 60 fault-striae couples (center stereonet, lower hemisphere projection), encompassing normal and strike-slip faults distributed over a wide range of orientations (right stereonet). Left diagram: tangent lineation diagram (Hoeppener, 1955). This pole projection method uses the poles of the fault planes in the lower hemisphere of the equal area net. The lineation is projected onto the poles with a short arrow indicating the sense of movement of hanging-wall block. Homogeneous groups of faults are identified by the subparallel lineation arrows which point out towards a common shortening axes. (B) Cross-cutting relationships of striations on fault surfaces (1 is older, heavy great circles and striations) and fault planes (dashed great circle is older fault). (C) Genetic grouping and separation of the heterogeneous dataset into two homogeneous subsets on the basis of relative age criteria.

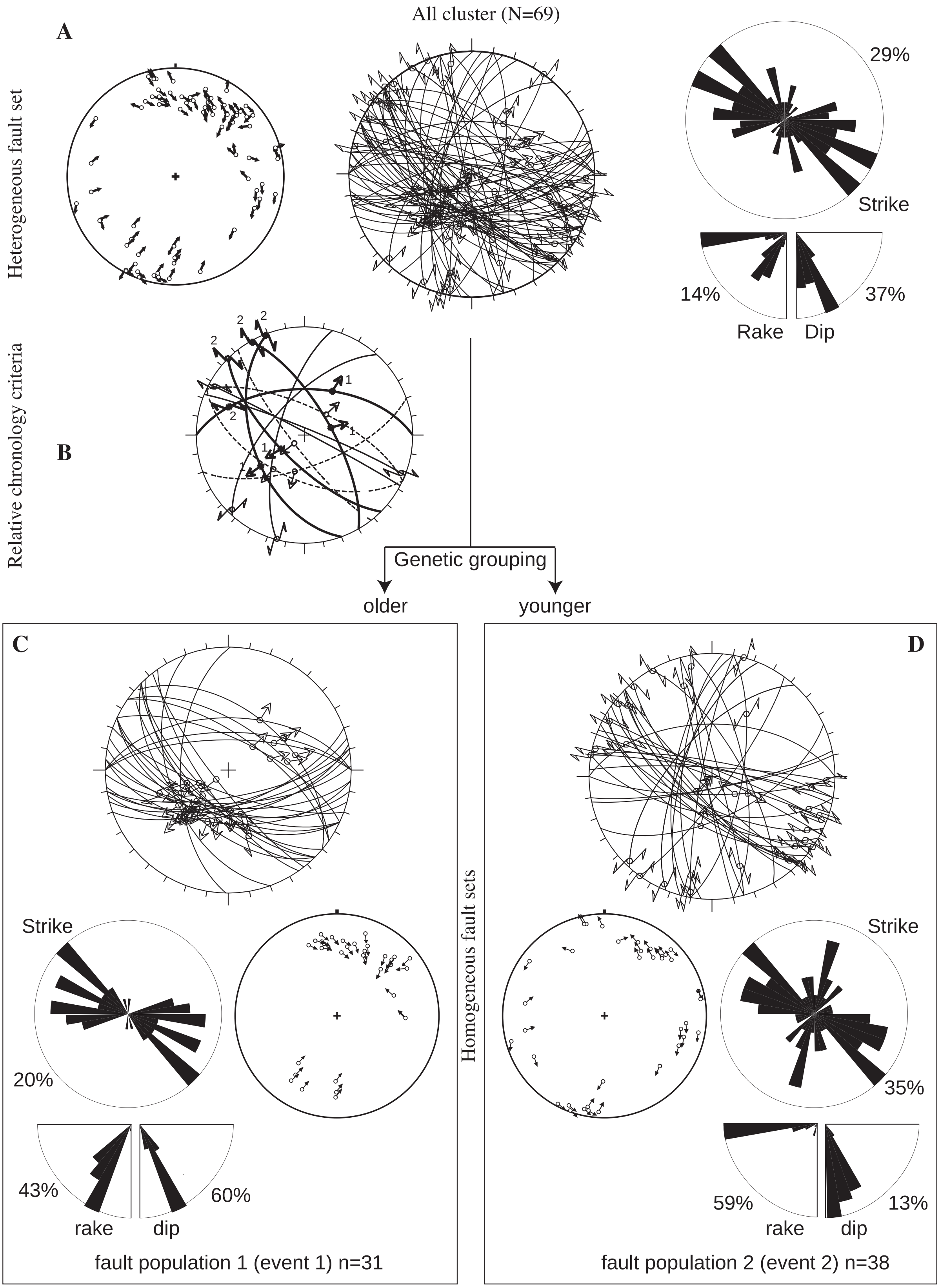
A
All cluster (N=69)
Heterogeneous fault set
29%
Strike
14%
37%
Rake
Dip
Relative chronology criteria
B
2
2
2
1
2
1
1
1
Genetic grouping
older
younger
C
Strike
20%
43%
60%
rake
dip
fault population 1 (event 1) n=31
Homogeneous fault sets
D
Strike
35%
59%
13%
rake
dip
fault population 2 (event 2) n=38

All fault-slip analysis techniques initially follow a two-dimensional Coulomb criterion for failure to guide inferences about the stresses responsible for faults in isotropic media (Anderson, 1951). In this state of initial failure (neoformed faults) and plane strain deformation, the intermediate stress and strain axes lie within the fault plane, and the maximum and minimum principal stress and strain axes lie in a plane containing the fault plane normal and the slip line (movement plane; Arthaud, 1969). The angle between the maximum principal stress axis and the fault plane is controlled by rock material properties (θ= 45° - Ø/2 with Ø the angle of internal friction). While a mean empiric value of θ=30° is a reasonably good approximation (Byerlee, 1968; Jaeger and Cook, 1979), natural observations call for a high variability of θ.

Our example site underwent superimposed stress states (or heterogeneous stress states) resulting in a complex geometrical distribution of faults, which depart from that simplified model. The different steps we addressed in our fault-slip analysis, in order to overcome that difficulty, tracks the procedure undertaken by Angelier (1984). The key point in our proceeding is that we favoured in this polyphased deformation case an approach that separates faults prior to stress inversions, with the expertise of the geologist.

Common to all these methods of fault-slip analysis are basic assumptions and limitations, which have been discussed in detail elsewhere (e.g. Carey and Brunier, 1974; Carey, 1979; Etchecopar et al., 1981; Angelier, 1984; Allmendinger et al., 1989; Angelier, 1989; Marrett and Allmendinger, 1990; Dupin et al., 1993; Pollard et al., 1993). Regardless of whether the stress or kinematic hypothesis is assumed, the inversion schemes are based on the simplified models of Wallace (1951) and Bott (1959) that all faults slip parallel the direction of maximum resolved shear stress (respectively shear strain) of one single and spatially homogeneous global stress stensor (respectively strain tensor). it is necessary to make some basic assumptions: (1) the rock volume should be isotropic and homogeneous, or in other words the deformation accumulated from many slip events distributed along fractures having a wide diversity of orientations; (2) displacements on faults should be incremental and faults should slip independently (mechanical interactions between faults); (3) the stress field should be uniform and steady during a given tectonic phase (mean state of stress); (4) the deformation is non rotational and stress and strain tensors are coaxial; (5) no post-faulting reorientation of the fault-slip data has occured. In general cases fault-slip data may depart widely from these basic assumptions, mainly because of strong local deformation, and stress variations due to pre-existing anisotropies and inherent rock heterogeneities.

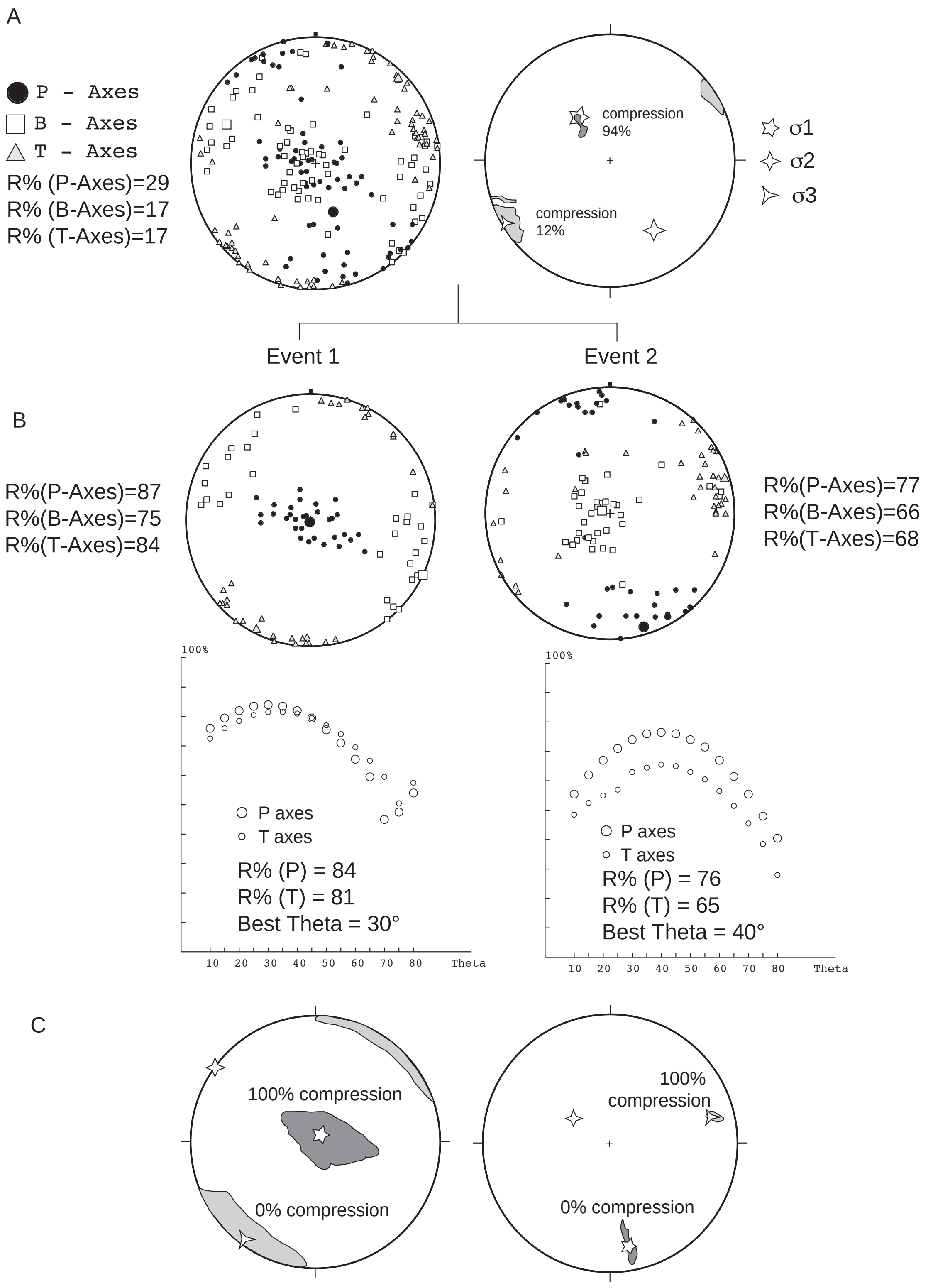

Fig. 4. (A) The graphical methods expressed via the P-B-T axes method and the Right Dihedra method. (A) Distribution of P-B-T axes of the heterogeneous fault set (left) and potential areas for σ1 and σ3 together with % of maximum compression and extension fields of the right dihedra method (right, dark gray and light gray, respectively). Results from the software TectonicVB (P-B-T axes) and Stess (right dihedra), see table 1. R% is a measure for clustering (maximum clustering is maximum R%, see in Ortner et al., 2002 for more details). (B) Top stereonets: Separation of the heterogeneous dataset into two homogeneous subsets via the P-B-T axes method. Bottom diagrams: calculated P-T axes stepwise for theta angles between 10 and 80° and vosualization of the clustering of the P (large open circles) and T axes (small open circles). The best theta angle for the dataset is evaluated according to maximum R%. (C) The right dihedra inversion of homogeneous sets of faults (Stress software results, see table 1). See text for more explanations and references.

2.1. Graphical methods

(1) The «P-B-T axes method» (Figure 4a and 4b), initially finalised for stress analysis using e twin lamellae in calcite (Turner, 1953), constructs for each fault plane a pressure (P) and tension (T) axis. This method also accommodates fault-slip analysis provided that a value of 30° (mean experimentally obtained value) for ϕ is used for calculations. The P and T axes (principal incremental shortening and extension axes, respectively) are perpendicular, and placed in bisector planes of the fault and auxiliary planes, in such a way to cause movement in the direction recorded for each fault. Vectorial means or conditioned least-squares fit are computed to locate orthogonalized loci of the kinematic axes for a given population of faults (Caputo and Caputo, 1988). The linked Bingham axes (Mardia, 1972) akin to the principal incremental shortening and extension axes are the equivalent of an unweighted moment tensor summation, where all the faults are given equal weight, and the kinematics are assumed to be scale-invariant (Marrett and Allmendinger, 1990). According to these authors, this will affect the accuracy of the method, as will e.g. any sampling bias with respect to the whole fault population, or any spatial heterogeneity of the strain. Weighting of the data may be qualitatively assessed by comparing the kinematics of largest faults on outcrops with all the minor faults from within a measurement station. Does a good correlation exist, then the fault kinematics are scale-invariant, which is the case in this study. Drawback of this method is that the ratio of principal stresses is not computed, that it recognizes sense of slip on the faults, and that it should theoretically be applied to neoformed faults in a homogeneous rock mass only, which is usually not realized in nature because preexisting anisotropies are generally the rule. The distribution of P and T axes akin to a single fault population however brings about insights concerning the kinematic regime (e.g. see in Ortner et al., 2002). Concerning our specific analysis, we obtained stable stress axes for both used softwares (Faultkin and TectonicVB), corresponding to a SWward oriented extensional axes T for the subset 1 in extension ([210,9] and [206.2] respectively) and stable T ([74,10] and [74,5] resp.) and P ([165,8] and [163,6] resp.) for the subset 2 (transcurrent). We refer to the table 1 for the complete parameters of the stress reconstructions.

(2) The right dihedra method (fig. 4a, right stereonet, fig. 4c) (e.g. Angelier and Mechler, 1977; Pfiffner and Burkhard, 1987), dynamically constrain the orientation of stress axes for a population of neoformed or inherited faults. It applies statistics to half space compression (P) and tension (T) dihedra, as defined by faults and their respective striation, for a set of faults. The geometrical centers of inferred compression and extension dihedra approximate the location of the maximum and miminum stress axes orientations respectively, provided that the number and variety of fault mechanisms are large enough (Angelier and Mechler, 1977). The oneness of the stress ratio is nevertheless not constrained by this method. Pfiffner and Burkhard (1979) however qualitatively discussed

	Graphical Methods					Numerical Methods			
	P-T-B Axes		P-T Right Dihedra			Numeric Dynamic Analysis	Direct Inversion		Stress Inversion
	Faultkin Linked Bingham Axes	TectonicVB	FaultKin	Tectonic VB	Stress	TectonicVB	TectonicVB	Stress	Invert
STEP 1 : All Faults	N= 69 θ=45° P (e_3) B (e_2) T(e_1) 152/76 335/14 245/1 Normalized magnitudes 0.13 0.11 -0.25 Deformation Type Transtensive	N=69 θ=30° P (e_3) B (e_2) T(e_1) 159/56 293/23 45/6 Deformation Type Axial extensive	N=69 σ1 σ2 σ3 326/53 247/5 % maximum compression 76% % maximum extension 88% Deformation Type Transtensive	N=69 σ1 σ2 σ3 359/85 151/3 241/2 Deformation Type Extension	N=69 σ1 σ2 σ3 323/56 148/34 239/2 % maximum compression 94% % maximum extension 88% Deformation Type Transtensive	N=69 θ=30° P (e_3) B (e_2) T(e_1) 170/78 324/10 55/4 ϕ=0.79 SM=28° n=65% Deformation Type Transtensive	N=69 σ1 σ2 σ3 179/8 56/75 271/12 ϕ=0.30 SM=23° n=54% Deformation Type Pure compressive	N=69 σ1 σ2 σ3 290/83 154/5 64/5 Normalized magnitudes 0.8 0.1 -0.9 ϕ=0.59 SM=32° n=46% Deformation Type Pure extensive	N=69 σ1 σ2 σ3 196/83 338/4 68/3 Normalized magnitudes -1 -0.99 -0.98 ϕ=0.97 SM=39° PAM=42° μ=0 n=41% Deformation Type Transtensive
STEP 2 : Subset 1 Faults Event 1	N=31 θ=45° P (e_3) B (e_2) T(e_1) 17/80 120/2 210/9 Normalized magnitudes 0.38 0.01 -0.38 Deformation Type Pure extensive	N=31 θ=30° P (e_3) B (e_2) T(e_1) 208/89 296/0 206/2 Deformation Type Extensive	N=31 σ1 σ2 σ3 108/57 196/10 % maximum compression 100% % maximum extension 100% Deformation Type Pure extensive	N=31 σ1 σ2 σ3 18/80 121/2 211/9 Deformation Type Extension	N=31 σ1 σ2 σ3 38/84 306/0 216/5 % maximum compression 100% % maximum extension 100% Deformation Type Pure extensive	N=31 θ=30° P (e_3) B (e_2) T(e_1) 008/89 114/0 204/0 ϕ=0.48 SM=13° n1=90% Deformation Type Pure extensive	N=31 σ1 σ2 σ3 159/74 332/15 62/1 ϕ=0.18 SM=9° n1=84% Deformation Type Radial extensive	N=31 σ1 σ2 σ3 66/82 309/3 219/7 Normalized magnitudes 0.9 -0.1 -0.8 ϕ=0.44 SM=12° n1=100% Deformation Type Pure extensive	N=28 σ1 σ2 σ3 134/83 318/6 228/0 Normalized magnitudes -1.01 -0.3 -0.18 ϕ=0.15 SM=10° PAM=18° μ=0.8 n1=100% Deformation Type Radial extensive
STEP 2 : Subset 2 Faults Event 2	N=38 θ=45° P (e_3) B (e_2) T(e_1) 165/8 292/77 74/10 Normalized magnitudes 0.35 -0.01 -0.34 Deformation Type Pure strike-slip	N= 38 θ=40° P (e_3) B (e_2) T(e_1) 163/6 288/85 74/5 Deformation Type Strike-slip	N=38 σ1 σ2 σ3 171/25 262/13 % maximum compression 100% % maximum extension 100% Deformation Type Pure strike-slip	N=38 σ1 σ2 σ3 166/12 311/75 75/8 Deformation Type Strike-slip	N=38 σ1 σ2 σ3 169/20 304/63 76/19 % maximum compression 100% % maximum extension 100% Deformation Type Strike-slip	N=38 θ=40° P (e_3) B (e_2) T(e_1) 162/8 291/76 71/10 ϕ=0.49 SM=9° n2=74% Deformation Type Pure strike-slip	N=38 σ1 σ2 σ3 171/4 254/86 081/3 ϕ=0.50 SM=6° n2=71% Deformation Type Pure strike-slip	N=38 σ1 σ2 σ3 167/13 333/76 76/3 Normalized magnitudes 0.9 -0.1 -0.8 ϕ=0.43 SM=12° n2=95% Deformation Type Pure strike-slip	N=41 σ1 σ2 σ3 160/11 300/74 68/9 Normalized magnitudes -1.17 -1.01 -0.47 ϕ=0.77 SM=10° PAM=18° μ=0.4 n2=61% Deformation Regime Transtensive

Table 1. Summary of fault-slip analysis data results by inversion from both kinematic and dynamic methods using several available software packages The computer-based algorithms used in this study comprise Faultkin (Marrett and Allmendinger, 1990), TektonicVB (Ortner, 1991), Stress (Villemin and Charlesworth, 1992) and Invert (Reches, 1987, 1992). The graphical analyses include the P-T-B Axes method (Turner, 1953; Marrett and Allmendinger, 1990), and the Right Dihedron method (Angelier and Mechler, 1977. Numerical stress analyses encompass the Numeric Dynamic Analysis method (Spang, 1972; Sperner et al., 1993), the Numeric Direct Inversion method (Angelier, 1979, 1984) and the Stress Inversion method (Reches, 1987, 1992). ∏ is the assumed angle between the maximum principal stress axis and the fault plane. N is number of faults at each step of the inversion procedure. P-B-T axes are the principal incremental shortening, intermediate and extension axes, respectively. σ1, σ2, and σ3 are the maximum, intermediate and minimum stress axes (σ1 ≥ σ2 ≥ σ3 ≥ 0). ϕ=(σ2-σ3)/(σ1-σ3) is the ratio of principal stress differences (shape factor). n, n1 and n2 are the final % of faults explained by the tensor solution, for the heterogeneous dataset, the homogeneous subset 1 and the homogeneous subset 2, respectively, according to the various fault selection criteria implemented in the methods. See text for other symbols explanation.

the pattern of density curves for coherent data sets in relation with the type of strain akin to the fault kinematics. We obtain also axes directions very close to the PBT method (Table 1).

Despite robust, both these graphical methods of fault-slip data inversion benefit of directness and ease of visualization, and are a necessary introductory step to test the mechanical compatibility of combined faults from each site. They also proved their efficiency to detect kinematic heterogeneities from a set of fault-slip data (Pfiffner and Burkhard, 1979; Carey-Gailhardis and Vergely, 1992; Marrett and Allmendinger, 1990). Mixed data sets are indicated in figure 4a both by the spread in P and T axes orientation, and by the lack of pure compression (100% compression) and pure extension (0% compression) fields. While the T axes show a strong clustering, the P and B axes describe a girdle pattern, indicating kinematically hererogeneous faulting. According to Marrett and Allmendinger (1990), triaxial deformation can lead to this kind of complex pattern, as will any anisotropy reactivation, strain compatibility constraints, or multiple deformations. The first two of these are particulary relevant to the data set, because of the multiplicity of fault orientations and the orthorombic fault pattern (Aydin and Reches, 1982), as well as reactivated faults. A simple visual separation of kinematic axes and faults attitude, corroborated by relative geochronology criteria, consequently allows two more homogeneous subsets of faults to be individualized, corresponding to an older extensional event 1 and a younger strike-slip event 2.

2.2. Numerical methods

Several numerical methods have been developed to find the best reduced stress tensor associated to a given set of faults. They aimed in particular to achieve a more complete and accurate approach to paleostress analysis, which requires: (a) evaluation of the best cohesion and friction coefficients of the discontinuities from the fault-slip inversion (e.g. Reches, 1987, 1992 ; Hardcastle, 1989), from which the mean angle θ may be adressed; (b) consideration of the stress ratio $\phi=(\sigma2-\sigma3)/(\sigma1-\sigma3)$, which influences both orientation of the principal stress axes and the slip direction (Bott, 1959).

(3) The numerical dynamic analysis (NDA) was originally designed to calculate the paleostress/strain tensor by plane-lineation-glide sense obtained from calcite twins (Spang, 1972). In that sense it is very similar to the P-B-T axes method (Turner, 1953). Later on it was adapted numerically for use with fault-slip analysis by Sperner et al. (1994), considering particular material properties method (θ= 30°). This method assumes an arbitrary maximum shear stress magnitude along each fault plane and the coincidence of the stress axes $\sigma1$ and $\sigma3$ with the P- and T-axis, respectively. It thus actually provides the kinematic axes of the deformation. Eigenvectors and eigenvalues of the bulk stress tensors determine the orientation and the relative values of the principal compression and extension axes. Homogeneous fault-slip data subsets previously separated from example site by

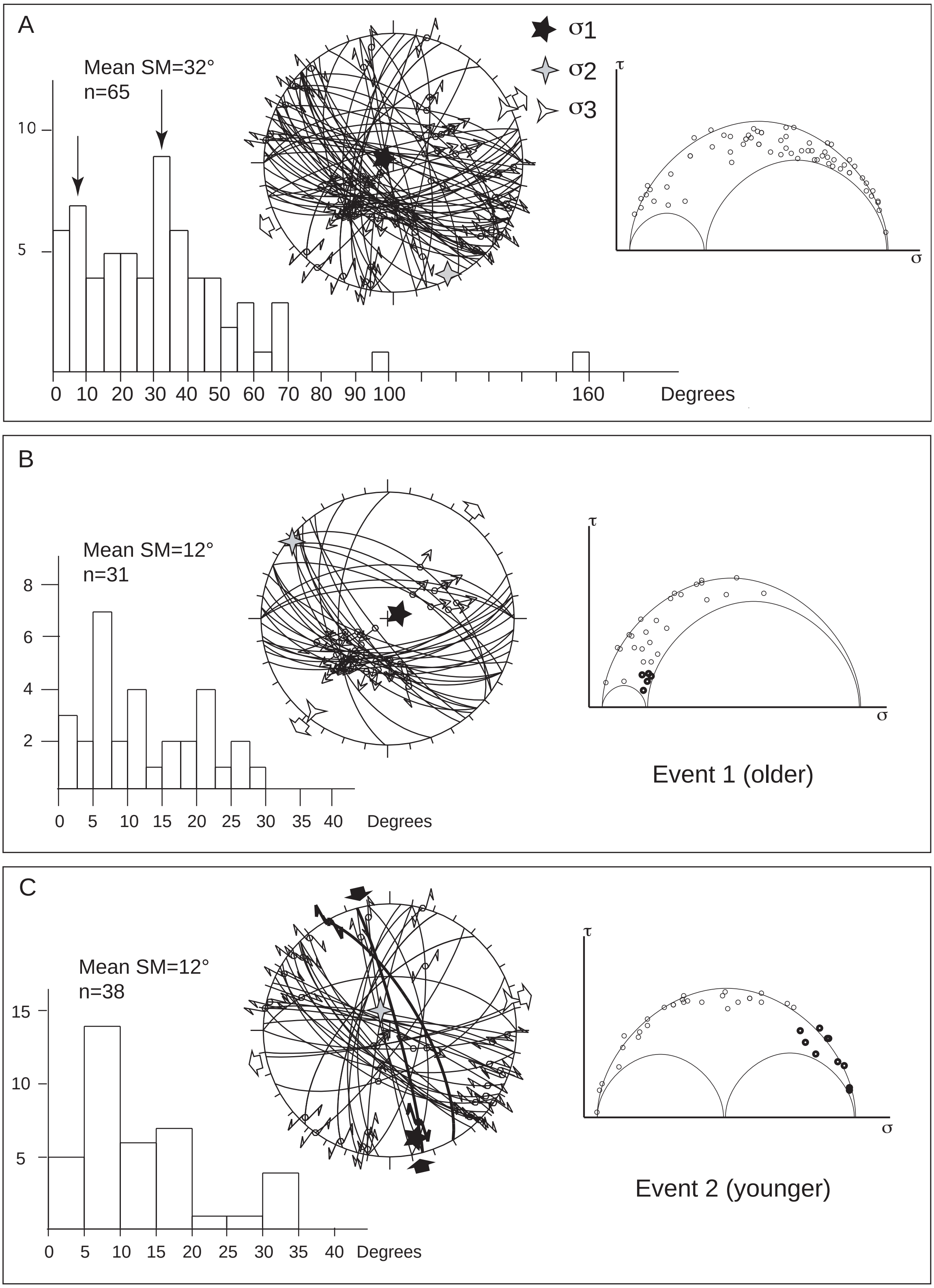

Fig. 5. Results of the direct inversion method using the software Stress. (A) The left stereonet represents the paleostress tensor computed for the whole dataset, with the faults great circle projection and slip projection (arrows), and the three principal stress axes σ1, σ2, and σ3. The histogram gives the statistical distribution of the angle between the measured striae and the computed ones (slip misfit SM, quality estimator for inversion). On the right, the unscaled Morh circle representation of the explained faults (TectonicVB software representation). (B) and (C) Homogeneous stress tensors calculated for the older and younger tectonic regimes, respectively. See text for more explanations.

the graphical means were computed with the numerical dynamic analysis algorithm (Table 1).

An alternative to extracting strain from faults is to seek a stress model that provides a best fit to the fault-slip data. We used three types of computer algorithms for finding the best-fit tensor, which are referred as stress inversion (Reches, 1987; Reches et al., 1992), direct inversion (Angelier, 1979; Angelier, 1984; Angelier, 1989; Angelier, 1990; Villemin and Charlesworth, 1992) methods, and Yamaji method (Yamaji, 2000). Note that other available algorithms have not been tested in this paper (e.g. Etchecopar et al., 1981; Gephart, 1990).

(4) The « direct inversion method » (figure 5) has extensively shown to give reliable results for paleostress analysis, provided that the data are distributed and free of outliers (monophase data sets with few spurious measurements). This method implements a routine inversion, based on Bott's equation (1959), which constitutes the underpinning of most modern paleostress analysis techniques. This routine aims at solving the four unknowns' problem, namely the orientations of the principal stresses and the stress shape ratio. The fitting procedure involves a least mean-square angular deviation between the observed slickensides and the directions of maximum shear stress predicted from the stress model. The most critical assumption involved is that of the homogeneous stress on the scale of the sampled domain, during the deformation. An internal check of this approach statistically expresses, via the fluctuation histogram, the range of angular deviations (misfit estimator SM, equivalent to the ANG value of Angelier) that the best-fit tensor yields. Ideally, the distribution of deviations forms a steep Gaussian distribution with the maximum at the left side. The presence of a second maximum could be an indication of an heterogeneous data set (figure 5a, arrows). The various sources of misfit imply that mean SM values may be as high as 39° (table 1). Etchecopar et al. (1981) and Armijo et al. (1982) apply inverse calculation to those subsets of data that show large misfits (figure 5a) from slip directions predicted from formerly determined stresses. Under this circumstances the search for the ideal best-fit stress tensor actually leads to the determination of the first spurious compromise tensor (figure 5a). This tensor is further used as a criterion for the separation of the first monophase data set from the whole data set. Next, those faults displaying the largest deviations are separated out and a second tensor found from the remaining data. The procedure is repeated until well-defined homogeneous subsets with small mean misfit angles (mean ANG≤12°, e.g. Angelier et al., 1985) are selected (figures 5b and 5c). We are aware that attempts to improve the solution by a process of rejecting spurious data to improve the best-fit tensor only increases the risk of artificial results. Yamaji (2003) critically assessed that those recursive methods may lead to unstable solutions when compared to other methods for the same data sets. The main difficulty that arises from the recursive method is that it doesn't treat stress solutions equally, as user's choice is involved during the processing of data. With the above limitations, the results are

expressed in terms of reduced stress tensors that give the orientations of the maximum (σ1), intermediate (σ2), and minimum (σ3) stress axes (σ1 ≥ σ2 ≥ σ3 ≥ 0), as well as the ratio of principal stress differences, ϕ=(σ2-σ3)/(σ1-σ3). This ratio Δ varies from 0 (σ2=σ3) to 1 (σ1=σ2), values that correspond to stress ellipsoïds symmetric around σ1 and σ3 axes (Angelier, 1975), respectively. Additionally, the mechanical compatibility of faults with stress tensor solutions was tested graphically by means of normalized Mohr circle diagrams (Figure 5), from which inherited and neoformed fault planes are detected. The state of stress on the fault planes with an insufficient slip misfit angle, resolved from the stress tensor solution of the full data set, is characterized either by high normal stresses or low shear stresses. The corresponding fault planes (mostly strike-slip faults in fig. 5a) are inconsistent with a reasonable failure criterion (Byerlees's law; Byerlee, 1978).

Tensor configurations derived by the direct inversion iterative method group into 2 subsets, both with σ3 horizontal (events 1 and 2, figures 5b and 5c). With this approach, one extensional model and one strike-slip model are extracted from the full fault-slip data set (figures 5b and 5c). In the extensional stress model, the initial failure condition of some normal faults is discredited by the normal and shear stress distribution on the fault planes, as shown by the data plot in the normalized Mohr circle diagram. About half of the data plot within the σ1-σ3 stress circle, indicating a non critical state of stress for initial failure on fault planes (fracture reactivation). Among those, the fault planes with a low shear stress to normal stress ratio (thick circles) are unlikely to slip under the state of stress resolved from the stress tensor, and should be cancelled from the fault-slip solution. The other half of the data plot on or close to the periphery of the σ1-σ3 stress circle and confirm a maximum shear stress distribution on fault planes due to initial failure conditions. Concerning the strike-slip model, most data plot near the periphery of the σ1-σ3 stress circle and confirm critical shear stresses on fault planes (initial failure conditions). Nevertheless the state of stress on some fault planes, resolved from the stress tensor solution, is characterized by unusual high normal stresses relative to shear stresses (figure 5c). Those anomalous fault planes should be discarded because they are unlikely to slip under the stress state predicted from the tensor solution.

(5) The stress inversion method (figure 6) of Reches (1987) is unique in incorporating failure conditions in the inversion scheme, via the Navier-Coulomb criterion. Provided that the slip events occurred under relatively uniform conditions, and that the magnitudes of the shear and normal stresses on the faults satisfy the Coulomb yield criterion, this method provides the orientations and relative magnitudes of the principal stresses, and constrains the mean coefficient of friction and the cohesion of the faults. Reches et al. (1992) introduce an additional angular deviation in the search for the best solution: the Principal Axes Misfit (PAM value), which depends on the coefficient of friction. This value quantifies the mean angular deviation, for the selected fault population, between

the principal axes of the ideal tensor for each fault (i.e. the one which minimizes the differential stress) and the axes of the general tensor calculated for the entire cluster. While other numerical methods of fault-slip inversion implicitly assume a non-realistic friction of coefficient value (º ≈ 0, Reches, 1987), it has been demonstrated that if considering the coefficient of friction together with the hypothesis of Wallace-Bott during the inversion process, the quality and stability of the solution is even much better (Célérier, 1988). Finally the quality of the solution is evaluated by considering both : (a) degrees of mean angular misfits as small as possible (PAM and SM) (b) a reasonable coefficient of friction, i.e. as close as possible to $\mu \approx 0.8$ (Byerlee, 1978) (c) a slip resisting ($C \geq 0$) mean cohesion.

The solution for all 69 faults, and friction values ranging from $\mu \approx 0.0$ to $\mu \approx 2.0$, show large misfit angles and two maxima (figure 6a). Thirty-four faults with SM>35° didn't fit the general solution and were automatically first deleted. The PAM diagram also indicates high misfit values, incompatible with a homogeneous data set (figure 6a). After these faults have been removed, the stress tensor is recalculated for the remaining faults. This procedure was repeated until the discrimination of two well-defined subsets, with small misfit angles (figure 6b, bottom). The original cluster of example site was split into a primary subset of 28 faults (corresponding to the older extensional event 1) and a secondary subset of 41 faults. The separation process was then reiterated for the latter subset; finally 28 faults have been grouped into the secondary subset (corresponding to the later compressional strike-slip event 2). The best solutions of the primary and secondary subsets are for $\mu \approx 0.8$ and $\mu \approx 0.4$, respectively (figure 6b, top and Table 1). The θ angles derived from these geological reasonable friction values are 26° and 35° respectively, which is reasonably close to the best θ angles for each subset cluster, 30° and 40° respectively. In order to evaluate the statistical fitting degree of the selected faults in each cluster to the stress configuration, the confidence margins of the solutions are determined for each subset by the sampling with replacement or bootstrapping method (Efron, 1982; Stuart, 1984; Michael, 1984). The principal axes of 500 subsidiary clusters, selected from the original subsets, form clouds around the principal axes of the best solution for both the subsets (figure 7b). In Figure 7c only 68.27 % of the solutions which are the closest to the best solution (i.e. they bound the range of ±1 standard deviation about the best solution) are considered. While the confi-

Fig. 6. Results of the semi-automatic stress inversion of Reches (1987). (A) The misfit angles calculated for the heterogeneous dataset, slip misfit (SM) and principal axes misfit (PAM) for the 69 faults measured in the field. (B) Stress tensor analysis of a primary susbet of 28 faults (older event 1) and final secondary subset of 28 faults (younger event 2). Top diagrams: caculated misfit angles (SM and PAM) versus a range of coefficients of friction for each cluster of faults (older and younger, left and right, respectively). The selected friction coefficient are 0.8 and 0.4 for each stress tensor akin to the primary and secondary subset, respectively. Middle diagrams: Stress ratio as a function of coefficent of friction for each subset. The rightmost stereonet (lower hemisphere, equal area projection) illustrates the orientation of the three principal stress axes $\sigma 1$ (circles), $\sigma 2$ (squares), and $\sigma 3$ (triangles) for the marked coefficient of frictions in the case of the secondary cluster (event 2). Solid symbols indicate the orientations of the principal stresses of the selected solution for $\mu = 0.4$. Bottom diagrams: SM and PAM for the primary (left) and secondary (right) cluster of faults. See text for more explanations.

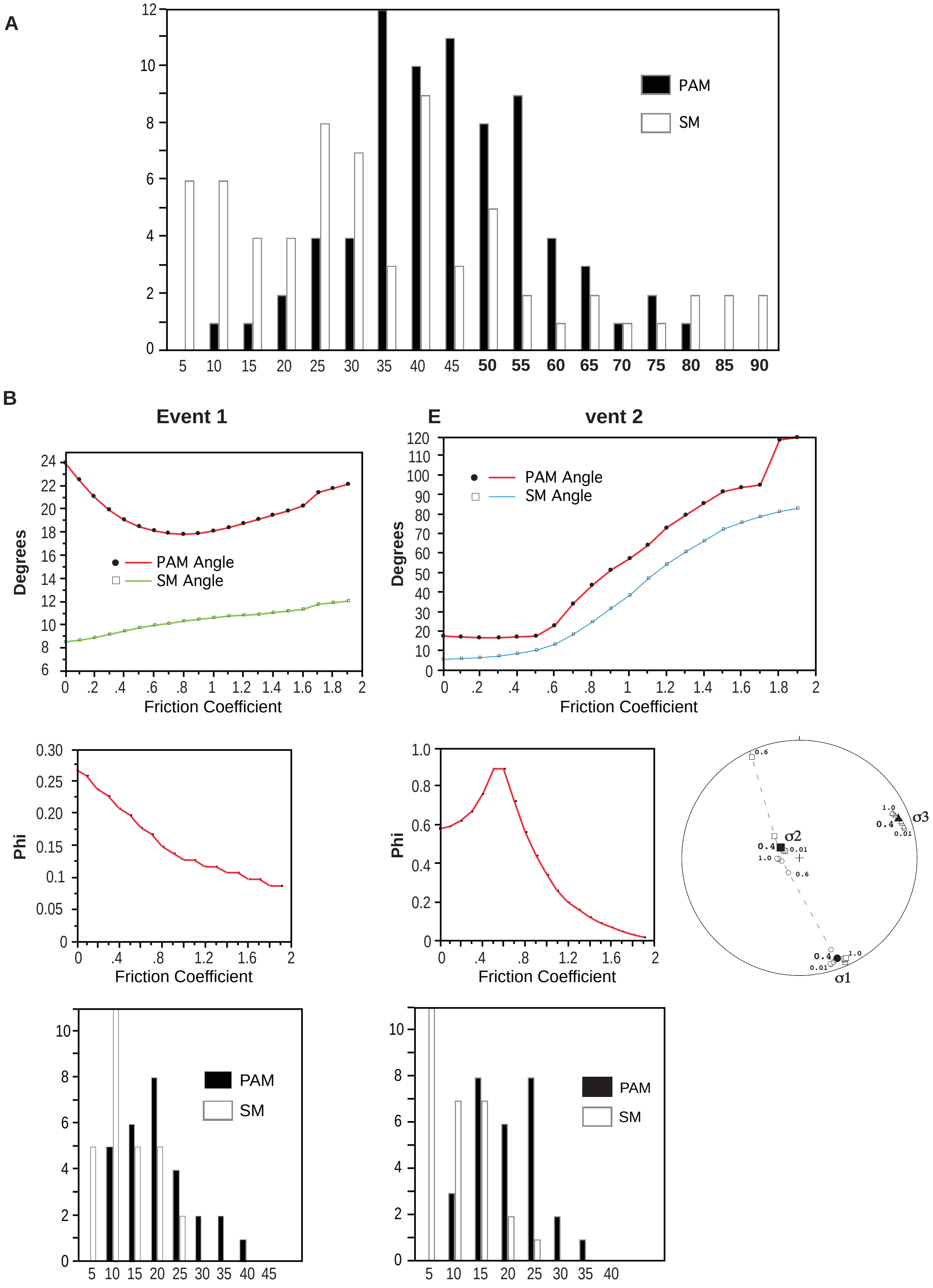
A
PAM
SM
0 2 4 6 8 10 12
5 10 15 20 25 30 35 40 45 50 55 60 65 70 75 80 85 90
B
Event 1
E vent 2
Degrees
PAM Angle
SM Angle
Friction Coefficient
0 .2 .4 .6 .8 1 1.2 1.4 1.6 1.8 2
6 8 10 12 14 16 18 20 22 24
0 10 20 30 40 50 60 70 80 90 100 110 120
Phi
0 0.05 0.1 0.15 0.20 0.25 0.30
0 0.2 0.4 0.6 0.8 1.0
0 .4 .8 1.2 1.6 2
σ1
σ2
σ3
0.01
0.4
0.6
1.0
0 2 4 6 8 10
5 10 15 20 25 30 35 40 45
5 10 15 20 25 30 35 40

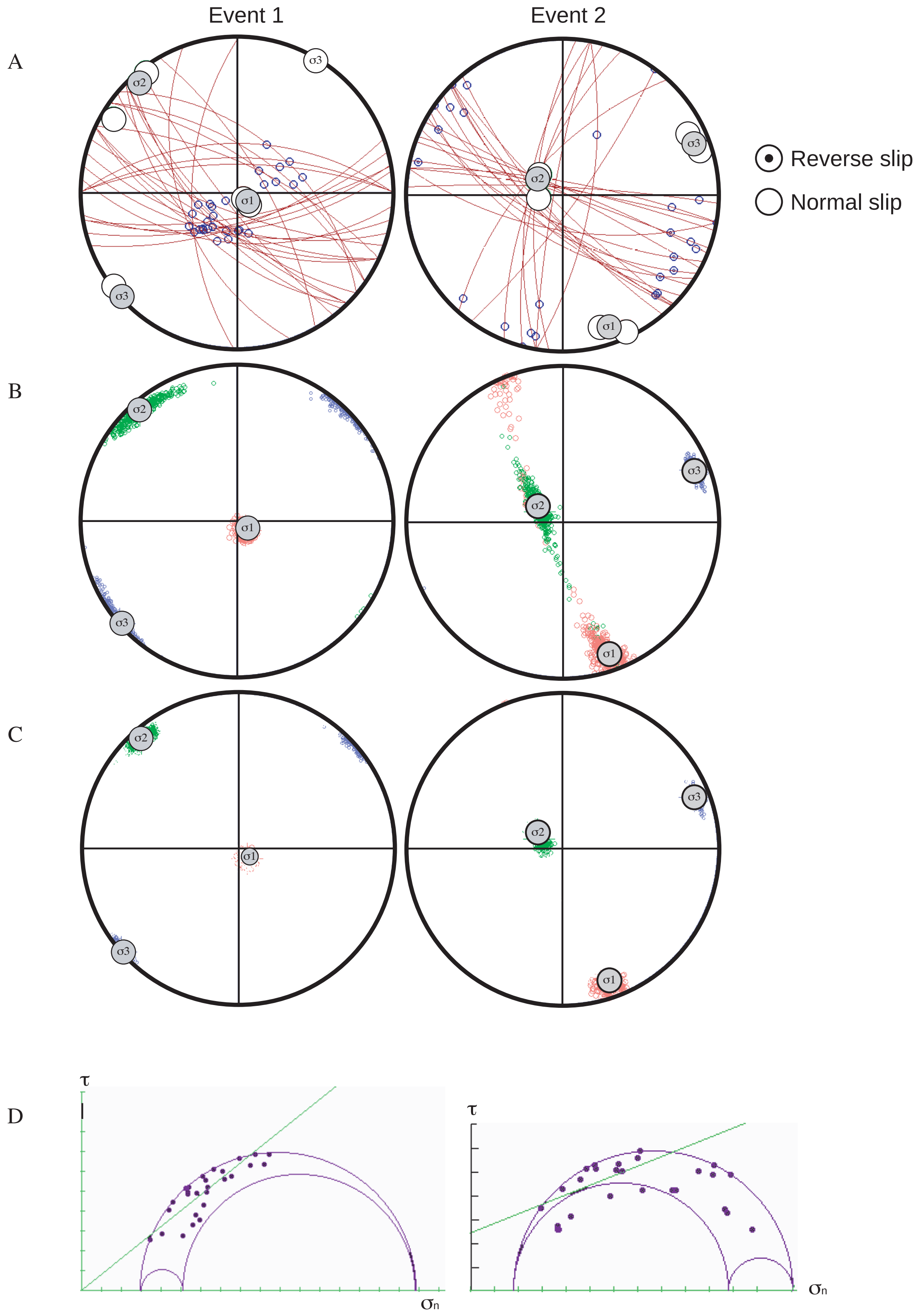

Fig. 7. (A) Stereoplots (lower hemisphere, equal area projection) of the faults, slip axes and calculated stress tensors akin to the primary and secondary cluster. Sense of slip is marked on the plot of the slip axes according to the legend. Principal stress axes are σ1, σ2 and σ3. (B) Stress solutions for the primary and secondary cluster (left and right, respectively) with 500 bootstraping solutions (see text) marked by small color circles forming three clouds about the principal axes. (C) Same as fig. 7b with ± 1 s.d. margins. (D) Unscaled Mohr circle representation of the explained faults by the stress tensor solution for the primary (left) and secondary (right) cluster.

dence margins for the location the principal axes are squeezed around best σ3 in both two stress solutions, the axial girdle drawn by σ1 and σ2 axes and their broad confidence margins for the secondary event makes the tensor solution somewhat unsteady (figure 7b). Indeed the tensor solutions fluctuate between plane strain and uniaxial shortening, although the ± 1 s.d. margins are concentrated around the best solution (figure 7d). The uniaxial shortening strain imposed during that later event (ϕ=0.77 for the best solution) is notwithstanding in good agreement with the possible permutation of σ1 and σ2 axes during the deformation.

3. Discussion and conclusions

The results of fault-slip inversion by the above methods for the example site are combined in figure 8 and table 1. Whatever the method used, either graphical or mathematical, the inversion always led to the separation on one heterogeneous data set into two homogeneous subsets, with cogent stress ratios and principal axes orientations, which relative age agrees with field observations. The primary older subset isolated from the different methods includes normal and oblique-normal faults, which moved in an extension regime, associated with a low dispersion of extension axes (the «outliers» corresponding to low ϕ values) toward the SW-SSW (figure 8b). The fault-slip data from this subset include NW-SE directed and west and east dipping conjugated normal faults. Other fractures approximately N-S and E-W running and with intermediate to high dip angles were also reactivated under this stress field. The secondary cluster encompasses a «quasi-conjugate» system (Angelier, 1979) of WNW-ESE and NW-SE striking dextral and oblique-dextral faults, combined with a NNE-SSW to NE-SW running sinistral and oblique-sinistral fault set (figure 8b). This strike-slip regime developed in response to NNW-directed shortening and ENE-directed extension. Some previously formed E-W and NW-SE directed faults, which do not fit the critical state of stress for failure, were reactivated during that slip event.

Globally, the results obtained with the different methods are very close each others, once the separation in two homogeneous subset of data have been achieved (Figure 8b, Table1). Thus, one can say that these methods are more or less equivalent, to determine a stress tensor, when the data are of sufficient quality. Our testing of various stress inversions methods allows to estimate the overall error made during such processes. We found around 10° of dispersion both for σ1, σ2, σ3 axes. It seems to be a mean error inherent of the stress inversion, and we can propose that a given stress tensor is know only in this error cone. So the reliability of a given inversion in a given site, should take into account such a 10° cone of possible variation. Note that our dataset was good enough and that with a lower quality one, the dispersion of the stress axes should be higher. Generally speaking, a single stress tensor should be analysed with much care, and a good paleostress analysis should be

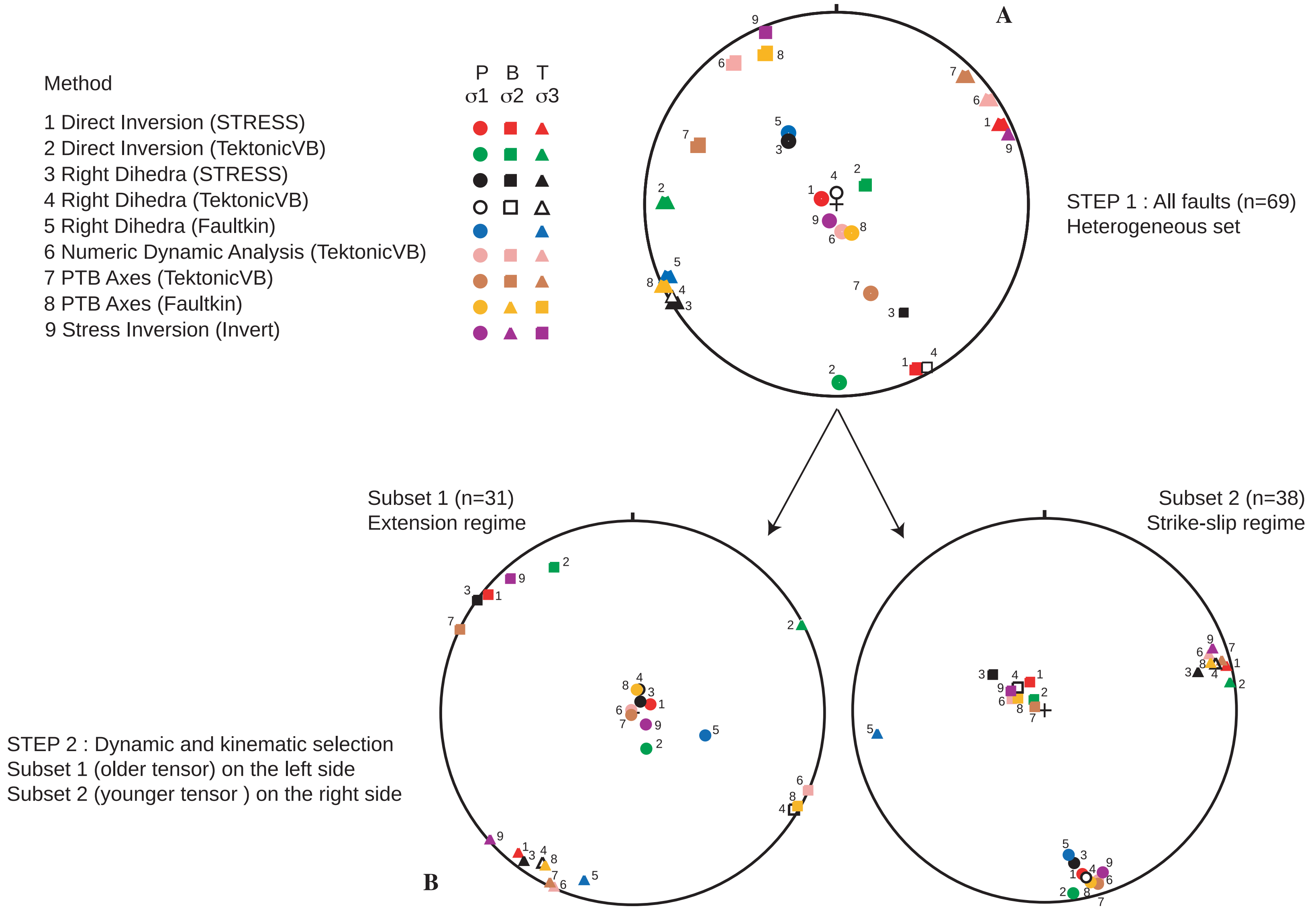

Fig. 8. Summary of the fault-slip inversion results for the here used methods, with lower hemisphere projection of principal incremental strain (P-B-T) and stress (σ1, σ2 and σ3) axes, according to the legend. (A) Results of the inversion schemes of the heterogeneous dataset (B) Results of the inversion schemes for the older (subset 1) and younger (subset 2) subsets of faults.

based on a statistical analysis of numerous tensors homogeneously distributed in a given area. On the contrary, the results obtained in terms of ϕ ratio are quite dispersed, and this information should be regarded with much care at the scale of a regional analysis. On this specific point, one should use for each site of a given area the same method/software to be able to regionally interpret the ϕ ratio distribution. Nevertheless, this ratio remains badly constrained, and could evolve quite a lot from a method to each other (see table 1).

Numerical methods are more rigorous because they perform a complete analysis in mechanical terms and selection criteria terms, which is expressed by lower percentages of explained faults by the tensor solution (cf Table 1). But neither the stress ratio nor the orientation of principal axes of the tensor solution are significantly affected by the odd data. The low angular dispersion of kinematic and stress axes (~10°) in both regimes of deformation (Figure 4b) is small relative to the scatter within individual data sets. This small discrepancy a posteriori supports the assumption that deformation is coaxial and that stress is homogeneous at the scale of sampling site. Moreover the solution for each subset of data is well constrained, which enlightens its unicity and stability.

From these outcomes we evidence that if one is more interested with the regional orientation of the principal axes than with a comprehensive analysis of faulting process (e.g. neoformed or inherited faults, magnitudes of principal axes), a « simple » graphical kinematic analysis (i.e. less computationally intensive) provides as reliable results as more complex numerical methods.

Actually, an accurate paleostress analysis should ideally integrate both graphical determinations of the overall stress tensors (general distribution of the axes, potential sectors of compression/extension), and numerical inversion, to better numerically constrain the parameters of the stress axes. We recommend thus to combine at least one graphical method with one numerical one to achieve a regional stress analysis. Actually, this approach could be enhanced by the application of a Yamaji-like or Gephart-like methods, which would provide information on the internal stability of the tensors.

REFERENCES

Allmendinger, R.W., R.A. Marrett, and T. Cladouhos, FAULTKIN-program, Dep. of Geol. Sc., Snee Hall, Cornell University, Ithaca, NY, 1989.

Anderson, E.M., The dynamics of faulting, Ed. Oliver et Boyd, 2nd ed., Edinburgh, 206, 1951.

Angelier, J., Sur l'analyse de mesures recueillies dans les sites faillés : l'utilité d'une confrontation entre les méthodes dynamiques et cinématiques, Comptes Rendus de l'Academie des Sciences de Paris - Series IIA - Earth and Planetary Science, 281, 1805-1808, 1975.

Angelier, J., Determination of the mean principal direction of stress for a given fault population., Tectonophysics, 56, 17-26, 1979.

Angelier, J., Tectonic analysis of fault data sets., Journal of Geophysical Research B: Solid Earth, 89, 5835-5848, 1984.

Angelier, J., From orientation to magnitude in paleostress determination using fault slip data., Journal of Structural Geology, 11, 37-50, 1989.

Angelier, J., Inversion of field data in fault tectonics to obtain the regional stress - A new rapid direct inversion method by analytical means, Geophysical Journal International, 103, 363-376, 1990.

Angelier, J., B. Colletta, and R.E. Anderson, Neogene paleostress changes in the Basin and Range: a case study at Hoover Dam, Nevada-Arizona, Geological Society of America Bulletin, 96, 347-361, 1985.

Angelier, J., and P. Mechler, Sur une méthode graphique de recherche des contraintes principales également utilisable en tectonique et en sismologie: la méthode des dièdres droits., Bulletin de la Société Géologique de France, 7, 1309-1318, 1977.

Arlegui-Crespo, L.E., and J.L. Simon-Gomez, Reliability of paleostress analysis from fault striations in near multi-directional extension stress fields. Example from the Ebro Basin, Spain, Journal of Structural Geology, 20, 827-840, 1998.

Armijo, R., E. Carey, and A. Cisternas, The inverse problem in microtectonics and the separation of tectonic phases, Tectonophysics, 82, 145-160, 1982.

Arthaud, F., Méthode de détermination graphique des directions de raccourcissement, d'allongement et intermédiaire d'une population de failles, Bulletin de la Société Géologique de France, 14, 12-17, 1969.

Aydin, A., and Z. Reches, Number and orientation of fault sets in the field and in experiments, Geology, 10, 107-112, 1982.

Bott , M.H., The mechanism of oblique slip faulting, Geol. Mag., 96, 109-117, 1959.

Byerlee, J.D., Brittle-ductile transition in rocks, Journal of Geophysical Research, 73, 4741-4750, 1968.

Caputo, M., and R. Caputo, Structural analysis: new analytical approach and applications, Ann. Tect., 2, 84-89, 1988.

Carey, E., Recherche des direction principales de contraintes associées au jeu d'une population de failles, Rev. Geogr. phys. Geol. dyn., 21, 57-66, 1979.

Carey, E., and B. Brunier, Analyse théorique et numérique d'un modèle mécanique élémentaire appliqué à l'étude d'une population de failles, Comptes Rendus de l'Academie des Sciences de Paris - Series IIA - Earth and Planetary Science, 279, 891-894, 1974.

Carey-Gailhardis, E., and P. Vergely, Graphical analysis of fault kinematics and focal mechanisms of earthquakes in terms of stress; the right dihedra method, use and pitfalls, Annales Tectonicae, VI, 3-9, 1992.

Casas, A.M., and J.L. Simon, Stress deflection in a tectonic compression field: a model for the northwestern Iberian Chain, Spain, Journal of Geophysical Research, 97, 7183-7192, 1992.

Célérier, B., How much does slip on a reactivated fault plane constrain the stress tensor?, Tectonics, 7, 1988.

Ciancaleoni, L., Brittle-ductile deformation during the last stages of the continental collision: geometry and kinematics of the major discontinuities in the Bergell and Insubric areas (east Switzerland, north Italy), Ph.D. thesis, University of Neuchâtel, Neuchâtel, 2005.

Dupin, J.M., W. Sassi, and J. Angelier, Homegeneous stress hypothesis and actual fault slip: a distinct element analysis, Journal of Structural Geology, 15, 1033-1043, 1993.

Efron, B., The Jacknife, the Bootstrap and other reampling plans, 92 pp., SIAM, Philadelphia, Pa., 1982.

Etchecopar, A., G. Vasseur, and M. Daignières, An inverse problem in microtectonics for the determination of stress tensor from fault striation analysis, Journal of Structural Geology, 3, 51-65, 1981.

Fleischmann, K.H., and M. Nemcok, Paleostress inversion of fault-slip data using the shear-stress solution of Means (1989), Tectonophysics, 196, 195-202, 1991.

Fry, N., Striated faults: visual appreciation of their constraint on possible paleostress tensors, Journal of Structural Geology, 21, 7-21, 1999.

Gephart, J.W., FMSI: A fortran program for inverting fault/ slickenside and earthquake focal mechanism data to obtain the regional stress tensor., Computer and Geosciences, 16, 953-989, 1990.

Gephart, J.W., and D.W. Forsyth, An improved method for determining the regional stress tensor using focal mechanism data: apllication to the San Fernando earthquake sequence, Journal of Geophysical Research B: Solid Earth, 89, 9305-9320, 1984.

Hardcastle, K.C., and L.S. Hills, BRUTE3 and SELECT: Quickbasic4 programs for determination of stress tensor configurations and separation of homogeneous populations of fault-slip data, Computer and Geosciences, 17, 23-43, 1991.

Hoeppener, R., Tektonik im Schiefergebirge., Geologische Rungshau, 44, 26-58, 1955.

Huang, Q., Computer-based method to separate heterogeneous sets of fault-slip data into sub-sets, Journal of Structural Geology, 10, 297-299, 1988.

Huber, R.K., and D. Marquer, Tertiary deformation and kinematics of the southern part of the Tambo and the Suretta nappes (Val Bregaglia, Eastern Swiss Alps), Schweiz. Mineral. Petrogr. Mitt., 76, 383-397, 1996.

Jaeger, J.C., and N.G.W. Cook, Fundamentals of rock mechanics, 593 pp., Chapman & Hall, London, 1979.

Liesa, C., and R.J. Lisle, Reliability of methods to separate stress tensors from heterogeneous fault-slip data, Journal of Structural Geology, 26, 559-572, 2004.

Lisle, R.J., Romsa: a Basic program for paleostress analysis using fault-striation data, Computers & Geosciences, 14, 255-259, 1988.

Mardia, K.V., Statistics of directional data, Academic, San Diego, California, 1972.

Marrett, R.A., and R.W. Allmendinger, Kinematic analysis of fault-slip data, Journal of Structural Geology, 12, 973-986, 1990.

Meyre, C., D. Marquer, S.M. Schmid, and L. Ciancaleoni, Syn-orogenic extension along the Forcola fault: correlation of Alpine deformations in the Tambo and Adula nappes (Eastern Pennine Alps), Eclogae Geol. Helv., 91, 409-420, 1998.

Michael, A.J., Determination of stress from slip data, faults and folds, J. Geophys. Res., 89, 11,517-11,526, 1984.

Nemcok, M., D. Kovac, and R.J. Lisle, A stress inversion procedure for polyphase calcite twin and fault slip data sets, Journal of Structural Geology, 21, 597-611, 1999.

Ortner, H., F. Reiter, and P. Acs, Easy handling of tectonic data: the programs TectonicVB for Mac and TectonicsFP for Windows(TM), Computers & Geosciences, 28, 1193-1200, 2002.

Pfiffner, O.A., and M. Burkhard, Determination of paleo-stress axes orientatins from fault, twin and earthquake data, Annales Tectonicae, 1/1, 48-57, 1987.

Pollard, D.D., S.D. Saltzer, and A.M. Rubin, Stress inversion: are they based on faulty assumptions ?, Journal of Structural Geology, 15, 1045-1054, 1993.

Reches, Z., Determination of the tectonic stress tensor from slip along faults that obey the Coulomb yield criterion, Tectonics, 6, 849-861, 1987.

Reches, Z., G. Baer, and Y. Hatzor, Constraints on the strength of the upper crust from stress inversion of fault slip data, Journal of Geophysical Research, 97, 12,481-12,493, 1992.

Rosenberg, C., A. Berger, and S.M. Schmid, Observation from the floor of a granitoid pluton: Inferences on the driving force of final emplacement, Geology, 23, 443-446, 1995.

Schmid, S.M., O.A. Pfiffner, N. Froitzheim, G. Schönborn, and E. Kissling, Geophysical-geological transect and tectonic evolution of the Swiss-Italian Alps, Tectonics, 15, 1036-1064, 1996a.

Shan, Y., H. Suen, and G. Lin, Separation of fault slip data: an objective-function algorithm based on hard division, Journal of Structural Geology, 25, 829-840, 2003.

Simon-Gomez, J.L., Analysis of a gradual change in stress regime (example from the eastern Iberian Chain, Spain), Tectonophysics, 124, 37-53, 1986.

Spang, J.H., Numerical method for dynamic analysis of calcite twin lamellae, Geological Society of America Bulletin, 83, 467-472, 1972.

Sperner, B., L. Ratschbacher, and R. Ott, Fault-striae analysis: a turbo pascal program package for graphical presentation and reduced stress-tensor calculation., Computers & Geosciences, 19, 1361-1388, 1993.

Stuart, A., The ideas of sampling, 91 pp., Griffin, C., High Wycombe, 1984.

Tomljenovic, B., and L. Csontos, Neogne-Quaternary structures in the border zone between Alps, Dinarides and Pannonian Basin (Hrvatsko zagorje and KArvolac Basins, Croatia), Int. J. Earth Sci. (Geol Rundsch), 90, 560-578, 2001.

Turner, F.J., Nature and dynamic interpretation of deformation lamellae in calcite of three marbles, American Journal Of Science, 251, 276-298, 1953.

Villemin, T., and H. Charlesworth, Stress, an interactive computer programm to determine paleostress axes using data from striated faults, in Cordillera transect and cordilleran tectonic workshop, Alberta, 1992.

Wallace, R.E., Geometry of shearing stress and relation to faulting, Journal of Geology, 59, 118-130, 1951.

Will, T.M., and R. Powell, A robust approach to the calculation of paleostress fields from fault plane data, Journal of Structural Geology, 13, 813-821, 1991.

Yamaji, A., The multiple inverse method : a new technique to separate stresses from heterogeneous fault-slip data., Journal of Structural Geology, 22, 441-452, 2000.

Yamaji, A., Are the solutions of stress inversion correct ? Visualization of their reliability and the separation of stresses from heterogeneous fault-slip data., Journal of Structural Geology, 25, 241-252, 2003.

Yin, Z.M., and G. Ranalli, Determination of tectonic stress field from fault slip data: toward a probabilistic model, Journal of Geophysical Research, 98, 12,165-12,176, 1993.

CHAPITRE 3
Part II

Lateral extrusion at the eastern border of the Lepontine dome of the Central Alps by the late Oligocene onwards (Bergell and Insubric areas, Eastern Central Alps)

LAURENT CIANCALEONI, DIDIER MARQUER, CHRISTIAN SUE

IN PREPARATION FOR: TECTONICS

Lateral extrusion at the eastern border of the Lepontine dome of the Central Alps by the late Oligocene onwards (Bergell and Insubric areas, Eastern Central Alps)

LAURENT CIANCALEONI, DIDIER MARQUER, CHRISTIAN SUE

ABSTRACT

The late fault pattern at the eastern border of the Lepontine dome of the Central Alps encompasses normal, oblique-slip and strike-slip faults. The faults formed under brittle-ductile conditions. The tectonic regime associated with these faults is distributed in space and time into extensional and transcurrent displacements, leading to lateral extrusion of the Eastern Central Alps by the late Oligocene onwards. Widespread normal faulting is a major long-lived event which led to orogen-parallel extension with a minor orogen-perpendicular component. Alternating and interfering dip-slip, oblique-slip and strike-slip motions on transversal and longitudinal fault systems ensure kinematic compatibility and suggests that both faulting episodes are the result of one major extensive to transtensive tectonic event. The fault-slip data analysis of the minor fault population is coherent for both the extensive and strike-slip tectonic regimes and yields a very consistent orientation of the extension axis parallel to the long axis of the Alpine belt. The far-field kinematic framework of the collision between the Adriatic and European plates and gravity failure in the core of the belt determine the direction of escape. Because of strong lateral confinement due to indentation along the Giudicarie-Pustertal indenter at the end of the Burdigalian, lateral extrusion loosed efficiency. As a result, the tectonic regime became more transcurrent/transpressive. This led in particular to strike-slip reactivation of previously formed normal faults. With on-going convergence, lateral extrusion that appears as a major geodynamic process in the core of the belt during the Neogene was then primarily relocated sideways in the Western and Eastern Alps according to free boundary availabilities.

1. Introduction

The Periadriatic Fault System (PFS) is the most important fault system in the Alps (Fig. 1). The Periadriatic Line and related segments and fault zones extend over more than 700 kilometers along strike of the Alpine Belt, mainly in an E-W direction. Traditionally, the PFS is considered to evidence deformations related to post-collisional (post-early Oligocene) history of the Alps (Schmid et al., 1989 and references therein). As a matter of fact, the dextral transpression between the Adriatic sub-plate and the European foreland along these late Alpine faults drastically modified the geometry of the Alpine chain by the late Oligocene onwards (e.g. Schmid et al., 1989; Ratschbacher et al., 1991b; Mancktelow and Pavlis, 1994; Steck and Hunziker, 1994; Schmid et al., 1996a; Schmid and Kissling, 2000), especially in its internal domain. An important aspect during these post-nappe tectonics is the partitioning of deformation between late extension and strike-slip faulting at the scale of the internal domain of the belt, or in other words, the distribution of the deformation field related to vertical and lateral extrusion (e.g. Tapponnier, 1977; Schmid et al., 1989; Tapponnier et al., 1990; Ratschbacher et al., 1991; Hubbard and Mancktelow, 1992; Frisch et al., 2000; Sue and Tricart, 2003; Seyferth and Henk, 2004). Although the kinematics of individual segments of the PFS have

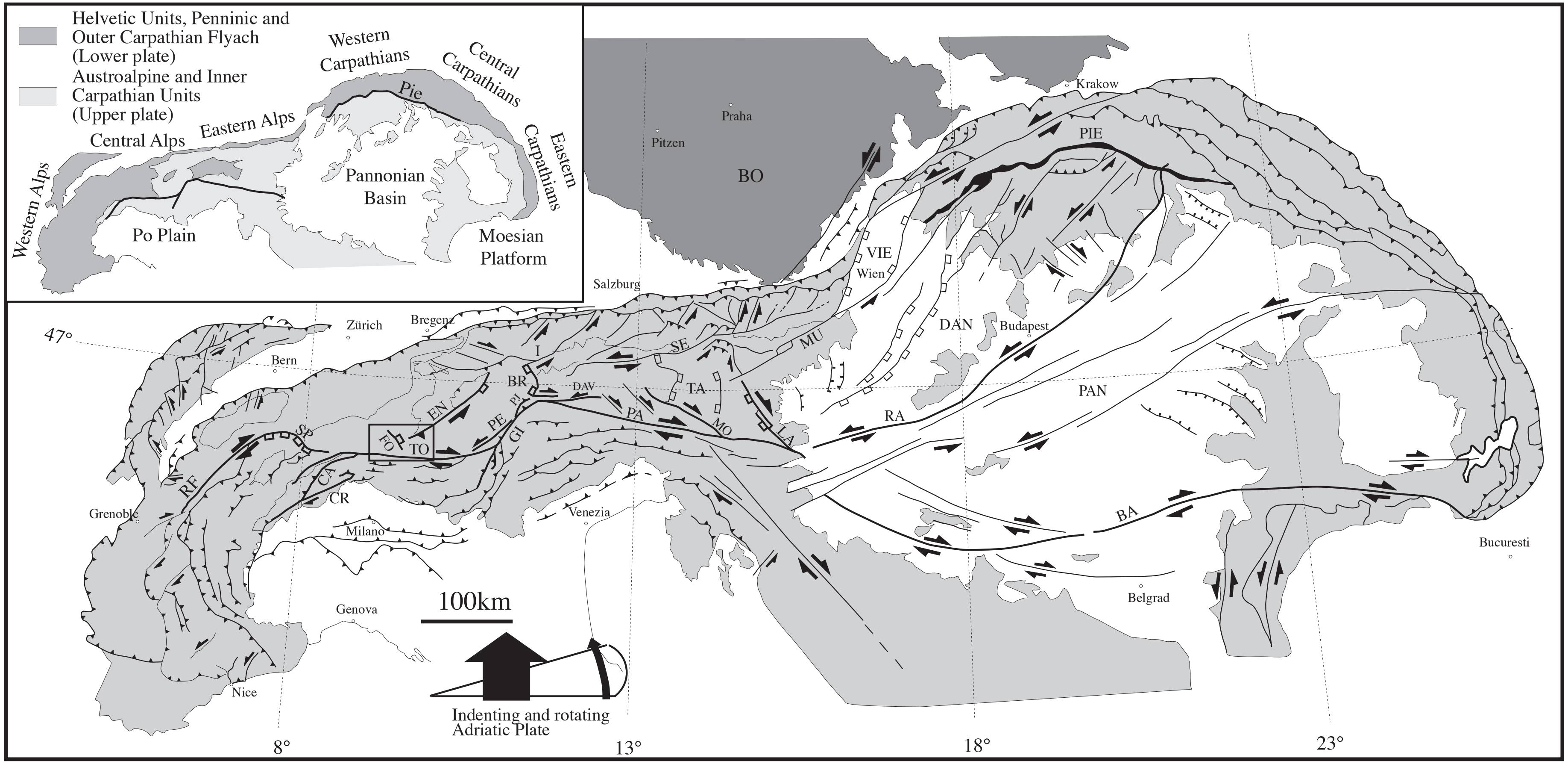

Fig. 1. The Periadriatic Line (thick black line) and related late Alpine faults, in the context of late Oligocene and Miocene kinematics in the Alps (Modified from Schmid et al., 1989; Ratschbacher et al., 1991; Becker and Peresson, 1996; Viola et al., 2001). Abbreviations related to segments of the Periadriatic Fault System and other late Alpine faults: BA, Balaton Line; BR, Brenner Fault; CA, Canavese Line; CR, Cremosina Fault; DAV, Defereggen-Anteselva-Vals Fault; EN, Engadine Line; FO, Forcola Fault; GI, Giudicarie Fault; I-Inntal Fault; LA, Lavanttal Fault; MO, Mölltal Fault; MU, Mur-Mürz Fault; PA, Periadriatic Line; PE, Peio Fault; PJ, Passeier-Jaufen Fault; RA, Raba Line; RF, Rhône Fault; SE, Salzachtal-Ennstal Fault; SP, Simplon Fault; TA, Tauernostrand Fault; TO, Tonale Fault. Other indications are: DAN, Danube Basin; VIE, Vienna Basin; PAN, Pannonian Basin; PIE, Pieniny Klippen Belt. Rectangle: study area. Inset, definition of tectono-stratigraphic units and geographical terms used in the text. Square: study area.

been studied in details, the main difficulty arises from linking systems of similar kinematics but that were active at significantly different times during on-going dextral transpression. Faced with this complexity, a detailed understanding of the kinematics, timing and magnitude of movements on this fault system is critical to any tectonic model of late alpine collision, and a preliminary to any paleogeographic reconstruction. The relative and/or absolute timing of deformation are probably the most critical factors we need in order to unravel the kinematic history of the PFS.

The post-nappe deformation history in the Bergell region, situated at the eastern margin of the Lepontine, is closely related to the well constrained timing (Oligo-Miocene) of the so-called Periadriatic intrusions (von Blanckenburg, 1992) and to the activity of three segments of the PFS (Figs. 1 and 2). Thus we benefit in that special area of good time markers of the deformation (intrusions) in close relationships with prominent late Alpine faults, which moreover the well-known geometry and kinematics look like other sub-systems of the PFS (fig. 1). In other words the temporal and kinematic evolution of this sub-system might represent at some extent geodynamic processes occurring elsewhere in the belt. For these reasons, the Bergell area, situated in the transition zone between the Central and Eastern Alps, appears to be in a key position for the understanding of the post-collision deformation processes in the internal domain of the belt.

While numerous structural studies place emphasis on the tectonic significance and importance of ductile deformations, only very few have been carried out on brittle and brittle-ductile deformations in the internal part of the collision belt. Although previous studies enlightened the importance of these late deformations on the actual nappe geometry of the Eastern Central Alps (Baudin et al., 1993; Schmid and Froitzheim, 1993; Huber and Marquer, 1996), the late-collisional brittle kinematics in the Bergell region have not been studied in details (see Passerini et al., 1991). In this study, we address the analysis of late Oligocene-early Miocene stress and strain fields recorded at different scales by brittle-ductile and brittle structures in the Bergell area. We further aim at assessing the degree of feedback between major faults and the internally deforming block in between them. To avoid problems due to previous deformations and strong mechanical anisotropy, we mainly carried out our investigations in the Tertiary intrusions occurring in the southern study area. Indeed such granitoid rocks, because of their homogeneous rheological behavior and widespread distribution in the crust, represent excellent targets to study paleostress and strain evolution from fault-slip data.

The results and interpretations of that local structural study will be compared with the geometry, kinematics and timing of deformation established so far on some segments of the PFS mentioned above. This record of late tectonic structures in the internal domain of a collision belt will bring new insights on the evolution of late Oligocene-early Miocene kinematics in this part of the Alps, as well

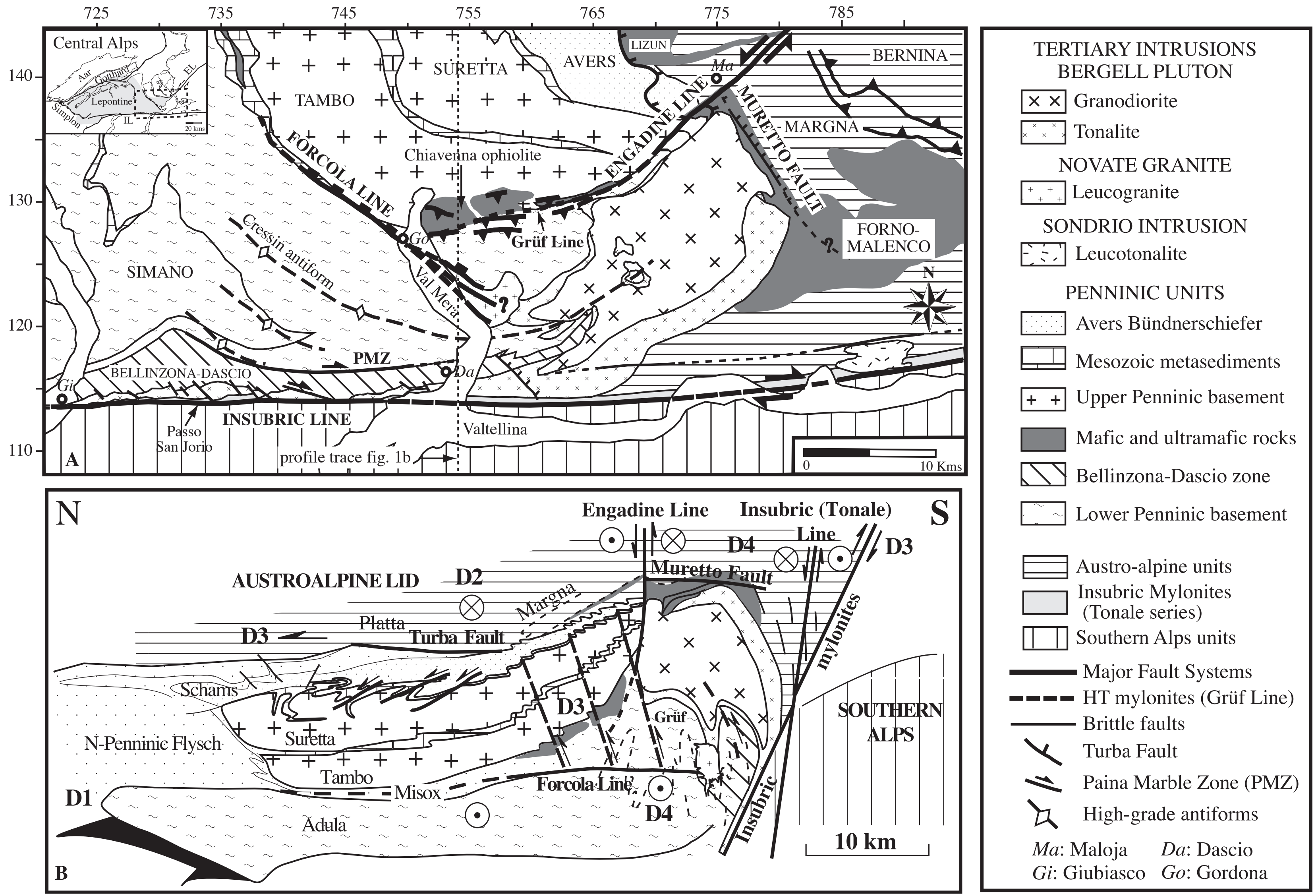

Fig. 2. (A) Geologic and tectonic setting of the Bergell and Insubric areas in the Eastern Central Alps. Question marks when the lateral prolongation of faults is uncertain. Modified from Rosenberg et al. (1995), Huber and Marquer (1996) and Meyre et al. (1998). (B) N-S geological profile along the Eastern Traverse. Modified from Schmid et al. (1996) and Huber and Marquer (1996). Regional deformation phases (D1-D4) are discussed in the text.

as the deformation processes associated with late denudation and lateral extrusion in the last stages of the continental collision.

2. Geological and tectonic framework

The investigated area belongs to the Pennine and Austro-alpine nappe stack of the Eastern Central Alps. No extensive description of the different units will be given here as a complete background of the Bergell Alps geology is detailed in a special volume referred as «Transition from Penninic to Austroalpine units in the Bergell Alps» (SMPM, volume 76, 1996 ; see more particularly the paper by Schmid et al. (1996b) therein for a detailed understanding of the regional geology in the Eastern Central Alps).

The Tertiary Bergell pluton, located at the eastern border of the Lepontine (fig. 2), intruded rocks of different metamorphic grade: the Pennine and Austroalpine domains were at greenschist to granulite facies conditions during emplacement. The Penninic nappe stack (regional D1 and D2 deformations on fig. 2) occurring to the west, north and east of the Bergell intrusion, encompasses from the bottom to the top: Lower Penninic basement (Simano and Adula basement nappes, including the Gruf unit), the Upper Penninic basement (Tambo and Suretta nappes, including the Chiavenna ophiolite and the Bellinzona-Dascio zone) and the Mesozoic metasedimentary cover rocks .The increase in metamorphic grade of the country rocks toward the west is associated with an increase in the depth of crystallization of the Bergell pluton (Reusser, 1987) due to syn to post-emplacement tilting (Rosenberg and Heller, 1997). The South Pennine ophiolitic zones include the Platta nappe, the Lizun, Forno and Malenco zones. The Austroalpine domain in the Bergell Alps comprises the Margna and Sella-Bernina nappes at the eastern border of the intrusion, while the Campo-Languard nappe and the mylonitised Tonale Series outcrop in the Southern Steep Belt (SSB, Milnes, 1974). Alpine amphibolite grade metamorphism is preserved locally south of the Bergell pluton (Lardelli, 1981). These nappes all together form the orogenic lid of the tectonic edifice intruded by the Bergell rocks.

The unmetamorphosed Permo-Mesozoic cover of the Southern Alps basement is exposed south of the Insubric Line (fig. 2). The jump in metamorphism across the Insubric Line between these units and the Austroalpine mylonitised series amounts at least 20 km of vertical throw along this major lineament, west of Bergell intrusion (regional D3 deformation, Hurford, 1986; Schmid et al., 1989, 1996a).

North of the Periadriatic Line, the Bergell pluton roots in the SSB, both steep pre-Alpine structures which represent the feeder zone of the Bergell suite (Milnes, 1974; Rosenberg et al., 1995).

This calk-alkaline pluton is a composite body of predominantly strongly foliated tonalite at its rim and weakly to undeformed granodiorite in its core, with minor amounts of gabbro, hornblendite, diorite, aplites and pegmatites (Wenk, 1973; Diethelm, 1989, fig. 2). The root zone is a east-west-striking and steeply north dipping tabular body of tonalite, parallel to the Insubric mylonitic belt (Rosenberg et al., 1995). At present, the most plausible cause for this magmatic episode may be hot asthenospheric counterflow after delamination of subducted lithosphere (von Blanckenburg and Davies, 1995; Gebauer, 1999). Because of the post-intrusive tilting of the pluton, an east-west profile through the magmatic body exposes a 10-km-thick interval in terms of crustal thickness (Trommsdorff and Nievergelt, 1983; Reusser, 1987). Berger and Gieré (1995) showed that the granodiorite crystallized slightly after the tonalite, which is consistent with radiometric ages rising 32 Ma for the tonalite and 30 Ma for the granodiorite (Von Blackenburg, 1992). According to Berger et al. (1996) the pluton ascended, emplaced and uplifted by vertical extrusion in relation to backthusting and backfolding within the Southern Steep Belt (D3, fig. 2), over the time span ranging from 33 to 28 Ma (Berger et al., 1996; Oberli et al., 1996). Synmagmatic shortening of the base of the pluton caused expansion and ballooning at higher crustal levels (Rosenberg et al., 1995). A N-S cross-section (Schmid et al., 1996a) reveals the strong exhumation of the southern study area, subsequent to this transpressive regional north-south shortening and east-west extension. This exhumation phase was also coeval with syn- to post-Bergell pluton brittle-ductile pro-thrusts, considered as antithetical conjugate sets to the vertical movements on the Insubric Mylonites (D3, Huber and Marquer, 1996). This pop-up structure permitted the Bergell pluton to be exhumed rapidly (e.g. Giger and Hurford, 1989; Oberli et al., 1996).

The small Tertiary tonalite intrusion of Sondrio-Triangia (Cornelius, 1915; Cornelius and Cornelius-Furlani, 1930; Lardelli, 1981), which cooled down to 350°C at 32-30 Ma (biotite K/Ar cooling ages, Giger, 1991), occurs immediately north of the Insubric Line, in the mylonitised Upper Austroalpine series, at the eastern border of the field area. The contact of the tonalite with country rocks is not clearly defined everywhere but lies parallel to the Tonale zone in the southern part of the intrusion (fig. 2). Lardelli (1981) also described discordant contacts to the Tonale series.

The granitic rocks of the Novate magmatic body and associated dyke swarm as well as many pegmatites and aplites intruded the Bergell pluton (more precisely the tonalitic body) and the SSB at 24-26 Ma (Gulson, 1973; Köppel and Grünenfelder, 1975; Gebauer, 1996; Hansmann, 1996; Romer et al., 1996; Liati et al., 2000). The Novate granite is a garnet bearing S-type leucogranite, not related to the calk-alkaline Bergell suite but rather derived from partial melting of crustal material during late-Alpine decompression. Following Schmid et al. (1996b), the intrusion of the Novate granite stock is connected to backthrusting along the Insubric Line (Schmid et al., 1989).

We name «Bergell block» the area comprised between four major faults, including segments of the Periadriatic Fault System in the Eastern Central Alps: the Insubric Line at the southern boundary, the Engadine Line in the north, the Forcola Line in the west and the Muretto Fault in the east (fig. 2). The Insubric Line has been studied so far and his complex kinematic history is now well established (e.g. Schmid et al., 1987; Heitzmann, 1987a; Schmid et al., 1989; Schmid et al., 1996a; Meier, 2003). The Insubric Line is represented by up to one km thick mylonite belt (the Tonale series, fig.2) south of the Bergell pluton. During the late Oligocene-Miocene, these mylonites first accommodated backthrusting towards the south under amphibolite facies temperature conditions («Insubric phase», Argand, 1916), and then transition gradually occurred to dextral strike-slip movement under progressive decreasing temperature conditions, from greenschist facies to very low grade metamorphic conditions (Schmid et al., 1989). With decreasing temperature conditions and vertical exhumation the deformation was more and more localized, giving way to a late cataclastic overprint (D4) associated with down-faulting of the Central Alps. This brittle deformation event post-dates mylonitisation and is restricted to the immediate contact with the Southern Alps (the Tonale Line, Fumasoli, 1974; Schmid et al., 1989). In contrast to the Central Alpine segments of the Periadriatic Line in the Lepontine region, no discrete jump in metamorphism or structural style (Schmid et al, 1987, 1989; Martin et al., 1991; Stipp et al., 2004) exists east of the Bergell area across this line. Accordingly, east of the Bergell pluton, only pure dextral strike-slip motion is documented (Wiedenbeck, 1986; Werling, 1992; Meier, 2003; Stipp et al., 2004). Depending on authors, right-lateral movements along the Insubric Line since the late Oligocene are assumed to be in the order of 30 to 60 kilometers (Heitzmann, 1987; Giger, 1991; Viola, 2000), or up to some 300 kilometers (Laubscher, 1971). According to the more recent studies, the latter displacement definetely appears to be largely overestimated.

The Engadine Line forms a major NE-SW trending steeply dipping discontinuity affecting the Penninic and Austroalpine nappe stack (fig. 2). It is generally considered as a major sinistral strike-slip fault, with lateral displacement varying between 3-6 km in the upper Engadine and up to 20 km in the lower Engadine (Trümpy, 1977). Schmid and Froitzheim (1993) presented a block rotation model which predicts downfaulting of the southeastern block in its northeastern part, sinistral horizontal off-set in its central part, and sinistral-oblique reverse faulting, highering the southeastern block, in its southwestern part. A brittle-ductile transition at the southwestern end of the fault is probable since no continuation of the line in terms of a brittle fault zone can be traced into the lower Val Bregaglia (Wenk, 1984; Ruzicka, 1997; Huber, 1999). The Grüf Line, a high-temperature fault zone that runs between the Adula-Grüf nappe and the Chiavenna ophiolite in lower Val Bregaglia, could indeed be the deep-seated equivalent of the cataclastic Engadine Line (Berger et al., 1996).

The Forcola mylonite zone (Forcola Line, Marquer, 1991) is a major ductile-brittle, high-angle, NW-SE striking, NE dipping, and north-easterly displacing extensional shear-zone, located at the top of Adula nappe (D4, fig. 2, Meyre et al., 1998). This post-Bergell normal fault reaches the Val Mera, where it is covered by Quaternary alluvial deposits (fig. 2), and splays further south inside the Novate granite stock (Meyre et al, 1998). Recently a new model of syn-kinematic emplacement of the Novate granite at the southernmost tip of the fault has been proposed (Ciancaleoni and Marquer, 2004). The Forcola normal fault offsets the Tambo nappe in its hangingwall relative to the Adula nappe in its footwall by a vertical amount of approximately 3 kilometers. The Forcola Line indicates post-Bergell orogen-parallel extension and unroofing of the Central Alps at the eastern border of the Lepontine dome. It is responsible pro-parte for the dome-like structure in the SE Lepontine zone in the late Oligocene (Meyre et al, 1998).

The late Alpine NNW-SSE oriented Muretto fault (Riklin, 1978; Peretti, 1985; Ring, 1994) strikes almost perpendicular to the Engadine Line and is exposed immediately northeast of the Bergell intrusion (D4, fig. 2). The kinematic evolution and origin of this fault is controversial, since the fault was first regarded as a strike-slip fault by Riklin (1978), then as a thrust by Trommsdorff and Nievergelt (1983), and finally as a dextral oblique-normal fault by Ring (1994). Those authors agree anyway in quantifying the vertical displacement along the main fault to be less than a few hundreds of meters (<600m). Spillmann (1993) proposed that a 10° sinistral rotation along an axis perpendicular to the fault plane was associated with the western block north up displacement. This leads to a differential vertical motion of 400 m between the northern and southern segments of the fault. Ring (1994) suggested that faulting at the Muretto fault zone is controlled by a local, near-field stress regime, caused by the Bergell pluton intrusion, at its northeastern tip.

3. Brittle deformation analysis

3.1. The regional fault network: tectonic lineaments in the Bergell and Insubric areas

Map scale faults cross-cutting the Tertiary intrusions were mapped by integration of remote sensing, digital elevation model (DEM), aerial photographs and structural analysis. The Landsat TM and DEM images with a 25m-pixel resolution were processed by numerical filtering such as directional lightening and spatial edge enhancement, guided by field-based and geological maps-based investigations (fig. 3). A continuous feedback between image analysis work sessions and field surveys allowed to refine the structural interpretations. At this stage, the main tool we used was the visual inspection of aerial photographs. Finally, about 50% of lineaments drawn as potential tectonic structures (faults or fault zones) were in turn checked out in the field and validated as field evidences justified their interpretation as brittle tectonic feature. Whatever their geomorphic expression in the

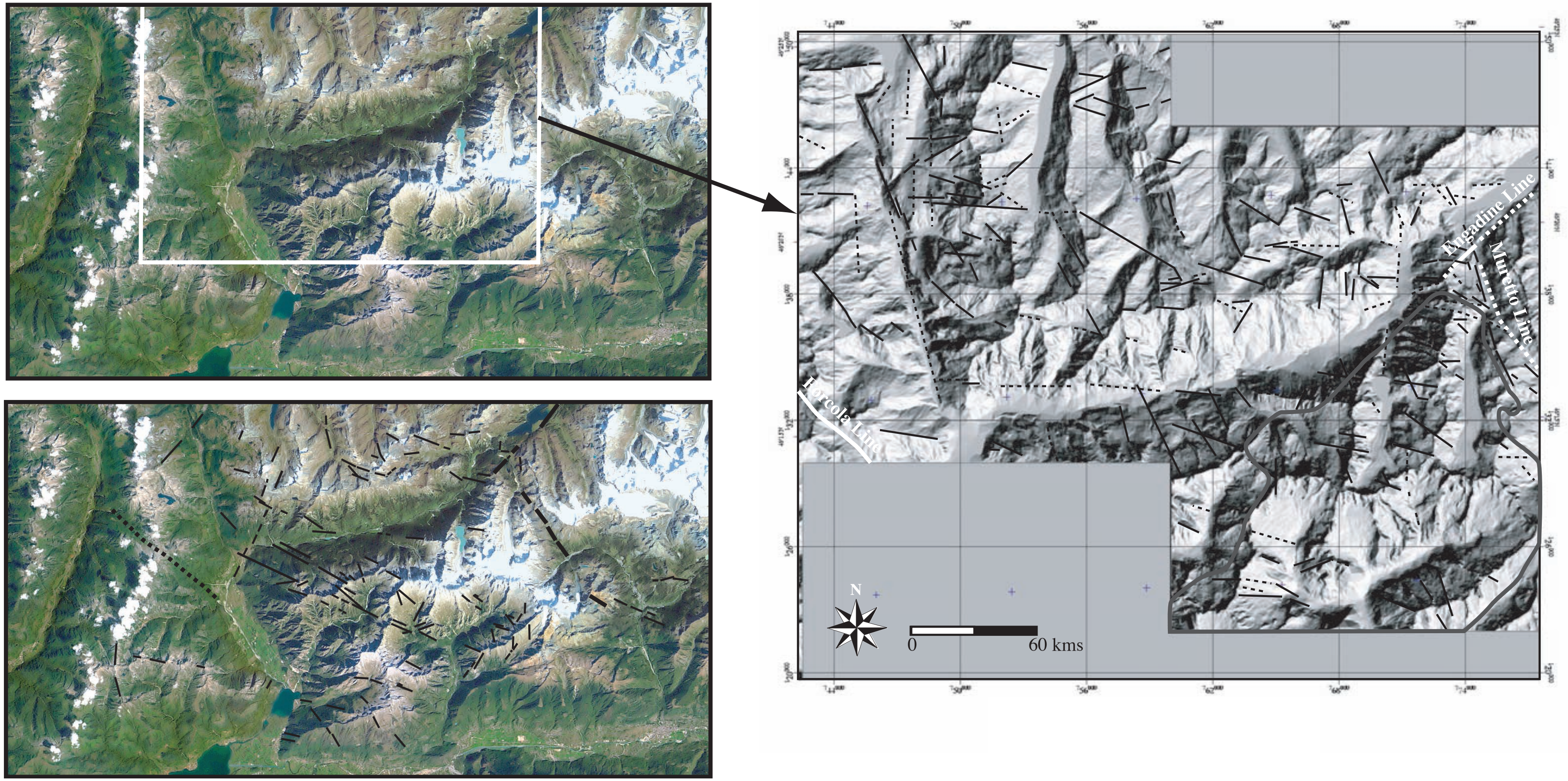

Fig. 3. Morphotectonic analysis of the Bergell and Insubric areas in the Eastern Central Alps. Left: Landsat TM image (25m resolution) with interpretation. Major lineaments are indicated by white arrows on the Landsat image. Upper left corner: 730-145 (Swiss coordinates). Lower right corner: 792-112 (Swiss coordinates). Right: DEM with 10m-resolution and lineament interpretation. Thick grey line: contour of the northeast part of the Bergell intrusion. Coordinates are given in Swiss coordinates.

field, deep and large trench associated with slope anomalies or smooth notch cutting-through the crest line, highly cataclastic and faulted zones, associated locally with gouge formation, characterize those corridors of deformation. In most cases the main fault plane was removed by selective erosion, and the kinematics were inferred from the intense secondary faulting along the corridor walls. In other cases however, direct observation of the striae on the master faults were possible .

Linear alignments on both sides of lateral valleys and crest lines have been repeatedly identified from both the Landsat TM and aerial images (fig. 3). We thus decided to extrapolate the observations and link the fault segments into longer faults, whenever obvious to us. This work led to the recognition of a pervasive network of regional faults, ranging from about 400 m to 10 kilometers in length (fig. 4). Most of those lineaments are distributed over a well-defined range of trends and associated kinematics, which determine four fault families:

(1) The first most representative fault family (about 50% of all linear trends) is oriented sub-NW-SE, encompassing WNW-ESE to NNW-SSE trends, with a maximum concentration around N045 (see rose diagram in fig. 4). Well-defined secondary peaks trend N115 and N 160. This family is quite equally occurring all over the investigated area. The maximum density of this fault family is nevertheless located at the eastern border of the Bergell intrusion, close to the Muretto Fault. This tectonic direction is also well represented in the central region of the Bergell intrusion (fig. 5) and along the Forcola Line and at the eastern side of Val Mera, for example in the Novate granite intrusion. There the specific relationships of the brittle structures with the Val Mera (NNW-SSE oriented large valley) make them more difficult to detect with the image analysis. Whatever their varying trend and dip direction or dip angle, three possible shear senses are associated to the faults: a typical normal to oblique-normal faulting movement and a strike-slip one, the former one pre-dating the latter one in most cases, when successive striations are present on the same fault planes.

(2) The second most represented fault family (circa 25% of all strikes) trends roughly N060 to N110 (sub-E-W orientation), with a maximum around N090 parallel to the Tonale Fault trend. Again a secondary peak may be identified and trends N070. Two major fault zones are associated with this family. To the south, in the Southern Steep Belt, E-W running faults parallel to the brittle Insubric Line and regularly distributed over a ca. 5 kms wide zone, emphasize a gradient of simple-shear deformation toward the Insubric Line. These faults could reasonably find their lateral prolongation inside and north of the Sondrio tonalite further east, where a similar set of faults has been identified. Their cumulated length would then extend over a minimum of 30 kms. The geomorphologic lateral expression of these lineaments, outside the Bergell rocks, is unfortunately hindered because of the thick vegetation in the south. Some of these faults are partly localized along the nappe contacts in

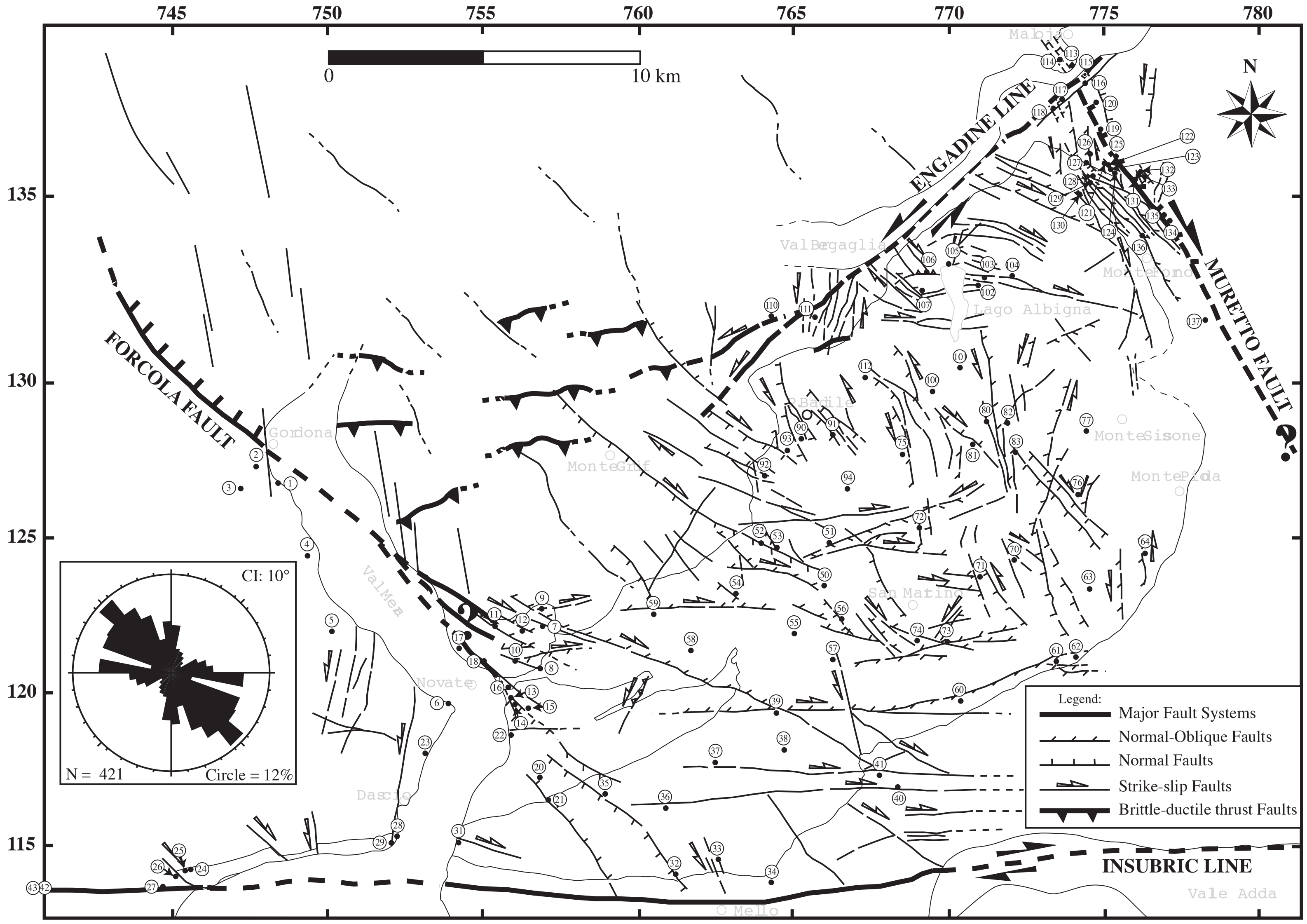

Fig. 4. Interpretative and interpolated fault network from integration of remote sensing analysis (aerial photographs, DEM, Landsat TM image), field surveys and geological maps inspection (Venzo et al., 1970; Schmid et al., 1996b; Huber, 1999). See section 3.1 for further explanations. Measurement stations for fault-slip analysis are reported (small black circles) and indicated by a number that refers to table 1. Left insert: directional analysis (rose diagram) of map-scale faults. Counting interval is 10°.

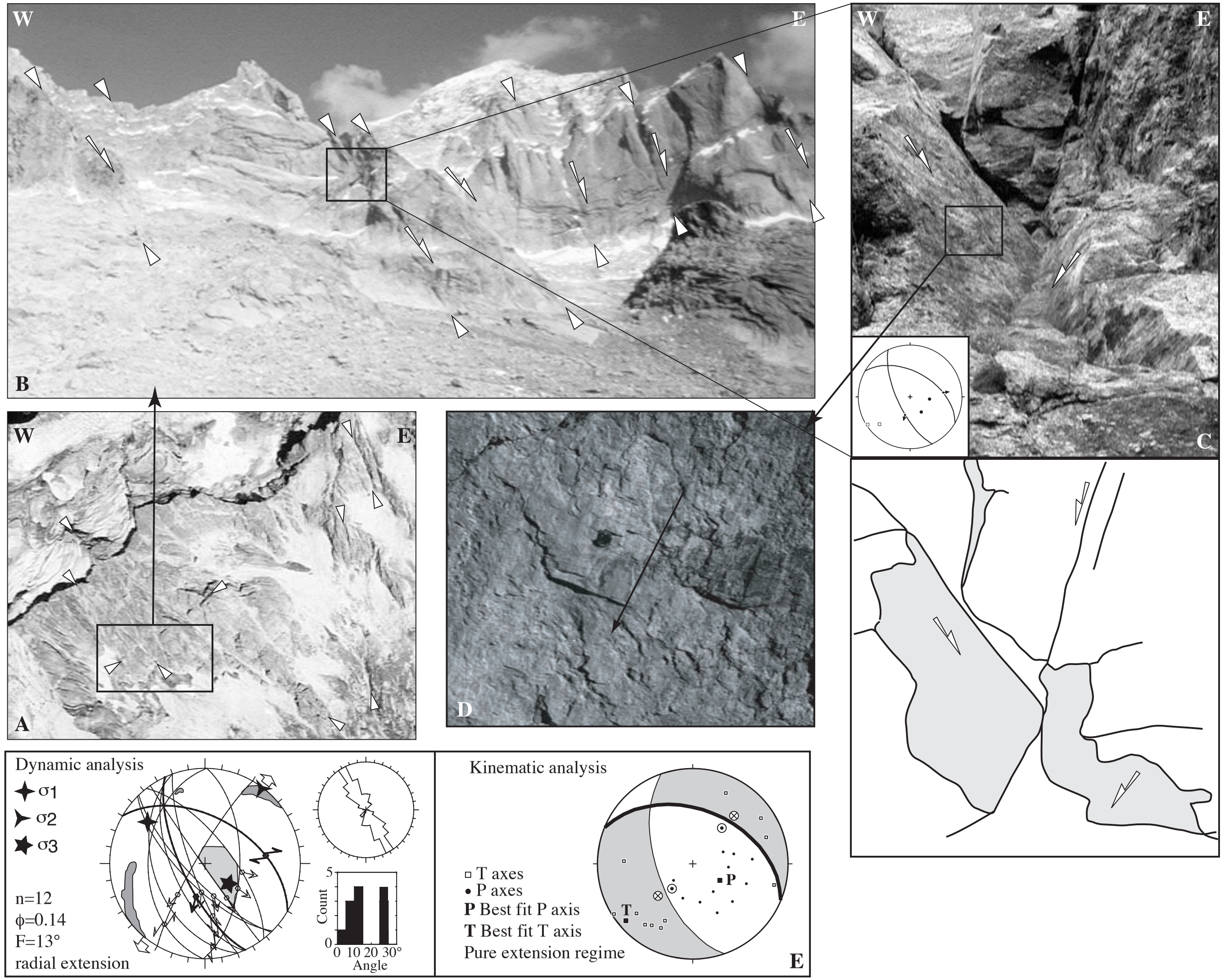

Fig. 5. Outcrop example of normal faulting at various scales and related fault-slip analysis. (A) Extract of aerial photograph view in the central part of the granodiorite (north side of Val Di Mello, Piz di Zocca area). A set of prominent transversal faults (NW to N trending) is clearly detectable within the geomorphology (white arrows delineate some of these faults) (B) Detail in the area of (A): set of transversal east dipping normal faults in the granodiorite. Faults are indicated by white arrows. (C) and (D) Detail of (B) with conjugated fault planes and striation on the east dipping fault plane. In (D) arrow indicates displacement of missing wall. (E) Dynamic (left) and kinematic analysis (right) of corresponding minor fault population. Left stereonets: lower hemisphere representation of faults (heavy black lines are faults viewed in C) and associated slip (arrows), principal stress axes (σ1, σ2 and σ3) symbolized by five-branch, four-branch and three-branch stars, respectively, from the direct inversion method and right dihedra inversion results with potential areas for σ1 and σ3 (light and dark grey areas, respectively). The small stereonet gives the statistical distribution of fault strikes. The histogram gives the statistical distribution of the angle between the measured striae and the computed ones. Right stereonet: results of P-B-T axes method in fault plane solution representation. See section 3.2.2. for more detailed explanations.

the SSB and reactivate them. Laterally the faults cut through the Bergell intrusion contact.

To the north, in the Lago Albigna area, an important fault zone is geomorphologically well expressed by sub E-W oriented ravines and slop anomalies, and by thick cataclasites and fault gouges (up to 1 meter) on the outcrop (fig. 6). The faults are either subvertical or steeply N dipping, with dip angles greater than 60°. In these major fault zones, slip lines are associated with dominantly dextral strike-slip movement. Early reverse striations, older than the horizontal ones, have also been found in places but have generally been erased by the more recent movements.

Elsewhere fault displacement associated to this family is usually normal to oblique-normal on the one hand, and dextral. The N070 striking family however typically slipped sinistrally with various amounts of oblique-slip component. Several km-scale fault segments akin to this longitudinal family and poorly expressed from the morphological point of view have been detected in the central Bergell intrusion, in a wide region centered around the San Martino area and west of it. Distributed over a ca. 5 kms wide zone, they constitute another secondary important fault zone.

(3) A third fault family is sub-N-S oriented (circa 15% of all linear trends). The associated major and minor peaks trend N000 and around N015, respectively. On the contrary of other fault families, this one is not represented by a major tectonic lineament in the field area. These faults are better revealed by our morphotectonic analysis in the central and eastern parts of the intrusion, in the San Martino and Monte Sissone areas. A prominent set of NNW-SSE to N-S directed faults also carves out the immediate hangingwall of the Forcola Line in the western part of the field area. At the outcrop scale however, the faults have been measured usually over the entire field area. Two possible senses of shear are relevant to the faults with intermediate to steep dippings: a normal to strong sinistral-oblique normal faulting movement and a typical sinistral strike-slip offset, the former one mainly pre-dating the latter one when evidences of fault reactivation are observed on the main fault planes.

(4) The last fault family is sub-NE-SW oriented (circa 10% of all linear trends) with corresponding strikes vary roughly between N030 to N050. This family is poorly drawn from our morphotectonic analysis but again is strongly developed on the outcrop scale, all over the investigated measurements sites. The kinematic analysis of the faults points out both a strong sinistral-oblique normal faulting displacement and a sinistral off-set, along discontinuities with intermediate to steep N and S dip angles. The major tectonic lineament matching these structures trend is the Engadine Line in the study area. No real gradient of hm- or km-scale brittle structures occurence toward the Engadine master fault is evidenced from the geomorphology. This may also be due to the particular relationships of the brittle structures with the local topographic depressions. A km-scale fault parallel to and

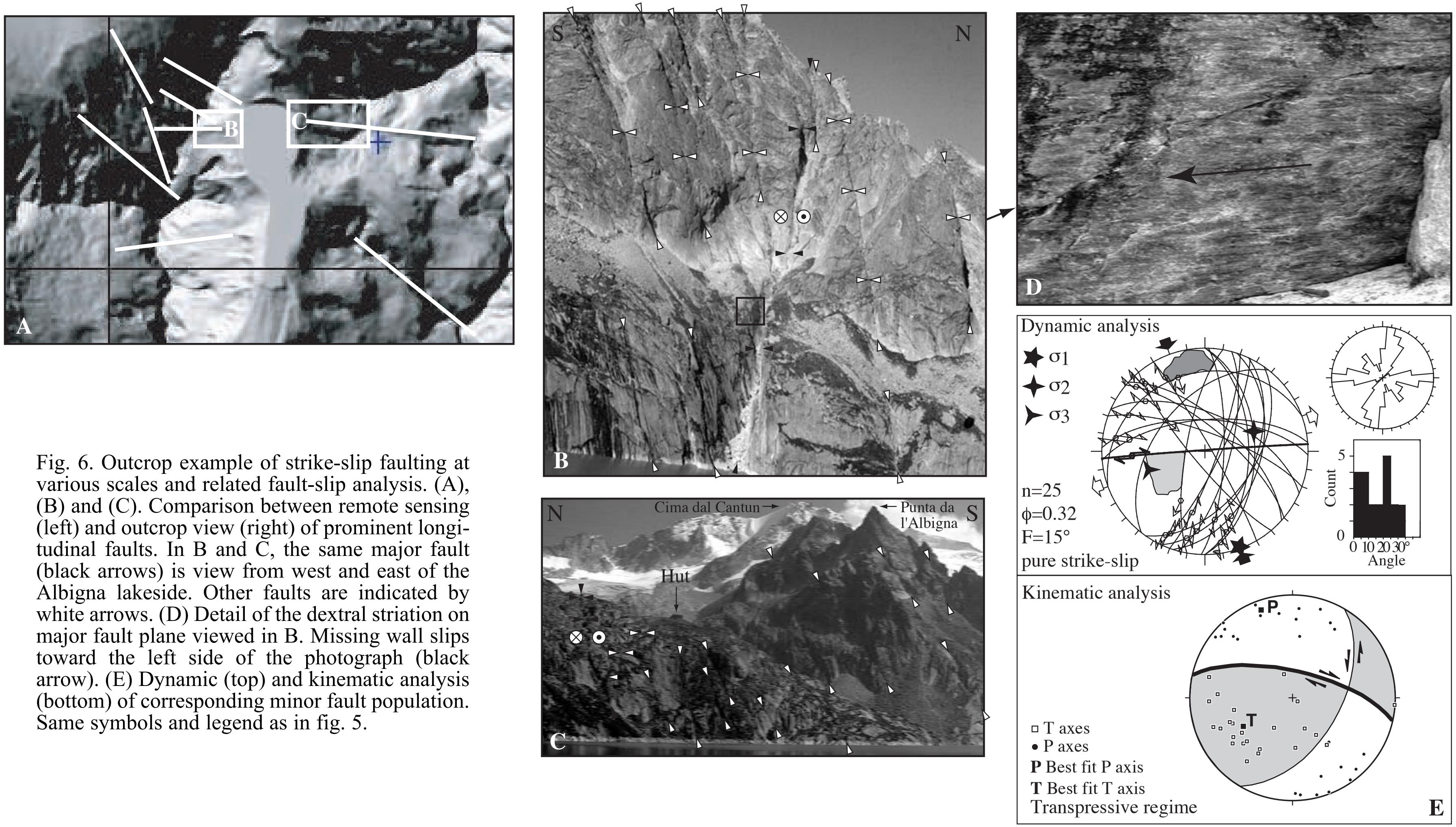

Fig. 6. Outcrop example of strike-slip faulting at various scales and related fault-slip analysis. (A), (B) and (C). Comparison between remote sensing (left) and outcrop view (right) of prominent longitudinal faults. In B and C, the same major fault (black arrows) is view from west and east of the Albigna lakeside. Other faults are indicated by white arrows. (D) Detail of the dextral striation on major fault plane viewed in B. Missing wall slips toward the left side of the photograph (black arrow). (E) Dynamic (top) and kinematic analysis (bottom) of corresponding minor fault population. Same symbols and legend as in fig. 5.

south of the Engadine Line may constitute the only important secondary structure detected in the field near Maloja. Clear sinistral kinematics associated with this secondary fault have however not been clearly established, due to outcrop conditions.

The cross-cutting relationships between fault families and kinematics (normal to oblique-normal faults and strike-slip faulting) are not obvious at the map-scale, mainly because the lateral prolongation of the faults is difficult to assess with certainty and the reliable observation of superposed striations are not the rule on the master fault planes. But as a work hypothesis we believe that the map-scale normal and oblique-normal transversal faults formed prior to or coeval with the longitudinal faults (that slip dextrally with various amounts dip-slip component) during a main transtensive tectonic event. Later however both fault systems have been reactivated as transcurrent faults. A breakdown into the analysis of fault populations at the meso-scale might bring about clear trends regarding the brittle slip events history, given the self-similar nature of the faulting process (e.g. Tchalenko, 1970).

3.2. Fault-slip data analysis

3.2.1. Data collection

Fault-slip data were sampled in the field over 120 measurements stations, which altogether represent ca. 3500 fault planes collected. Most of the stations (70%) have been set inside Tertiary intrusions (Bergell intrusion, Triangia tonalite, Novate granite), the rest of the stations encompassing high-grade country rocks from Penninic and Austrolapine units (fig. 4). We investigated the kinematics of brittle deformation from fault geometry and structure at various scales. Some examples of map-scale faults geometry (e.g. typical conjugated normal faults) are given in fig. 7. At the micro-tectonic, scale, we recorded mainly faults with structures indicative of slip direction and shear-sense (fig. 7). Grooves and striations from abrasion during slip or elongate chlorite and epidote crystals present in dilatational fault-surface jogs delineate slip direction (fig. 7b,c). The sense of movement along the slickenside was inferred from kinematic indicators, mostly fibrous minerals (chlorite, epidote, serpentine, talc) or quartz and calcite grown behind fault steps, rough and smooth facets on the fault plane, but also from secondary shear fractures, such as synthetic and antithetic shears (Riedel and Riedel-conjugated shears) or tension fractures (fig. 7g, e.g. Hancock, 1985; Petit, 1987). As much as outcrop conditions allowed it, the more shear-sense indicators and corroborating structures combined, the better the confidence level assigned to the slip-sense determination. The quality of slip-sense was classified in the field as certain, probable, inferred or unknown. In individual stations, fault families characterized by a well-defined and narrow range of orientation and slip direction, and with obvious offset sense, were used to infer the kinematics of questionable striae-bearing fault

Table 1. Synthetic table of the kinematic and stress analysis computed from fault-slip data.

#	Locality (& reference name)	Rock type	N	RDM P% / T%	G (number of data)	P (e_3)	B (e_2)	T(e_1)	σ_1	σ_2	σ_3	Φ	n_1/n_2	Fm (°)/ Fmax (°)	n_3/nev	Kinematic regime	Relative chronology (n observations)
1	Gordona waterfall	AGU	33	90/100	1 (n=19)	217/75	318/03	049/15								pe	1 (5)
	(GORDW*)				2 (n=14)	141/02	288/88	051/01								pss	
2	Gordona Road	AGU	52	86/96	1 (n=20)	206/77	328/07	059/11								pe	1 (14)
	(GORDR1*)				2 (n=32)	295/20	144/67	029/10								pss	
3	Gordona Road	AGU	43	83/88	1? (n=21)	202/70	337/14	071/13								pe	no
	(GORDR2*)				2? (n=22)	162/18	045/55	262/29								pss	
4	San Pietro (SANPTR1*)	AGU	15	100/100	1 ?	212/65	341/16	077/18								pe	no
5	Era (ERA1*)	AGU	12	100/100	1 ?	206/45	333/31	082/29								pe	no
6	San Fedelino/Casenda (SANFD1)	AGU	9	100/100	1 ?	182/57	325/27	064/17								pe	no
7	Val Codera-Cola Path (VCCOLA1*)	NG	31	100/100	1	154/52	326/38	059/04								pe	1 (1)
8	Val Codera-Cola Path (VCCOLA2)	BT	36	83/88	1 (n=17)	197/74	338/13	070/10	180/69	339/20	072/07	0.51	18/16	19/37	2/0	pe	1 (1)
					2 (n=19)	158/09	262/56	062/33	157/05	250/27	058/63	0.37	18/15	19/36	3/1	pr	
9	Val Codera-Codera East (VCCDR*)	NG	41	90/92	1 (n=35)	156/59	335/31	065/01								pe	1 (1)
					2 (n=6)	163/11	261/38	59/50								c	
10	Val Codera-Old Quarry (VCQAV*)	BT	18	100/100	1 ?	179/70	340/19	072/06	181/49	338/39	077/12	0.64	18/14	17/33	4/1	pe	no
11	Val Codera-Btta Fobbia (VCBF*)	NG	15	100/100	2 ?	146/41	338/48	242/06								pss	no
12	Val Codera-Path Gallery (VCGAL*)	NG	34	97/97	1 ?	173/61	333/27	067/09								pe	no
13	San Giorgio (VRSG1)	AGG	13	100/100	2 ?	135/06	235/56	041/34								pss	no
14	San Giorgio (VRSG2*)	NGD	44	100/100	1 ?	142/51	334/38	239/06								pe	no
15	San Giorgio (VRSG3*)	NGD	24	100/100	1 ?	079/71	333/05	241/18	078/76	323/06	231/12	0.19	23/21	17/31	2/1	re	no
16	San Giorgio (VRSG4*)	BT/NVD	53	92/94	1 (n=31)	338/66	163/24	072/02								nss	1 (4)
					2 (n=22)	162/01	040/89	252/01	169/07	065/64	263/25	0.31	22/18	19/31	4/0	pss	
17	Novate Mezzola-Riva Quarry (NOVMQ1)	NG	31	96/100	1	283/72	163/10	070/15	230/75	332/03	063/15	0.36	31/24	10/35	7/2	pe	1 (4)
18	Novate Mezzola- Old Quarry (NOVMQ2)	NG	35	97/100	1 (n=30)	074/87	343/00	253/08	044/83	138/00	229/07	0.30	30/29	12/30	1/0	pe	1 (3)
					2 (n=5)	127/14	248/65	032/21	282/22	146/60	019/19	0.72	5/5	11/22	0/0	nss	
20	Valle Dei Ratti Fume (VALRT1)	BDZ	14	92/92	1 (n=5)	338/73	135/16	227/06								re	1 (1)
					2 (n=9)	334/10	235/44	074/45								pss	
21	Valle Priasca (VALPR1)	BDZ/BT	28	92/96	1 ?	130/68	341/19	247/10	123/68	311/21	220/03	0.13	27/23	17/38	4/1	re	no
22	Verceia-Road Tunnel (VERCT*)	AGU	3	100/100	1 ?	143/43	002/39	254/21								pe	no
23	Albonico N-Stream (STBALB1*)	AGU	40	97/97	2 ?	163/01	337/89	073/00								pss	no
24	Livo-Vico (STBVICO 1)	BT	34	97/100	2 ?	143/22	285/63	047/15	151/21	265/46	045/36	0.10	34/28	14/38	6/1	rss	no
25	Livo-Vico (STBVICO 2)	BT	88	79/87	1 (n=26)	077/67	326/09	232/21	088/69	335/08	242/19	0.25	26/25	11/40	1/0	re	1 (11), 2 (2)
					2 (n=62)	148/15	322/75	058/02	154/12	061/16	279/70	0.09	62/52	16/40	10/3	rss	
26	Livo-Vico (STBVICO3)	BT	46	91/88	1 ? (n=11)	122/63	290/26	022/05	150/68	355/20	262/08	0.06	11/11	15/32	0/0	re	no
					2 ? (n=35)	146/19	308/70	054/06	152/19	341/70	243/03	0.12	35/28	12/37	7/1	rss	
27	Livo-Canyon (STBLIVOC1)	BT	53	84/86	1 (n=18)	046/85	152/01	242/04	110/80	329/08	238/06	0.68	27/22	14/37	5/0	pe	1 (2), 4 (1)
					2 (n=35)	146/05	323/85	056/00	330/06	235/36	068/53	0.30	26/18	12/34	8/2	pr	
28	Dascio Road (DASCIORD1*)	BT	34	93/90	1 (n=6)	301/73	164/13	071/11								pe	1 (1)
					2 (n=28)	169/06	261/11	052/77	166/04	257/11	057/79	0.58	34/22	15/39	12/1	pr	
29	Dascio Road (DASCIORD2*)	BT	11	100/100	2a (n=7)	021/06	290/14	132/75								pr	4 (4)
					2b (n=4)	309/02	042/56	217/34								pss	
31	Bocca D'Adda-Quarry	BT	61	86/93	1 (n=17)	104/70	339/12	245/16	087/75	334/06	242/13	0.41	18/15	20/37	3/0	pe	1 (3)
	(DASCIOADDA1)				2 (n=44)	158/07	262/63	065/26	159/09	269/66	065/22	0.14	43/34	13/36	9/0	rss	

Table 1. Continued

#	Locality (& reference name)	Rock type	N	RDM P% / T%	G (number of data)	P (e_3)	B (e_2)	T(e_1)	σ_1	σ_2	σ_3	Φ	n_1/n_2	Fm (°)/ Fmax (°)	n_3/nev	Kinematic regime	Relative chronology (n observations)
32	Mello-Bioggio-Prati Aragno (MELPA)	BT	35	71/88	1 (n=20)	094/63	326/17	230/20	091/73	332/09	240/15	0.26	22/19	12/35	3/1	re	1 (3)
					2 (n=15)	355/06	259/44	091/45	337/09	067/02	169/80	0.32	13/10	17/40	3/0	pr	
33	Mello-Poira Di Fuori (MELPDF)	BT	43	100/88	2	156/01	247/65	066/25	154/21	284/59	056/21	0.22	31/27	16/38	16/2	rss	4 (5), anti-4 (1)
34	Roncaglia-Poira Di Dentro (STBRPD)	AU	7	100/100	2 ?	329/02	063/63	239/26								pss	no
35	Val Dei Ratti-Valle Codogno (VDRVC)	BT	22	95/100	1 (n=14)	122/65	323/23	230/08	136/76	323/14	233/02	0.50	14/13	13/37	1/0	pe	1 (3)
					2 (n=8)	155/13	292/72	062/12	159/08	290/78	067/09	0.27	8/8	16/30	0/0	pss	
36	Mello North-Monte Sciesa (STBMTES)	BT	27	96/100	1 (n=8)	079/66	341/03	250/23	118/74	346/11	254/12	0.34	8/8	12/38	0/0	pe	1(3)
					2 (n=19)	136/01	238/87	046/03	138/01	046/71	229/19	0.01	19/19	13/27	0/0	rss	
37	Val Dei Ratti-Passo Colino (VDRPCOL)	BT	22	100/100	2	147/09	332/81	237/01	152/06	247/38	054/51	0.11	22/20	12/31	2/0	rss	1 (1)
38	Valle Spluga-Casera Desenigo (VSPCDD)	BT	22	95/100	1 ?				198/88	331/01	061/02	0.83	22/14	13/40	8/0	nss	1 (2), 2 (2)
					2 ?	156/43	326/47	062/05								nss	
39	Valle Spluga-Laghetti (VSPLAG1)	BG	16	100/93	2	157/19	251/13	014/67	145/08	237/14	026/74	0.89	16/12	21/40	4/1	c	4 (1), 1 (2)
40	Cevo (Val Masino) (STBCEVO)	AS	37	97/97	2 ?	152/14	341/76	242/02	149/09	306/80	058/04	0.23	37/35	9/26	2/1	rss	no
41	Valle Spluga-Cerosolo (VSPCER1)	BT	13	92/92	2 ?	167/12	060/52	266/35								pss	no
42	Passo San Jorio-Tonalite (PASSOSJ1)	BT	19	100/91	2 ?	305/00	213/86	035/04	136/03	231/60	045/30	0.21	19/14	16/37	5/1	pss	no
43	Passo San Jorio (PASSOSJ2*)	TS	17	100/100	2 ?	142/16	047/14	279/68	150/10	241/07	007/78	0.15	17/16	14/35	1/1	c	no
50	Corte Vecchia Path (VDBCV1)	BT	11	90/100	1 ?	191/46	323/33	071/26								pe	no
51	Corte Vecchia Path (VDBCV2)	BT	5	100/100	1	330/49	197/31	091/24								nss	1 (1)
52	Passo Dell' Oro (OMIO1PDO)	BG	32	93/100	1 ?	154/39	298/45	048/18	191/72	314/10	046/14	0.83	32/26	16/39	6/1	nss	no
53	Cima Barbacan-Monte Boris (OMIO4CBMB	BG	36	97/97	1 ?	111/62	307/27	214/06	131/77	296/12	027/03	0.49	35/28	16/37	7/2	pe	no
54	Passo Ligoncio (OMIO2PASL*)	BG	23	82/82	1 ?	085/43	338/18	231/41								pe	no
55	Btta Medacio (OMIO3BAMD)	BG	61	95/95	1 ?	147/42	306/45	047/11	143/70	297/18	029/08	0.59	44/39	16/36	5/1	pe	no
					2 ?				153/08	054/49	250/40	0.19	17/15	16/38	2/1	rss	
56	Merdarola Path (VBDBMERD1)	BG	12	100/100	1	102/71	311/17	218/09	141/77	299/12	030/05	0.31	12/10	20/40	2/0	pe	1 (1)
57	Merdarola Path (VBDBMERD2)	BG	26	96/96	2 ?	356/03	260/66	087/24	347/03	251/67	079/23	0.62	26/25	11/29	1/0	pss	no
58	Val Dei Ratti-Rif. Volta (VDRRIFV)	BG	35	71/88	1 (n=19)	131/74	308/16	038/01	100/61	300/27	206/08	0.56	19/16	19/37	3/0	pe	1 (1), 3 (1)
					2 (n=16)	144/13	239/23	027/63	147/03	057/09	257/80	0.21	16/13	14/32	3/1	rss	4 (1), anti-4 (1)
59	West Pizzo Ligoncio (VDRPZLIG)	BG	53	74/70	1 (n=25)	137/81	308/09	038/01	184/83	306/04	036/06	0.33	25/16	15/34	9/0	pe	1 (8), 2 (1), 3 (1)
					2 (n=28)	171/11	326/77	080/05	166/22	268/27	042/54	0.17	28/19	14/37	9/1	rss	4 (3)
60	Filorera-Cataeggio (VSBFC)	BT	26	96/96	1 (n=17)	312/71	090/15	183/12	286/51	077/05	177/14	0.78	17/17	14/39	0/0	nss	1 (1), 3(1)
					2 (n=9)	344/08	235/65	077/23	161/06	276/76	070/13	0.50	9/9	14/33	0/0	pss	
61	Val Di Sasso Bisolo-Foppa (VSBF1)	BT	56	82/85	1 (n=25)	035/85	137/01	227/05	167/84	322/50	052/02	0.48	47/31	16/39	16/4	pe	1 (2), 3(1)
					2 (n=31)	151/10	275/73	058/14								pss	
62	Val Di Sasso Bisolo-Foppa (VSBF2)	BT	78	76/88	1 (n=31)	017/80	120/02	210/09	066/82	309/03	219/07	0.18	31/31	12/29	0/0	re	1 (8)
					2 (n=38)	165/08	292/77	074/10	167/13	333/76	076/03	0.43	47/38	12/34	9/0	pss	
63	Val Preda Rossa-Passo Basset (VPRPB)	BT	24	87/100	1 (n=14)	136/72	336/17	244/06	147/71	334/19	243/02	0.38	14/12	15/28	2/0	pe	1(2)
					2 (n=10)	339/01	247/68	069/21	160/05	259/63	067/27	0.27	10/10	8/17	0/0	pss	
64	Refugio Ponti (VPRRP1)	BT	28	100/100	1 (n=10)	003/76	131/08	222/11	323/79	127/11	218/03	0.49	9/8	11/25	1/0	pe	1 (1), 3? (1)
					2 (n=18)	161/01	253/52	070/38	340/02	246/59	072/31	0.41	19/18	13/32	1/0	pss	
70	Temola Path (VDMTEM1)	BG	8	100/100	2 ?	348/13	237/58	085/29								pss	no
71	Ca di Carna (VDMCC)	BG	13	100/100	1 ? (n=6)	079/71	322/09	229/17								pe	no
					2 ? (n=7)	157/17	278/59	059/25								pss	

Table 1. Continued

#	Locality (& reference name)	Rock type	N	RDM P% / T%	G (number of data)	P (e_3)	B (e_2)	T(e_1)	σ_1	σ_2	σ_3	Φ	n_1/n_2	Fm (°)/ Fmax (°)	n_3/nev	Kinematic regime	Relative chronology (n observations)
72	Val di Mello-Casera del Ferro (VDMCF)	BG	20	95/100	1 ? (n=7)	092/62	308/23	211/15	101/64	282/26	192/00	0.29	7/7	13/27	0/0	pe	no
					2 ? (n=13)	299/07	118/83	209/00	306/07	130/83	036/00	0.30	13/13	14/26	0/0	pss	
73	Val Masino-San Martino (VMSANM1)	BG	38	86/90	1 (n=20)	149/67	309/22	042/07	132/67	312/23	222/00	0.26	20/16	8/20	4/0	re	1 (2)
					2 (n=18)	157/11	276/69	063/18	165/15	299/68	071/15	0.62	18/17	16/37	1/0	pss	
74	Val Masino-San Martino (VMSANM2)	BG	40	92/97	1 (n=22)	144/70	331/19	240/02	134/76	335/13	244/05	0.47	22/20	10/31	2/0	pe	1 (3)
					2 (n=18)	157/13	318/76	066/04	155/13	248/45	053/42	0.10	18/18	12/38	0/0	rss	
75	Valle Del Ferro-P. Ferro (VDMPZF)	BG	26	92/100	1 (n=13)	134/55	321/35	042/02	155/69	322/20	054/04	0.47	13/13	9/38	0/0	pe	1 (2)
					2 (n=13)	144/14	267/65	048/20	154/15	271/59	056/26	0.32	13/12	14/31	1/1	pss	
76	Alpe Cameraccio (VDMALPC)	BG	34	94/97	1				172/68	340/22	072/04	0.92	34/25	17/38	9/0	nss	1(2), 2(1)
					2 ?	168/16	006/74	260/05								nss	
77	Valle Torrone-Pso Cameraccio (VDMPCAM	BG	27	92/100	1	136/59	332/30	238/07	115/81	328/07	238/05	0.58	27/24	13/38	3/0	pe	1(2), 2(1)
80	East Passo Zocca (VDMREFALL1)	BG	47	85/95	1 (n=27)	157/74	340/16	250/01	157/68	343/22	252/02	0.39	27/24	17/40	3/0	pe	1? (1)
					2 (n=20)	163/10	318/79	072/04	158/16	356/73	249/05	0.27	20/18	19/38	2/0	pss	
81	East Passo Zocca (VDMREFALL2)	BG	53	94/96	1 (n=12)	121/63	324/25	230/09	131/63	306/26	037/02	0.14	12/12	13/30	0/0	re	1? (1), 4(3)
					2 (n=41)	153/11	258/53	056/35	152/11	245/13	022/73	0.15	41/31	18/37	10/4	c	
82	East Passo Zocca (VDMREFALL3)	BG	17	94/90	1? (n=8)	094/84	330/03	239/05								nss	no
					2 ? (n=9)	178/04	272/47	084/42								pss	
83	Il Pianone (VDMREFALLPIA)	BG	5	100/100	2 ?	007/28	164/60	272/10								pss	no
90	Pizzo Badile (VPOREFGPB)	BG	52	88/88	1 (n=34)	057/81	158/02	248/08	076/77	334/03	243/13	0.45	34/28	12/30	6/1	pe	1(3), 2(1), 3 (2)
					2 (n=18)	133/23	261/56	032/24	150/17	262/50	048/34	0.10	18/15	16/37	3/0	rss	
91	Pizzo Cengalo (VPOREFGPC)	BG	62	93/87	1 ?	137/18	302/72	046/04	132/30	329/59	226/08	0.19	62/47	10/39	15/13	rss	no
92	Pizzo Sceroia (VPORIFGPS)	BG	32	93/93	2	138/03	238/75	048/15	147/06	267/79	056/10	0.28	32/24	20/40	8/3	pss	1 (1)
93	Pizzo Porcellizzo (VPORIFGPP)	BG	43	81/93	1 (n=23)	073/74	314/08	222/14	112/77	319/11	228/06	0.24	23/18	14/38	5/1	re	1 (3)
					2 (n=20)	140/03	233/51	047/38	143/03	237/55	051/35	0.19	20/18	14/29	2/0	rss	
94	Valle Porcellizzo (VPO1)	BG	15	100/100	1 ?				311/81	145/08	055/02	0.78	15/13	20/38	2/0	nss	no
					2 ?	150/33	327/57	059/01								pss	
100	Albigna Lago-Vadrec (ALBVAD1)	BG	23	91/95	1 ?	142/42	339/47	240/09	126/71	337/17	244/09	0.75	18/16	14/32	3/0	nss	1 (1), 2(1)
					2				141/08	268/64	048/25	0.17	5/4	6/11	1/0	rss	
101	Albigna Lago-Vadrec (ALBVAD2)	BG	22	86/90	1 (n=10)	071/66	337/02	246/24								pe	1 (1)
					2 (n=12)	165/15	277/54	065/32								pss	
102	Albigna-East Lake Hut Path (ALBR)	BG	8	100/100	2 ?	150/05	277/82	059/06								pss	no
103	Albigna Hut (ALBHUT)	BG	57	96/96	1 ? (n=10)	015/52	209/37	114/07	001/52	237/24	134/28	0.25	14/12	18/38	2/1	re	no
					2 ?(n=47)	010/08	180/81	280/01	007/09	208/80	098/03	0.26	43/40	16/38	3/2	pss	
104	Pass Da Casnil Path (ALBPC1)	BG	6	100/100	2 ?	138/34	318/56	228/00								pss	no
105	Albigna-Barrage (ALBBAR1)	BG	69	97/98	1 (n=25)	355/63	178/27	088/01	348/45	186/44	087/09	0.70	40/37	12/36	3/0	pe	1 (2)
					2 (n=44)	000/15	243/60	097/25	001/16	251/51	102/34	0.42	29/25	12/33	4/0	pss	
106	Albigna-West Lake Path (ALBWL)	BG	25	100/100	2a				292/34	035/18	148/50	0.67	4/4	10/20	0/0	pr	4 (3)
					2b	340/10	080/44	240/44	160/02	068/48	252/42	0.32	21/21	15/40	0/0	pss	
107	Albigna-Roda Val Neve (ALBRVN1)	BG	19	100/100	2 ?	140/05	252/76	049/13	161/42	309/43	056/16	0.54	19/15	15/40	4/2	pss	1 (2)
110	Val Bondasca-Selvartigh (VBO1)	TG	8	100/100	1 ?	135/45	327/44	231/06								pss	no
111	Val Bondasca-Cant Ganda (VBO2)	AGU	32	93/93	2	170/03	275/77	080/13	356/08	207/81	087/05	0.57	25/25	13/38	0/0	pss	3 (1)
									315/03	049/49	222/41	0.15	7/6	10/23	1/0	c	

Table 1. Continued

#	Locality (& reference name)	Rock type	N	RDM P% / T%	G (number of data)	P (e_3)	B (e_2)	T(e_1)	σ_1	σ_2	σ_3	Φ	n_1/n_2	Fm (°)/ Fmax (°)	n_3/nev	Kinematic regime	Relative chronology (n observations)
112	Val Bondasca-Cap. Sciora (VBOALPSC)	BG	46	86/86	1 (n=14)	056/77	324/00	234/13	099/83	323/05	233/05	0.40	12/12	19/30	0/0	pe	1 (2)
					2 (n=32)	331/04	068/60	239/30	159/03	064/59	251/31	0.20	34/30	15/40	4/0	rss	
113	Maloja-Orden Path (MALORD1)	AU	7	100/100	1 ?	185/60	333/27	070/14								pe	no
114	Maloja-Road (MALR1)	AU	41	92/97	1 ?	202/54	325/21	066/28								pe	3(3), 1(1), 2(1)
115	Orden-River (ORDRV1*)	AU	92	89/89	1 ? (n=43)	168/42	018/44	272/15	171/58	352/32	262/00	0.20	43/32	13/38	11/3	re	1 (2), 2 (3), 3 (2)
					2 ? (n=49)	151/06	288/81	061/06	156/08	249/16	040/72	0.24	49/35	16/39	14/3	c	
116	Orden-Bosch Furcela (ORDBF1*)	MFU	24	100/100	2 ?	328/29	175/58	064/11								pss	no
117	Piz Salacina-Pass Caval (PIZSAL1)	MFU	19	100/100	1	279/54	166/16	066/31	253/74	140/06	048/14	0.42	19/16	14/38	3/1	pe	1 (2)
118	Piz Salacina-Pass Caval (PIZSAL2)	MFU	19	90/80	1 ? (n=14)	241/65	137/06	044/24	180/73	289/06	021/16	0.28	19/12	20/38	7/1	pe	no
					2 ? (n=5)	129/09	253/75	037/12								rss	
119	Plan Canin-Alp Cavloc path (VFOAC)	MFU	9	100/100	1 ?	082/74	326/07	235/14								pe	no
120	Lagh Cavloc-Orden path (VFOCAVORD)	MFU	21	80/100	1 ?(n=10)	015/77	162/10	253/07	359/77	157/12	248/04	0.29	10/9	8/16	1/0	pe	no
					2 ? (n=11)	320/01	224/78	051/12	320/05	148/86	053/00	0.04	11/9	16/37	2/0	rss	
121	Plan Canin-Dam & river (VMUDAM1)	MFU	64	84/93	1 ? (n=24)	132/75	316/15	226/1	125/75	283/14	014/05	0.13	23/17	16/38	6/1	re	1 (4), 2 (2), 3 (4)
					2 ? (n=40)	164/09	270/60	069/28	160/08	261/53	064/36	0.23	41/33	18/40	8/2	rss	
122	Plan Canin-South Dam (VMUDAM2)	MFU	9	100/100	2 ?	173/08	275/55	077/34								pss	no
123	Plan Canin-SE Dam (VMUDAM3)	MFU	19	84/94	1 ?	162/25	317/62	067/10	193/68	328/16	063/15	0.61	19/11	13/37	8/2	pe	1 (2), 3(1)
124	Plan Canin-SE Dam (VMUDAM4)	MFU	9	100/100	2 ?	335/41	146/48	241/05								nss	no
125	Val Muretto-Plan Canin (VMUPC1)	MFU	40	92/92	1 ? (n=19)	173/71	289/08	021/17								pe	1 (3), 2 (1)
					2 ? (n=21)	148/13	281/71	055/14								pss	
126	Piz Murtaira-I Forn (PIZMURT1)	MFU	17	100/94	2	326/13	223/42	069/45								pss	1 (1), 4 (1)
127	Piz Murtaira (PIZMURT2)	BG	23	91/95	2 (n=13)	134/75	336/14	245/05	139/74	334/16	243/04	0.13	13/13	13/25	0/0	re	3 (1)
					1 (n=10)	157/10	262/54	060/34	165/13	272/52	065/35	0.41	10/9	10/27	1/1	pss	
128	Val Forno-West Side (VFOWS1)	BG	15	100/100	1 ?	166/70	345/20	075/00								pe	no
129	Val Forno-West Side (VFOWS2)	BG	22	100/100	2 ?	168/14	303/70	075/14								pss	no
130	Val Forno-West Side (VFOWS4)	BG	72	77/86	1 (n=36)	135/80	328/09	238/02								pe	1 (13), 3 (1)
					2 (n=36)	174/13	296/66	079/19								pss	
131	Val Muretto-West Piz Fedoz (VMPF1)	MFU	14	100/100	1 ?	232/56	331/06	065/33	162/11	265/48	063/40	0.81	14/13	15/24	1/0	nss	no
132	Val Muretto-West Piz Fedoz (VMPF2)	MFU	22	100/100	2	009/71	153/16	246/11	341/76	147/14	238/03	0.44	21/18	12/33	3/0	pe	3 (1)
133	Val Muretto-West Piz Fedoz (VMPF3)	MFU	16	87/100	1 ? (n=12)	071/65	164/01	254/24								pe	1 (3), 3 (1)
					2 ? (n=4)	304/08	203/54	040/35								pss	
134	Val Muretto-SE Muretto Pass (VMUPM1)	AU	45	91/90	2 (n=20)	194/52	339/32	080/17								pe	3 (1)
					1 (n=25)	165/13	351/77	255/01								pss	
135	Val Muretto-Muretto Pass (VMUPM2)	MFU	46	92/97	1 (n=28)	082/75	315/09	223/12								pe	1(1), 3? (1)
					2 (n=18)	135/24	319/66	226/02								pss	
136	Val Muretto-Muretto Pass (VMUPM3)	AU	25	92/96	1 (n=9)	118/73	317/16	225/05								pe	1(2)
					2 (n=16)	177/14	289/55	078/31								pss	
137	Val Muretto SE-Alpe Vazzeda sup (VMVAZ)	MFU	7	100/100	2	180/26	313/54	078/23								pss	3 (1)
140	Site Mangialdo (TRGMANG1*)	TT	30	93/93	1 ?	168/71	305/14	038/12	156/70	299/16	032/11	0.13	30/24	16/34	6/0	re	no
141	Lago Di Triangia (TRGLAGO1*)	TT	13	100/100	1 ?	083/76	321/08	229/12	118/72	337/14	245/11	0.14	13/12	18/40	1/0	re	no
142	Lago Di Triangia (TRGLAGO2*)	TT	17	94/90	1 ?	151/78	314/11	044/03	321/72	150/17	059/03	0.71	17/12	13/36	5/0	nss	no

Table 1. Continued

#	Locality (& reference name)	Rock type	N	RDM P% / T%	G (number of data)	P (e_3)	B (e_2)	T(e_1)	σ_1	σ_2	σ_3	Φ	n_1/n_2	Fm (°)/ Fmax (°)	n_3/nev	Kinematic regime	Relative chronology (n observations)
143	Pratti Vesolo (TRGPRV1*)	TT	26	85/100	1 ?				315/61	152/28	058/07	0.38	10/9	16/34	1/0	pe	no
					2 ?	349/17	212/67	083/15	178/31	338/57	083/09	0.43	16/14	13/35	2/1	pss	
144	Pratti Vesolo (TRGPRV2)	TT	36	91/100	1	175/66	313/19	048/15	221/76	321/02	052/13	0.38	15/12	8/22	3/0	pe	1 (4)
					2	147/06	250/64	054/25	155/10	246/05	005/79	0.15	21/20	11/31	1/0	rss	
145	Ligari (TRGLIGA1*)	TT	12	91/100	1 ? 2 ?	140/18	351/69	233/10	124/81	328/09	237/04	0.81	12/9	26/39	3/1	nss	no
146	Ligari (TRGLIGA2*)	TT	34	90/100	1 ?	189/76	315/08	047/11	270/76	140/09	048/11	0.55	28/25	16/37	3/0	pe	no
					2 ?				334/31	230/22	110/50	0.27	6/6	18/26	0/0	rss	
147	Ligari (TRGLIGA3*)	TT	7	90/90	1 ?	264/53	137/24	035/26								nss	no
148	Pratti Rolla (TRGPRR1*)	TT	32	96/93	1 ?	156/58	315/30	050/09	157/72	314/17	046/07	0.53	28/20	17/38	8/2	pe	no
149	Pratti Rolla (TRGPRR2)	TT	16	93/90	2	315/18	110/70	222/08	129/00	220/63	039/27	0.20	12/9	16/34	3/1	rss	1 (1)
					1				349/54	242/12	144/34	0.20	4/3	15/27	1/0	re	
150	Triangia village	TT	4	100/100	1 ?	018/78	121/03	211/12								pe	no

Table 1. # is reference number of the sites. Locality is site name (* indicates that deformation locally occurred under brittle-ductile conditions). Rock types are AGU-Adula-Grüf Unit gneisses, BDZ are Bellinzona-Dascio Zone gneisses and schists, BG is Bergell Granodiorite, BT is Bergell Tonalite, NG is Novate Granite, NGD are Novate Granite related dykes, TT is Triangia (Sondrio) Tonalite, TG is Truzzo granite and gneiss, MFU are Malenco-Forno Unit micaschists and mafic to ultramafic rocks, AU are Austro-Alpine Unit gneisses and micaschists, TS are Tonale Series mylonites. N is the total number of measured faults. RDM is the Right Dihedra Method inversion of the N faults (% of maximum compression and extension axes in the solution), see text for details. G is the tensor group according to relative chronology criteria (question marks when no such criteria have been observed or criteria are complex), 1 is older (n: number of faults in the data subset). P (e3), B (e2), T(e1) are azimuth and dip of principal kinematic axes. σ1, σ2, and σ3 are azimuth and dip of principal stress axes. ϕ is the stress ellipsoid shape factor. n1 is the number of faults used for stress analysis after genetic grouping, n2 is the final number of faults after final separation by the stress tensor analysis, n3 is number of data with F values > 35° (i.e. total number of rejected faults). Fm and Fmax are average and maximum angle between measured slickenside and calculated theoretical shear stress on a plane, respectively. nev is "negative expected value": observed shear sense along a fault plane that is contradictory to the calculated maximum shear stress (i.e. number of kinematic incompatibilities). Kinematic regime as defined by Guiraud et al. (1989): pe, pure extensive; re, radial extensive; nss, normal strike-slip; pss, pure strike-slip; rss, reverse strike-slip; pr, pure reverse; c, constrictive. Relative chronology criteria (number of observations): 1: extension ante-compression, 2: extension syn-compression; 3: extension post-compression; 4: strike-slip post reverse (question mark when criterion is doubtful). Measurement stations are located in figs. 4, .

planes («inferred» confidence level). The magnitude of slip on each fault is generally unknown as good markers of relative displacement are rare within the intrusions. In few cases however, some dikes, xenoliths or magmatic schlieren were displaced in the order of centimeters to meters, along individual faults which observed trace lengths range from meters to hundred of meters (fig. 7d, e).

In the field some particular fault relationships support the recognition of successive slip events and the relative age of slickensides (fig. 7c). We paid a special attention to collect systematically such relative chronology criteria. Indeed crosscutting relationships between faults, mutual offsets, as well as superposed or curved slickenside lineations on fault planes, indicated successive slip events in 60% (72 sites of 120) of our measurement sites (table 1). Simple statistics applied to relative chronology observations in table 1, further indicate that in 61% of the polyphased cases, extensional structures predate transcurrent ones. The remaining 39% concern sites where such relative chronology observations are either mostly non systematic (31%) or the contrary (8% only). Concerning the total number of relative chronology observations, 71% of them validate the former case, while 8% and 11% of them deal with non-systematic observations or with the latter case, respectively. The remaining 10% observations deal with the compressional structures only, for which strike-slip faulting post-dates reverse faulting in 9% cases.

But we were also faced with the small number of geochronological data in comparison to the number of brittle measures from a particular site. It was thus necessary to extrapolate the relative chronology established on the basis of a few observations to all data collected in that site. We are aware that this statistical approach obviously suffers sternness, since locally the relative chronology criteria were reversed or inconsistent, in comparison to other sites. Amongst sites with no relative chronology, half of them are dominated by normal faulting while the other half deals with essentially strike-slip deformation. In first approximation, these statistics might point out the complexity of faulting events in the Bergell area and particularly the non-systematic character of faults relative age in nearly half cases. This might indicate that locally the faulting events occurred roughly at the same time, during a single tectonic event. On the other hand, given the number of observations and the tendency of observed extensional striations to pre-date the transcurrent ones, this would rather indicate that extensional faulting, probably together with oblique-slip faulting, once dominated deformation over later transcurrent faulting, in the Bergell area. Size and surface morphology of slickensides (fiber-coated or polished) was also recorded on the field, with the hope it could be indicative of relative age of movements (i.e. fiber-coated slip lines older than polished ones, for the same lithology, fig. 6b,c,g). This approach however did bring about clear trends at the local scale only. Indeed, the local observation of discrete low-angle scratches overimposed on down-dip chlorite-epidote coated striae supports a relative chronology of movements under progressively cooler conditions. The

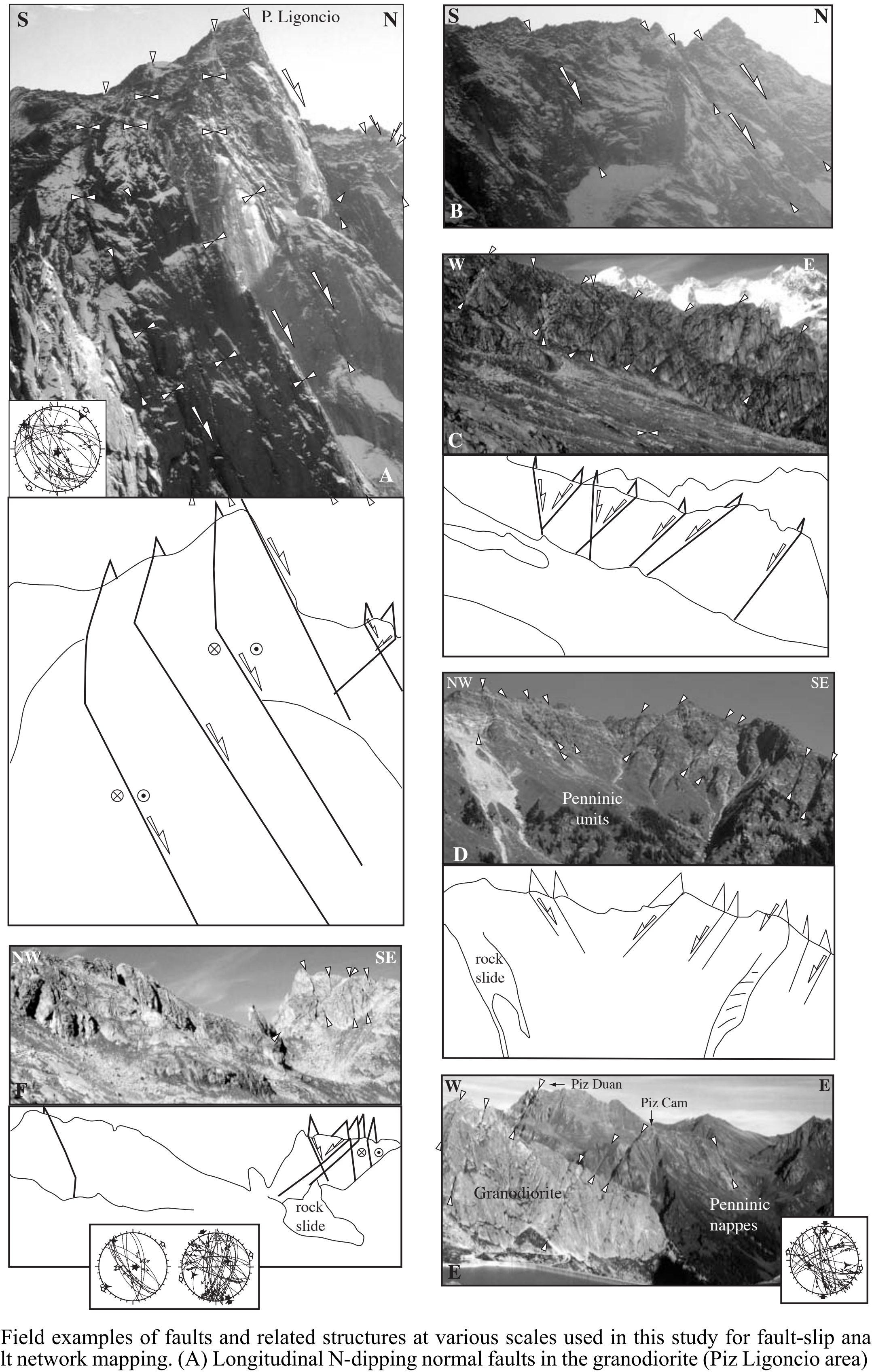

Fig. 7. Field examples of faults and related structures at various scales used in this study for fault-slip analysis and fault network mapping. (A) Longitudinal N-dipping normal faults in the granodiorite (Piz Ligoncio area) with interpretation. Slip on this set of faults is regionally partitioned into normal to normal-oblique dextral or dextral slip. Later dextral strike-slip reactivation is also common on this set of faults. White arrows delineate faults trace. (B) Idem immediatly north of photograph (A). (C) Conjugated set of transversal normal faults in the granodiorite (Monte Boris area). (D) Conjugated set of transversal normal faults in the Penninic nappes north of the Bergell intrusion (Tambo-Suretta nappes). (E) Prominent transversal faults in the Peninnic units (background) and in the granodiorite (foreground). In the granodiorite the faults trend roughly N-S and are sinistral (stereonet). View from

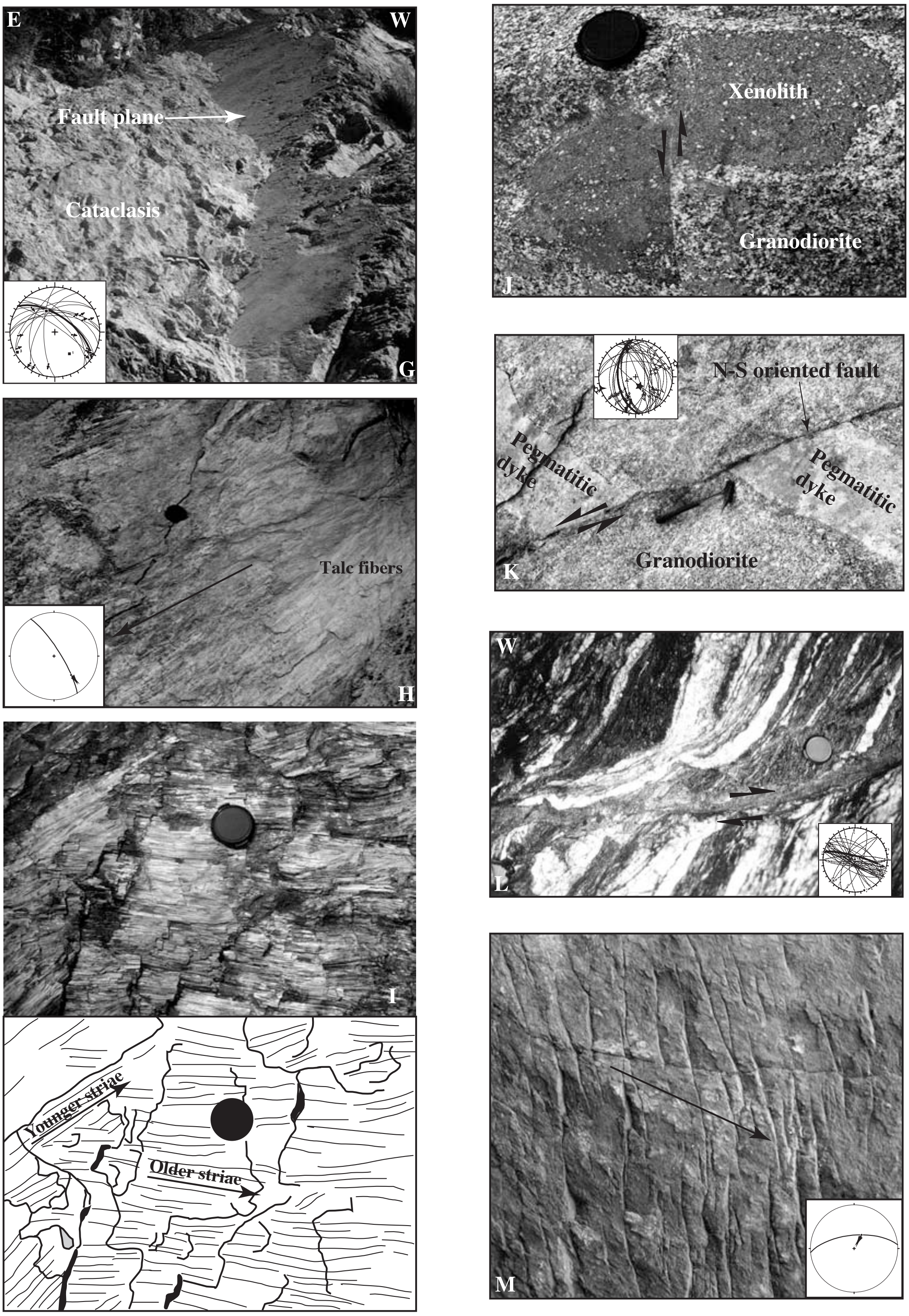

the lago Albigna looking north. (F) Conjugated NW-SE directed normal faults (left stereonet, area of measurement station n°112) and later sinistral strike-slip faults (right stereonet). On the left of the photograph a series of regularly spaced joints, which are non-systematically reactivated. (G) Strike-slip fault plane in the Novate granite and cataclasis in the vicinity of the fault. The stereonet gives the local minor fault population (thick line is the main fault plane). (H) Serpentine-talc coated fault surface in the Malenco ultramafics. Fiber steps indicate a dextral-oblique normal sense of shear. The arrow points toward sense of displacement of missing wall. (I) Striae superposition (serpentine fibers) on a fault surface, indicative of successive slip events. The high-angle striation is younger than the low-angle one. Arrows indicate displacement of missing wall. (J) and (K) Examples of small-scale sinistral strike-slip offset in the granodiorite. (L) Brittle-ductile shear band associated with dextral shear (C/S relationships) in gneisses of the Bellinzona-Dascio zone. (M) Secondary shear structures on a fault surface. The missing wall slips toward the right of the photograph. The stereonet gives the fault plane and striation.

reciprocal was accordingly scarcely observed on the field. More generally however both dip-slip, oblique-slip and strike-slip movements occurred regionally under progressively cooler conditions. Depending on outcrop conditions and structural complexity at least 10, but mostly 30 or more fault planes and striations were measured. In stations with heterogeneous data sets, we tried when it was possible to oversample the number of faults related to a particular stage of deformation. As we were interested in dense sampling of stress and strain orientation stations, we included a few stations with less than 10 fault-slip data. It is obvious that the quality of paleostress determination increases with the number and with the variety of orientations of fault-slip data collected at one site. Some results in table 1 are obviously of limited intrinsic value because the number of data (less than 10) is scarcely larger than the number of unknows. However these sites are not abundant (13% of all sites, 50% of them being set outside the tertiary intrusions) and their results fit generally well with the general frame of paleostress tensors and kinematic axes calculated from larger data sets.

3.2.2. Paleostress and incremental strain computation: the methods

Because each method of fault-slip analysis benefit of their own advantages and particular information (Angelier, 1975), which collectively may be helpful to test and improve the quality of results, we implemented in this study both dynamic and kinematic inversion methods, either numerical or graphical, to derive principal stress and strain axes orientation and ratio (see e.g. figs. 5 and 6). We share the view of Wotjal and Pershing (1991) and Twiss and Unruh (1998) that fault-slip analysis better substantiate sets of faults that together accommodate small strain increments in the deformation history and thus that kinematic interpretations are in general more reliable than dynamic ones. For clarity, we'll use in the following pages either the terms stress or strain axes, in agreement with the signification originally given by the authors of the different inversion schemes. The computer-based fault-slip analysis packages Stress (Villemin and Charlesworth, 1992) and Faultkin (Allmendinger et al., 1989; Marrett and Allmendinger, 1990) provided us the logistics to process our fault-slip data.

The quality and quantity of field data, as well as their spatial distribution, determined the selection of the method used for the inversion. For example, the method of P-B-T axes (Turner, 1953) or the P-T Right Dihedron method (Angelier and Mechler, 1977) were preferred to the direct inversion method (Angelier, 1979) when the data were scarce and poorly distributed. The former methods proved their efficiency to detect kinematic heterogeneities from a set of fault-slip data (Marrett and Allmendinger, 1990; Carey-Gailhardis and Vergely, 1992). Mixed data sets are indicated both by a large spread in P and T axes orientation, and by the lack of pure compression (100% compression) and pure extension (0% compression) fields, respectively. Following Carey-Gailhardis and Vergely

(1992) the right-dihedra method was used as a first step in the fault-slip analysis process, in order to test a priori the degree of kinematic compatibility of all faults within a given dataset (see table 1).

On the other hand, a standard paleostress analysis (e.g. the direct inversion method of Angelier, 1984) provide useful results in the case of numerous fault reactivations in anisotropic rocks resulting in oblique-slip movements on fault planes with scattered fault orientations. As this method doesn't recognize sense of movement on the faults it is thus well-suited for common cases when only a few sure shear senses are recorded on the field. In principle any kinematic analysis would fail in both these circumstances, which is obvious at least for the latter one. The direct inversion method has also proven to fail for particular deformation settings, such as strongly asymmetric fault sets or conjugate fault planes, especially with regard to principal axes ratio which is controlled by faults oblique to stress axes (e.g. Angelier, 1984; Sperner et al., 1993; Adam et al., 2000). Under these conditions a kinematic approach was also favored.

Faults and shear-zones formed at the brittle-ductile transition were preferentially analyzed by the kinematic approach albeit the paleostress inversion method has proven to yield reliable results within limitations and was also tested (see Srivastava et al., 1995 and table 1).

Common to all these methods of fault-slip analysis are basic assumptions and limitations, which have been discussed in detail elsewhere (e.g. Carey and Brunier, 1974; Carey, 1979; Etchecopar et al., 1981; Angelier, 1984; Allmendinger et al., 1989; Angelier, 1989; Dupin et al., 1993; Pollard et al., 1993). Regardless of whether the stress or kinematic hypothesis is assumed, the inversion schemes are based on the simplified models of Wallace (1951) and Bott (1959) that all faults slip parallel the direction of maximum resolved shear stress (respectively shear strain) of one single and spatially homogeneous global stress tensor (respectively strain tensor). Several major requirements ensue from that working hypothesis and from each other: (1) displacements on faults are small enough to give no way to mechanical interactions between faults, and neighboring faults slip independently; (2) faults slipped from a mean state of stress (uniform and steady); (3) the deformation is non rotational and stress and strain tensors are coaxial; (3) no post-faulting reorientation of the fault-slip data has occurred; (4) blocks separated by faults are not internally strained, and no plastic deformation accompanied slip (no rotations); (5) the deformation accumulated from many slip events distributed along fractures having a wide diversity of orientations (notion of isotropy and homogeneity of the rock volume); (6) fault kinematics are scale-invariant and sampling is representative of the faults network. The last assumption is more specifically in relation with the resolution of the principal incremental shortening (P) and extension axes (T), and linked Bingham axes (e.g. Marrett and Allmendinger, 1990). Weighting of the data was qualitatively assessed by comparing the kinematics of the largest faults on outcrop with all the minor faults from the same measurement station. A good correlation comes out, thus the fault-kinematics is scale-invariant (e.g. figs. 5 and 6). To ensure that minor faults population in subsets were representative of the bulk deformation, we paid a special attention to always compare the minor faults attitudes and kinematics with map-scale faults. We are aware that our fault-slip data may depart widely from these basic assumptions, mainly because of strong local deformation, and stress variations due to preexisting anisotropies and inherent rock heterogeneities. We tried to satisfy at best the basic assumptions by collecting data preferentially away from high-strain zones (cataclastic centers of major faults), where simple-shear and block rotations may occur. Particular faults attitudes, inherent to the imposed deformation regime in high-strain zones, may reduce the accuracy of stress tensors results (Wotjal and Pershing, 1991). However some of our measurement stations have been set along or in the close vicinity of major faults since even for domains near major faults, where simple-shear deformation is expected, paleostress analysis seems to provide meaningful results (Wotjal and Pershing, 1991). In such cases the errors related to violations of the basic assumptions generally do not exceed those inherent to field data gathering and inversion techniques (Pollard et al. 1993; Dupin et al., 1993). In order to check out the homogeneity of stress tensor requirement only fault-slip data from stations no larger than quarry size have been computed. Lithologies are essentially granitoid rocks of the Tertiary intrusions, which are considered as isotropic rocks, even though locally they are foliated (especially the Bergell tonalite). Additionally, fault-slip data have been collected within metamorphic and strongly foliated country rocks and the inversion schemes repeated. Odd stress axes orientation due to rock anisotropy's weight on the stress tensor computation could then be eventually spotted, by direct comparison with the stress tensors that we calculated within the isotropic intrusions. Despite all these precautions consistent relative chronology criteria in our measurement stations put into question the homogeneity of stress tensor over the data acquisition area, as they clearly show evidence for superposed stress states in a large amount of cases. In such circumstances, superimposed stress states (or heterogeneous stress states) result e.g. in a complex geometrical distribution of faults. The key point in our proceeding is that we favored in polyphased deformation cases an approach that separates faults prior to stress inversions. In other words the solution was first to split the heterogeneous data sets into individual homogeneous subsets of faults, based primarily on geological constraints as observed in the field. Otherwise, when we lacked field evidences, the different steps we addressed in our fault-slip analysis, in order to overcome that difficulty, tracks the procedure undertaken by Angelier (1984). The computation run is then tested for validity against the consistent relative chronology criteria akin to particular fault families observed elsewhere in the field. Faults attitudes and kinematics in subsets, as well as paleostress results, are surprisingly very homogeneous from site to site.

Finally good arguments for both the dominance of coaxial deformation and homogeneous stress states within our stations stem from the high regional consistency of the computed tensors (see e.g. table 1). Moreover direct inversion stress tensors results generally match the orientations of incremental strain axes derived by the kinematic analysis of our fault-slip measurements, all over the data acquisition area. Principal axes of stress and strain are thus a posteriori parallel in most situations, and we consider that deformation is coaxial within the blocks separated by map-scale faults.

3.2.3. Paleostress and strain results

With the above limitations, the results are expressed in terms of reduced stress and/or strain tensors (e.g. Angelier, 1984) that give the orientations of the maximum ($\sigma1$), intermediate ($\sigma2$), and minimum ($\sigma3$) stress axes ($\sigma1 \geq \sigma2 \geq \sigma3 \geq 0$), respectively the short (e3), intermediate (e2), and long (e1) kinematic axes ($e3 \leq e2 \leq e1$), as well as the ratio of principal stress differences $\phi = (\sigma2-\sigma3)/(\sigma1-\sigma3)$ (table 1). This ratio ϕ varies from 0 ($\sigma2=\sigma3$) to 1 ($\sigma1=\sigma2$), values that correspond to stress ellipsoids symmetric around $\sigma1$ and $\sigma3$ axes (Angelier, 1975), respectively. Guiraud et al. (1989) and Delvaux et al. (1997) presented a classification of nine main deviatoric stress tensors that characterize different theoretical types of deformation by combining the possible spatial orientations of ϕ (kinematic regime, table 1). Similarly, the spatial distribution of P and T axes from a set of fault-striae couples yields inferences on the shape of the strain ellipsoid (e.g. figs. 5e and 6e). The reduced stress tensors are primarily grouped into paleostress stages (or tensor group) as a function of relative age order and/or mechanical separation of faults (table 1). As a last resort, stress regime and orientation of the principal stress axes helped to fit the reduced stress tensors with one group. In a next step, the succession of brittle events locally established in various sites can then be correlated throughout large areas on the basis of consistencies in stress regimes and corresponding trends, as well as consistencies in fault geometries and kinematics. A regional paleostress field can be proposed for each tectonic event, or for each stress regime in a particular tectonic event (figs. 5 and 6). The quality of results for each site is evaluated a priori through: (1) the total number of measurements per site and/or per group, and the ratio of mechanically compatible faults after final separation by the direct inversion; (2) the average fluctuation F (mean slip misfit value, see table 1); ideal homogeneous sets of faults should have mean F≤10° (Angelier et al., 1985). Some particular faults with individual high fluctuation (30°<F<40°) did not significantly change the stress solution nor in directional terms neither in ϕ ratio variation terms, and thus did not perturb the stability of the computation. In such a case, although the mean fluctuation may be increased up to 20° (the total mean fluctuation is 15°) and the tensor may have a lower quality, we decided not to discard these faults from the final solution. We are aware that the mechanical coherency between faults in such sites is lowered, but as far as the kinematic compatibility of faults remains high, we still believe that the fault

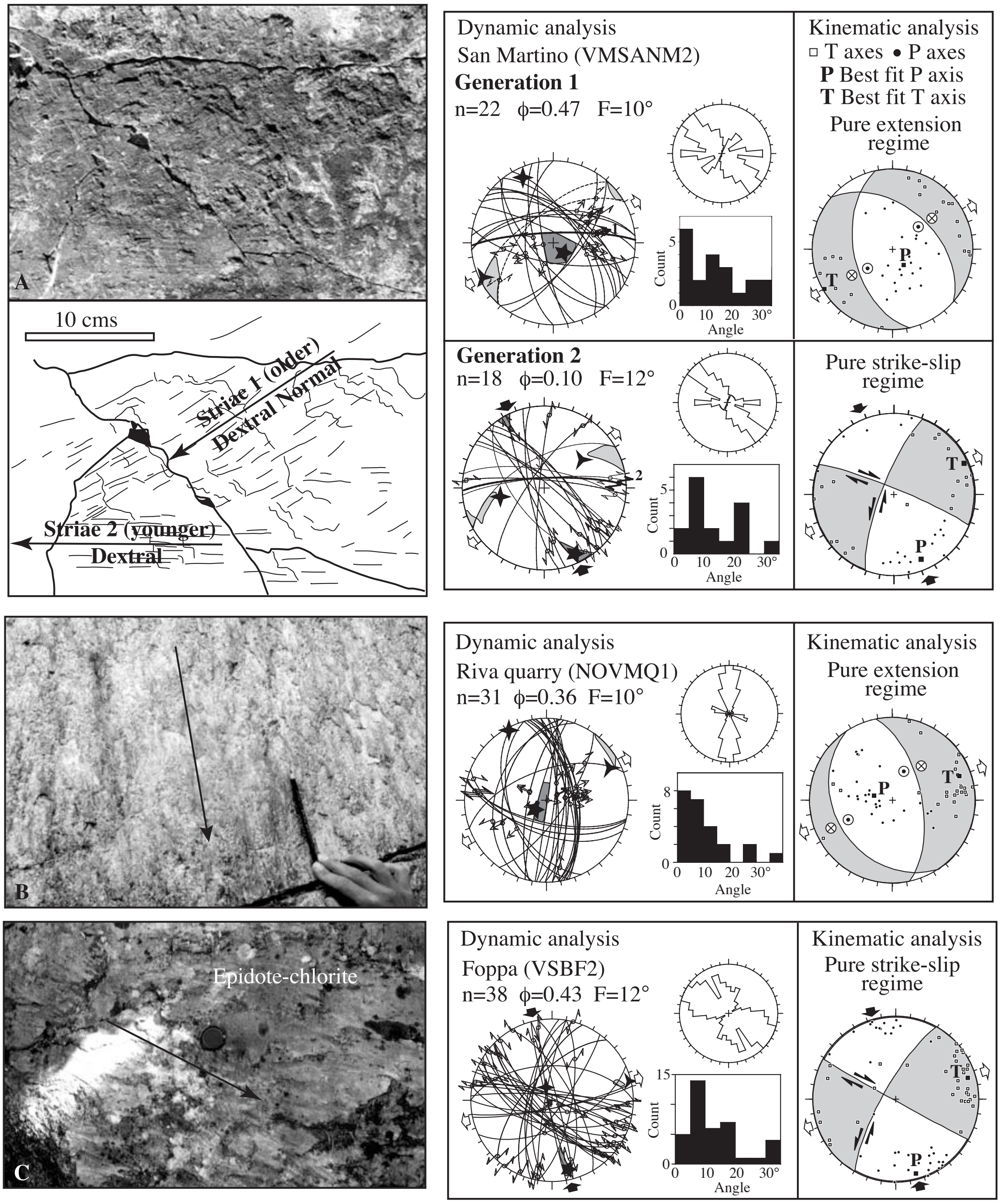

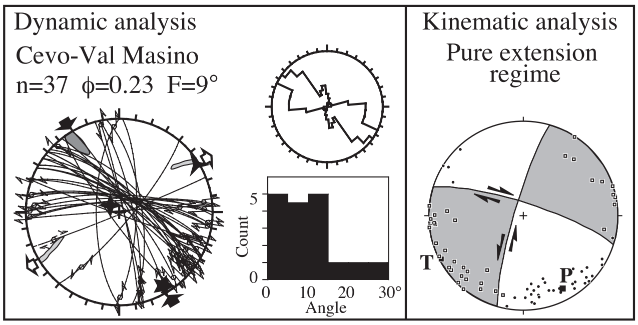

Fig. 8. Typical paleostress tensors computed in the studied area. Outcrop examples (left column) and corresponding fault-slip analysis (right column). (A) Polyphased measurement site as indicated by superposed striations on a fault surface. Dextral oblique-normal striation (1) is older and cross cutted by pure dextral strike-slip thin striation (2) due to fault plane reactivation. (B) Typical example of extensive tectonic regime computed in the studied area. Steps on the fault plane indicate down-faulting of the missing wall. (C) Typical example of strike-slip tectonic regime computed in the studied area. Epidote-chlorite coated fault surface, mineral steps indicate a sinistral sense of shear.

population keeps homogeneous; (3) the coherency and similarity between dynamic and kinematic solutions (P-T Right Dihedra and/or P-B-T axes methods) obtained from the same (sub-)sets of fault-striae couples when both methods have been used (e.g. figs. 5e and 6e)

Some typical examples of paleostress and incremental strain inversions for each tensor group in the studied area, including a polyphased case, are plotted on fig. 8. Two main sorts of tectonic regime akin to down-dip, oblique and sub-horizontal striations come out from the fault-slip analysis: extensive (fig. 8b) and strike-slip regimes (fig. 8c), respectively. In the former case, σ1 and P axes are close to the vertical, and are exchanged by the σ2 and B axes in the latter case, the short (σ3), respectively long (T), axis of the stress, respectively strain, ellipsoid remaining close to the horizontal in both cases. There is a good agreement between the direct inversion, right dihedra and P-B-T axes methods. In particular, the low ϕ ratio associated with the younger slip increments in the polyphased cases (fig. 8a, bottom) is also reflected by the half girdle-like potential area for σ3 (permutation between the intermediate and short axes of the stress ellipsoid, in a transpressive tectonic regime). Similarly the low ϕ ratio and the girdle-like potential area for σ3 associated with the extensional event in fig. 5e reflect the local radial extensive type of deformation associated with the fault-slip data. It is noteworthy that the possibility for such permutations associated with low ϕ ratios is actually poorly documented by the dispersion of individual P and T axes of the fault population (right diagram in fig. 8a). In the strike-slip regime illustrated in fig. 6e however, the tendency to high dip angles for about 25% of T axes might reflect the relative low ϕ ratio deduced from the direct inversion method.

The full fault-striae couples database, together with corresponding stress and strain tensors projected on the horizontal plane, is plotted in figs. 9 and 10 (extensive and transcurrent tectonic regimes, respectively). The regional distribution of the stress and kinematic axes is projected on structural maps for each paleostress stage, i.e. the normal and transcurrent regimes of deformation, together with map-scale faults (figs. 11 and 12, respectively). All fault-slip analysis sites are localized on figs. 4, 11 and 12.

Minor faults are organized into fault families defined by a trend interval and associated striations that match up the large-scale fault arrays. This points out the regionally good agreement between the structures at the map and microtectonic scales. At least three fault families have been observed in most measurement sites, with changing density according mainly to local brittle tectonics features. No one differences between the tensor groups stem from the fault trend analysis alone, i.e. all fault families are associated to both the extensional and transcurrent regimes. On the other hand some fault families comparatively prevail over the others in each tensor group. Essentially the striation

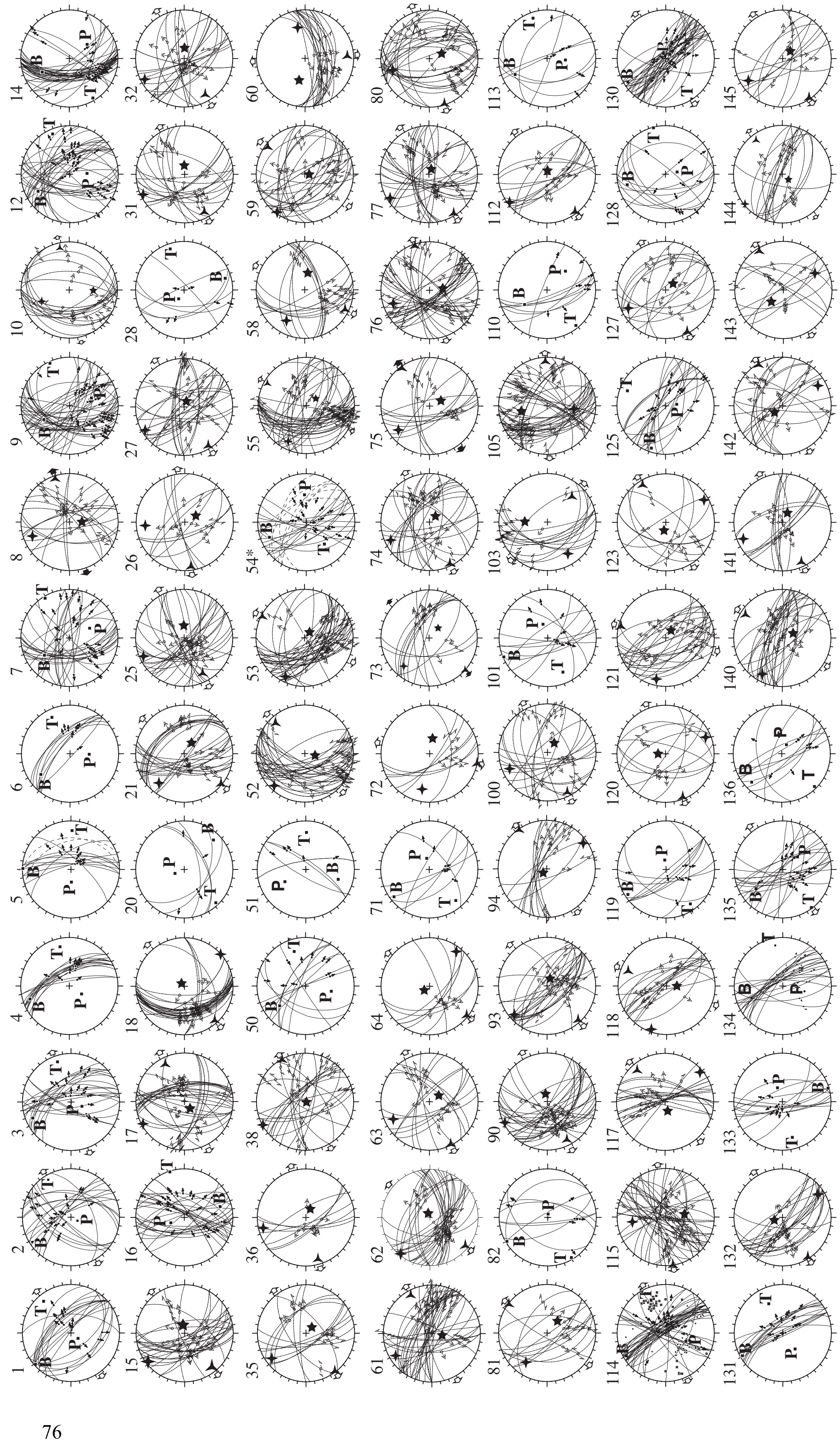

Fig. 9. The complete database associated with the extensional tectonic regime (direct inversion or P-B-T axes method). See table 1 and figs.7, 11 and 12 for detailed results and measurement site location.

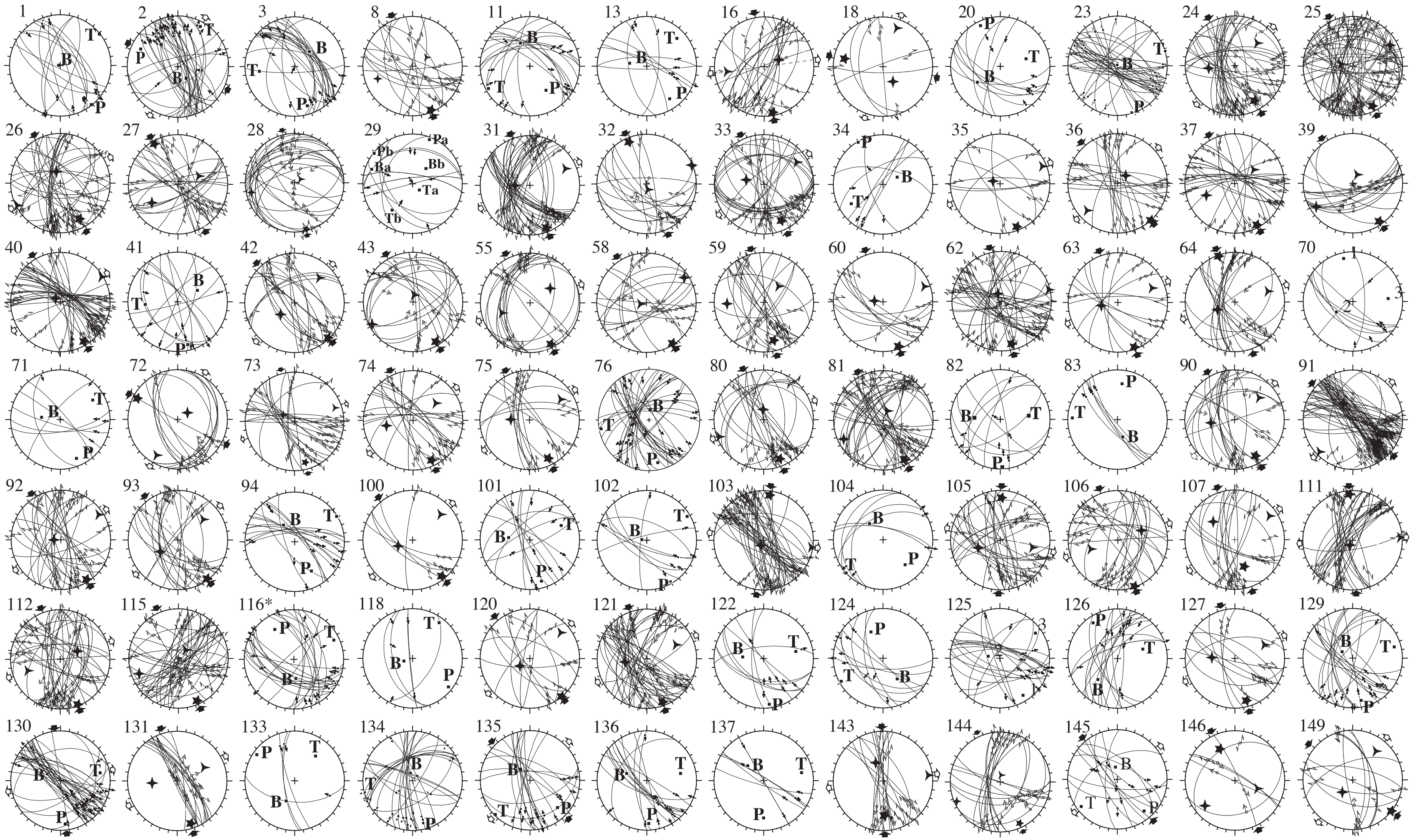

Fig. 10. The complete database associated with the strike-slip tectonic regime (direct inversion or P-B-T axes method). See table 1 and figs.7, 11 and 12 for detailed results and measurement site location.

rake associated with each fault family obviously change for the successive paleostress stages (compare figs. 9 and 10) and help to associate fault-slip data and tensor group.

The kinematic and stress axes deduced from the fault-slip data akin to the extensional regime of deformation indicate a well-defined mean NW-SE trending extension direction (fig. 11a,b). The extension and shortening axes show respectively shallow and steep dips, indeed suggesting the development of the minor faults under a normal extensional tectonic regime (fig. 11b). More in details, the trend of the T and $\sigma 3$ axes is principally ENE-WSW oriented in the western and southwestern part of the Bergell region (i.e. in the Val Mera-Novate and Insubric areas) as well as at the northeastern border of the intrusion in the Muretto and Engadine regions. Conversely, in the main body of the intrusion, i.e. in the central Bergell area, the extension is mainly NE-SW to scarcely more NNE-SSW directed (fig. 11a). In the Triangia intrusion, further east and in the vicinity of the Insubric Line, the extension nicely trends NW-SE. All over the data acquisition area, the orientation of the principal axes of stress matches the incremental strain axes one within the error limits inherent to dynamic and kinematic methods. The coaxial deformation assumption is thus a posteriori verified. The ϕ ratios are mostly centered on 0.5 (70% of them), values that indicate a nearly pure normal tectonic regime, and strengthen the overall consistency in the extension direction (fig. 11c and table 1). Despite ca. 20% and 10% of the Δ ratios have values lower than 0.25 and higher than 0.75, respectively, and correspond to radial extensive and transtensive kinematic regimes, respectively, the extension axes remain steadily oriented. Thus the ϕ ratio variations have actually no weight on the extension direction. Of note is the tendency for fault-slip data within the SSB are Insubric areas to yield low ϕ ratios (table 1). For example, the occurrence of curved normal fault planes in the tonalite tail, with intermediate to steep west dips and progressive NW-SE to E-W and eventually ENE-WSW trends, is in line with a radial extensive kinematic regime (see e.g. site n° 25 in fig. 9).

Tensors are calculated from sets of minor faults organized into (quasi-)conjugated systems (Angelier, 1979) spanning four major trend intervals (fig. 9): (1) approximately NW-SE striking and neoformed normal faults, with primarily moderate to steep dips to the north and south, show downdip to normal-oblique displacements. Top to NE and SW-directed hanging wall movements are quite equally parceled out; (2) oblique-normal relative offsets are common on NNW to NNE striking fault sets, distributed over W and E steep to intermediate dips; (3) an equatorial data set, mostly north dipping, south dipping in minority, with generally intermediate to high dip angles, also accommodated slip with a minor orogen-perpendicular to mainly an important oblique-normal dextral or dextral-oblique normal component; (4) sub-NE-SW strike: somewhat less represented even at the minor scale, the intermediate- to high-angle faults dip to the N and S, and slip with a strong strike-slip oblique normal component. Whatever the fault set, the discontinuity planes are commonly chlorite-epidote-quartz coated.

The two first families, i.e. the transversal faults, are by far the most represented at the microtectonic scale during the extensional event. The transversal faults are also the most represented ones in the morphotectonic analysis. This supports the key role of the corresponding large-scale structures to the orogen-parallel extension. The transversal faults are thus outstanding structures to form in response to the imposed stress regime and seem to control the overall orogen-parallel extension. The longitudinal faults conversely accommodate various amounts of transversal and/or sideways escape of tectonic blocks.

The strike-slip shearing commonly overimposed on the earlier extensional structures, with a strong tendency to erase previous slip indicators on the numerous and distributed reactivated fault planes (fig. 8a). The stress tensors related to conjugate sets of strike-slip faults, either in the absence of accompanying normal faults (ca. 50% of non-polyphased sites) or with typical normal fault reactivation, gives indications for active strike-slip faulting at some stage of the deformation history. This phase is characterized by a nicely defined mean NNW-SSE directed compression and ENE-WSW directed extension (fig. 12a,b). The kinematic and dynamic fault-slip data analyses indeed reveal a transcurrent tectonic regime, with both the P and T axes of the strain ellipsoid, respectively σ1 and σ3 of the stress ellipsoid, sub-horizontal. The ϕ ratio distribution is however typically bimodal. About 50% of the fault-slip data are associated with a ratio value close to 0.5 (pure strike-slip type of deformation), while the remaining data set encompasses mainly uniaxial compressive stress solutions (transpressive kinematic regime, fig. 12b.c). Low ϕ ratios are actually related to similar σ2 and σ3 magnitudes. Consequently spatial permutations between the maximum and intermediate stress axes are made easy, which is also mirrored by the axial girdle-like contouring of the σ3 and T axes in fig. 12b. It is noteworthy that many of those tensors with the minimum stress axis close to the vertical are localized within the SSB and Insubric areas (fig. 12a). The direction of the σ1 and P axes is however very homogeneous over the study area. Accordingly, the horizontal stretch direction akin to the transcurrency is quite stable and lies sub-parallel to the one gathered from the extensional regime of deformation (compare figs. 11 and 12). This suggests obvious bulk strain compatibility between extensional and transcurrent regimes. It is thus suggested that both regimes belong to the same tectonic event. Tensors are commonly constrained by a set of neo-formed and/or reactivated and quasi-conjugated approximately NW-SE to E-W striking dextral strike-slip faults, with moderate to steep dip angles, and NNE-SSW to NNW-SSE striking sinistral strike-slip faults, with intermediate to steep dips (fig. 10). Neoformed reverse faults and/or reactivated faults with a strong strike-slip oblique reverse offset component, are not rare at the microtectonic scale within our measurement stations, especially in the southern field area. Surprisingly steep sinistral minor faults sub-

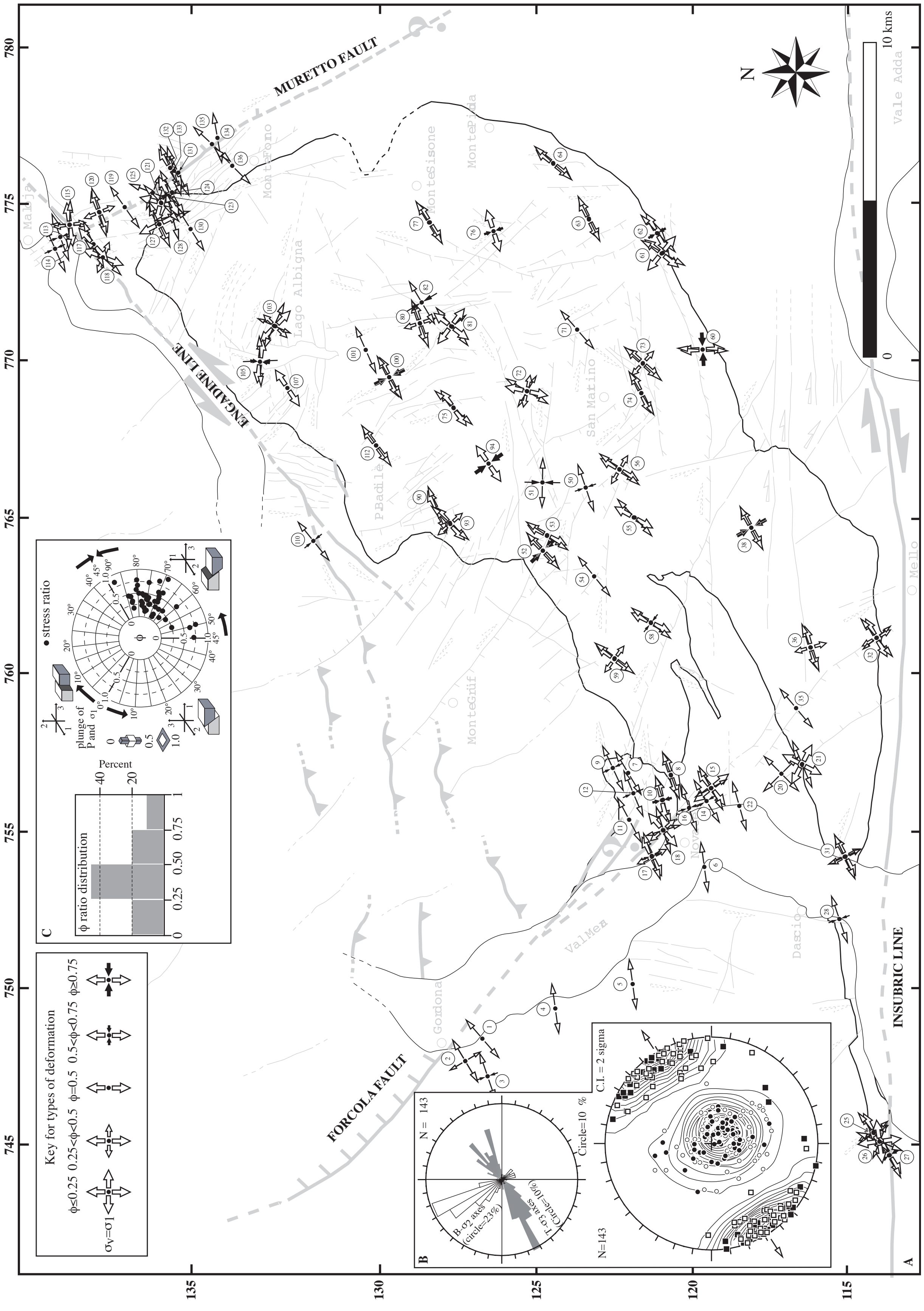
A
B
C
MURETTO FAULT
ENGADINE LINE
FORCOLA FAULT
INSUBRIC LINE
N
10 kms
0
Maloja
Monte Forno
Monte Sisone
Lago Albigna
San Martino
P.Badile
Monte Gruf
Val Mera
Gordona
Dascio
Mello
Vale Adda
780
775
770
765
760
755
750
745
135
130
125
120
115
Key for types of deformation
σv=σ1
φ≤0.25
0.25<φ<0.5
φ=0.5
0.5<φ<0.75
φ≥0.75
φ ratio distribution
Percent
stress ratio
plunge of P and σ1
N = 143
B-σ2 axes (circle=23%)
T-σ3 axes (Circle=10%)
Circle=10 %
C.I. = 2 sigma
N=143

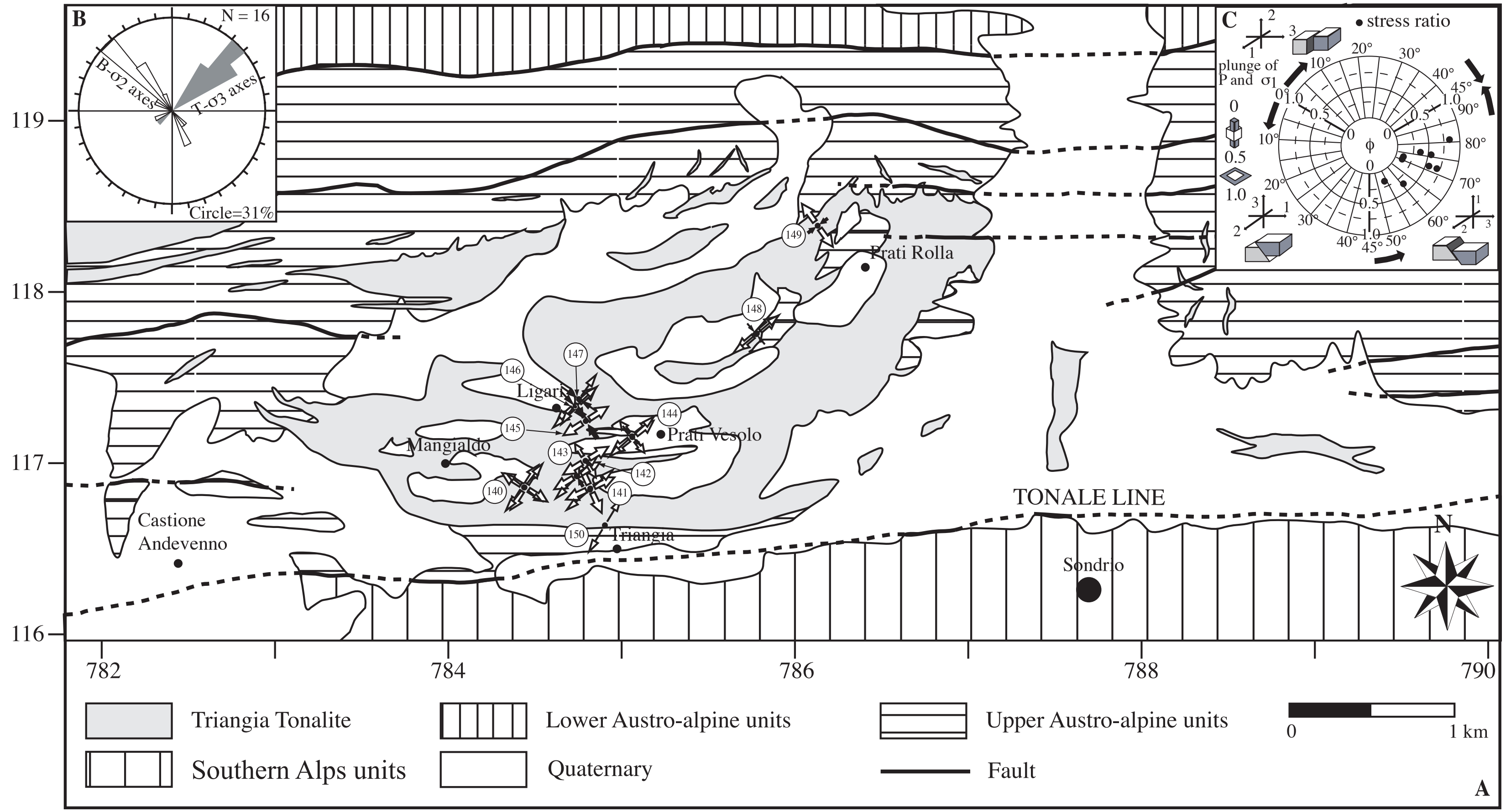

Fig. 11. (A) Paleostress (large arrows) and incremental strain (thin arrows) maps for the extension tectonic regime. Key for stress symbols and related kinematic regime is given in upper left insert. Black and white arrows: shortening and extension directions, respectively. Dashed kinematic arrow on fault network: likely younger reactivating shear (B) Statistical orientation distribution of shortening and extension axes. Top: rose diagram of strike of shortening (B and σ2 axes) and extension axes (T and σ3 axes) at 10° count interval. Bottom: lower hemisphere projection of maximum principal stress and incremental strain axes (black and white circles, respectively) and minimum principal stress and incremental strain axes (black and white squares, respectively), with 2σKamb contouring. White arrows indicate mean direction of extension. (C) Statistical analysis of ϕ ratios distribution (left) and stress-ratio plots of calculated stress ratio ($\phi = (\sigma2-\sigma3)/(\sigma1-\sigma3)$) with $\phi = 0$, uniaxial tension; $\phi = 1$, uniaxial compression) and plunge of σ1 for the reverse, normal and strike-slip faulting tectonic regimes (adapted from Oncken, 1988). The σ1 stress axes dip primarily close to the vertical, which corresponds to the extensional regime of deformation observed. See text for more explanations.

parallel to the Engadine Line are the dominant structures only in the vicinity of the master fault, conjugated with dextral transversal faults (e.g. sites n° 105, 111, 115 and 121). Elsewhere this fault family is generally less represented relative to the typical families akin to the transcurrent movements. Pure sinistral shearing however was found within strongly localized centimeter-scale wide greenschist facies shear-zones oriented parallel to the Engadine Line in the granodioritic body (close to site n° 54, fig. 4). This might actually point out a relative early strain field related to the conjugated activity of the sinistral Engadine Line and dextral Insubric Line (Schmid and Froitzheim, 1993). This is discussed hereafter in section 4.

The late brittle transcurrent paleostress field is globally linked to the right-lateral movements along the longitudinal faults conjugated to the left-lateral transcurrent movements along the transversal ones. This induces pure shear deformation within the Bergell block associated with an orogen-parallel stretch. Strike-slip displacememts are important in the southern part of the field, along the typical Tonale dextral strike-slip fault system, encompassing both Riedel shears (Fumasoli, 1974) and a set of E-W running faults in a ca. 5 kms wide zone which extends at least from the Paina Marble Zone in the west (Heitzmann, 1987a, fig. 2) to the Triangia intrusion.

3.3 Minor fault populations along the PFS segments in the Bergell Alps

3.3.1. The Insubric Line

Good exposures of the Tonale Line (the brittle part of the Insubric Line) are rare because Quaternary alluvial deposits cover most of them. Nevertheless a spectacular outcrop in the Livo canyon (Fumasoli, 1974) allows the master plane to be directly investigated. Here the fault plane juxtaposes the unmetamorphosed South Alpine limestones and the high-grade rocks of the tonalite root zone (fig. 13a). These limestones are strongly cataclasized and brecciated in the vicinity of the master fault (fig. 13b), and so is the tonalite. Veins and micro-breccia, filled with chlorite, epidote, quartz and carbonates are abundant in the tonalite, until at least some ten of meters away from the master fault. The master fault is coated by striated breccia fragments enclosed in a carbonatitic and quartz matrix. Carbonate and silica rich fluid activity led to a crusting over that gave the master fault its spectacular smooth appearance and makes the striae difficult to identify. In places however, striations and grooves perpendicular to the intersection between the master fault plane and Riedel shears to it, could be measured and interpreted as pinning down the slip motion. Those striae are subhorizontal, with rake angles smaller than 20°E, with a maximum at 5°E, on the master fault that dips 70°-80° north and strikes E-W (fig. 13c). Minor faults in the tonalite are numerous a few meters away from the master fault. Fault clusters encompass variably oriented conjugated strike-slip fault sets and reactivated fault sets. Indeed some NW-SE to NNW-SSE faults are two-striae bearing in a few cases.

These faults have steep west and east dips, and bear that common down-dip normal striation evolving on a few planes into an oblique-normal relative offset, and later strike-dip reactivation (rake ≤ 35°). The stress tensor solution associated with these minor faults incorporates the master Tonale fault plane and is characterized by a relative high stress ratio value ($\phi = 0.68$). Dextral slip on the Tonale master fault appears therefore to occur in transtensive conditions (constrictional strain). This is also reflected by the mixed P and B axes along a NW-SE directed great circle in the kinematic analysis (fig. 13d, right stereonet). Conjugated sets of strike-slip faults include E-W steeply dipping north and south dextral faults, with NNW-SSE sinistral and oblique-sinistral faults, as well as NW-SE steeply dipping dextral to oblique-dextral faults, with NNE-SSW steeply east dipping sinistral and oblique-sinistral faults. Other sets include reverse and oblique-reverse faults, ENE-WSW oriented and mostly steeply to moderately south dipping (site n° 27 on fig. 10). The best fit tensor to these faults indicates a transpressive tectonic regime associated with low ϕ ratio value (table 2) and scattering of B and T axes along a NE-SW oriented great circle. The fault-slip analysis of this fault array makes thus apparent a NE-SW extension direction, while the shortening direction is either sub-vertical or sub-horizontal and NW-SE oriented (table 1 and figs. 11 and 12). The corresponding tectonic regimes, early transtensive and later transpressive, are however incompatible.

Another outcrop was investigated in the western Bergell region, at Passo San Jorio (fig. 2). There the tonalite tail and the Tonale series are separated from the Southern Alps units by the Insubric Line. The Tonale brittle master fault is however not spectacularly exposed within the geomorphology. Both reverse conjugated and strike-slip chlorite and epidote bearing brittle faults, including classic Riedel shears, carve out the tonalite tail and the leucocratic greenschist facies dextral mylonites typical of the Insubric Line. Again the mylonites are strongly cataclasized and brecciated, the closer to the Southern Alps units, the cooler the deformation. The low ϕ ratios (< 0.30) characteristics of both these outcrops produce the best fits to the faults. Again uniaxial compressive stress models are reasonably in good agreement with the strike-slip and less-numerous reverse faults in the populations sampled in the vicinity of the Insubric Line (fig. 12).

3.3.2. *The brittle-ductile Engadine Line*

Good exposure of the master fault is found near Maloja Pass, in the creek bed of the Orlegna river near Orden, 1 km SE of Maloja pass (site n°115 on fig. 4). No striations can be found on the subvertical master fault, which has been completely sealed by fluids. For this reason, striations were measured on subsidiary faults within ca. 100m to the master fault. The orientation of these subsidiary faults, strike and dip of striations and the sense of shear on these planes were recorded in order to determine the principal stress and incremental strain axes. The fault rocks in these outcrops consist

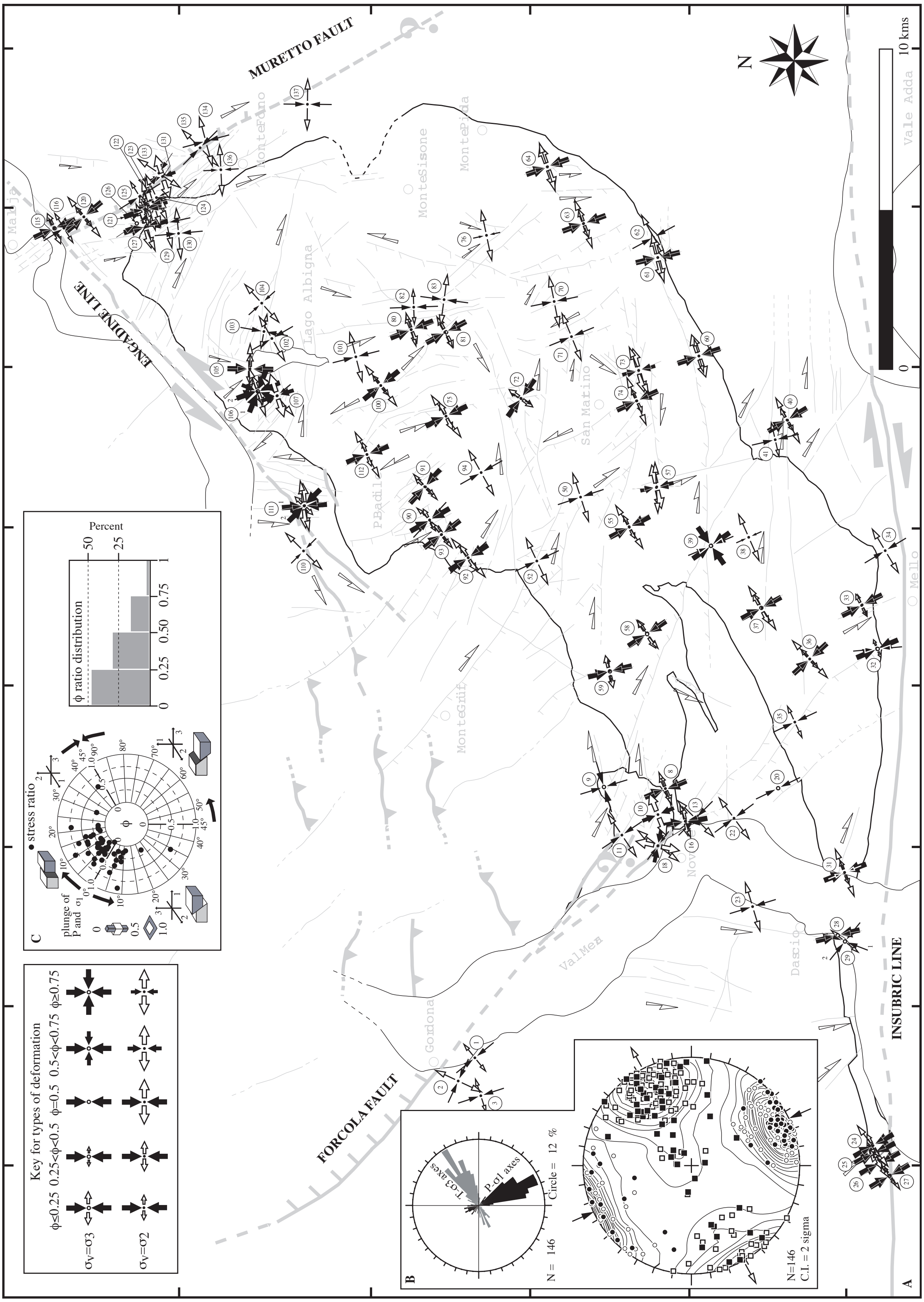
MURETTO FAULT
ENGADINE LINE
FORCOLA FAULT
INSUBRIC LINE
Maloja
Monte Forno
Monte Sisone
Monte Pioda
Lago Albigna
P.Badile
San Marino
Monte Gruf
Novate
Val Mera
Gordona
Dasio
Mello
Vale Adda
N
0
10 kms
780
775
770
765
760
755
750
745
135
130
125
120
115
Key for types of deformation
φ≤0.25
0.25<φ<0.5
φ=0.5
0.5<φ<0.75
φ≥0.75
σv=σ3
σv=σ2
C
stress ratio
plunge of P and σ1
φ ratio distribution
Percent
50
25
0
0.25
0.50
0.75
1
B
N = 146
Circle = 12 %
P-σ1 axes
T-σ3 axes
N=146
C.I. = 2 sigma
A

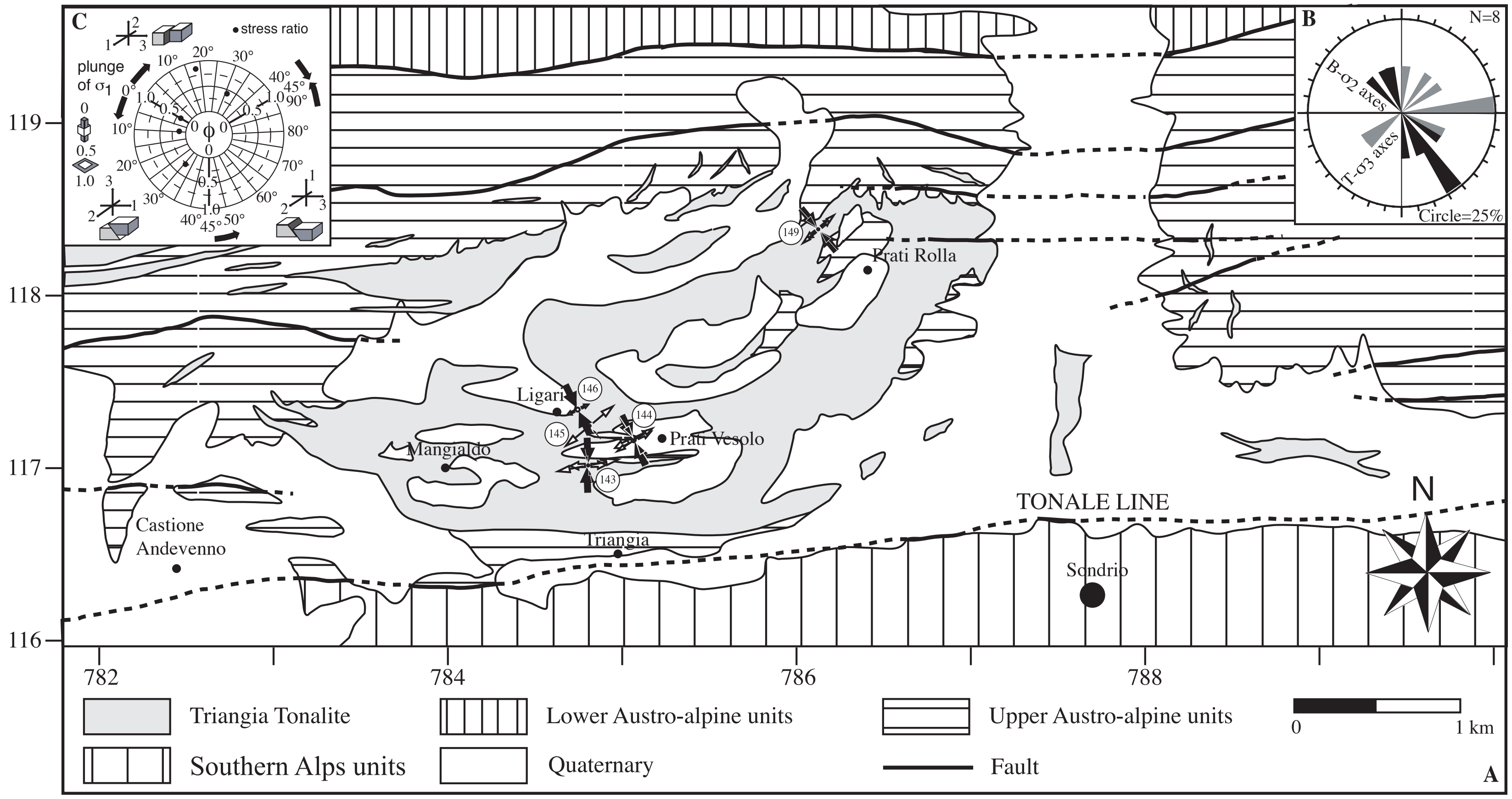

Fig. 12. (A) Paleostress (large arrows) and incremental strain (thin arrows) maps for the transcurrent tectonic regime. Key for stress symbols and related kinematic regime is given in upper left insert. Black and white arrows: shortening and extension directions, respectively. (B) and (C) Statistical orientation analysis of shortening (P and and σ1) and extension (T and σ3) axes. Same symbols and legend as in fig. 11. In (C), the σ1 stress axes dip shallowly and are distributed primarily in the strike-slip regime part of the diagram, and to less extent in the thrust tectonic regime part of the diagram. See text for more explanations.

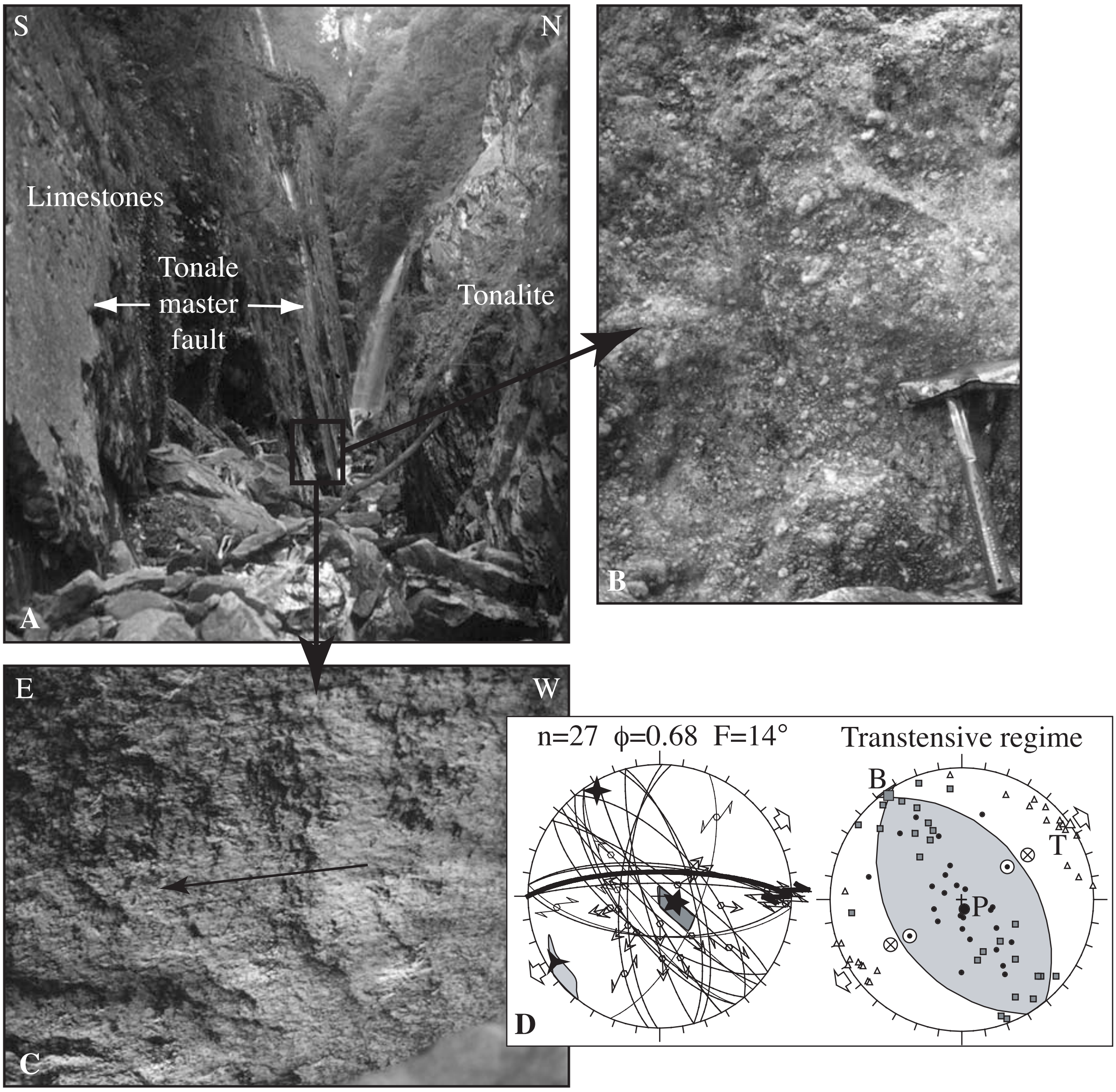

Fig. 13. Tonale master fault and related structures in the Livo canyon. (A) View of the master fault plane (left) that puts into contact the south Alpine limestones (left) with the the tonalite tail (right). (B) and (C) Detail of tectonic breccias and striation on the master fault plane. The sense of shear is dextral (arrow indicates displacement of the missing wall). (D) Dynamic and kinematic analysis of minor fault population in the vicinity of the master fault plane (heavy black line is the Tonale master fault). Circles, squares and triangles in the right stereonet are P, B and T axes, respectively. See text for more explanations.

of brittle-ductile faults and shear-zones (fig. 14) with a wide distribution of orientations. These sliding surfaces bear fibrous striae, mainly built of quartz, calcite and chlorite aggregates. It is worth mentioning that the style of the local deformation, i.e. purely brittle versus various amounts of rock plasticity, actually depends on the nature of the lithology. While gneisses of the Margna nappe are dissected by faults (fig. 14d) and brittle-ductile shear-zones (en-echelon vein arrays, fig. 14b,c), the amphibolites of the Forno unit typically behaved under stress in a more ductile way, as shown by the C/S structures characteristics of the ductile deformation (fig. 14). These ductile shear bands within the amphibolites evolve into or are dissected by cataclastic shear-zones, as indicated by the striated appearance of shear surfaces. This supports conditions of slip close to ductile-brittle transition.

The faults and shear zones organize in an array of conjugated sets. The first and main set is represented by N040-N060E directed brittle-ductile shear zones, steeply E dipping, and bearing a variable intermediate to high-angle dipping striation. Within these shear zones, the Forno amphibolites show sigmoid-shaped lenses between adjacent shear-bands, and the C/S relationships are indicative of a consistent sinistral to sinistral-oblique reverse movement. Some N020-N030E directed shear zones, with variable E or W steep dips, again with low-angle to intermediate dipping striations, anastomose or crosscut the previous ones. The sense of shear is sinistral-oblique for this set, which could be interpreted as a Riedel set to the main NE-SW directed set. The last set is documented by E-W to NW-SE directed more cataclastic shear zones, subvertical, cross-cutting generally all the previous structures, and showing dextral-oblique to dextral strike-slip offsets. Essentially the dip direction of the slickenside helps to separate the fault-slip data into two paleostress states (fig. 14e and table 1). The results of the fault kinematic and dynamic analyses reveal two regimes of deformation: a radial extensive and a transpressive one associated in each case with low ϕ ratios (table 1). Accordingly, the T axes akin to each tectonic regime are widely scattered, and show shallow to steep dip angles, in agreement with the uniaxial stress solutions, respectively. These models are indeed reasonable good fits to the strike-slip, down-dip and oblique-slip faults with a normal and reverse offset component, associated with the extensional and transcurrent regimes, respectively. The direction of shortening and extension obtained from both methods is steady as compared to the regional tendency. Regarding the T-σ3 orientation, the 15-25° discrepancies between data sets are small relative to the scatter within individual data sets, and probably are insignificant. Note that the local relative slip chronology observations are non systematic, making hazardous the chronology of stress events recognized elsewhere. The local radial extensive and transpressive kinematic regimes are nevertheless hardly compatible and can not be coeval. This might support the likelihood of complex fault reactivation in the Engadine fault vicinity.

Another site was investigated for the deformations correlated with the Engadine Line. It is located in the area of Bosch de la Furcela within the Forno amphibolites, about 150m south of the master fault (site n° 116 in fig. 4). A conjugated system of WNW-ESE and N-S oriented brittle-ductile shear zones point out with the kinematic analysis a typical NNW-SSE directed compression and an ENE-WSW directed extension. The fault kinematics are compatible with the analysis of minor faults and brittle-ductile shear zones in the vicinity of the master fault.

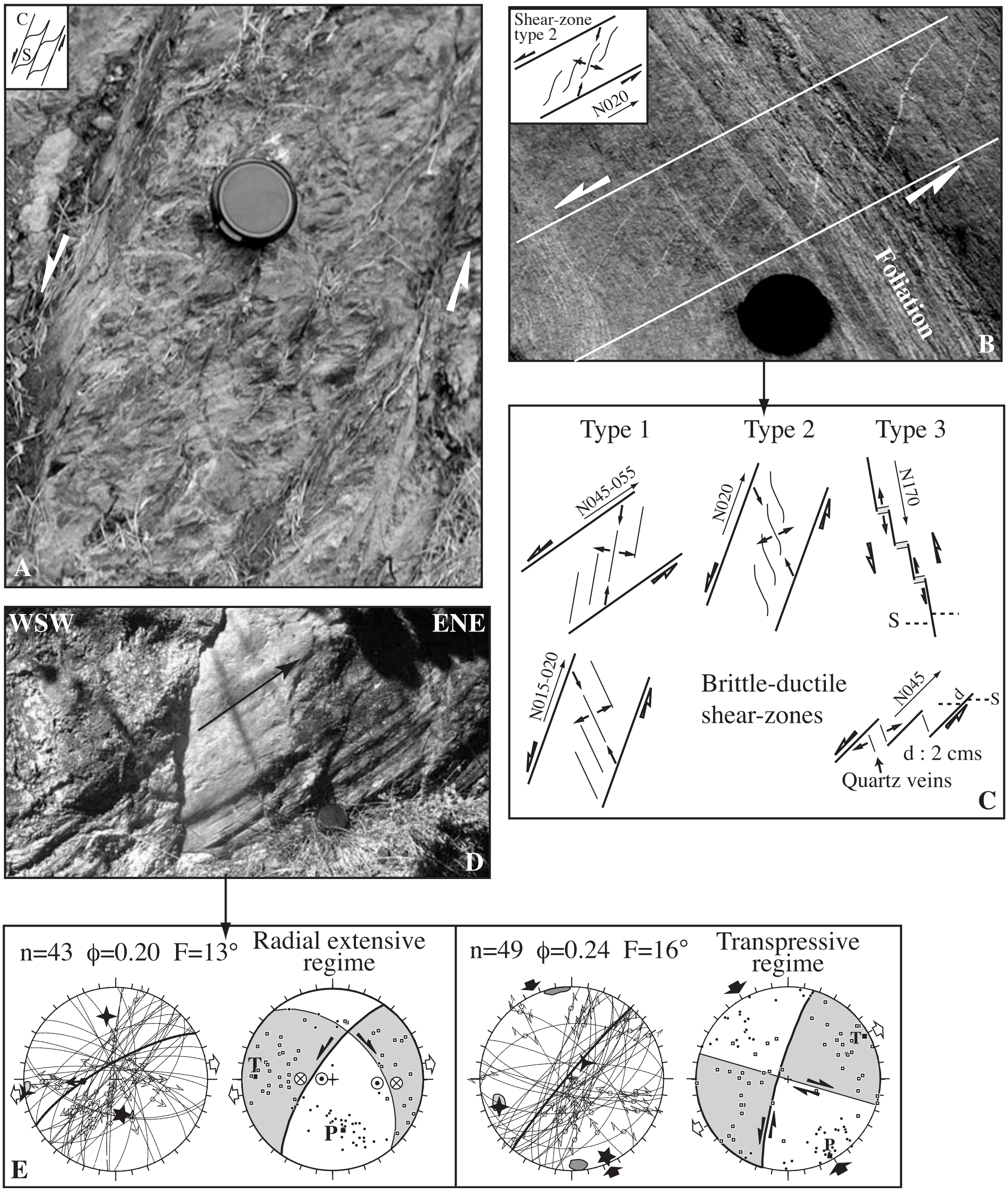

Fig. 14. Subsidiary brittle and brittle-ductile faults in the immediate vicinity of the Engadine master fault. (A) Brittle-ductile shear bands in the Forno amphibolites. C/S relationships indicate a sinistral sense of shear. (B) and (C) En-echelon vein arrays in the gneisses of the Margna nappe. The en-echelon geometry (type 1 to 3) indicates right stepping in various sets of sinistral shear-zones with potential orientations that close-match the brittle fault attitudes and kinematics (compare with E). Small convergent and divergent arrows indicate direction of incremental shortening and extension within the shear-zone, at 45° of the en-echelon array. (D) Brittle fault plane in the Margna gneisses. Grooves and striations indicate a sinistral-oblique normal sense of shear (the missing wall moves toward the right of the photograph as indicated by the arrow). (E) Dynamic and kinematic analysis of the local minor brittle and brittle-ductile fault population akin to the extensional (left) and transcurrent (right) tectonic regimes. Heavy line in the left most stereonet represents the great circle projection of the fault plane viewed in (D). In the right side, the heavy line great circle projection is that of a prominent fault plane interpreted to be the master Engadine fault.

3.3.3. The brittle Muretto Line

On the contrary to other major faults in the area, this fault zone (fig. 4) developed only in the brittle field. The Muretto fault runs within the Forno unit along the Val Muretto in the NW-SE to NNW-SSE direction (figs. 3 and 4). Albeit a single discrete main fault plane may be observed in places, dipping steeply to the NE, numerous parallel secondary faults both sides of the main fault in the Forno unit and Margna nappe (Peretti, 1985) better substantiate a wide fault zone. Some of them clearly affect the Bergell granodiorite (e.g. sites n° 127 to 130 in fig. 4). Thus brittle faulting at the Muretto fault essentially post-dates the Bergell emplacement and cooling. The main argument for relating the secondary faults zones and minor fault populations to the Muretto phase is their spatial relationship to the master fault, and the characteristic alteration of host rocks. Typical outcrops show cataclastic fault rocks and breccia, in which centimeter to meter-scale thick gouge materials have a clayey, brown and carbonatitic appearance (fig. 15a,b). In the vicinity of fault zones linked to the Muretto fault, a typical rusty brown bleaching and alteration of the intact rock occurs. Characteristics are also the precipitation of Fe-rich dolomites and Fe-Cu-Zn-(Pb-As) sulphide deposits within fault breccias (Peretti, 1983). Opened quartz and carbonate veins are frequent (fig. 15c), with antitaxial and/or syntaxial fibers growth, and pin down the evidence, together with the intense hydrothermal alteration of host rocks, for fluid low and crack-seal processes in this fault zone. Numerous fault zones are fractured in an array of minor fault rocks and gouge layers that have a wide distribution of dips and orientations. Subsidiary minor fault surfaces bear fibrous striae, built of quartz, chlorite and/or epidote aggregates, or simply a mechanical overprint. In the anastomosing gouge layers, striae orientation has been measured at the contact with the intact rock (fig. 15a,b). Fibers orientation delineating the slickensides show strong variations from one fault zone to another. The striations on the fault planes dip in a wide range of orientation, from down-dip to intermediate (35-55°) and low-angle dips (0-35°) (figs. 9 and 10). The most interesting feature observed on the fault surfaces, are serpentine and talc-bearing curved slickensides in the Forno-Malenco mafic rocks, suggesting a continuous rotation of the striation from a down-dip orientation to a low-angle dip one from which a progressive change in the fault movement can be deduced. These structures could however be related to the pre-Alpine history of the mafic rocks and must be regarded with caution. Again, the main argument for relating these talc-serpentine bearing fault surfaces to the Muretto phase, is the good agreement of the computed strain axes with the Alpine brittle phase. Because most sites revealed evidences of striations superimposition on the fault planes and complex crosscutting relationships, successive slip movements occurred on the same fault planes. Sporadically observed low-angle striations on the rim of quartz veins supports a scenario of σ1-σ2 stress permutation following opening (fig. 15b). Albeit non systematic, such relative chronology criteria allowed us to analyze separately faults with different geometries and/or tectonic regimes. Locally several cycles of superposed downdip and sub-horizontal slickenlines even occurred on the same fracture planes. Associated slip movements are mainly consistent with normal, oblique-normal and strike-slip displacement. These observations primarily suggest that transcurrent and extensional brittle structures at the Muretto fault and related fault zones have occurred roughly at the same time. The transition from extension to strike-slip faulting, and vice versa, has occurred rapidly and recurrently during continuous and discontinuous slip cycles. The displacement magnitude on the outcrop-scale faults is difficult to assess in most cases, but crosscutting relationships indicates no offsets or offsets not exceeding the cm- to m-range.

The minor fault population in the Muretto fault zones covers a pattern of (quasi-)conjugated faults that strike mainly NW-SE to N-S (see e.g. sites n° 121, 130 and 133 in fig. 9). An additional conjugated set of E-W to ENE-WSW striking faults also fit the computed tensors (see e.g. sites n° 125 and 135 in fig. 9), together with a minor NE-SW directed set (sites n° 123 and 128). According to the large spread in the striae orientation on the fault surfaces, the rock masses were displaced in a normal to oblique-normal way during the extensional regime. This led to a NE-SW to ENE-WSW directed extension associated with low to intermediate ϕ ratios (radial extensive to pure normal kinematic regime, respectively, fig. 11 and table 1). The NNW-SSE to NW-SE directed shortening axis akin to the transcurrent regime typically bisects a bi-conjugated array of dextral NW-SE and E-W striking faults, and sinistral N-S to NE-SW striking faults (see e.g. sites n° 121, 125 and 129). The strongly variable low to high ϕ ratios corroborate the complex association of pure strike-slip and oblique-strike-slip displacements as well as minor reverse ones (table 1). The T-$\sigma 3$ orientation associated with the extensional and transcurrent regime is stable and mimics the one obtained in the vicinity of the Engadine Line (figs. 11 and 12). The shortening axes lie on a NNW-SSE trending great circle and show a wide range of dips, from subhorizontal to intermediate and steeply inclined. By comparison with the stress and kinematic history recognized regionally, all these elements might suggest a steady and/or discontinuous evolution from normal faulting to dextral strike-slip tectonic regime in the Muretto fault zone. Both the extensional and transcurrent tectonic regimes led to orogen-parallel extension (figs. 11 and 12).

The Muretto fault ends at its northernmost part by splaying into a set of NW-SE to NNW-SSE trending secondary faults in the Forno zone. Some of them, kinematically compatible with the Muretto extension clearly cross-cut the Engadine Line brittle-ductile shear-zones at Orden (fig. 4) and might be related to the diffuse northern end of the Muretto fault. Still further to the NW, in the Passo del Maloja (site n° 114), crosscutting relationships between similar Muretto fault compatible extensional structures and Engadine Line compatible transcurrent structures are non-systematic. Together with the similarity in the stress and strain axes and kinematic regimes at both faults, this

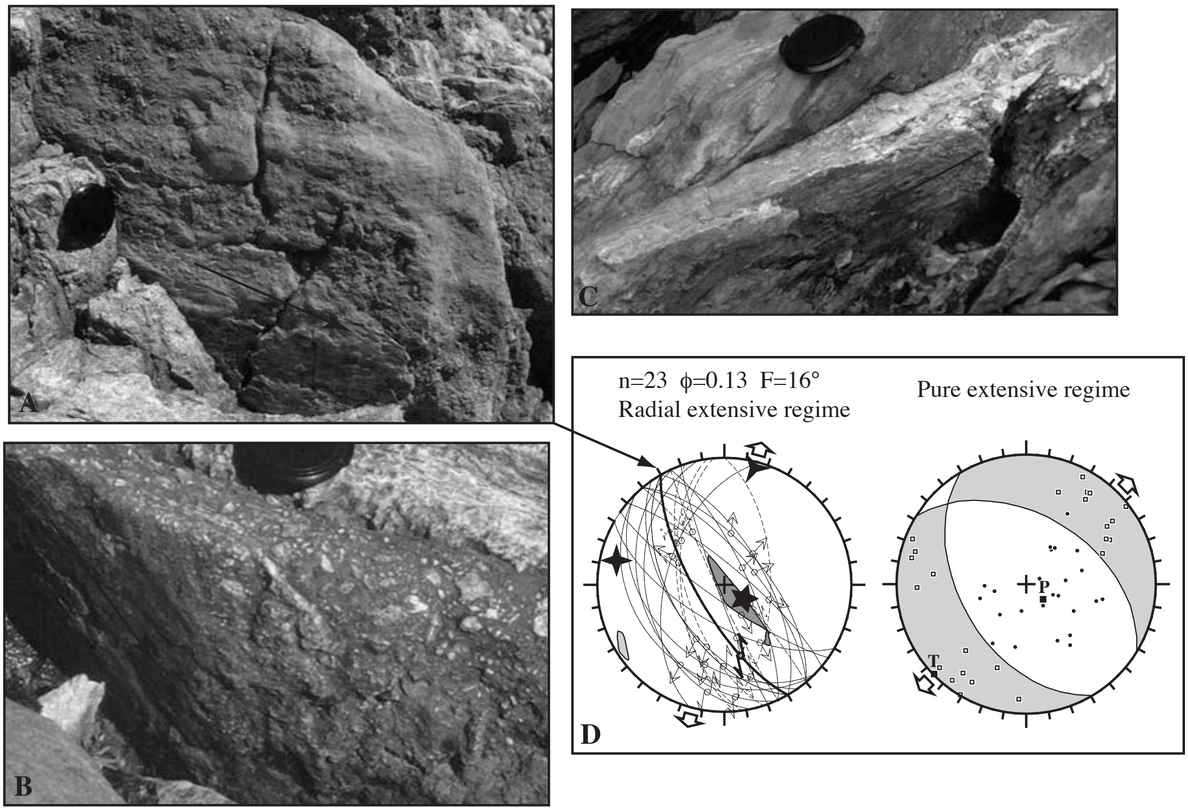

Fig. 15. (A) and (B) Typical outcrops of cataclastic fault rocks and breccia in the Muretto fault zone, with gouge materials having a clayey brown appearance. Striations occur at the gouge layer contact with the host rock. (C) Widespread veining indicates the activity of crack-seal processes during fracturation. Note that the rim of the vein is striated, which points out stress permutations after opening. (D) Example of fault dynamic (left) and kinematic (right) analysis of minor fault populations in the Muretto fault zone. Despite a reasonable fluctuation, the stress solution obtained from the direct inversion method appears to be quite unstable as compared to the right dihedra and P-B-T axes method.

seems to indicate a coeval brittle mode of faulting in response to the regional far-field kinematic framework. These observations are difficult to reconcile with the hypothesis of a local near-field stress pattern at the eastern border of the Bergell intrusion, as suggested by Ring (1994).

3.3.4. The brittle-ductile Forcola Line

Excellent outcrops of the Forcola extension phase are found by the western side of Val Mera and in the Novate granite intrusion. With on-going deformation and progressive cooling, the typical structures of the greenschist facies ductile deformation evolved into quartz and chlorite striae bearing faults. While the kinematic analysis of the mylonitic part of the deformation has been studied in details elsewhere (Meyre et al., 1998; Ciancaleoni and Marquer, 2004), this section addresses the fault-slip analysis of faults and shear-bands formed across the brittle-ductile transition. Fault-striae couples indicate, with the graphical methods, an ENE-ESW oriented extension (fig. 11) which is suitable and compatible with the extension direction deduced from foliation-stretching lineation pairs of the ductile deformation. Tensors are typically computed from quasi-conjugated sets of NW-SE to N-S oriented and NE-SW oriented faults, bearing down-dip to oblique slip lines (see e.g. sites n° 1, 2 and 3 in fig. 9). A late joint system akin to the latter set was also commonly observed in the field, cross-cutting the mylonitic rocks. In the Novate intrusion and related dykes an additional quasi-conjugated set of E-W directed faults, again with down-dip to oblique normal striations, helps to constrain the tensors (see e.g. sites n° 7 and 12 in fig. 10). The Δ ratios as well as the scattering of T axes indicate pure normal to radial extensive type of deformation (table 1). Shallowly dipping striations on these fault families, overprinting in places the normal ones, are associated to the transcurrent regime. The extension direction appears to be slightly rotated clockwise toward the southern tip of the fault (from NE to ENE trending).

4.Timing of deformation

At this stage, it is necessary to tentatively link the documented extensional and transcurrent tectonic regimes and associated kinematic framework with the available relative and absolute timing constraints in the Bergell and Insubric areas. The timing of major faults and Tertiary intrusions emplacement and cooling history in the Bergell area is well constrained by numerous published geochronological ages (see e.g. a compilation in Hansmann, 1996), and structural studies (e.g. Rosenberg et al., 1995; Berger et al., 1996). This extensive database is now discussed since it allows reliable lower limit timing estimates for the brittle-ductile and brittle structures recorded within the intrusions.

The interpretation of biotite and muscovite cooling ages, with the systems Rb/Sr and K/Ar, are somewhat hampered because the Bergell region underwent eastward tilting during the ductile dextral backthrusting event (Reusser, 1987; Rosenberg and Heller, 1997). All published ages indeed corroborate that the Bergell body cooled down to ca. 300°C (i.e. the ductile-brittle transition for quartzo-feldspathic rocks) in the time span 23-26 Ma and 17-23 Ma in its central and eastern part, and western part, respectively (Hansmann, 1996). After cooling below 300°C the Tertiary intrusions shared the cooling history of the country rocks. Apatite and zircon fission track ages (AFT and ZFT, respectively) from the pluton and host rocks indicate temperature conditions of the brittle field within the 10-24 Ma range (Rahn et al., 2004 and references therein). The common observation of epidote-chlorite-quartz coated fault and shear band surfaces within the Bergell pluton indicates greenschist facies conditions. With on going cooling and exhumation of the intrusion the last slip increments were recorded by a mechanical overprint in near-surface conditions. The above cited cooling ages provide the basis for the viability of such displacements between 30 Ma (emplacement of the granodiorite) and 25 Ma (lower greenschist facies conditions) for brittle-ductile deformations, and later than 24 Ma (older ZFT age) for brittle only deformations. We do not exclude that some various amounts of plasticity may be associated with the epidote-chlorite bearing brittle fault planes. Locally structures characteristics of the ductile deformation (e.g. sigmoid lenses and C-S relationships) evolving into brittle structures have indeed been observed on the field (e.g. figs. 7 and 14a). Accordingly, some centimeters thick localized transversal, longitudinal and NE-SW directed shear-zones within the granodiorite, oblique-normal, dextral and sinistral respectively, indicate early orogen-parallel stretch under upper to intermediate greenschist facies temperature conditions. This geometry and kinematics is strongly compatible with the structures and kinematic framework of the extensional and transcurrent brittle tectonics. Published cooling curves for the granodiorite imply that such shear-zones localized slip at ca. 26-28 Ma (Hansmann, 1996 and references therein).

In the Muretto and Engadine fault zones, faulting was associated with hydrothermal activity and various amounts of rock plasticity, respectively (figs. 14a and 15a). In the southern Muretto fault zone, observed fault surfaces within the Malenco ultramafics commonly bear serpentine-epidote-chlorite slickenlines. All the investigated fault zones are situated within the contact aureole of the Bergell intrusion, in places where temperatures in order of 400-450°C in the north and lower than 400°C (antigorite-brucite-diopside-chlorite stability zone) in the south prevailed during heat advection soon after intrusion (Trommsdorff and Connolly, 1996). Cooling of the contact aureole down to 300°C was then achieved at 28 Ma (Hansmann, 1996 and references therein) while ZFT and AFT ages indicate brittle conditions in the 10-24 Ma time range (Rahn et al., 2004 and references therein). On the basis of these elements, we suggest that both the sinistral brittle-plastic deformation at the Engadine Line and brittle deformation associated with intense hydrothermal activity and contact metamorphism mineral coated fault planes at the Muretto fault likely already occurred during progressive cooling of the Bergell contact aureole, i.e. at ca. 28 Ma. Deformation then essentially long-lasted cooling of the eastern granodiorite and contact aureole below 300°C (mica K-Ar and Rb-Sr ages at 25-28 Ma, Hansmann, 1996 and references therein), as postulated by the post-intrusion age for these fault zones (Riklin, 1978; Liniger, 1992; Schmid and Froitzheim, 1993; Puschnig, 1996). In agreement with our statement, Berger et al. (1996) and Schmid and Froitzheim (1993) proposed that movements along the Engadine Line were feasible during the late Oligocene. Regarding the vertical offset due to block rotation models along both faults (Riklin, 1978; Schmid and Froitzheim, 1993; Spillmann, 1993), no abrupt offset of zircon and apatite fission-track ages occurs at the Muretto and Engadine faults (see Chapter 5). This supports that significant vertical movements associated with sinistral shear and normal faulting along the Engadine and Muretto faults, respectively, ceased during the Burdigalian times. Minor differential throw along-strike of the Muretto fault could however suggest younger (post-Serravallian) slip increments in this complex fault zone.

Numerous ca. 25 Ma old migmatites and pegmatitic, aplitic and Novate type (garnet-bearing) dykes in the Bergell and Insubric areas (U-Pb formation ages and mica K-Ar and Rb-Sr cooling ages between 20 and 28 Ma, Hansmann, 1996 and references therein; Gebauer, 1996; Schärer et al., 1996) reflect a final thermal pulse connected to extensive magmatic and fluid activity after formation of the SSB. This age is in agreement with the emplacement age of the Novate granite (Liati et al., 2000) at the southernmost tip of the Forcola Line (Ciancaleoni and Marquer, 2004). According to these authors, the fault was still active during the progressive cooling of the granite, which subsequently heterogeneously deformed under increasingly brittle conditions. Additionally, AFT and ZFT profiles across the Forcola Line support that significant vertical movements along the fault ceased during the Burdigalian times (Rahn et al., 2004; Chapter 5). The orogen-parallel extension along the Forcola mylonites is therefore constrained between about 25 Ma (minimum upper age estimate) and 16-20 Ma (ZFT ages, maximum lower age estimate). Within the hangingwall of the Forcola Line, late transversal high-angle normal faults down-faulting the east (fig. 4, Huber and Marquer, 1996), support orogen-parallel brittle extension in the early Miocene (mica Rb-Sr and K-Ar ages in the 18-25 Ma time range and ZFT ages at 18-22 Ma, Hansmann, 1996 and references therein; Hunziker et al., 1992). In particular, the AFT pattern is disrupted at a prominent set of transversal faults as young as the early Upper Miocene (Chapter 5). More generally, the AFT data in the eastern Lepontine suggest that other faults with a relative minor vertical component of displacement stretch the belt both cross and along-strike, from the Middle Miocene onwards (i.e. post-Forcola extension).

The post-kinematic intrusion of pegmatitic dykes cross-cutting the Insubric phase mylonites and the SSB of the Lepontine dome at ca. 25 Ma documents the end of the Insubric phase ductile deformation. Early purely dextral strike-slip shearing and heterogeneous deformation under lower grenschist facies conditions overprints the Oligocene Triangia tonalite (Meier, 2003) and is contemporaneous with cooling of this intrusion down to ca. 300°C at 32-30 Ma (Giger, 1991). A 30 Ma old pseudotachylyte formation akin to the surrounding lower greenschist facies mylonites supports this interpretation (Meier, 2003) and is structurally and temporally correlated with dextral shearing on the Tonale fault zone in the Giudicarie region further east (Müller et al., 2001; Stipp et al., 2004). As the Triangia intrusion cooled down below 300°C at ca. 23 Ma (closure of one available ZFT age, Giger, 1991), the later cataclastic overprint overimposed on the ductile structures and associated with the regional extensional and transcurrent tectonic regimes was already feasible between 30 and 23 Ma. Accordingly, the youngest dated event is a cataclastic overprint in relation with dextral strike-slip and pseudotachylyte formation on the Tonale master fault and its Riedel shears (Fumasoli, 1974; Schmid et al., 1989; Werling, 1992) at 20.6 Ma and 16.4 Ma east and west of the Bergell area, respectively (Müller et al., 2001). Because the Tonale fault zone is offset by secondary faults related to the Giudicarie Fault sinistral reactivation at ca. 17 Ma in the Adamello region (Viola et al., 2001, the last dextral strike-slip movements along the Tonale fault took place during the Burdigalian (Stipp et al., 2 004). Near Passo San Jorio (fig. 2) the ages from K-Ar dating of illite in fault gouges related to a normal fault parallel to and immediately south of the Tonale master Fault on the one hand, and related to a typical dextral Riedel shear dissecting the tonalite tail on the other hand, yield 21.5 ± 5.5 Ma and 19.9 ± 2.6 Ma, respectively (Zwingmann and Mancktelow, 2004). These ages lie both within the 16-22 Ma range for pseudotachylyte dating related to right-lateral slip on the PFS (Müller et al., 2001), and within the 20-25 Ma range for cooling down to 300-350°C for the tonalite tail and Tonale series (micas K-Ar et Rb-Sr cooling ages, see review in Hansmann, 1996). According to these ages, down-slip faulting in the vicinity of the Tonale fault might be slightly older than the strike-slip movement on it. Structural observations accordingly describe the dated Riedel fault as being largely truncated by the late brittle dextral oblique-reverse slip on the Tonale fault (Zwingmann and Mancktelow, 2004). Yet, regarding this segment of the Tonale fault adjacent to the Lepontine dome, the AFT and ZFT data suggest a rapid change in the kinematics of movement, located in the Val Mera-Como lake area (fig. 2), leading to oblique slip and block rotation during the Middle Miocene to Upper Miocene (Chapter 5). Differential throw along-strike resulted in the relative uplift of the Central and Western Lepontine (western block) and downfaulting of the Bergell pluton (eastern block).

In summary, timing constraints along the major bounding faults support that orogen-parallel stretch was already active tentatively at ca. 28 Ma. Accordingly, greenschist facies deformations within the pluton obviously support that the bulk kinematic framework combining extensional and transcurrent displacements associated with an orogen-parallel stretch was established soon after the intrusion emplacement and rapid exhumation. With cooling and on-going exhumation, the deformation became increasingly cataclastic and mechanical scratches progressively replaced fibrous minerals on the fault rock surfaces. We tentatively divide the orogen-parallel displacement into a two-fold stage. First, a major long-lived orogen-parallel extension phase was accommodated by a combination of strike-slip and normal fault displacements under progressively cooling conditions. This phase was essentially active between ca. 28-17 Ma. This doesn't preclude any younger minor normal faulting along and cross-strike of the belt during the Neogene times, due to the uplift pattern of the Eastern Central Alps. Second, prevailing strike-slip reactivation akin in part to transpressive strain is conversely placed at ca. 17-18 Ma. A lower age estimate for the transcurrent movement is difficult to assess but according to fission-track data dextral oblique slip and block rotation during the Middle Miocene to Upper Miocene might have occurred on the Tonale fault. On the other hand, no

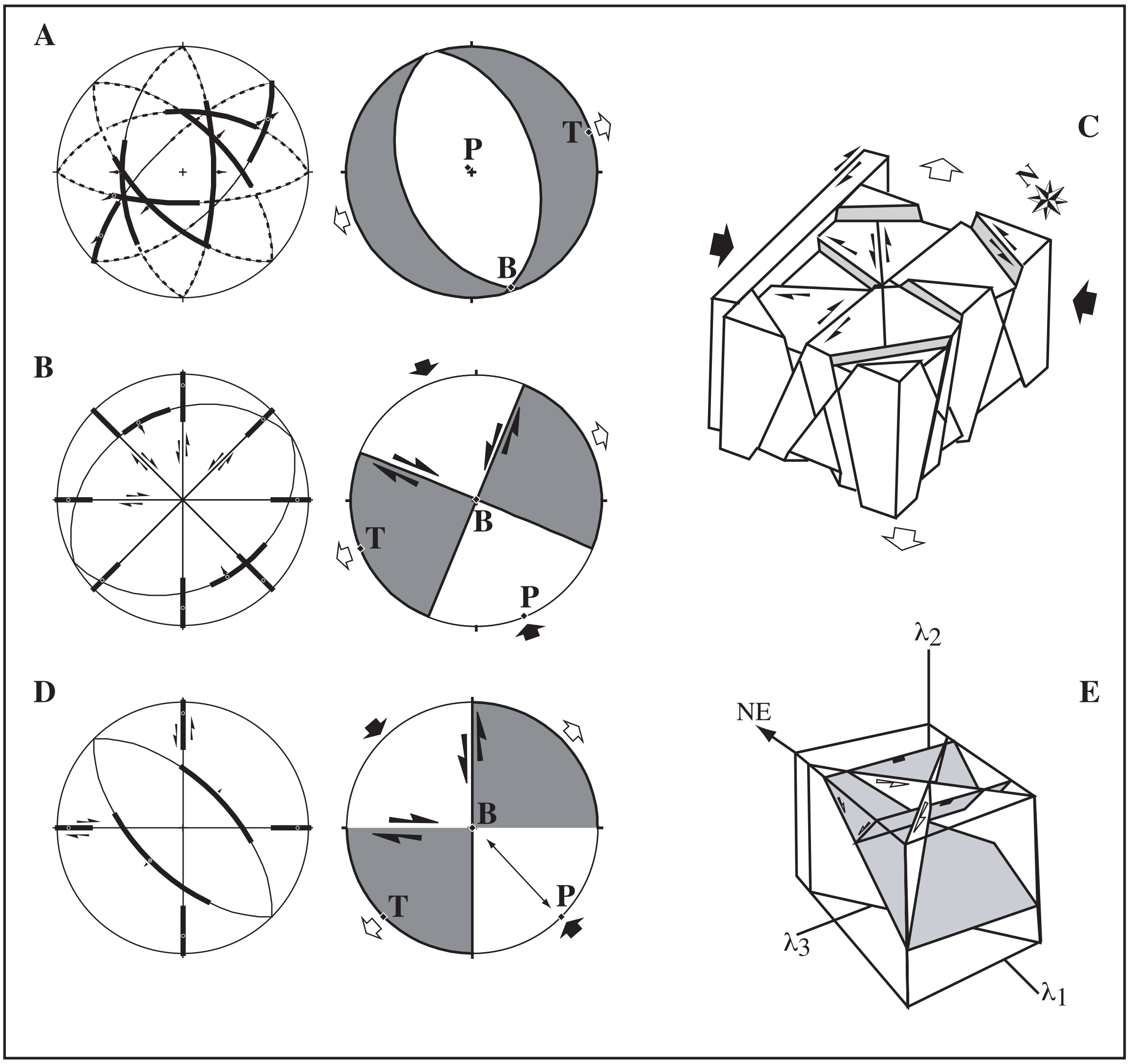

Fig. 16. Lower hemisphere projection summarizing attitudes of major fault sets and slip directions (left stereonets) associated with (A) the extensive tectonic regime, (B) the transcurrent tectonic regime, together with mean representative fault plane solution (right stereonets). Heavy lines represent the estimated range of slip vector orientation. Dashed lines in (A) are the generally observed strike-slip reactivation domains on previously formed normal faults. (C) Interpretative 3D view of the bulk fault pattern and associated kinematics in the Bergell and Insubric areas (D) Interpretation of normal plus strike-slip faults as an orthorhombic fault system, and mean representative fault plane solution (right stereonets). The component of vertical shortening is explained by permutations between the maximum and intermediate principal axes. (E) 3D view of the orthorombic fault system interpretation.

ages related to dextral shear at the Tonale fault younger than 16 Ma are currently reported. This age is in agreement with the suggested end of brittle dextral slip on the Tonale fault in the Giudicarie region (Viola et al., 20001; Stipp et al., 2004).

5. Discussion

We used a multi-scale approach to characterize the post-nappe tectonic evolution under brittle-ductile to brittle conditions at the eastern border of the Lepontine dome of the Central Alps. Late normal faulting at all scales investigated is widespread in this internal part of the belt during the late

Oligocene and Neogene, but part of the deformation observed is also associated with transcurrent movements. The mapping of the fault network is coherent with the outcrop analyses and with the paleostress and incremental strain reconstructions.

Stress and strain results

The results of the kinematic and dynamic analysis of the brittle and brittle-ductile deformations in the Bergell and Insubric areas, using minor fault populations, are correlable from one site to another. Both the similarities in the pattern of stereographic results from different sites and the consistency of stress and strain axes orientations obtained by dynamic and kinematic methods at each site further corroborates the suitability and stability of the results. Good arguments for both the dominance of coaxial deformation and homogeneous stress states within our stations and at the fault-bounded blocks scale stem from (a) the parallelism of the principal axes of stress and incremental strain in most situations, and (b) the high regional consistency of the computed tensors (figs. 11 and 12). The assumption that fault movement is parallel to the direction of resolved shear stress is in general valid. Local effects on the calculated stress tensors in high-strain zones can however not be ruled out, but we suggest that fault interactions do not appreciably affect the computed stress tensor. Whereas the stress and strain tensors yield adequate information about the general state of stress and kinematics of the fault populations, some resulting high fluctuation of the fault-striae data requires a more detailed discussion about the timing and interaction of normal and strike-slip faults.

The fault population in the Bergell pluton is actually complex and expressed by pairs of transversal and longitudinal conjugated neoformed and/or reactivated faults (fig. 16a, b). This fault pattern includes at all scales strike-slip, oblique normal and normal faults, and minor reverse faults at the microtectonic scale, developed under brittle-ductile to brittle conditions (fig. 16c). Multiple slickenline sets and multiple fault patterns are classically interpreted as the result of one or more faulting events. In the case of newly-formed faults under Andersonian plane-strain conditions, the principal stress directions can be inferred from conjugated sets of strike-slip or normal faults having their mean slip line nearly perpendicular to the faults intersection (Anderson, 1951). Movement on pre-existing planes of weakness is typically oblique-slip. Various sets of normal faults formed under varying stress state conditions: initial failure and oblique-slip reactivation occurred in relation with critical and non-critical states of stress, respectively. So did the strike-slip faults. Their development implies local changes in the orientation of the maximum principal stress axis from horizontal to vertical for strike-slip and normal faulting, respectively (fig. 16a, b).

Are strike-slip and normal faulting to occur simultaneously, then oblique-slip faults must be expected because of complex faulted-block kinematics. Similar slickenfiber geometry, mineralogy or absence of mineralogy, and sequence of mineral growth of coated fault surfaces (i.e. epidote-chlorite, chlorite, and dry conditions) indeed suggest that the sets of faults formed under similar cooling conditions. Despite late trancurrent movements have been shown to reactivate normal faults, the strike-slip and normal faults appear to some extent roughly contemporaneous (see section 3.2.1, fig. 16c). The strike-slip and normal faults actually have the same symmetry axis and all together these coeval faults divide the parent rock into block geometries that close-match rhomboedron-shaped features in map view (fig. 16d, e), with the major difference they are not necessarily arranged in a biconjugate array (e.g. Oertel, 1965; Aydin and Reches, 1982; Reches, 1983b; Krantz, 1989). This type of complex fault pattern is characteristic of faulting in response to three-dimensional non-plane strain but doesn't satisfy a stress-controlled deformation theory which provides only Coulomb patterns even under three-dimensional loading (Oertel, 1965; Reches, 1978; Johnson, 1995; Nieto-Samaniego, 1999). It is a requirement in this alternative interpretation that boundary conditions determine the strain in two principal directions. The interpretation of these faults as an orthorombic set suggests nearly orogen-perpendicular contraction (NW-SE to NNW-SSE directed) and orogen-parallel extension (NE-SW to ENE-WSW directed), plus a component of vertical shortening.

The wide extent and regional importance of normal faults together with the duration time estimates for the extensional event (see section 4) makes it obvious that normal faulting was however a long-term dominant deformation process. Both stress tensors for normal and strike-slip faults are characterized by the very similar sub-horizontal orientation of the minimum principal stress axis (NE top ENE trending). With this approach, the late Oligocene-early Miocene tectonic evolution of the Bergell Alps can be described in terms of two successively prevailing and interplaying paleostress states and deformation episodes during one single tectonic event that led to the major orogen-parallel stretch. Accordingly, the minor fault distribution was split into two successive coaxial stages with more homogeneous subsets and lower fluctuation. The overall stress pattern can be explained by the permutation between $\sigma1$ and $\sigma2$ principal stress axes, $\sigma3$ remaining sub-horizontal and belt-parallel oriented. Alternating and interfering normal and oblique-slip motions on the tranversal and longitudinal fault systems, as well as prominent strike-slip reactivation of normal faults ensure kinematic compatibility and suggests that both faulting episodes are the result of one major extensive to transtensive tectonic event. A similar history is indicated by curved fibers from down-dip to horizontal orientation on fault surfaces in several stations.

The bimodal distribution of stress ratios akin to the each paleostress tensor population yields further constraints on the tectonic evolution. In contrast to the transtension scheme, high stress ratios associated with paleostress calculations are few. Under this stress configuration, the magnitudes of $\sigma1$ and $\sigma2$ differ and permutations between these two principal stress axes are hampered. In contrast, vertical or horizontal axially symmetric compression stress models produce reasonable good fits to the faults. In the case of σ1 vertical, the low ϕ ratios bear witness to the minor radial part, or in other word the orogen-perpendicular part, of the extension. Down-dip slip lines on the longitudinal faults, together with oblique-slip slickenlines on sets of the transversal fault system, commonly accommodate such strain in the Bergell area. Accordingly, in transtensive experiments strain is partitioned between sub-parallel strike-slip faults and normal faults with no or limited horizontal offset, at low angle to the orogen long axis (e.g. Schreurs and Colletta, 1998). This might support the feasibilty of transtensive strains in the Bergell area. In the case of σ3 vertical, the uniaxial compressive stress models are a reasonable good fit to both the pure strike-slip and reactivated strike-slip oblique-reverse faults on the one hand, and lesser reverse faults in the populations on the other hand. Low Δ ratios actually deal with nearly equal magnitudes of σ2 and σ3. The subsequent permutation between these principal stress axes yields a stress configuration that accommodates minor strain in the vertical direction and reflects a more transpressional paleostress field. But on the whole the Δ ratio variations have actually poor weight on the stability of extension direction. These results suggest therefore that the far-field kinematic framework and boundary conditions maintained the bulk stretch direction orogen-parallel oriented all over the late Oligocene-Neogene times. Local transtensive and transpressive strains are however difficult top reconcile with a single stress configuration and need to be separated in time.

Fault-slip analysis results in the context of Alpine Tertiary tectonics

The estimated maximum shortening and maximum principal stress direction in the Bergell and Insubric areas coincide fairly with the relative motion of the Adria and European plates since early Oligocene until late Miocene (Dewey et al., 1989). Extensional and contractional lateral displacements accommodated by mylonitic deformation as well as by brittle faulting is thus assumed to be a result of the convergence between the two plates. According to this scheme, the intraplate stress recorded in the Bergell area (European plate) is taken to be transmitted across the plate boundary from the interplate slip vector of Adria, between 35 Ma and 9 Ma (Dewey et al., 1989). The consecutive motion of the fault-bounded Bergell block and other internal blocks was mainly eastward, in the direction parallel to the long axis of the belt.

Lateral extrusion is a typical process associated with plate convergence and dominated by strike-slip and normal faulting (Tapponnier, 1977; Tapponnier et al., 1986; Ratschbacher et al., 1991a, b). On the basis of these essentials, we relate the extensional and transcurrent tensor groups and the fault pattern to the eastward lateral extrusion of the Eastern Central Alps in response to the on-going convergence between the Adria and European plates. We refer this lateral extrusion to a two-fold mech-

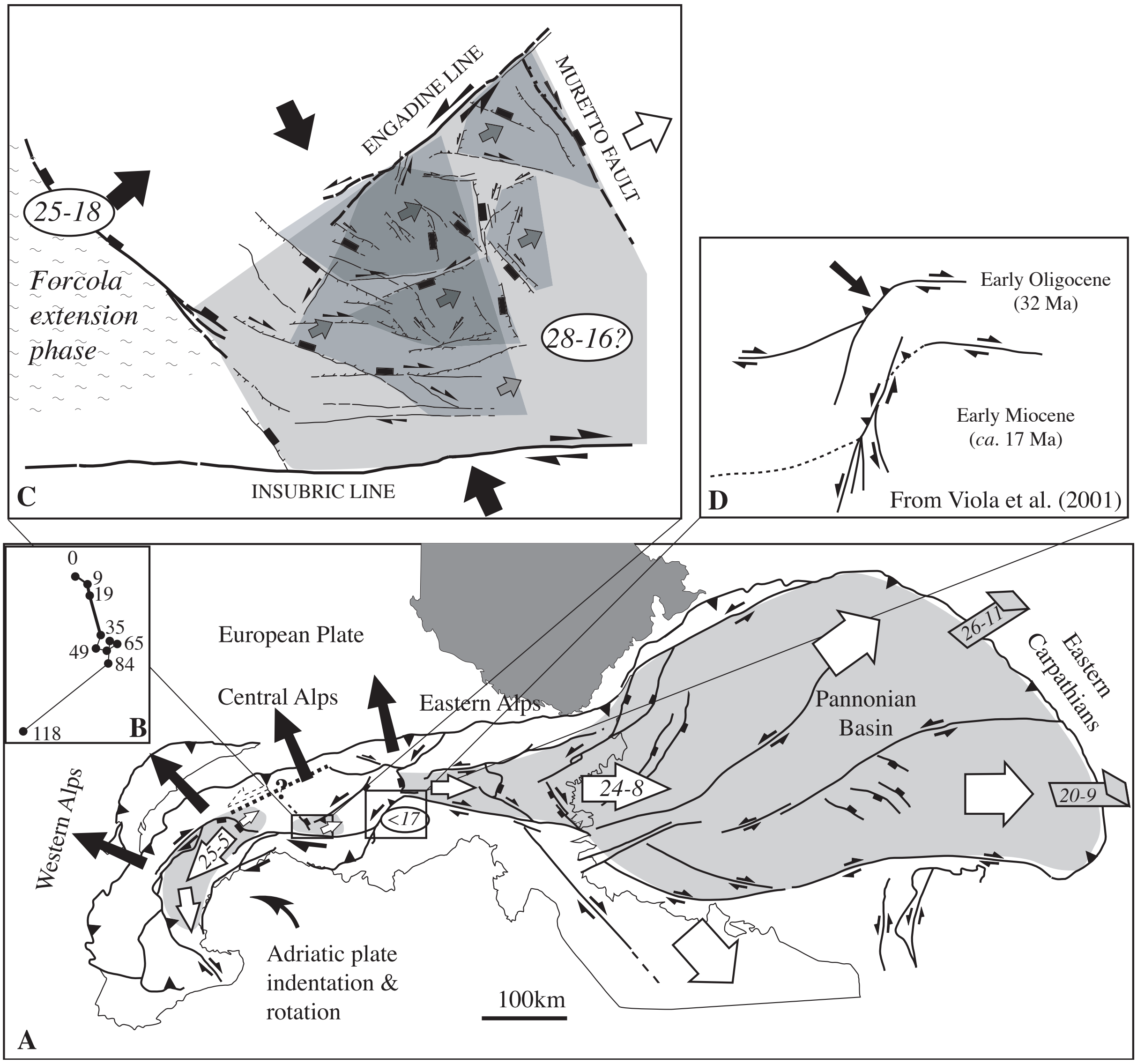

Fig. 17. (A) Overview of the orogen-parallel and lateral extrusion domains (light grey shaded areas) in the core of the Alps by the late Oligocene to early Miocene onwards. Modified from Platt et al., 1989), Decker and Peresson (1996), Dick, 2000), Bistacchi et al. (2001), Champagnac et al. (2004). Open large arrows indicate direction of tectonic escape. Numbers refer to the times of deformation in million years. Grey arrows refer to thrusting and subduction in the Eastern Carpathians. Black arrows indicate mean shortening direction across the belt by the late Oligocene onwards. (B) Africa-Europe plate-motion path calculated for the location of Torino (Italy) from Africa-Europe poles determined by Dewey et al. (1989) (C) Schematic kinematic model of orogen-parallel extension and eastward lateral extrusion at the eastern border of the Lepontine dome by the late Oligocene onwards. Conjugate strike-slip faults define imbricate wedge-shaped blocks (grey shaded areas) that accommodate orogen-perpendicular contraction and orogen-parallel extension. (D) Evolution of the Giudicarie Fault System since 32 Ma (from Viola et al., 2001). The Giudicarie fault represents an original dextral restraining bend in the Periadriatic fault, before sinistral reactivation at ca. 17 Ma.

anism (in agreement with the nomenclature by Ratschbacher et al., 1991a) which includes: (1) an extensional escape of the Bergell region, kinematically accommodated by normal faulting along various sets of transversal faults but also by the longitudinal faults by a combination of dip-slip, oblique-slip and strike-slip displacements according to spatial and temporal stress variations; (2) a lateral escape of the Eastern Central Alps along conjugated strike-slip faults (e.g. the Insubric and Engadine lines, Schmid and Froitzheim, 1993) and reactivated normal and oblique-normal faults, with minor neoformed normal faults, as a result of on-going convergence. A major issue of lateral extrusion models is that orogen-parallel extension by normal faulting following rapid surface uplift in the hinterland occurs already during the early stages of convergence (e.g. Ratschbacher et al., 1991a; Seyferth and Henk, 2004). Although orogen-parallel extension is therefore intimately related to continental collision (Seyferth and Henk, 2004), further discussion regarding the driving force for extension processes in the Eastern Central Alps is necessary.

(1) The long-term extensional deformation by widespread normal faulting at all scales investigated indicates a buoyancy imbalance and minor topographic readjustment along and cross-strike of the belt without significant crustal thinning. The state of stress is predominantly controlled by gravitational induced stresses due to load ($\sigma v = \sigma 1$) or by topographic gradients ($\sigma h = \sigma 3$). Tectonic stresses ($\sigma H = \sigma 2$) transmitted by the plate-tectonic stress field are much lower than the buoyancy forces and are eventually nearly in the same order as the minimum principal horizontal stress ($\sigma h = \sigma 3$). According to this scheme, slab break-off re-equilibration (von Blanckenburg and Davies, 1995) is a plausible mechanism in the Eastern Central Alps that might explain the observed extension pattern. Slab break-off is unique in that he likely triggered the observed rapid surface uplift and heating at the end of the Oligocene (e.g. Giger and Hurford, 1989; Gebauer, 1999). Additionally, the considerable heat input that triggered melting of the lower crust to produce S-type granites (e.g. Novate granite) not necessarily exposed at the surface and numerous dykes at ca. 25 Ma (Gebauer, 1999; Liati et al., 2000), as well as the occurrence of Tertiary migmatites of the same age (see review in Hansmann, 1996) might evidence that the continental crust was partially molten in the late Oligocene to beginning Miocene. Extension of the upper crust over a thermally weakened layer is a workable mechanism that likely contributes to the syn-convergence collapse of the belt (e.g. Seyferth and Henk, 2004). Accordingly, within the Bergell, the sets of faults leading to the orogen-parallel stretch were active during and controlled the emplacement of the Novate intrusion (Ciancaleoni and Marquer, 2004). Because the far-field kinematic framework and boundary conditions (sideways escape of the Central Alps) control the extension direction, the upper crust primarily moves in the orogen-parallel direction and much lesser in the orogen-perpendicular one.

Shallow extension over a deep indenter is an alternative plausible mechanism that might explain the brittle extension of the upper crust. This model implies deep compressional tectonics and overall shortening across the belt. This is documented by lower crustal wedging and outward growth of the orogen at ca. 20 Ma (foreland propagation of deformation in the Southern Alps and uplift of the External Crystalline Massives, e.g. Schmid et al., 1996a and references therein; Schmid and Kissling, 2000). Indentation of the Adriatic lower crust into the European upper crust led to uplift and buoyancy imbalance in the central part of the Alps. Since prominent normal faulting associated with enhanced lateral extrusion is primarily older than Langhian (end of the Forcola phase), we suggest that shallow extension which depends on the deep structure of the belt might essentially explain the minor topographic readjustments and tectonic denudation along and cross-strike of the belt due to differential uplift pattern in the core of the belt by the middle Miocene onwards. This scenario doesn't imply much orogen-parallel extension and lateral extrusion.

(2) Although extension is a major tectonic feature in the Eastern Lepontine, the interplay between driving forces for extension and the sideways displacement of Adria actually triggers a switch from an extension state to a more transcurrent state. The stress tensors related to conjugate sets of strike-slip faults, either in the absence of accompanying normal faults (ca. 50% of non-polyphased sites) or with typical normal fault reactivation, gives indications for prevailing strike-slip faulting at some stages of the deformation history. The computed tensors maintain the orogen-parallel extension, as horizontal transmitted tectonic stresses are increased up to a critical state ($\sigma H = \sigma 1$) significantly greater than the gravitational stresses, inducing rupturing and active strike-slip faulting. At the local scale, normal faulting dominated sites without strike-slip features (remaining 50% of non-polyphased sites) nevertheless indicates that local extension is most probably still working out during the prevailing transcurrent regime. Conjugated sets of strike-slip faults define sets of triangular wedges that lead to escape. In particular, late transcurrent processes are prominent along the southern longitudinal dextral strike-slip fault zone (fig. 4), coeval with the late cataclastic overprint of the Insubric and Paina mylonites (Fumasoli, 1974; Schmid et al., 1989; Heitzmann, 1987b). Because the Tonale Line slips at high-angle to $\sigma 1$, it must be weaker than the surrounding crust, because other potential fault planes at lower angles to $\sigma 1$ have more shear stress resolved on them but didn't produce much offset. The large-scale dextral shear-zone at the retro-side therefore allows the sideways displacement of the Adria and European plates. Together with the weak Engadine Line (Schmid and Froitzheim, 1993), it accommodated most of the lateral escape. High-strains in the wrench zone are testified by significant block rotations in the tonalite tail. The consistency of results of paleostress and strain analyses suggests that plate motion of Adria relative to Europe has driven dextral slip on the Insubric Line and sinistral slip on the Engadine Line, and dominantly pure shear deformation in the area in between them, the Bergell block. Longitudinal dextral to dextral-oblique normal faults are however not restricted to the Tonale fault vicinity but are quite regularly distributed at the scale of Bergell and Insubric areas. Because the Adria rotates counterclockwise during indentation distributed dextral strike-slip shearing and orogen-parallel extension in the hinterland is expected (fig. 17a). Indeed the large-scale divergent shortening vector between the Western Alps and western Central Alps on the one hand, and the Eastern Central Alps on the other hand, has to be accommodated by NE-SW extension and bulk transtensive tectonics in the Bergell region.

In contrast, the common uniaxial compressive stress models akin to the transcurrent regime are significant since they represent half of the stress solutions. On the whole, the late alpine tectonic regime in this part of the Central Alps evolved through time from an extensive strain state (with oscillations between more transtensive to more radial extensive kinematic regimes at the local scale) toward a more transcurrent and transpressive strain state. While stress permutations between σ1 and σ2 with σ3 fixed horizontal elegantly solve the transition from extensional to strike-slip faulting in a bulk transtensional kinematic regime at the local scale, it is difficult to reconcile with coeval stress permutations between σ2 and σ3 with σ1 fixed horizontal. This statement in turn leads us to address the problem of boundary conditions, and in particular the degree of lateral confinement. Limitations with fitting these observations with the lateral extrusion model are discussed successively.

A major requirement of lateral extrusion models is the need for an unconfined lateral margin (free boundary) where the crust is expelled. Such a free boundary in the Eastern Central Alps is speculative but may be found in the Carpathian region, where subduction and lateral convergence is documented by the early Miocene onwards (Ratschbacher et al., 1991a; Decker and Peresson, 1996). In the late Oligocene, lateral escape toward this region was accommodated along the Canavese-Insubric indenter and across the Giudicarie fault system that represents an original dextral restraining bend in the Periadriatic fault by this time (fig. 17d, Viola et al., 2001). This implies that most of the extrusion structures in the Bergell region are pre-dated by later indentation along the Giudicarie-Pustertal indenter and sinistral reactivation of the Giudicarie fault in the Middle to Lower Miocene (circa 17-6 Ma; e.g. Viola et al., 2001; Martin et al., 1991; Schönborn, 1992). The eastern lateral margin was consequently strongly constrained from the Middle Miocene onwards, avoiding any significant lateral extrusion from then. We suggest that this major event induced a drastic change in the boundary conditions and subsequent bulk stress field in the Bergell area. This triggered transcurrent reactivation of early normal faults and complex block kinematics movements leading eventually to strain accommodation in the vertical direction.

Modeling results of lateral extrusion suggest that under conditions of lateral confinement, orogen-parallel extension still occurs but is reduced by a factor of 2 to 4 depending on experiment conditions (Seyferth and Henk, 2004). In the Bergell Alps, the major Forcola extension phase is accordingly constrained between ca. 25 Ma and 18 Ma (Ciancaleoni et al., 2004), which doesn't preclude any further normal faulting due to strain accommodation and/or minor topographic readjustment along and cross-strike of the belt (see section 4). Thus the end of the Forcola activity fairly coincides both with: (1) the sinistral reactivation of the Giudicarie fault at 17 Ma east of the Bergell region (onset of lateral confinement, Viola et al., 2001); (2) the sinistral offset of the cataclastic Tonale Fault by Giuducarie related secondary faults, implying that the last significant dextral strike-slip movements on the Tonale fault took place during the Burdigalian (Stipp et al., 2004); (3) the cessation of vertical movements due to block rotation along the sinistral Engadine Line (Schmid and Froitzheim, 1993) during the Burdigalian, giving an upper age limit (Langhian) for localized sinistral slip on this fault (Chapter 5); (4) the beginning of Neogene westward extension of the Brenner fault at the tip of the Giudicarie-Pustertal indenter; this fault accommodated the onset of the main exhumation phase of the Tauern Window at ca. 20-18 Ma (Fügenschuh et al., 1997) coeval with lateral extrusion of the Eastern Alps (e.g. Ratschbacher et al., 1991b; Frisch et al., 1998); (5) the onset of maximum normal faulting displacement along the Rhone-Simplon line at 18-15 Ma (Grasemann and Mancktelow, 1993); this fault accommodated west-directed tectonic unroofing of the western Lepontine dome by the early Neogene onwards (Schlunegger and Willett, 1999; Zwingmann and Mancktelow, 2004). These chronological constraints strongly support that a major far-field kinematic reorganization akin to the Alpine convergence occurred near the Oligocene-Miocene boundary and in particular during the Burdigalian times. Back to the Bergell area of the Eastern Central Alps, we suggest that the efficiency of lateral extrusion has strongly fallen off by this time onwards. Significant lateral extrusion and orogen-parallel extension due to on-going convergence was then shifted at the western border of the Lepontine and in the Eastern Alps.

The lateral extrusion hypothesis emphasizes the role of a large-scale major set of conjugated strike-slip faults that intersect or merge toward one another and eventually toward a major normal fault (e.g. the Rhone-Simplon system or the Brenner-Inntal-Pustertal system in fig. 1). All together, these bounding faults define a wedge-shaped crustal block that accommodates orogen-parallel extension and orogen-perpendicular contraction (fig. 17a). Secondary sets of similar wedge-shape blocks with transversal normal faults in their inside progressively grow during progressive deformation (e.g. Ratschbacher et al., 1991b). In the Bergell Alps, such a crustal wedged-shape block (the Bergell block) is represented at first sight by the strike-slip Tonale and Engadine faults on the one hand, and by the Forcola normal fault on the other hand. Their kinematics accommodates roughly E-W extension and N-S compression near the Oligocene-Miocene boundary (fig. 17c). Into details however, these major faults are not connected to each other (fig. 2). In particular, the Forcola fault extends essentially on the northern side of the Engadine fault, where his trace gets progressively lost (fig. 2). So do many secondary normal faults parallel to the Forcola Line in its hangingwall. In other words, we lack a northern major sinistral strike-slip bounding fault to be in keeping with a lateral extrusion scheme (heavy dashed line and question mark in fig. 17a). Such a prominent crustal fault has not been presently mapped. This statement likely addresses the scale problem. By analogy with the imbricated nature of extruding wedges characteristics of the typical lateral extrusion geometry in the Eastern Alps, the problem is solved if we consider the Bergell block as a secondary wedge-shaped block of a larger extrusion system. But in this hypothesis we still lack the northern boundary running possibly through the Penninic domain. Down to the Bergell block, behind the complex pattern of strike-slip and normal faults, several secondary wedge-shaped blocks encompassing normal faults can be drawn (fig. 17c). Such geometry seems to be available by the lineament analysis within the Penninic units north of the Engadine Line (fig. 3). This supports the scale problem hypothesis.

6. Conclusions

We characterized the late deformation processes under brittle-ductile and brittle conditions in the Bergell region of the Eastern Central Alps. At all scales investigated, the fault population is made of normal faults, oblique-slip faults and strike-slip faults. Much lesser thrust faults occur only at the microtectonic scale. The tectonic regime associated with these faults is distributed in space and time into extensional and transcurrent displacements, leading to lateral extrusion of the Eastern Central Alps by the late Oligocene onwards. The paleostress and incremental strain field is characterized by a consistent orientation of the short, respectively long, axis of the stress, respectively strain, ellipsoid parallel to the long axis of the belt. Widespread normal faulting is a major long-lived event which led to orogen-parallel extension with a minor orogen-perpendicular component. Buoyancy forces in the core of the belt and above all the far-field kinematic framework of the collision between the Adriatic and European plates determine the direction of escape. In particular, distributed and conjugated sets of strike-slip faults define triangular wedges that accommodate the escape of the Eastern Central Alps in response to sideways displacement of Adria. A major change in the boundary conditions (lateral confinement) at ca. 17 Ma marked the transition from the extensive/transtensive tectonic regime to a more transcurrent (and eventually transpressive) one reactivating previously formed faults, because lateral extrusion efficiency was diminished by this time. On-going significant orogen-parallel extension was then primarily relocated sideways at the western border of the Lepontine and in the Eastern Alps (Ratschbacher et al., 1991b; Hubbard and Mancktelow, 1992; Bistacchi et al., 2001; Champagnac et al., 2004).

Lateral extrusion in the core of the Alpine belt during the last stages of the continental collision is therefore an outstanding deformation process that predominates everywhere along strike of the belt. In that sense lateral extrusion must be definitely considered as tectonic process characteristics of the late Alpine geodynamics since the Neogene. Accordingly, preliminary results of the brittle tectonics of the Lepontine dome of the Central Alps appear to be strongly coherent with this scenario (Allanic et al., 2005).

REFERENCES

Adam, J., C.-D. Reuther, M. Grasso, and L. Torelli, Active fault kinematics and crustal stresses along the ionian margin of southeastern Sicily, Tectonophysics, 326, 217-239, 2000.

Allanic, C., C. Sue, J.D. Champagnac, B. Delacou, and M. Burkhard, New constraints on the brittle deformation in the Lepontine Alps, from paleostress and pseudotachylites analyses, in European Geosciences Union 2005, Vienna, Austria, 24 - 29 April 2005, 2005.

Allmendinger, R.W., R.A. Marrett, and T. Cladouhos, FAULTKIN-program, Dep. of Geol. Sc., Snee Hall, Cornell University, Ithaca, NY, 1989.

Anderson, E.M., The dynamics of faulting, Ed. Oliver et Boyd, 2nd ed., Edinburgh, 206, 1951.

Angelier, J., Sur l'analyse de mesures recueillies dans les sites faillés : l'utilité d'une confrontation entre les méthodes dynamiques et cinématiques, Comptes Rendus de l'Academie des Sciences de Paris - Series IIA - Earth and Planetary Science, 281, 1805-1808, 1975.

Angelier, J., Determination of the mean principal direction of stress for a given fault population., Tectonophysics, 56, 17-26, 1979.

Angelier, J., Tectonic analysis of fault data sets., Journal of Geophysical Research B: Solid Earth, 89, 5835-5848, 1984.

Angelier, J., From orientation to magnitude in paleostress determination using fault slip data., Journal of Structural Geology, 11, 37-50, 1989.

Angelier, J., B. Colletta, and R.E. Anderson, Neogene paleostress changes in the Basin and Range: a case study at Hoover Dam, Nevada-Arizona, Geological Society of America Bulletin, 96, 347-361, 1985.

Angelier, J., and P. Mechler, Sur une méthode graphique de recherche des contraintes principales également utilisable en tectonique et en sismologie: la méthode des dièdres droits., Bulletin de la Société Géologique de France, 7, 1309-1318, 1977.

Argand, E., Sur l'arc des Alpes Occidentales, Eclog. Geol. Helv., 14, 145-204, 1916.

Aydin, A., and Z. Reches, Number and orientation of fault sets in the field and in experiments, Geology, 10, 107-112, 1982.

Baudin, T., D. Marquer, and F. Persoz, Basement-cover relationships in the Tambo nappe (Central Alps, Switzerland): geometry, structures and kinematics, J. struct. Geol., 15, 543-553, 1993.

Berger, A., and R. Gieré, Structural observations at the eastern contact of the Bergell pluton, Schweiz Miner. Petr. Mitt., 75, 1995.

Berger, A., C. Rosenberg, and S.M. Schmid, Ascent, emplacement and exhumation of the Bergell pluton within the Southern Steep Belt of the Central Alps, Schweiz Miner. Petr. Mitt., 76, 357-382, 1996.

Bistacchi, A., G.V. Dal Piaz, M. Massironi, M. Zattin, and M.L. Balestrieri, The Aosta-Ranzola extensional fault system and Oligocene- Present evolution of the Austroalpine-Penninic wedge in the northwestern Alps, International Journal of Earth Sciences, 90, 654-667, 2001.

Bott , M.H., The mechanism of oblique slip faulting, Geol. Mag., 96, 109-117, 1959.

Carey, E., Recherche des direction principales de contraintes associées au jeu d'une population de failles, Rev. Geogr. phys. Geol. dyn., 21, 57-66, 1979.

Carey, E., and B. Brunier, Analyse théorique et numérique d'un modèle mécanique élémentaire appliqué à l'étude d'une population de failles, Comptes Rendus de l'Academie des Sciences de Paris - Series IIA - Earth and Planetary Science, 279, 891-894, 1974.

Carey-Gailhardis, E., and P. Vergely, Graphical analysis of fault kinematics and focal mechanisms of earthquakes in terms of stress; the right dihedra method, use and pitfalls, Annales Tectonicae, VI, 3-9, 1992.

Champagnac, J.D., C. Sue, B. Delacou, and M. Burkhard, Brittle deformation in the inner north-western Alps: from early orogen-parallel extrusion to late orogen-perpendicular collapse, Terra Nova, 16, 232-242, 2004.

Ciancaleoni, L., Brittle-ductile deformation during the last stages of the continental collision: geometry and kinematics of the major discontinuities in the Bergell and Insubric areas (east Switzerland, north Italy), Ph.D. thesis, University of Neuchâtel, Neuchâtel, 2005.

Ciancaleoni, L., and D. Marquer, Syn-extension leucogranite emplacement during convergence in the Eastern Central Alps: case example from the Novate intrusion, in Swiss Geoscience Meeting 2004, Université de Lausanne, 2004.

Cornelius, H.P., Zur Kenntnis der wurzelregion im unteren Veltlin, N. Jb. Mineral., 40, 1915.

Cornelius, H.P., and M. Cornelius-Furlani, Die Insubrische Linie vom Tession bis zum Tonale-Pass, Denkschr. Akad. Wiss. Math. Klasse, 102, 208-301, 1930.

Decker, K., and H. Peresson, Tertiary kinematics in the Alpine-Carpathian-Pannonian system: links between thrusting, transform faulting and crustal extension., in Oil and gas in Alpidic thrustbelts and basins of Central and Eastern Europe. EAGE Special Publication, vol. 5, edited by G. Wessely and W. Liebl, pp. 69-77, 1996.

Delvaux, D., R. Moeys, G. Stapel, C. Petit, K. Levi, A. Miroshnichenko, V. Ruzhich, and V. San'kov, Paleostress reconstructions and geodynamics of the Baikal region, Central Asia, Part 2. Cenozoic rifting, Tectonophysics, 282, 1-38, 1997.

Dewey, J.F., M.L. Helman, E. Turco, D.H.W. Hutton, and S.D. Knott, Kinematics of the Western Mediterranean, in Alpine Tectonics, vol. 45, edited by M.P. Coward, Dietrich, D., Park, R.G., pp. 265-283, Geol. Soc. London Spec. Publ., London, 1989.

Dick, P., Tectonic transport directions in the Helvetic-subalpine thrust system of the NW-alpine Arc., unpublished Ph.D thesis thesis, Neuchâtel, 2000.

Diethelm, K.H., Petrographische und geochemische Untersuchungen an basischen Gesteinen der Bergeller Intrusion, Ph.D. thesis, ETH Zürich, Zürich, 1989.

Dupin, J.M., W. Sassi, and J. Angelier, Homegeneous stress hypothesis and actual fault slip: a distinct element analysis, Journal of Structural Geology, 15, 1033-1043, 1993.

Engelder, T., Stress regimes in the lithosphere, Princeton Univ. Press, Princeton, 1993.

Etchecopar, A., G. Vasseur, and M. Daignières, An inverse problem in microtectonics for the determination of stress tensor from fault striation analysis, Journal of Structural Geology, 3, 51-65, 1981.

Frisch, W., I. Dunkl, and J. Kuhlemann, Post-collisional orogen-parallel large-scale extension in the Eastern Alps, Tectonophysics, 327, 239-265, 2000.

Frisch, W., J. Kuhlemann, I. Dunkl, and A. Brugel, Palinspastic reconstruction and topographic evolution of the eastern Alps during late Tertiary tectonic extrusion, Tectonophysics, 297, 1-15, 1998.

Fügenschuh, B., D. Seward, and N.S. Mancktelow, Exhumation in a convergent orogen: the western Tauern Window, Terra Nova, 9, 213-217, 1997.

Fumasoli, M.W., Geologie des Gebietes nördlich une südlich der Jorio-Tonale-Linie im westen von Gravedona (Como, Italia), PhD diss. thesis, 230 pp., Universität Zürich ETH, Zürich, 1974.

Gebauer, D., A P-T-t path for a high pressure ultramafic rock-associations and their felsic country-rocks based on SHRIMP dating of magmatic and metamorphic zircon domains. Example: Alpe Arami (Central Swiss Alps), in Earth Processes: Reading the Isotopic Code, vol. 95, edited by A. Basu and S.R. Hart, pp. 307-328, Geophys. Monogr. Ser., 1996.

Gebauer, D., Alpine geochronology of the Central and Western Alps: new constraints for a complex geodynamic evolution, Schweiz. Mineral. Petrogr. Mitt., 79, 191-208, 1999.

Giger, M., Geochronologische und petrographische studien an Geröllen und Sedimenten der Gonfolite-Lombarda Gruppe (Südschweiz und Norditalien) und hir Vergleich mit dem alpinen Hinterland, PhD diss. thesis, 227 pp., Universität Bern, Bern, 1991.

Giger, M., and A.J. Hurford, Tertiary intrusives of the Central Alps: their Tertiary uplift, erosion, redeposition and burial in the south-alpine foreland., Eclog. Geol. Helv., 82, 857-866, 1989.

Grasemann, B., and N. Mancktelow, Two-dimensional thermal modelling of normal faulting: the Simplon Fault Zone, Central Alps, Switzerland, Tectonophysics, 225, 155-165, 1993.

Guiraud, M., O. Laborde, and H. Philip, Characterization of various types of deformation and their corresponding deviatoric stress tensors using microfault analysis, Tectonophysics, 170, 289-316, 1989.

Gulson, B.L., Age relations in the Bergell region of the South-East Swiss Alps: With some geochemical comparisons, Eclog. Geol. Helv., 66, 293-313, 1973.

Hancock, P.L., Brittle microtectonics: principles and practice, Journal of Structural Geology, 7, 437-457, 1985.

Hansmann, W., Age determination on the Tertiary Masino-Bregaglia (Bergell) intrusives (Italy, Switzerland): a review, Schweiz. Mineral. Petrogr. Mitt., 76, 421-451, 1996.

Heitzmann, P., Evidence of late oligocene/early miocene backthrusting in the central alpine "root zone", Geodinamica Acta, 1, 183-192, 1987a.

Heitzmann, P., Calcite mylonites in the Central Alpine "root zone", Tectonophysics, 135, 207-215, 1987b.

Hubbard, M., and N.S. Mancktelow, Lateral displacement during Neogene convergence in the western and central Alps, Geology, 20, 943-946, 1992.

Huber, R.K., Tectonometamorphic evolution of the Eastern Pennine Alps during Tertiary continental collision: Structural and petrological relationships between Suretta-, Tambo-, Chiavenna and Gruf units (Switzerland/Italy), PhD thesis, University of Neuchâtel., Neuchâtel, 1999.

Huber, R.K., and D. Marquer, Tertiary deformation and kinematics of the southern part of the Tambo and the Suretta nappes (Val Bregaglia, Eastern Swiss Alps), Schweiz. Mineral. Petrogr. Mitt., 76, 383-397, 1996.

Hunziker, J.C., J. Desmons, and G. Martinotti, Thirty-two years of geochronological work in the Central and Western Alps: a review on seven maps, Mémoires de Géologie (Lausanne), 13, 1992.

Hurford, A.J., Cooling and uplift patterns in the Lepontine Alps, South Central Switzerland and an age of vertical movement on the Insubric fault line, Contrib. Mineral. Petrol., 92, 413-427, 1986.

Ida, Y., Effects of the crustal stress on the growth of of dykes: conditions of intrusion and extrusion of magma, J. Geophys. Res., 104, 17,897-17,909, 1999.

Johnson, A.M., Orientations of faults determined by premonitory shear zones, Tectonophysics, 247, 161-238, 1995.

Köppel, V., and M. Grünenfelder, Concordant U-Pb ages of monazite and xenotime from the Central Alps and the timing of the high temperature Alpine metamorphism, a preliminary report, Schweiz Miner. Petr. Mitt., 55, 129-132, 1975.

Krantz, R.W., Orthorombic fault patterns: The odd axis model and slip vector orientations, Tectonics, 8, 483-495, 1989.

Lardelli, T., Die Tonalelinie in unteren Veltlin, PhD diss. thesis, 221 pp., ETH Zürich, Zürich, 1981.

Laubscher, H.P., The large-scale kinematics of the western Alps and the northern Appennines and its palinspastic implications, American Journal Of Science, 271, 193-226, 1971.

Liati, A., D. Gebauer, and M. Fanning, U-Pb SHRIMP dating of zircon from the Novate granite (Bergell, Central Alps): evidence for Oligocene-Miocene magmatism, Jurassic/Cretaceous continental rifting and opening of the Valais trough, Schweiz Miner. Petr. Mitt., 80, 305-316, 2000.

$

Liniger, M.H., Der ostalpin-penninische Grenzbereich im Gebiet der nördlichen Margna-Decke (Graubünden, Schweiz), Ph. D. diss. thesis, ETH Zürich, Zürich, 1992.

Mancktelow, N.S., and T.L. Pavlis, Fold-fault relationships in low-angle detachment systems, Tectonics, 13, 668-685, 1994.

Marquer, D., Structures et cinématique des déformations alpines dans le granite de Truzzo (Nappe de Tambo: Alpes centrales suisses), Eclogae geol. Helv., 84, 107-123, 1991.

Marrett, R., and D.C.P. Peacock, Strain and stress, Journal of Structural Geology, 21, 1057-1063, 1999.

Marrett, R.A., and R.W. Allmendinger, Kinematic analysis of fault-slip data, Journal of Structural Geology, 12, 973-986, 1990.

Martin, S., G. Prosser, and L. Santini, Alpine deformation along the Periadriatic lineament in the Italian Eastern Alps, Ann. Tect., 5, 118-140, 1991.

Meier, A., The Periadriatic Fault System in Valtellina (N-Italy) and evolution of the southwestern segment of the Eastern Alps, PhD diss. thesis, 190 pp., ETH Zurïch, Zurïch, 2003.

Meyre, C., D. Marquer, S.M. Schmid, and L. Ciancaleoni, Syn-orogenic extension along the Forcola fault: correlation of Alpine deformations in the Tambo and Adula nappes (Eastern Pennine Alps), Eclogae Geol. Helv., 91, 409-420, 1998.

Milnes, A.G., Post-nappe folding in the western Lepontine Alps, Eclog. Geol. Helv., 67, 333-348, 1974.

Müller, W., G. Prosser, N. Mancktelow, I.M. Villa, S.P. Kelley, G. Viola, and F. Oberli, Geochronological constraints on the evolution of the Periadriatic Fault System (Alps), Int. J. Earth Sci. (Geol Rundsch), 90, 623-653, 2001.

Nieto-Samaniego, A.F., Stress, strain and fault patterns, Journal of Structural Geology, 21, 1065-1070, 1999.

Oberli, F., M. Meier, A. Berger, C. Rosenberg, and R. Gieré, 230Th/238U disequilibrium systematics in U-Th-Pb dating: nuisance or powerful tool in geochronometry ?, in 6th V.M. Goldschmidt Conference, Heidelberg, 1996.

Oertel, G., The mechanism of faulting in clay experiments, Tectonophysics, 2, 343-393, 1965.

Oncken, O., Aspects of the reconstruction of the stress history of a fold and thrust belt (Rhenish massif, Federal Republic Of Germany), Tectonophysics, 152, 19-40, 1988.

Passerini, P., G. Sguazzoni, and M. Marcucci, Mesoscopic faults in the Bregaglia (Bergell) massif, Central Alps, Tectonophysics, 198, 53-72, 1991.

Peretti, A., Geologie und Petrographie der Forno-Serie. Piz Dei Rossi, Diploma diss. thesis, ETH Zürich, Zürich, 1983.

Peretti, A., Der Monte-del-Forno-Komplex am Bergell-Ostrand: Seine Lithostratigraphie, alpine tektonik und metamorphose, Eclog. Geol. Helv., 78, 23-48, 1985.

Petit, J.P., Criteria for the sense of movement on fault surfaces in brittle rocks, J. Struct. Geol., 9, 597-608, 1987.

Platt, J.P., J.H. Behrmann, P.C. Cunningham, J.W. Dewey, M. Helman, M. Parish, M.G. Shepley, S. Wallis, and P.J. Westom, Kinematics of the Alpine arc and the motion history of Adria, Nature, 337, 158-161, 1989.

Pollard, D.D., Strain and stress: discussion, Journal of Structural Geology, 22, 1359-1367, 2000.

Pollard, D.D., S.D. Saltzer, and A.M. Rubin, Stress inversion: are they based on faulty assumptions ?, Journal of Structural Geology, 15, 1045-1054, 1993.

Puschnig, A.R., Regional and emplacement-related structures at the northeastern border of the Bergell intrusion (Monte Del Forno, Rhetic Alps), Schweiz Miner. Petr. Mitt., 76, 399-420, 1996.

Rahn, M.K., L. Ciancaleoni, Fügenschuh B., and D. Marquer, FT data between Lepontine dome and Bergell intrusion: key area for the late exhumation of the Central Alps ?, in Swiss Geoscience Meeting 2004, Université de Lausanne, 2004.

Ratschbacher, L., W. Frisch, H.-G. Linzer, and O. Merle, Lateral extrusion in the Eastern Alps; part 2: structural analysis, Tectonics, 10, 257-271, 1991b.

Ratschbacher, L., O. Merle, P. Davy, and P.R. Cobbold, Lateral extrusion in the Eastern Alps; Part 1, Boundary conditions and experiments scaled for gravity., Tectonics, 10, 245-256, 1991.

Ratschbacher, L., O. Merle, P. Davy, and P.R. Cobbold, Lateral extrusion in the Eastern Alps; Part 1, Boundary conditions and experiments scaled for gravity., Tectonics, 10, 245-256, 1991a.

Reches, Z., Analysis of faulting in three-dimensional strain field, Tectonophysics, 47, 109-129, 1978.

Reches, Z., Faulting of rocks in three-dimensional strain fields. II. Theoretical analysis, Tectonophysics, 95, 133-156, 1983b.

Reusser, E., Phasenbeziehungen im Tonalit der Bergell Intrusion, PhD Diss. thesis, ETHZ, Zürich, 1987.

Riklin, K., Strukturen und Metamorphose im Bereich der südlichen Muretto-Linie, Schweiz Miner. Petr. Mitt., 58, 345-356, 1978.

Ring, U., The kinematics of the late Alpine Muretto fault and its relation to dextral transpression across the Periadriatic Line, Eclog. Geol. Helv., 87, 811-831, 1994.

Roberts, J.L., The intrusion of magma into brittle rocks, in Mechanisms of Igneous Intrusion, Geol. J. Spec. Issue, vol. 2, edited by N. Newall and H. Rast, Geol. Soc., Liverpool, U.K., 1970.

Romer, R.L., U. Schärer, and A. Steck, Alpine and pre-Alpine magmatism in the root zone of the Western Central Alps, Contrib. Min. Pet., 123, 138-158, 1996.

Rosenberg, C., A. Berger, and S.M. Schmid, Observation from the floor of a granitoid pluton: Inferences on the driving force of final emplacement, Geology, 23, 443-446, 1995.

Rosenberg, C.L., and F. Heller, Tilting of the Bergell pluton and Central Lepontine area: combined evidence from paleomagnetic, structural and petrological data, Eclogae Geol. Helv., 90, 345-356, 1997.

Ruzicka, J.W., Der Nordland des Grüf-Komplexes und seine Beziehung zur Engadiner Linie, Diploma diss. thesis, Universität Basel, Basel, 1997.

Schärer, U., M. Cosca, A. Steck, and J.C. Hunziker, Termination of major ductile strike-slip shear and differential cooling along the Insubric Line (Central Alps): U-Pb, Rb-Sr and 40Ar/39Ar ages of cross-cutting pegmatites, Earth and Planetary Science Letters, 142, 331-351, 1996.

Schlunegger, F., and S. Willett, Spatial and temporal variations in exhumation of the central Swiss Alps and implications for exhumation mechanisms, in Exhumation processes: Normal Faulting, Ductile Flow and Erosion, vol. 154, Special Publication, edited by U. Ring, M.T. Brandon, G.S. Lister and S.D. Willett, pp. 157-179, Geological Society Special Publication, London, 1999.

Schmid, S.M., H.R. Aebli, F. Heller, and A. Zingg, The role of the Periadriatic Line in the tectonic evolution of the Alps, in Alpine Tectonics, vol. 45, edited by M.P. Coward, D. Dietrich and R.G. Park, pp. 153-171, Geological Society Special Publication, London, 1989.

Schmid, S.M., A. Berger, C. Davidson, R. Gieré, J. Hermann, P. Nievergelt, A.R. Puschnig, and C. Rosenberg, The Bergell pluton (Southern Switzerland, Northern Italy): Overview accompanying a geological-tectonic map of the intrusion and surrounding country rocks, Schweiz. Mineral. Petrogr. Mitt., 76, 329-355, 1996b.

Schmid, S.M., and N. Froitzheim, Oblique slip and block rotation along the Engadine line, Eclogae geol. Helv., 86, 569-593, 1993.

Schmid, S.M., and E. Kissling, The arc of the western Alps in the light of geophysical data on deep crustal structure, Tectonics, 19, 62-85, 2000.

Schmid, S.M., O.A. Pfiffner, N. Froitzheim, G. Schönborn, and E. Kissling, Geophysical-geological transect and tectonic evolution of the Swiss-Italian Alps, Tectonics, 15, 1036-1064, 1996a.

Schmid, S.M., A. Zingg, and M. Handy, The kinematics of movements along the Insubric Line and the emplacement of the Ivrea Zone, Tectonophysics, 135, 47-66., 1987.

Schönborn, G., Alpine tectonics and kinematic models of the central Southern Alps, Mem. Sci. Geol., XLIV, 229-393, 1992.

Schreurs, G., and B. Colletta, Analogue modelling of faulting in zones of continental transpression and transtension, in Continental transpressional and transtensional tectonics, vol. 135, edited by R.E. Holdsworth, R.A. Strachan and J.F. Dewey, pp. 59-79, Geological Society of London Special Publications, London, 1998.

Seyferth, M., and A. Henk, Syn-convergent exhumation and lateral extrusion in continental collision zones - insights from three-dimensional numerical models, Tectonophysics, 382, 1-29, 2004.

Sperner, B., L. Ratschbacher, and R. Ott, Fault-striae analysis: a turbo pascal program package for graphical presentation and reduced stress-tensor calculation., Computers & Geosciences, 19, 1361-1388, 1993.

Spillmann, P., Die Geologie des penninisch-ostalpinen Grenzbereichs im südlichen Bernina-Gebirge, Ph. D. diss. thesis, ETH Zürich, Zürich, 1993.

Srivastava, D., C., R.J. Lisle, and S. Vandycke, Shear zones as a new type of paleostress indicator, Journal of Structural Geology, 17, 663-676, 1995.

Steck, A., and J.C. Hunziker, The Tertiary structural and thermal evolution of the Central Alps: compressional and extensional structures in an orogenic belt, Tectonophysics, 238, 229-254, 1994.

Stipp, M., B. Fügenschuh, L.P. Gromet, H. Stünitz, and S.M. Schmid, Contemporaneous plutonism and strike-slip faulting: A case study from the Tonale fault zone north of the Adamello pluton (Italian Alps), Tectonics, 23, 2004.

Sue, C., and P. Tricart, Neogene to ongoing normal faulting in the inner western Alps: a major evolution of the late alpine tectonics, Tectonics, 22, 2003.

Suppe, J., Principles of structural geology, Prentice Hall, Old Tappan, N. J., 1985.

Tapponnier, P., Evolution tectonique du système alpin en Méditerranée : Poinçonnement et écrasement rigide-plastique, Bulletin de la Société Géologique de France, 7, 437-460, 1977.

Tapponnier, P., B. Meyer, J.P. Avouac, G. Peltzer, Y. Gaudemer, G. Shunmin, X. Hongfa, Y. Kelun, C. Zhitai, C. Shuahua, and D. Huagang, Active Thrusting and folding in the Qilian Shan, and decoupling between upper crust ans mantle in northeast Tibet, Earth and Planetary Science Letters, 97, 382-403, 1990.

Tapponnier, P., G. Peltzer, and R. Armijo, On the mechanics of the collision between India and Asia, in Collision Tectonics, vol. 19, edited by M.P. Coward and A.C. Ries, pp. 115-157, Geol. Soc. Spec. Publ., 1986.

Tchalenko, J.S., Similarities between shear zones of different magnitudes, Bull. Geol. Soc. Am., 81, 1625-1640, 1970.

Trommsdorff, V., and J.A.D. Connolly, The ultramafic contact aureole about the Bregaglia (Bergell) tonalite: isograds and a thermal model, Schweiz Miner. Petr. Mitt., 76, 537-547, 1996.

Trommsdorff, V., and P. Nievergelt, The Bregaglia (Bergell) Iorio inrusive and its field relations, Mem. Soc. Geol. It, 26, 55-68, 1983.

Trümpy, R., The Engadine Line: a sinistral wrench fault in the Central Alps, Mem. Geol. Soc. China, 2, 1-17, 1977.

Turner, F.J., Nature and dynamic interpretation of deformation lamellae in calcite of three marbles, American Journal Of Science, 251, 276-298, 1953.

Twiss, R.J., and J.R. Unruh, Analysis of fault slip inversion: Do they constrain stress or strain rate?, Journal of Geophysical Research B: Solid Earth, 103, 12205-12222, 1998.

Venzo, S., R. Crespi, G. Schiavinato, and G. Fagnani, Carta geologico-petrografica delle alpi Insubriche Valtellinesi tra la Val Masino e la Val Malenco (Sondrio), Memorie della Soc. It. Scienze Naturali e del Museo Civico di Storia Naturale, XIX, 1970.

Villemin, T., and H. Charlesworth, Stress, an interactive computer programm to determine paleostress axes using data from striated faults, in Cordillera transect and cordilleran tectonic workshop, Alberta, 1992.

Viola, G., Kinematics and timing of the Periadriatic fault system in the Giudicarie region (Central-Eastern Alps), Ph. D. diss. thesis, ETH Zürich, Zürich, 2000.

Viola, G., N. Mancktelow, and D. Seward, Late Oligocene-Neogene evolution of the Europe-Adria collision: New structural and geochronological evidence from the Giudicarie Fault System (Italian Eastern Alps), Tectonics, 20, 999-1020, 2001.

von Blanckenburg, F., Combined high precision chronometry and geochemical tracing using accessory minerals applied to the Central-Alpine Bergell intrusion, Chemical Geology, 100, 19-40, 1992.

von Blanckenburg, F., and J.H. Davies, Slab breakoff: A model for syncollisional magmatism and tectonics in the Alps, Tectonics, 14/1, 120-131, 1995.

Wallace, R.E., Geometry of shearing stress and relation to faulting, Journal of Geology, 59, 118-130, 1951.

Watterson, J., The future of failure: stress or strain?, Journal of Structural Geology, 21, 939-948, 1999.

Wenk, E., Brittle-ductile transition zone in the northern Bergell Alps, Geol. Rdsch., 73, 419-431, 1984.

Wenk, H.R., The structure of the Bergell Alps. Part III, Eclog. Geol. Helv., 66, 255-291, 1973.

Werling, E., Tonale-, Pejo- une Judicarien-Linie: Kinematik, Mikrostrukturen und Metamorphose von tektoniken aus räumlich interferierenden, aber verschiedenaltrigen Verwerfungszonen, Ph. D. diss. thesis, ETH Zürich, Zürich, 1992.

Wiedenbeck, M., Structural and isotopic age profile across the Insubric Line, Mello, Valtellina, N. Italy, Schweiz. mineral. petrogr. Mitt., 66, 211-227, 1986.

Wotjal, S., and J. Pershing, Paleostresses associated with faults of large offset, Journal of Structural Geology, 13, 49-62, 1991.

Zwingmann, H., and N. Mancktelow, Timing of Alpine fault gouges, Earth and Planetary Science Letters, 223, 415-425, 2004.

Chapter 4

Syn-extension leucogranite emplacement during convergence in the Eastern Central Alps: case example from the Novate intrusion.

LAURENT CIANCALEONI, DIDIER MARQUER

IN PREPARATION FOR : TERRA NOVA

Syn-extension leucogranite emplacement during convergence in the Eastern Central Alps: case example from the Novate intrusion.

LAURENT CIANCALEONI, DIDIER MARQUER

ABSTRACT

The ca. 25 Ma old Novate intrusion is a late Alpine leucogranite that intruded in the Eastern Central Alps the late structures of dextral backthrusting along the Periadriatic Fault System (PFS). This leucogranite bears a spatial and temporal relationship with a segment of the PFS, the Forcola extensional mylonites, which accommodated orogen-parallel extension in the early Miocene. The Novate granite was heterogeneously deformed under conditions of the amphibolite-greenschist facies transition. The deformation inside the magmatic is characterized by strongly localized and anastomozed ductile shear zones surrounding lenses of weakly deformed granite and later faults formed at the brittle-ductile transition. These structures developed progressively during cooling of the intrusion. The fault kinematic analysis of the conjugated shear-zones indicates a non-coaxial deformation associated with an orogen-parallel extension strongly compatible with that at the Forcola mylonites. We propose that the Novate leucogranite was emplaced syn-extension at 25 Ma under mid-crustal conditions, at the southern tip of the Forcola fault. A model of extensional jog opening by vertical shearing along the Forcola shear zone promoted the space available for magma ascent and emplacement, upward transfer being sustained by the buoyant nature of the magma. This emplacement model along an active extensional shear zone simply solves the space problem for magma accommodation.

1. Introduction

Over the last decades pluton emplacement in the crust has been described in a wide range of tectonic settings, either compressive (D'Lemos et al., 1992; Brown and Solar, 1998), transcurrent (Hutton and Reavy, 1992) or extensional (Hutton et al., 1990; Scaillet et al., 1995). Common to these studies is the general spatial and temporal relationship between magmatic bodies and crustal shear-zones, and the resolution of the "space problem", i.e. the space needed to accommodate magma (e.g. Brown, 1994, and references therein). Consequently, regional tectonic structures are believed to control to some extent the ascent and emplacement of some plutons, either by creating space (Hutton et al., 1990; D'Lemos et al., 1992) or by arresting ascent (Clemens et al., 1997; Roman-Berdiel et al., 1997) or by triggering melt generation (Strong and Hanmer, 1981; Vauchez et al., 1997). It is implicit in that interpretation that crustal anatexis and granite segregation, ascent and emplacement are contemporaneous of the shearing environment (Sawyer, 1994).

In the case of Oligocene magmatism in the Alps, such causal relationship between deformation and melting has been reviewed (Rosenberg, 2004). This calc-alcaline magmatism is spatially and temporally associated with transpressive deformation along the Periadriatic Fault System (PFS) during convergence beween the Adria and European plates (e.g. Berger et al., 1996). In this paper we address the syn-tectonic emplacement of a late Alpine leucogranite, the Novate intrusion, at the Oligocene-Miocene boundary. We propose that this granitic body was intruded at eastern border of the Lepontine dome of the Central Alps along an active extensional segment of the PFS, the Forcola mylonites (Meyre et al., 1998). We suggest that the shear-zone acted as a dilatant site that accommodated magma emplacement, providing a simple answer to the space problem.

2. Geological setting

The Periadriatic Fault System (PFS) extends over more than 700 kilometers along strike of the Alpine Belt, mainly in an E-W direction. Traditionally, the PFS is considered to evidence deformations related to the post-collisional history of the Alps (Schmid et al., 1989 and references therein), as a result of the convergence between the Adriatic sub-plate and the European foreland. In the Central Alps, it is represented by a mylonitic belt of several kms in width, the Insubric Mylonites and the Southern Steep Belt (Milnes, 1974; Schmid et al., 1996b). The Oligocene Periadriatic plutons, including the Bergell pluton of the eastern Central Alps (fig. 1), are found in the vicinity of the PFS. In the Berg ell region, the post-nape deformation history is closely related to the well constrained timing of three of the Per Adriatic intrusions (von Blanckenburg, 1992): the Bergell tonalite and granodiorite (32 and 30 Ma; von Blanckenburg, 1992), the Sondrio tonalite (Biotite K/Ar cooling ages of 30-32 Ma; Giger, 1991) and the Novate leucogranite (24-26 Ma; Liati et al., 2000 and references therein) (fig.1). The late Oligocene post-collisional dextral transpression across the Insubric Mylonites belt has driven (D3 and D4 regional deformation in fig. 1): (1) backfolding and backthrusting of the Central Alps over the Southern Alps, providing up to ca. 20 kms relative vertical displacement, and very rapid exhumation of the Bergell area (Giger and Hurford, 1989; Berger et al., 1996); (2) ascent, syn-magmatic shortening and folding at the base of the Bergell pluton and ballooning at higher crustal levels (Rosenberg et al., 1995); (3) dextral offset of 30 to 100 kms summed up over the ductile and brittle displacement (Heitzmann, 1987a; Schmid et al., 1996a; Viola et al., 2001).

The Novate granite is a garnet bearing S-type two-mica leucogranite, not related to the calc-alcaline Bergell suite but rather derived from partial melting of crustal material during late-Alpine decompression (e.g. Oschidari and Ziegler, 1992; Von Blanckenburg et al., 1992). Magma formation must therefore have occurred during exhumation of the Bergell pluton in relation with backthrusting along the Insubric Line, before final intrusion of the main Novate granite stock. West of Val Mera, early Novate-related dikes are accordingly contemporaneous with the last stages of synmagmatic Bergell folding and migmatization of the host rocks (Hafner, 1993). But generally the Novate gran-

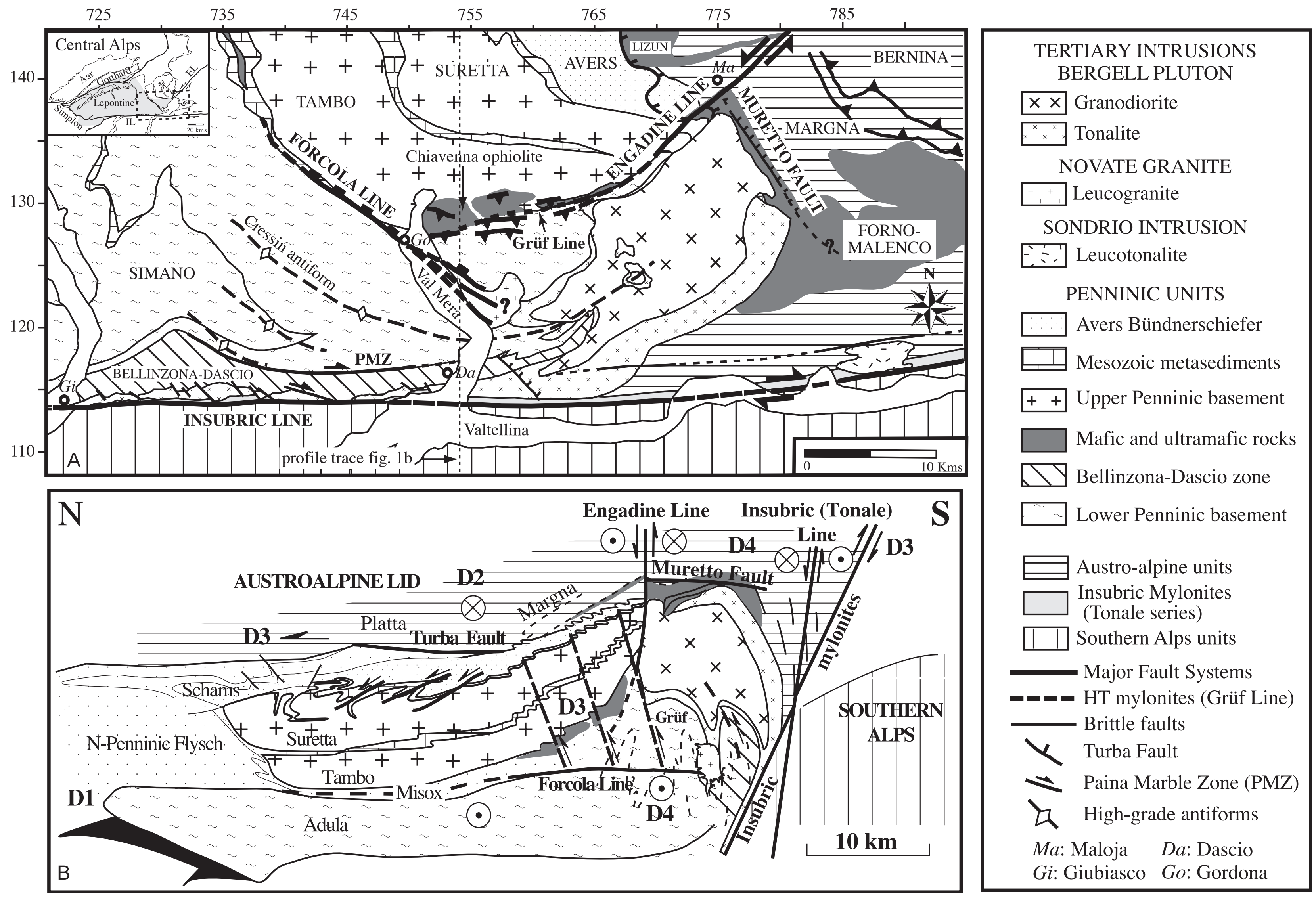

Fig. 1. (A) Geologic and tectonic setting of the Bergell and Insubric areas in the Eastern Central Alps. Question marks when the lateral prolongation of faults is uncertain. Modified from Rosenberg et al. (1995), Huber and Marquer (1996) and Meyre et al. (1998). (B) N-S geological profile along the Eastern Traverse. Modified from Schmid et al. (1996) and Huber and Marquer (1996). Regional deformation phases (D1-D4) are discussed in Meyre et al. (1998) and in the text.

ite and associated dike swarm crosscuts the late structures of the Southern Steep Belt and the Bergell pluton (fig. 1, Wenk, 1973; Schmid et al., 1996b). On the basis of U-Pb Shrimp dating of inherited zircons from the Novate granite, the source rocks of the pluton lie probably within continental crust of the Central Alpine Valais domain on either or both sides of the Valais ocean (Liati et al., 2000).

The margin of the Novate body is extremely irregular in details (see in Schmid et al., 1996b). In map view the Novate granite displays a typical en cornue shape (fig. 1). The southeastern contact trends NE-SW and contains numerous tonalite blocks (stoping). The western and northern contacts, albeit partly covered by Quaternary alluvial deposits, are clearly linear in map view and elongated in the NW-SE direction, i.e. parallel to the Forcola fault trend. The overall shape of the Novate granite located in the workable prolongation of the Forcola fault suggests a spatial relationship between the magmatic body and this crustal scale shear-zone.

3. The Forcola mylonites

Outcropping northwest of the Novate granite, this normal fault reaches the Val Mera, where it is covered by the Quaternary (fig. 1), and has been actually proposed to splay further south inside the Novate granite (Meyre et al, 1998). The Forcola mylonite zone (Marquer, 1991) is a major high-angle NE dipping and north-easterly displacing greenschist facies extensional shear-zone, located at the top of the penninic Adula nappe (Meyre et al, 1998, see chapter 2). The Forcola normal fault offsets the Tambo nappe in its hangingwall relative to the Adula nappe in its footwall by a vertical amount of approximately 3 kilometers (Meyre et al, 1998). On the outcrop, C-S relationships and shear-bands are typical structures of the ductile deformation. High-angle shear-bands gradually evolved into quartz-chlorite striae bearing brittle faults. These microstructures are interpreted as coeval progressive sets of shear bands associated with on-going Forcola deformation under cooling conditions and across the brittle-ductile transition. The onset of this is extensive phase has been tentatively constrained between 18 and 24 Ma on the basis of cooling ages in surrounding nappes (Meyre et al., 1998). Thus it post-dates backthrusting and decompression.

Albeit the trace of the fault gets lost east of Val Mera, a likely splay termination of the extensional mylonites further south inside the Novate granite has been proposed on the basis of foliation maps in country rocks of the Novate (Meyre et al., 1998). Accordingly, south of the pluton, no greenschist facies mylonites akin to the Forcola extension have been mapped so far. Conversely, brittle extension south of Novate is widespread, normal faulting in particular is compatible with the regional orogen-parallel extension (see chapter 3, part II).

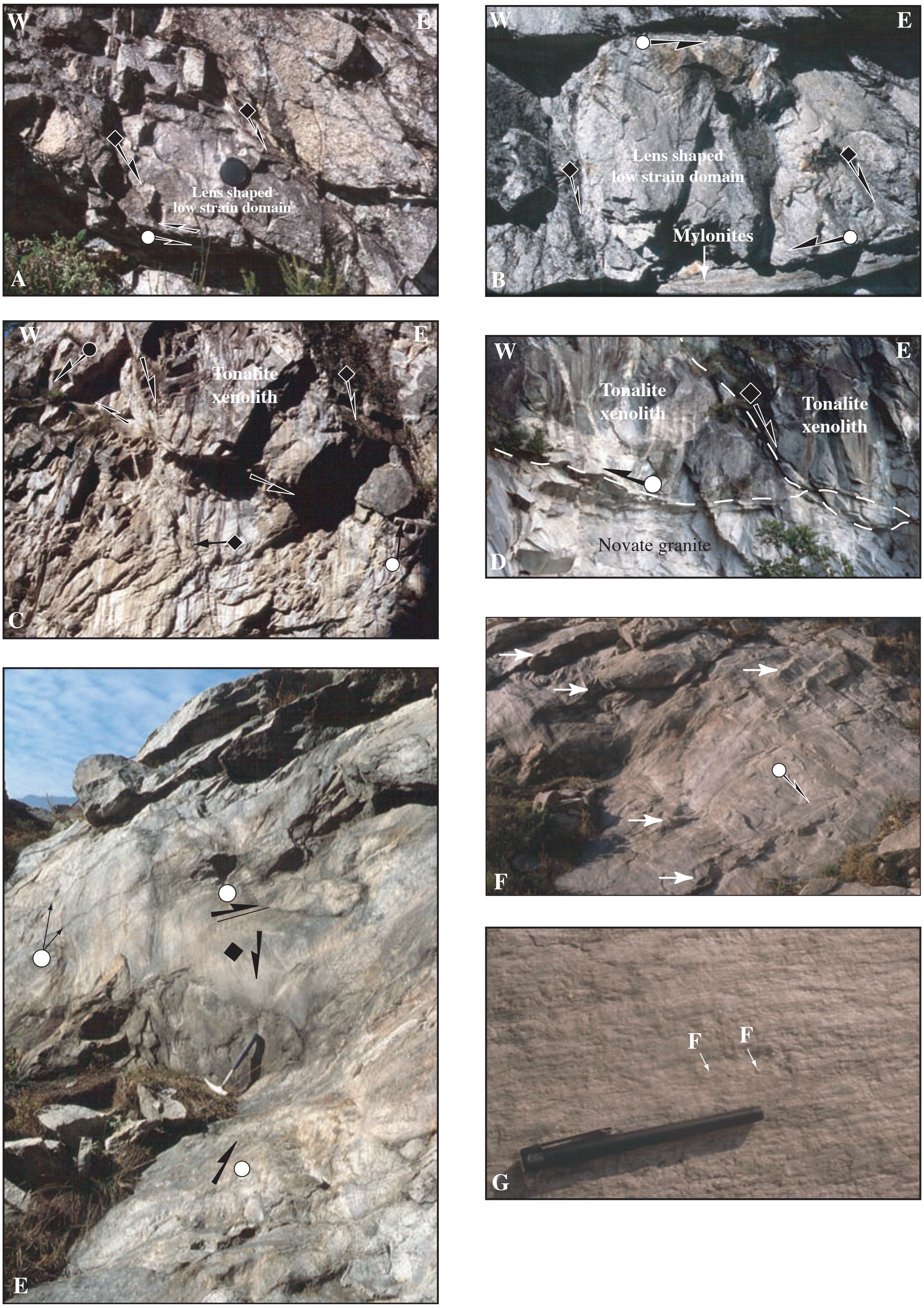

Fig. 2. Field examples at various scales of the heterogeneous deformation pattern in the Novate granite (A) and (B) Small scale conjugated shear zones surrounding lenses of weakly deformed granite. For symbols explanation, see fig. 4. Arrows show sense of shear on slip surfaces. (C) and (D) Large scale conjugated shear zones surrounding lenses-shaped domains of low strain. Note that the shear zones have the tendency to wrap around tonalite xenoliths.The vertical side of the photograph is about 30m and 10m in (C) and (D), respectively. (E) Another example of conjugated shear zones. The plane in foreground is a flat-lying shear zone (top WSW) conjugated with a vertical shear zone (behind hammer, top ESE). Note that shear zones anastomose and deform each other. On the vertical plane, the trace of other flat-lying shear zones is visible. (F) View from above of the flat lying mylonitic planes. The stretching lineation is parallel to the arrow. This shear plane is transected by a set of later transversal faults (white arrows). (G) Detail view of the streching lineation in mylonitic shear zones. Note in particular that the feldspar phase (F) forms clasts that are plastically stretched.

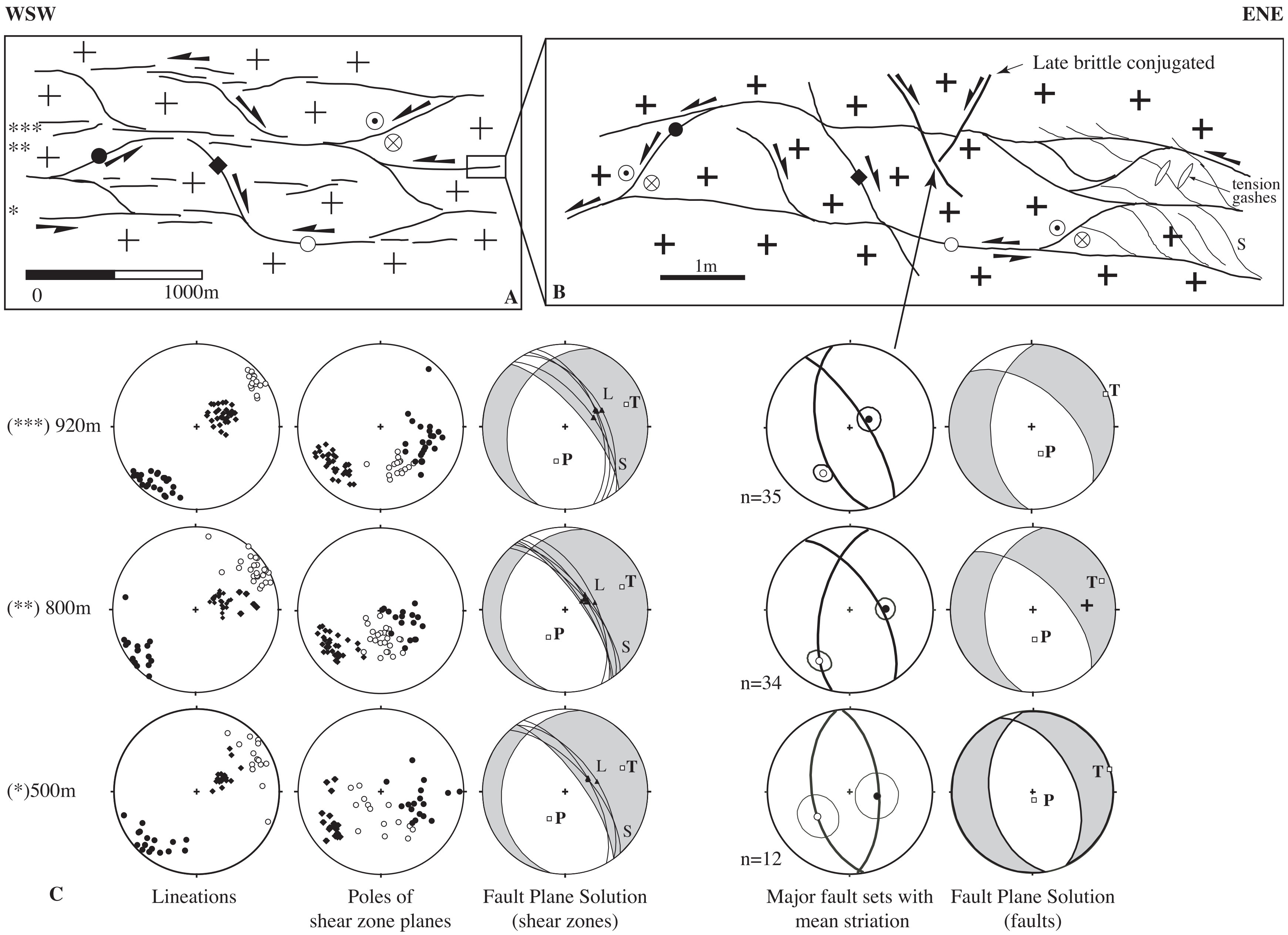
WSW
ENE
***
**
*
0
1000m
A
B
Late brittle conjugated
tension gashes
S
1m
(***) 920m
(**) 800m
(*)500m
L
T
P
S
n=35
n=34
n=12
C
Lineations
Poles of shear zone planes
Fault Plane Solution (shear zones)
Major fault sets with mean striation
Fault Plane Solution (faults)

Fig. 3. Shear-zone pattern and strain analysis in the Novate Intrusion. (A) Simplified ENE-WSW vertical cross-section (parallel to the XZ plane of deformation) in the Novate granite showing the strain distribution. Measurement stations are located by one to three stars (*) at the different altitudes (on the left of the diagram). Major conjugate sets of shear zones are discussed in the text and are indicated by open and full circles for shear zones with a westward shear sense, and by black squares for shear zones with an eastward shear sense. (B) Illustration of the deformation at the outcrop scale. Note the invariance of the deformation pattern at various scales. (C) Strain analysis. Same symbols as in (A). For each location, the stereonets (lower hemisphere projection) on the left side illustrate the dominant strain pattern: lineations, poles of shear zones and kinematic analysis using Faultkin (Allmendinger et al., 1989). For the kinematic analysis, the shear zone plane-stretching lineation pairs as used in a similar way to the fault-striae couples of a classical fault-slip analysis (e.g. Marrett and Allmendinger, 1990). White and grey shaded areas are the pression and tension quadrants, respectively. P and T are the best fit compression and tension axes, respectively. Great circles (S) and black triangles (L) on the fault plane solution diagrams are the schistosity and lineation measured in the low strain domains. The stereonets on the right side refer to the kinematic analysis of the major sets of brittle-ductile faults at the outcrop scale. + symbol at site ** is mean pole to tension gashes (incremental extension direction). Mean east and west dipping fault planes with corresponding mean striation (99% confidence cone) are plotted.

4. Heterogeneous deformation and strain distribution in the Novate granite

In plutonic rocks with an initially homogeneous and isotropic structure, heterogeneous deformation is essentially localized into arrays of anastomozing shear-zones. These shear-zones surround domains of weakly deformed rocks and more homogeneous strain (e.g. Mitra, 1979; Ramsay and Allison, 1979; Bell, 1981; Choukroune and Gapais, 1983; Gapais et al., 1987b; Marquer, 1991; Marquer et al., 1996) The bulk shear zone patterns are described as slip surfaces that accommodate most of the total deformation. Therefore they have been used as reliable shear criteria and strain markers (Gapais et al., 1987a).

In the Novate granite, the deformation is very heterogeneous and characterized by strongly localized and anastomozed ductile shear zones surrounding lenses of weakly deformed granite and faults formed at the brittle-ductile transition. Ductile shear-zones are evidenced by the occurrence of mylonites and ultramylonites. This heterogeneous deformation is present at all scales of observation (figs. 2 and 3).

Large volumes of granite with no fabric or with a weak magmatic foliation dipping shallowly to the NE are preserved. A weak schistosity and stretching lineation occurs in the core of the lenses and become intense close to and inside the high-strain zones. Shear-zone patterns have been analyzed at different altitudes within the granite on a vertical profile (fig. 3a,c). The bulk shear-zone pattern is described in terms of shear zone plane, stretching lineation and associated shear sense. The schistosity (XY plane of deformation) measured in the core of the weakly deformed lenses shows quite a constant average N150° strike (parallel to the Y direction) and ENE steep dip (great circle S in stereograms, fig. 3c), and bears a nearly down-dip stretching lineation (L, black triangles in stereograms fig. 4). The shear zone pattern is illustrated by conjugate shear zones intersecting close to the Y direction. The first set consists of shallowly dipping shear zones with a ENE-WSW oriented stretching lineation and a top to the SSW sense of shear (open and full circles in fig. 3). The second set deals with steeply to moderately inclined shear zones toward the NE, and associated with a nearly

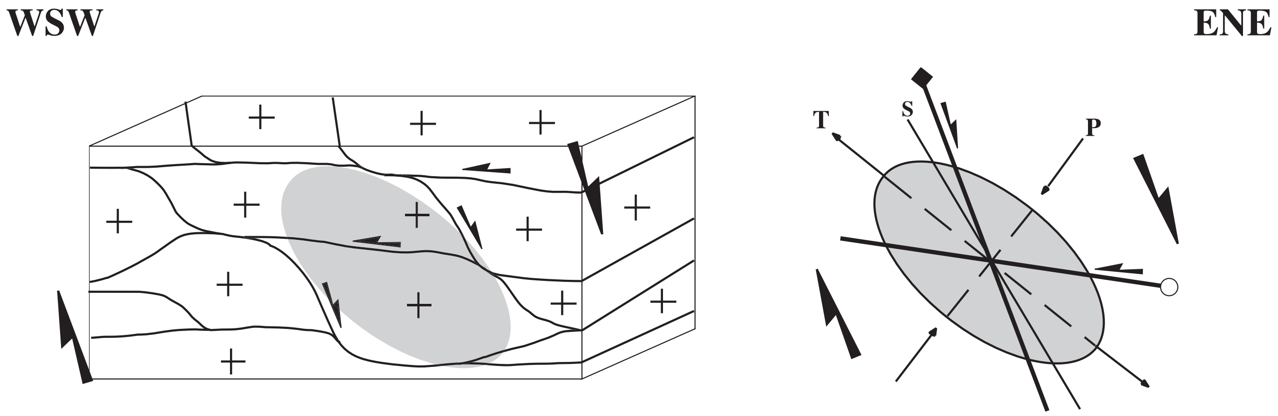

Fig. 4. Kinematic interpretation of the deformation in the Novate granite. The large arrows correspond to the dominant shear system. Symbols are the same as in fig. 4. Light grey shaded ellipsoid corresponds to the incremental strain ellipsoid. P and T are the resolved compression and tension axes, respectively, of the fault kinematic analysis. S is the average of the schistosity and lineation measured in the field. See text for more explanations.

down-dip lineation (full squares in fig. 3). The shear sense is top to the NE for this set. Locally this set appears to be reactivated under cooler conditions and slips with an oblique-normal offset. Both set of shear zones are quite equally parceled out.

The strain is also concentrated in a major set of steep brittle-ductile narrow E-dipping normal faults (typically less than 1 cm wide, fig. 3b,c), with various amounts of penetrative deformation (i.e. plasticity) versus purely brittle deformation (non penetrative deformation), conjugated with a generally pure brittle conjugated set of W-dipping normal faults. The former ones commonly show down-dip to oblique-normal dextral striations on the slip surfaces and lie in a sub-parallel orientation to the steep ductile shear-zone. They anastomose with or crosscut the flat-lying shear zones. Locally however they are also cross-cutted by the flat lying shear zones, which suggests that both slip systems are coeval and grew during progressive deformation. On the other hand, the latter major set of faults generally appears to offset the ductile flat lying shear-zones and must be somewhat younger (fig. 3b). The sense of shear for this set is oblique-normal sinistral.

The fault kinematic analysis of the brittle and ductile shear zones (Marquer et al., 1996; Srivastava et al., 1995) and the resulting principal incremental strain axes (P and T axes) are compared with the strain axes (X and Z axes of the finite deformation) deduced from the schistosity-stretching lineation couples measured in the lens-shaped domains of low strain. The schistosity lies close to a great circle delimiting the tension and compression quadrants, and is at low angle to the steep set of ductile and brittle-ductile shear zones. Additionally, it is placed in an asymmetric position with respect to the calculated extension field. Conversely, the lineation dips slightly oblique with respect to the resolved T axis (fig 3c). The fault kinematic analysis of the conjugated shear-zones and the bulk asymmetry between the resolved T axis and the average of schistosity-stretching lineation couples indicates a non-coaxial deformation associated with a ENE-WSW directed extension (fig. 4). The orientation of the P and T axes of the shear zone pattern are thought to be close to the principal axes of the incremental strain ellipsoid (light grey in fig. 4), as compared to the principal axes of the finite strain ellipsoid deduced from the S-L couples.

Regarding the fault kinematics analysis of the major sets of brittle and brittle-ductile faults, the resolved P and T axes orientation is consistent with that of the ductile shear-zone pattern. The bulk displacement pattern along faults and the orientation of the bulk strain field akin to the penetrative deformation in the Novate granite are therefore strongly compatible. This suggests that all the slip surfaces encompassing ductile and brittle structures worked together to accommodate the bulk of the deformation. No evidences of brittle fracturing as a precursor to strain localization was observed in the field. Alternatively, as a working hypothesis, ductile and brittle structures might reasonably have developed at different stages of cooling of the intrusion.

The geometry and kinematics of deformation inside the Novate granite are strongly compatible with that of the Forcola mylonites (compare with fig. 5 in Meyre et al., 1998; see chapter 2). In other words, the bulk strain pattern inside the Novate granite corroborates a spatial relationship with the extensional shear zone and the granitic body.

5. P-T conditions of mylonitisation

A strong gradient of deformation characterizes the shear-zones affecting the Novate granite (fig. 3b). In the various stages of progressive deformation, the constitute minerals (quartz, K-feldspar, plagioclase, biotite, white mica) do not deform in the same way, depending on the nature of the mineral phase considered and the original grain size (fig. 5).

The microstructures of deformation from the weakly deformed rocks to high-strained rocks are expressed by (1) a strong decrease in grain size at the onset of deformation by transgranular fracturing of the feldspar phase essentially, (2) the plastic behavior of quartz through all stages of progressive deformation, while both K-feldspar (Kfs) and plagioclase (Pl) primarily fractured and recrystallized along micro-shear bands and at grain margins (incipient and marginal recrystallization) in association with chemical changes, (3) essentially the destabilisation of the feldspar phase, in the presence of a water rich fluid phase and the growth and neocrystallization of new minerals, leading to an assemblage quartz + oligoclase ± albite + phengite + biotite ± epidote ± grenat in the high-strained zones (mylonites and ultramylonites), (4) the non-cataclastic granular flow of oligoclase-rich (with lesser albite) polyphase aggregates in the high-strain domains (Stünitz and Fitzgerald, 1993).

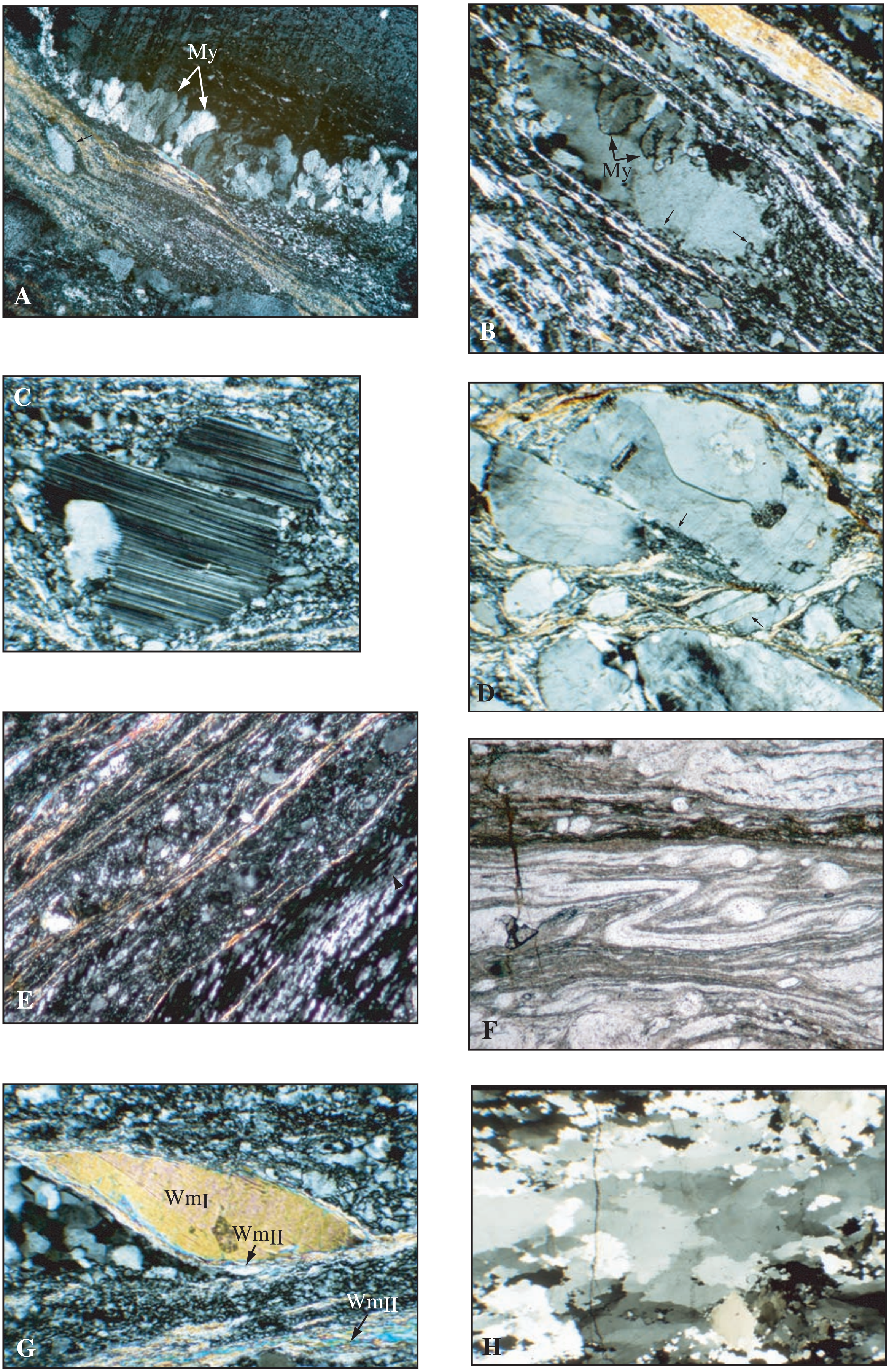
My
A
My
B
C
D
E
F
WmI
WmII
WmII
G
H

Granular-flow of albite-rich polyphased aggregates has been proposed as a viable mechanism for metamorphic grade lower than 450°C (Fitzgerald and Stünitz, 1993; Stünitz and Fitzgerald, 1993). In the Novate mylonites, typical mantles of very fine-grained feldspar develop around cores of old grains (core-and-mantle structures). The composition of newly formed plagioclase (typically less than 20 microns in grain size) shows lower An content (An 8-20) that the parent plagioclase (An 15-30), but is dominated by oligoclase and lesser albite. The recrystallized K-feldspar is stable (ca. Or 90) in low to intermediate deformation stages and seems to be relictual and progressively replaced by new grains of feldspar more albitic in composition in the fined grain matrix. Perthitic exsolutions in the core of Kfs and deformation-induced K-feldspar replacement by myrmekites along their grain boundaries parallel to the foliation attest of the activity of diffusion processes at the grain- or agregate-scale during the deformation. The frequent occurrence of myrmekites (An 10-15) with increasing strain indicates that the Ca-bearing plagioclase (oligoclase) was stable. Accordingly, the occurence of dominantly recrystallized oligoclase is taken as an indicator of amphibolite conditions during mylonitization (Yardley, 1989). This precludes in particular the neoformation of retrograde mineral phases such as epidote at some stages of the deformation. In the litterature, myrmekites have been commonly described in upper greenschist facies to lower amphibolite facies (see a review in Fitzgerald and Stünitz, 1993).

Quartz and micas form polycrystalline and almost monophased interconnected weak layers, deviated around feldspars porphyroclasts. Quartz dynamically recrystallizes primarily by dominant subgrain rotation (SR) and limited grain boundary migration (GBM), albeit in the steep top down to ENE mylonites GBM has been observed as a dominant mechanism over SR. For the quartz phase, the transition from GBM to SR dominant mechanism, and from SR to bulging recrystallization

Fig. 5 (facing page): Examples of microstructures in the Novate mylonites. (A) Myrmekite (My) lobes fringing a large porphyroclast of K-feldspar. The myrmekite has sharp and generally rounded boundaries against the K-feldspar. The myrmekite passes into fine-grained and recrystallized aggregates of quartz and plagioclase (mostly oligoclase) in the matrix. In the fine grained-matrix, a feldspar (σ-type) is dynamically recrystallized and shows a core and mantle structure (black arrow). Field of view is 3.5 mm. (B) K-felspar porphyropclast with margimal myrmekites (My) and incipient recrystallisation. The fine-grained matrix is made o f a polyphased aggregate of oligoclase (± albite) and quartz. Note that pure quartz layers are coarser-grained. Top right of the photograph: white mica-fish. Neoformed fine-grain phengite forms isloated layers. Field of view is 3.5 mm. (C) Plagioclase porphyroclast with a mantle of dynamically recrystallized feldspar and transected by a shear band, in a matrix of feldspar-quartz aggregates. Field of view is 3.5 mm. (D) Microfault (synthetic shear) transecting a K-feldspar. Recrystallized fine-grained felsdpar occurs along the fracture zone (arrow). Another feldspar grain is transected by antithetic micro-shears (bottom right of the photograph). Field of view is 3.5 mm (E) Pure quartz layer showing dynamic recrystallization by subgrain rotation (bottom right) into a matrix of oligoclase (± albite) + quartz. This quartz layer shows a strong shape preferred orientation, sense of shear is dextral. Neoformed and/or recrystallized biotite and phengite form isolated layers. Field of view is 3.5 mm. (F) Fold of pure quartz layer within the fine-grain matrix of oligoclase-quartz aggregates and neoformed biotite layers. These pure quartz domains are mechanically stronger than oligoclase-quartz mixtures. Field of view is 3.5 mm. (G) Primary mica-fish porphyroclast (WmI) with recrystallized/neoformed small micas (WmII) at the edges and along tails. Note the coarse-grained quartz layer as compared to the fine-grained feldspar-quartz matrix. Sense of shear shear is sinistral. Field of view is 3.5 mm. (H) Pure quartz layer that shows dynamic recrystallization by dominant grain boundary migration. Sample from steep normal shear zones with top down to the east sense of shear (right of photograph). Field of view is 3.5 mm.

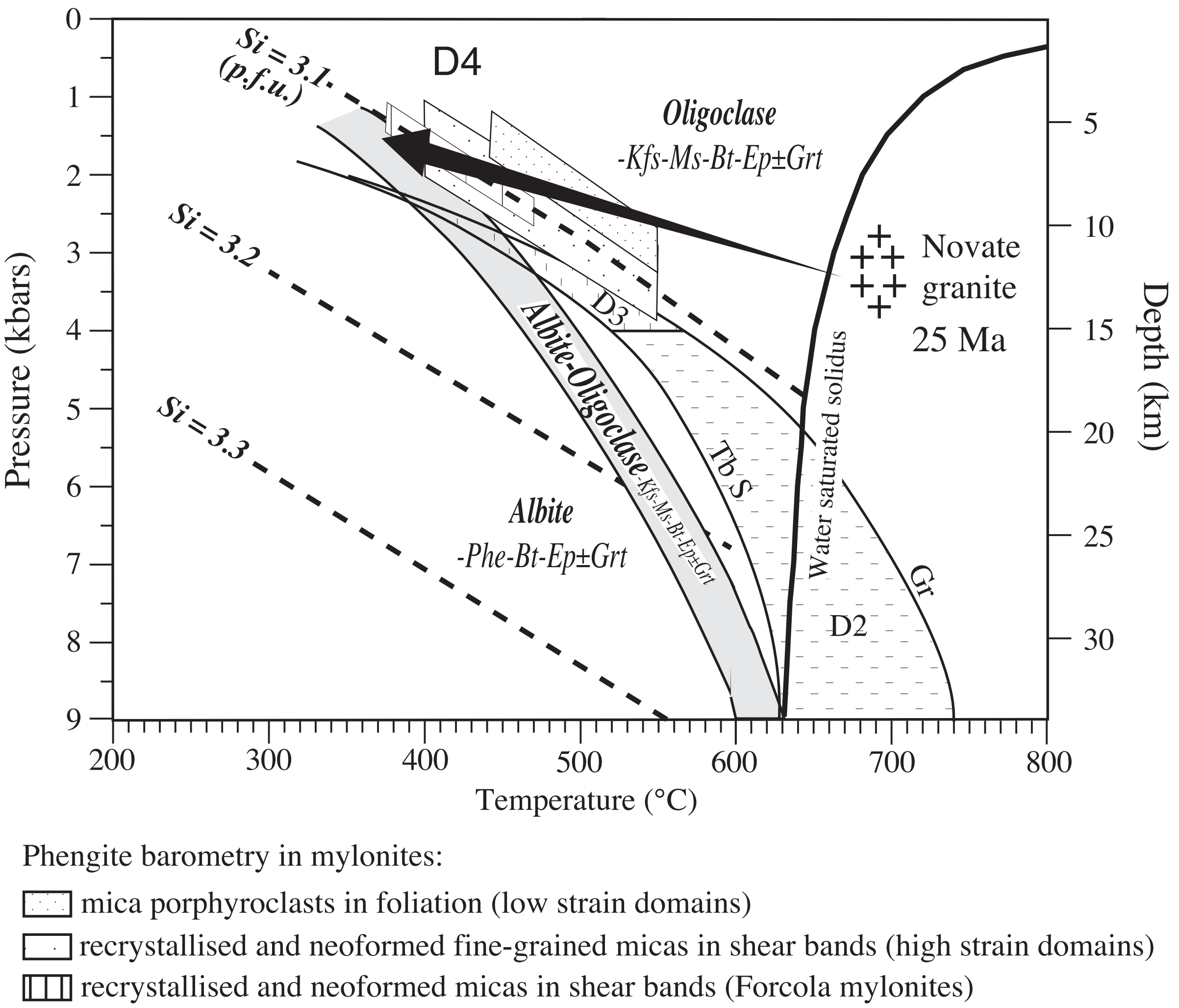

Fig. 6. P-T diagram akin to the heterogeneous deformation in the Novate granite (regional D4 deformation phase). The temperature range is discussed in the text. Phengite barometry with Si content (p.f.u.) (shaded boxes) is based on Massone and Schreyer (1987). Si content values are given for low strain domain microstructures (schistosity S oblique to shear bands C) and high strain domain microstructures (no S-C obliquity). Stability field for feldspar phase is from Maruyama et al. (1983). P-T path for the southern Tambo and Suretta nappe, and Gruf unit, is taken from Huber (1999). Field of dehydration melting of biotite-bearing assemblages from Whitney (1988).

mechanism, is documented at the amphibolite-greenschist facies transition and at ca. 400°C, respectively, for natural strain rates (see e.g. Stipp et al., 2002).

A P-T path for the Novate granite and conditions of mylonite formation is summarized on fig. 6. The microstructural observations suggest that deformation leading to mylonites in the Novate proceeded over a temperature range of Lower Amphibolite Facies conditions down to Upper and Middle Greenshist Facies conditions. The phengitic substitutions in white micas (phengite barometry, Massone and Schreyer, 1987) from the low and high strain domains (mica-fishes and fine-grained micas, respectively) have similar low Si-content of ca. 3.1, somewhat higher for the newly grown phengites (fig. 6). These values are roughly similar to the Si content in phengites from shear bands of the Forcola mylonites.

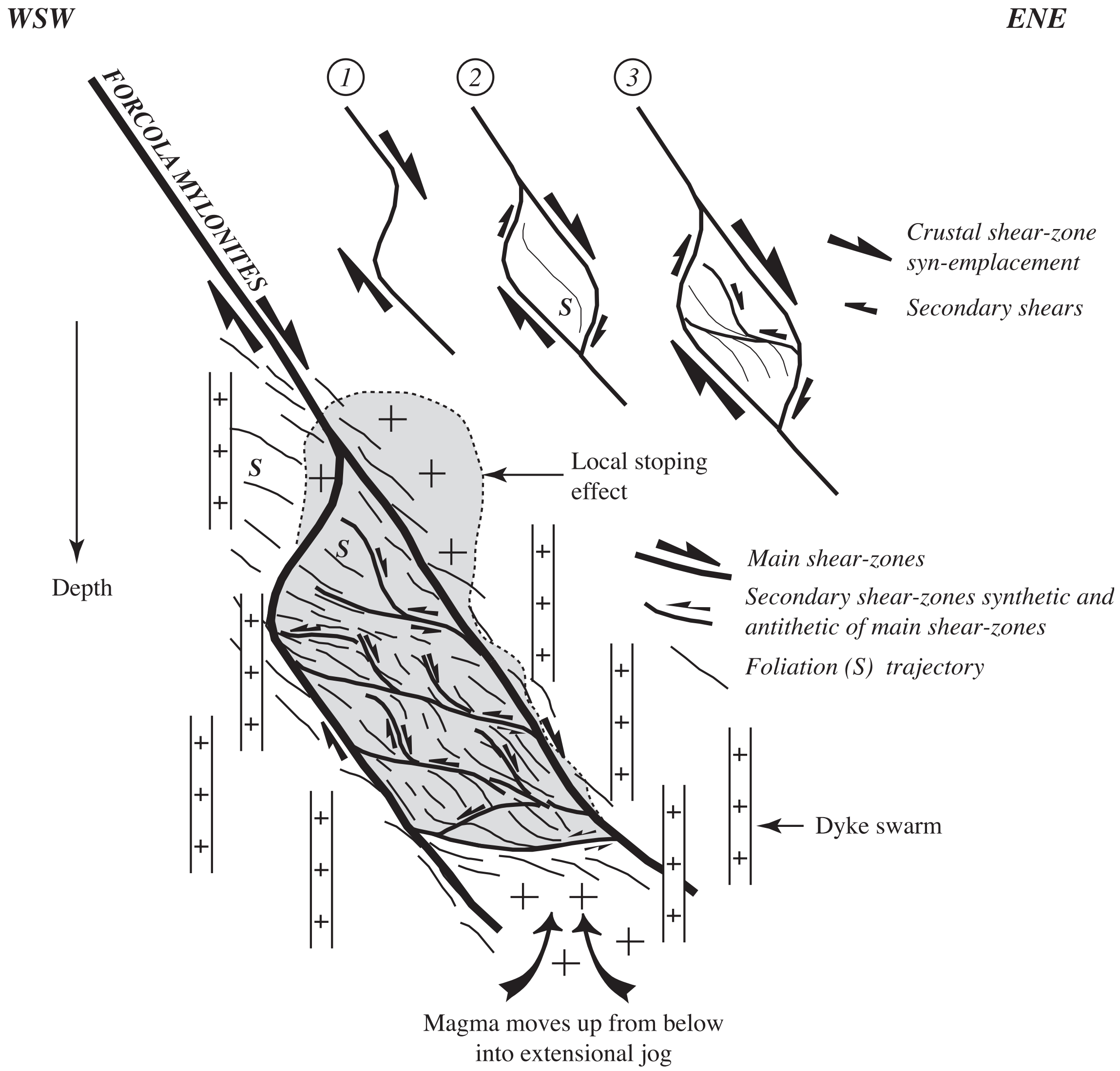

Fig. 7. Sketch model in vertical section depicting the mechanism for the upward transfer of magma and emplacement within an active extensional crustal shear zone. The magma infills passively the extensional jog from below. Solid state deformation (secondary shear zones synthetic and antithetic of main shear zones) develops progressively within the dilatant site soon after magma transfer by on-going shearing. Local minor stopping effect may modify the granite contacts as the granite spread laterally and/or upward during and after the main magma stock was passively emplaced (dashed line). The granitic dyke swarm associated with the intrusion further evidence for host rocks brittle extension during at all stages of emplacement.

6. Cooling data

Numerous thermochronological data from the Novate granite and country rocks are available in the literature (see a review in Hansmann, 1996). On this basis, the cooling history of the Novate granite and country rocks has been discussed in details (e.g. Hansmann, 1996 and references therein; Liati et al., 2000). Published cooling curves indicate that the Novate granite intruded at 24-25 Ma Ma rocks of the Southern Steep Belt that were at ca. 500°C (western tonalite), while country rocks of the Bergell pluton structurally above the Novate body already cooled down at ca. 300°C (Hansmann, 1996). In particular a sample from the Gruf unit situated structurally above the granite yields a biotite Rb-Sr age of 26.8 ± 1.5 Ma (see in Hansmann, 1996). Assuming a geothermal gradient of 30°C/Ma, these data further suggest that the Novate granite intruded within a mid-crustal P-T environment. Assuming that the blocking temperature concept is valid, initial high mean cooling rates of 140-175°C/Ma between ca. 25 Ma (U-Pb age and presumed temperature of emplacement > 640°C, solidus temperature) and 23 Ma (cooling down to 350°C, muscovite K-Ar age), and 75°C/Ma until 22 Ma (cooling down to 300°C, biotite K-Ar and Rb-Sr ages) have been proposed for one granitic sample (Hansmann, 1996 and references therein). More generally the published biotite and muscovite K-Ar and Rb-Sr ages indicate that the Novate rocks cooled down to temperature conditions of 300-350°C (lower greenschist facies) in the beginning Miocene (23-21 Ma age interval). Further cooling down across the brittle-ductile transition occurred by the Burdigalian onwards (zircon and apatite fission track ages at ca. 18-20 Ma and ca. 11-17 Ma, respectively, see fig. 2 in chapter 4).

Alternatively, ignoring the blocking temperature concept, initial cooling rates of 89°C/Ma to 68°C/Ma between ca. 24 Ma (emplacement age, zircon U-Pb) and 19 Ma (zircon fission track ages) are reported, depending on the assumed crystallization temperature (Liati et al., 2000 and references therein).

Taking the blocking temperature concept into account and a emplacement age of 25 Ma, published cooling curves indicate that the Novate granite cooled down to a temperature range corresponding to the conditions of the greenschist-amphibolite facies (ca. 500°C) at 23-24 Ma (Wagner et al., 1979; Hansmann, 1996), i..e. soon after the intrusion emplacement. Alternatively, taking a mean value of 80°C/Ma and an emplacement age of 24 Ma (average of initial cooling rates and monazite U-Pb, respectively) proposed by Liati et al., 2000), this temperature range is reached at 21-23 Ma. These radiometric data support that the shear zone pattern inside the Novate intrusion was active soon after the intrusion emplacement, when cooling down to conditions of the amphibolite-greenschist facies transition were reached. Deformation was then maintained across the brittle-ductile transition and was accommodated by faulting at ca. 19 Ma in the brittle field.

7. Discussion and conclusions

The strain within the Novate pluton is heterogeneous and distributed in vertical section at the scale of the magmatic body. The conjugated shear zone pattern indicates a non-coaxial deformation in an extensional setting strongly compatible with the kinematics of deformation along the Forcola mylonites, i.e. associated with an orogen-parallel extension. The mylonites in the Novate granite initially localized slip under conditions of the lower amphibolite facies/upper greenschist facies to middle greenschist facies conditions. These temperature conditions where reached during fast cooling of the intrusion, soon after emplacement. The last slip increments occurred when rocks pierced down through the ductile-brittle transition. The bulk strain pattern in the magmatic body frozen under progressively cooling conditions and the shape of the Novate pluton in map view at its northeastern side therefore corroborate a spatial and temporal relationship between the magmatic body and the crustal scale extensional shear zone.

A single major mylonitic zone akin to the Forcola fault was not found within the intrusion. Such a zone, if any, most probably occurs at the straight northeastern border of the intrusion, or alternatively at its western side covered by the alluvial plain. Another solution would be the splay termination sealed within the intrusion as proposed by Meyre et al. (1998). Whatever the solution, our structural and petrographic results support the likelihood of active extensional shearing during or soon after magma emplacement.

We suggest therefore that the Novate leucogranite was emplaced syn-extension at 25 Ma under mid-crustal conditions, at the southern tip of a crustal scale extensional shear zone: the Forcola mylonites. On the basis of the shear-zone pattern geometry inside the magmatic body, we propose a simple releasing bend opening emplacement model in vertical section (fig. 7). The extensional jog opened by vertical shearing along the Forcola shear zone promoted the space available for magma ascent and emplacement, upward transfer being sustained by the buoyant nature of the magma. During cooling of the granite, secondary shears within the intrusion developed in response to the extensional shearing environment. Numerous dilatational granite dykes in the vicinity of the intrusion further evidence for host rocks brittle extension during emplacement. The tectonically generated space for magma accommodation makes the Novate granite a permitted intrusion (Hutton, 1988). In such a case the structures of the host wall rocks are mainly not deflected or deformed by the intrusion itself. Since the host rocks were principally passive during the ascent and emplacement of the granite, ductile diapiric uprise in particular is not an applicable emplacement mechanism for the Novate granite. We do not exclude however that stopping effects modified the granite contact with host rocks as the granite spread laterally during and after the magma was passively emplaced. This could in particular make the bounding shear zone blind to observation. This emplacement model along an active extensional shear zone simply solves the space problem (Hutton et al., 1990).

REFERENCES

Allanic, C., Sue, C., Champagnac, J. D., Delacou, B. and Burkhard, M. (2005). New constraints on the brittle deformation in the Lepontine Alps, from paleostress and pseudotachylites analyses. European Geosciences Union 2005, Vienna, Austria, 24 - 29 April 2005.

Allmendinger, R.W., R.A. Marrett, and T. Cladouhos, FAULTKIN-program, Dep. of Geol. Sc., Snee Hall, Cornell University, Ithaca, NY, 1989.

Bell, T.H., Foliation development: the contribution, geometry and significance of progressive bulk, inhomegeneous shortening, Tectonophysics, 75, 273-296, 1981.

Berger, A., C. Rosenberg, and S.M. Schmid, Ascent, emplacement and exhumation of the Bergell pluton within the Southern Steep Belt of the Central Alps, Schweiz Miner. Petr. Mitt., 76, 357-382, 1996.

Brown, M., The generation, segregation, ascent and emplacement of granite magma: the migmatite-to-crustally-derived granite connection in thickened orogens, Earth-Science Reviews, 36, 83-130, 1994.

Brown, M., and G.S. Solar, Granite ascent and emplacement during contractional deformation in convergent orogens, Journal of Structural Geology, 20, 1365-1393, 1998.

Choukroune, P., and D. Gapais, Strain pattern in the Aar granite (Central Alps): orthogneiss developed by bulk inhomeogeneous flattening, Journal of Structural Geology, 5, 411-418, 1983.

Clemens, J.D., N. Petford, and C.K. Mawer, Ascent mechanisms of granitic magmas: causes and consequences, in Deformation-enhanced fluid transport in the Earth's crust and mantle, Mineral. Soc. Ser., vol. 8, edited by H. B., pp. 145-172, Chapman and Hall, New York, 1997.

D'Lemos, R.S., M. Brown, and R.A. Strachan, Granite magma generation, ascent and emplacement within a transpressional orogen, Journal Of The Geological Society Of London, 149, 487-490, 1992.

Fitzgerald, P.G., and H. Stünitz, Deformation of granitoïds at low metamorphic grade. Part I: reactions and grain size reduction, Tectonophysics, 221, 269-297, 1993.

Gapais, D., P. Bale, P. Choukroune, P. Cobbold, Y. Mahdjoub, and D. Marquer, Bulk kinematics from shear zone patterns: some field examples, J. Struct. Geol., 9, 635-646, 1987a.

Gapais, D., P. Bale, P. Choukroune, P. Cobbold, Y. Mahjoub, and D. Marquer, Bulk kinematics from shear zone patterns: some field examples, Journal of Structural Geology, 9, 635-646, 1987b.

Giger, M., Geochronologische und petrographische studien an Geröllen und Sedimenten der Gonfolite-Lombarda Gruppe (Südschweiz und Norditalien) und hir Vergleich mit dem alpinen Hinterland, PhD diss. thesis, 227 pp., Universität Bern, Bern, 1991.

Giger, M., and A.J. Hurford, Tertiary intrusives of the Central Alps: their Tertiary uplift, erosion, redeposition and burial in the south-alpine foreland., Eclog. Geol. Helv., 82, 857-866, 1989.

Hafner, M., Strukturgeologische und geochemische Untersuchungen von leukokraten Granit-Gängen und Migmatiten der südlichen Adula am Monte Peschiera (Italy), Diploma thesis, Basel, 1993.

Hansmann, W., Age determination on the Tertiary Masino-Bregaglia (Bergell) intrusives (Italy, Switzerland): a review, Schweiz. Mineral. Petrogr. Mitt., 76, 421-451, 1996.

Heitzmann, P., Evidence of late oligocene/early miocene backthrusting in the central alpine "root zone", Geodinamica Acta, 1, 183-192, 1987a.

Huber, R.K., Tectonometamorphic evolution of the Eastern Pennine Alps during Tertiary continental collision: Structural and petrological relationships between Suretta-, Tambo-, Chiavenna and Gruf units (Switzerland/Italy), PhD thesis, University of Neuchâtel., Neuchâtel, 1999.

Hutton, D.H.W., Granite emplacement mechanisms and tectonic controls: inferences from deformation studies, Transactions of the Royal Society of Edinburgh: Earth Sciences, 79, 245-255, 1988.

Hutton, D.H.W., T. Dempster, P.E. Brown, and S.D. Becker, A new mechanism of granite emplacement: intrusion in active extensional shear zones, Nature, 343, 452-455, 1990.

Hutton, D.H.W., and R.S. Reavy, Strike-slip tectonics and granite petrogenesis, Tectonics, 11, 960-967, 1992.

Liati, A., D. Gebauer, and M. Fanning, U-Pb SHRIMP dating of zircon from the Novate granite (Bergell, Central Alps): evidence for Oligocene-Miocene magmatism, Jurassic/Cretaceous continental rifting and opening of the Valais trough, Schweiz Miner. Petr. Mitt., 80, 305-316, 2000.

Marquer, D., Structures et cinématique des déformations alpines dans le granite de Truzzo (Nappe de Tambo: Alpes centrales suisses), Eclogae geol. Helv., 84, 107-123, 1991.

Marquer, D., N. Challandes, and T. Baudin, Shear zone patterns and strain partitioning at the scale of a Penninic nappe: the Suretta nappe (Eastern Swiss Alps). J. Struct. Geol., 18, 753-764, 1996.

Marrett, R.A., and R.W. Allmendinger, Kinematic analysis of fault-slip data, Journal of Structural Geology, 12, 973-986, 1990.

Maruyama, S., K. Susuki, and J.G. Liou, Greenschist-amphibolite transition equilibria at low pressures, J. Petr., 24, 583-604, 1983.

Massone, H.J., and W. Schreyer, Phengite geobarometry based on the limiting assemblage with K-feldspar, phologopite and quartz, Contrib. Mineral. Petrol., 96, 212-224, 1987.

Meyre, C., D. Marquer, S.M. Schmid, and L. Ciancaleoni, Syn-orogenic extension along the Forcola fault: correlation of Alpine deformations in the Tambo and Adula nappes (Eastern Pennine Alps), Eclogae Geol. Helv., 91, 409-420, 1998.

Milnes, A.G., Post-nappe folding in the western Lepontine Alps, Eclog. Geol. Helv., 67, 333-348, 1974.

Mitra, G., Ductile deformation zones in Blue Ridge basement rocks and estimation of finite strains, Bull. Geol. Soc. Am., 90, 935-951, 1979.

Oschidari, H., and U.R.F. Ziegler, Vergleichende Sm-Nd und Rb-Sr Untersuchungen an Bergeller Geröllen aus der Gonfolite Lombarda ("Südalpine Molasse") und an Bergeller und Novate-Granitoiden des Ursprungsgebietes, Eclogae. Geol. Helv., 85, 375-384, 1992.

Ramsay, J.G., and I. Allison, Structural analysis of shear zones in an Alpinised Hercynian granite (Maggia Lappen, Pennine zone, Central Alps), Schweiz Miner. Petr. Mitt., 59, 251-279, 1979.

Roman-Berdiel, T.D., D. Gapais, and J.P. Brun, Granite intrusion along strike-slip zones in experiment and nature, American Journal Of Science, 297, 651-678, 1997.

Rosenberg, C., Shear zones and magma ascent: a model based on a review on the Tertiary magmatism in the Alps, Tectonics, 23, 2004.

Sawyer, E.W., Melt segregation in the continental crust, Geology, 22, 1019-1022, 1994.

Scaillet, B., A. Pêcher, P. Rochette, and M. Champenois, The Gangotri granite (Garhwal Himalaya): Laccolithic emplacement in an extending collision belt, Journal of Geophysical Research, 100, 585-607, 1995.

Schmid, S.M., H.R. Aebli, F. Heller, and A. Zingg, The role of the Periadriatic Line in the tectonic evolution of the Alps, in Alpine Tectonics, vol. 45, edited by M.P. Coward, D. Dietrich and R.G. Park, pp. 153-171, Geological Society Special Publication, London, 1989.

Schmid, S.M., A. Berger, C. Davidson, R. Gieré, J. Hermann, P. Nievergelt, A.R. Puschnig, and C. Rosenberg, The Bergell pluton (Southern Switzerland, Northern Italy): Overview accompanying a geological-tectonic map of the intrusion and surrounding country rocks, Schweiz. Mineral. Petrogr. Mitt., 76, 329-355, 1996b.

Schmid, S.M., O.A. Pfiffner, N. Froitzheim, G. Schönborn, and E. Kissling, Geophysical-geological transect and tectonic evolution of the Swiss-Italian Alps, Tectonics, 15, 1036-1064, 1996a.

Srivastava, D., C., R.J. Lisle, and S. Vandycke, Shear zones as a new type of paleostress indicator, Journal of Structural Geology, 17, 663-676, 1995.

Stipp, M., H. Stünitz, R. Heilbronner, and S. Schmid, The eastern Tonale fault zone: a "natural" laboratory for crystal plastic deformation over a temperature range from 250°C to 700°C, Journal of Structural Geology, 24, 1861-1884, 2002.

Strong, D.F., and S.K. Hanmer, The leucogranites of southern Britanny: origin by faulting, frictional heating, fluid flux and fractional melting, Can. Miner., 19, 163-176, 1981.

Stünitz, H., and P.G. Fitzgerald, Deformation of granitoïds at low metamorphic grade. Part II: granular flow in albite-rich mylonites, Tectonophysics, 221, 299-324, 1993.

Vauchez, A., S. Pacheco Neves, and A. Tommasi, Transcurrent shear zones and magma emplacement in neoproterozoic belts of Brazil, in Granite: from segregation of melt to emplacement fabrics, edited by J.L. Bouchez, D.H.W. Hutton and W.E. Stephens, Kluwer Acad., Norwell, Mass., 1997.

Viola, G., N. Mancktelow, and D. Seward, Late Oligocene-Neogene evolution of the Europe-Adria collision: New structural and geochronological evidence from the Giudicarie Fault System (Italian Eastern Alps), Tectonics, 20, 999-1020, 2001.

von Blanckenburg, F., Combined high precision chronometry and geochemical tracing using accessory minerals applied to the Central-Alpine Bergell intrusion, Chemical Geology, 100, 19-40, 1992.

Von Blanckenburg, F., G. Früh-Green, K.H. Diethelm, and P. Stille, Nd-, Sr-, O-isotopic and chemical evidence for a two stage contamination history of mantle magma in the Central Alpine Bergell intrusion, Contrib. Mineral. Petrol., 110, 33-45, 1992.

Wagner, G.A., D.S. Miller, and E. Jäger, Fission track ages on apatite of Bergell rocks from Central Alps and Bergell boulders in Oligocene sediments, Earth and Planetary Science Letters, 45, 355-360, 1979.

Wenk, H.R., The structure of the Bergell Alps. Part III, Eclog. Geol. Helv., 66, 255-291, 1973.

Whitney, J.A., The origin of granite: the role and source of water in the evolution of granitic magmas, Geological Society of America Bulletin, 100, 1886-1897, 1988.

Yardley, B.W.D., An introduction to metamorphic petrology, Essex, 1989.

Chapter 5

Neogene kinematics of the Periadriatic Fault System and late exhumation history at the eastern border of the Lepontine (Bergell area, Eastern Central Alps): constraints from fission-track dating

LAURENT CIANCALEONI, BERNHARD FÜGENSCHUH, MEINERT RAHN, DIDIER MARQUER

Neogene kinematics of the Periadriatic Fault System and late exhumation history at the eastern border of the Lepontine (Bergell area, Eastern Central Alps): constraints from fission-track dating

LAURENT CIANCALEONI, BERNHARD FÜGENSCHUH, MEINERT RAHN, DIDIER MARQUER

ABSTRACT

The available zircon and apatite fission-track (FT) data in the eastern Lepontine of the Central Alps, including new dates, are investigated in order to decipher the late cooling and tectonic history of that part of the Alpine belt. This study provides new constraints regarding the Neogene activity of the PFS segments in the eastern Lepontine. No abrupt offset of zircon and apatite fission-track ages occurs at the Forcola, Muretto and Engadine faults, giving an upper age limit (Langhian) for significant vertical movements along these faults.

Rather the fission-track ages depict a horizontal steady gradient of decreasing cooling ages from S to N and from E to W, regardless of sampling elevation. This late cooling pattern is actually part of a cross and along-strike broader gradient associated with migration of the time of enhanced cooling and exhumation toward the external massifs and deeper levels of the Lepontine. The post-20 Ma outward growth of the orogen stage primarily led to cross and along-strike tilting, respectively, in the rear of the relatively more uplifted regions, and to the onset of exhumation due to erosion. Accordingly, the overall tilting progressively dies out in the Bergell and Briançonnais areas of the eastern Lepontine, off the external massifs thrust-formed culmination.

Fission track data in the eastern Lepontine further evidence that exhumation proceeded at moderate to high mean exhumation rates in the range of 0.50 to 1.6 km.Ma^{-1} in the early Lower Miocene over lower and steady mean exhumation rates of ca. 0.20-0.25 km.Ma^{-1} during the late Lower Miocene to beginning Upper Miocene. It is suggested that the observed decrease in mean exhumation rate at ca. 20 Ma documents a decrease in the erosional unroofing efficiency following the enhanced isostatic adjustement in response to the backthrusting event. This is supported by the onset of thrusting in the external massifs and Southern Alps by this time, when the orogen was no more in a steady state.

Locally the age gradient is discontinuous, and there may be a discrete jump of ca. 4 Ma in the apatite fission-track ages at a set of late transversal faults running across the Forcola Line, with a normal fault component downfaulting the east, as part of the broader gradient. South of this area, the FT data further suggest a rapid change in kinematics along-strike of the Tonale fault, due to oblique slip and block rotation. These tectonic features, as well as other minor to moderate fault (re-)activation in the hinterland are reasonably explained by strain accomodation and/or minor isostatic readjustement guided by the differential Neogene exhumation pattern of the Central Alps.

1. Introduction

The late-collisional tectonic and exhumation history of the Central Alps is strongly linked to the tectonic style along the Peridadriatic Fault System (PFS), a major late-alpine tectonic feature formed in response to convergence between the Apulian microplate and the European foreland (e.g. Schmid et al., 1989). Whether this pattern of exhumation was driven by tectonics or erosion requires a positive feedback between high cooling rates, chronology of movements on tectonic structures and thermal structure of the lithosphere and remains a matter of debate (Schmid et al., 1989; Grasemann and Mancktelow, 1993; Schmid et al., 1996a; Schlunegger and Willett, 1999).

Wagner et al. (1979) pointed out that the Bergell intrusives and nearby rocks in the eastern Lepontine dome of the Central Alps uplifted earlier (during the Rupelian) and more rapidly, but with a decreasing rate (from the early Miocene), than the surrounding area from which they are separated by three faults including segments of the PFS (the Insubric, Engadine and Muretto faults, fig. 1), suggesting such a positive feedback. Moreover, on the basis of mineral cooling ages from the Bergell area (see e.g. age compilation in Hunziker et al., 1992; Hansmann, 1996), a hypothetical Neogene differential exhumation may be reasonably investigated that would have occurred at the tectonic contact between the Lower and Upper Penninic nappes, namely the Forcola Line (fig. 1, Marquer, 1991). This additional segment of the PFS was already active in the late Oligocene (Ciancaleoni et al., 2004; fig. 1). Younger fault kinematics at the brittle-ductile transition and below it, which occurred near the Oligocene-Miocene boundary in the Bergell area, include: (1) dextral strike-slip along the sub-vertical Tonale Fault, i.e. the cataclastic expression of the Insubric Line, with associated down-faulting of the Central Alps relative to the Southern Alps (Fumasoli, 1974; Schmid et al., 1989), (2) differential uplift by 4 kms of the Bergell intrusion with respect to the northern Penninic units, caused by block rotation along the sinistral Engadine Line (Schmid and Froitzheim, 1993), (3) orogen-parallel extension along the Forcola normal fault, which relatively displaced rocks by at least some 3 kms of crustal thickness (Meyre et al., 1998) and along the Muretto Fault (e.g. Ring, 1994).

The upper age limit of the termination of brittle (-ductile) vertical motions on Periadriatic faults in the Bergell area is inaccurately known. But according to the break in slope from previously published exhumation rates in the whole Central Alps (e.g. Hurford et al., 1989), on-going distributed vertical motions in the eastern Lepontine seems to provide only limited exhumation driven by tectonics during the Neogene.

In this paper we address the regional scale pattern of fission-track dates and the low-temperature exhumation history of fault-bounded blocks in the eastern Lepontine. We present new zircon and apatite fission-track ages from samples collected along several cross-sections perpendicular to the main discontinuities. We also provide a new synthesis of fission-track data available in the Bergell and Insubric areas of the Eastern Central Alps, including previously unpublished fission-track ages. Our aim is to re-examine the Neogene kinematics of the Periadriactic Faults in the light of fission-track thermochronology, and to better constrain the duration of fault displacement on these main tectonic features of the Bergell area. In a final step, the results are discussed regarding the exhumation pattern and the large-scale tectonic evolution of the Central Alps during the Neogene.

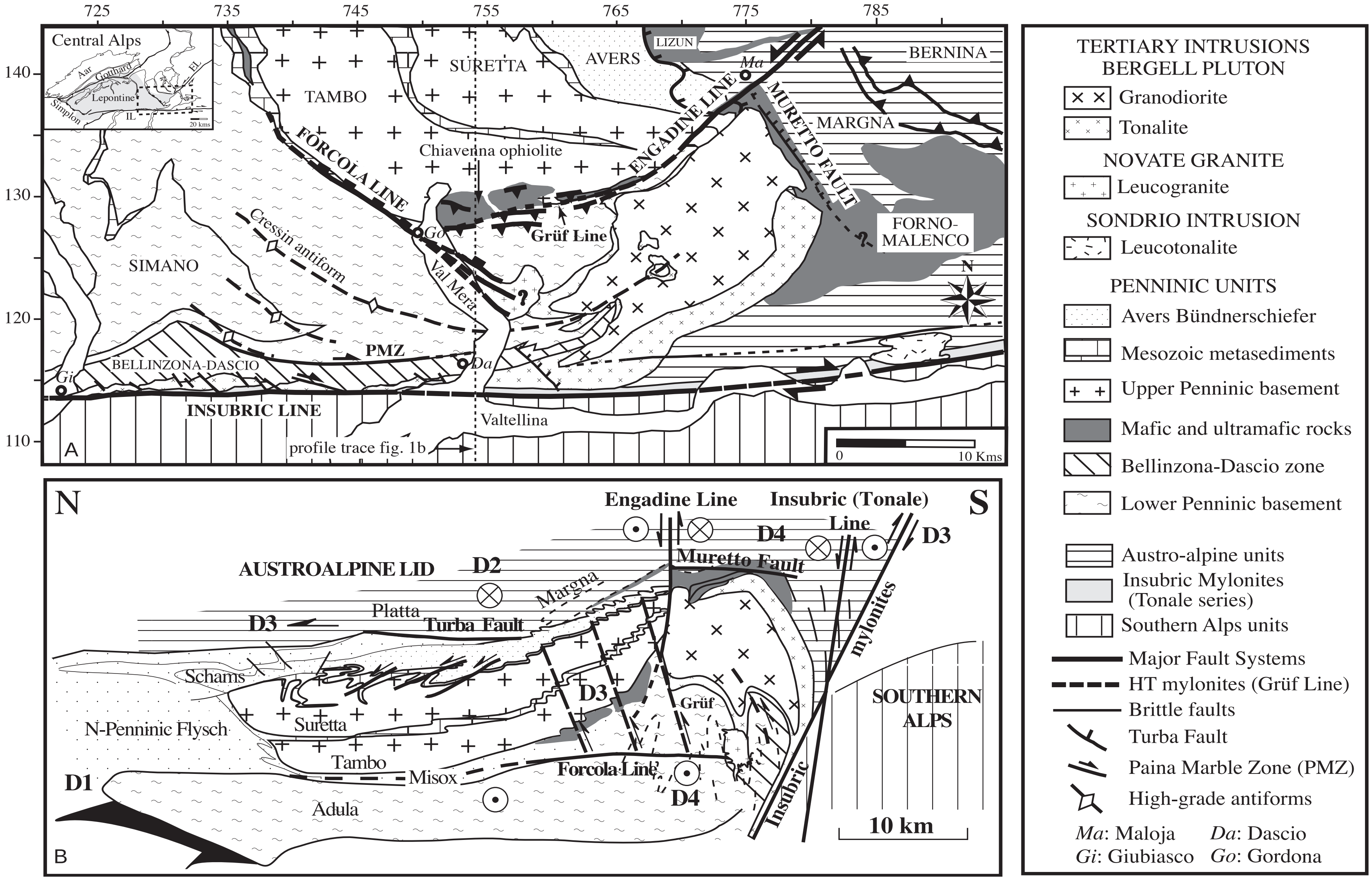

Fig. 1. (A) Geologic and tectonic setting of the Bergell and Insubric areas in the Eastern Central Alps. Question marks when the lateral prolongation of faults is uncertain. Modified from Rosenberg et al., 1995, Huber and Marquer, 1996 and Meyre et al.,1998. (B) N-S geological profile along the Eastern Traverse. Modified from Schmid et al., 1996 and Huber and Marquer, 1996. Regional deformation phases (D1-D4) are discussed in the text.

2. Geological and tectonic setting

The Bergell area and the Southern Steep Belt (SSB; Milnes, 1974) respectively confine the eastern and southern extent of the high-grade Tertiary Lepontine Dome (Niggli, 1970). As a first approximation and in longitudinal section, the dome has a mirror symmetry: the west-dipping foliations in the Simplon Alps become flat-lying in the central part, while the upper Penninic nappe sequence is tilted by 25° to the east on average in the Bergell region (fig. 1a, Merle et al., 1989). A extensive description of the whole nappe edifice in the Bergell region, from the lower Penninic to the Upper Austroalpine units and the Southern Alps, is given in Schmid et al. (1996b). In this section we summarize the main structural evolution of the Bergell area during the Oligo-Miocene. The stacking of the Adula, Tambo and Suretta nappes results from early Tertiary convergent tectonics, when the thinned continental Briançonnais crust (Tambo and Suretta) and the south European margin (Adula) successively subducted underneath the Austroalpine-Apulian plate (orogenic lid). By the end of the Eocene rapid exhumation following subduction (leading to eclogite facies in Adula) established the entire nappe pile, which reached peak metamorphic conditions (upper greenschist to upper amphibolite facies, from top to bottom of the Briançonnais nappe edifice) by that time (D1, fig. 1b; Meyre et al., 1998 and references therein). During the late Eocene-early Oligocene on-going N-S compression in the deeper nappes was accompanied by crustal thinning with a stretch parallel to the Alpine chain (and locally associated with detachment faulting e.g. Turba Mylonite Zone, Nievergelt et al., 1996) in the upper parts of the nappe pile (D2, fig. 1b).

The post-nappe refolding and deformation history in the Bergell region (D3 and D4, fig. 1b) is closely related to the well constrained timing of three of the Periadriatic intrusions: the Bergell tonalite and granodiorite (32 and 30 Ma; von Blanckenburg, 1992), the Sondrio tonalite (Bi K-Ar cooling ages of 30-32 Ma; Giger, 1991) and the Novate leucogranite (24 Ma; Liati et al., 2000) (fig.1). At present, the most plausible cause for this magmatic episode may be hot asthenospheric counterflow after delamination of subducted lithosphere (von Blanckenburg and Davies, 1995; Gebauer, 1999). The Novate granite is a garnet bearing S-type leucogranite, not related to the calk-alkaline Bergell suite but derived from partial melting of crustal material during late-Alpine decompression. The Bergell pluton roots in the SSB and the adjacent Insubric Line, both steep pre-Alpine structures which represent the feeder zone of the Bergell composite body (Rosenberg et al., 1995). Late continental collision under retrograde conditions promoted the strong differential and very rapid uplift of the Bergell area (D3) during the dextral backthrusting and backfolding of the Central Alps over the Southern Alps by up to ca. 20 kms relative vertical displacement along the Insubric mylonites (Insubric phase of Argand, 1916; Schmid et al., 1989; Rosenberg et al., 1995). This exhumation event at a rate of 5 mm/year (Giger and Hurford, 1989) long lived between 32 and 25 Ma

(Oberli et al., 1996; Gebauer, 1996), and was associated with local conjugated sets of brittle-ductile south dipping steep pro-thrusts (fig. 1; Huber and Marquer, 1996).

Differential exhumation of the Bergell intrusion and adjacent units is also accommodated north of the pluton by the Engadine and Grüf Lines (Schmid and Froitzheim, 1993; Berger et al., 1996). The Grüf Line, at the contact between the Adula-Grüf nappe and the Chiavenna ophiolite, is a high-temperature vertical mylonite zone kinematically highering the Adula-Grüf unit, that has been tentatively proposed to be the deep-seated and westernmost equivalent of the brittle Engadine Line. A brittle-ductile transition represented by greenschist facies sinistral mylonites indeed occurs into the lower Val Bregaglia area (Wenk, 1984; Ruzicka, 1997; Huber, 1999) that explains why no continuation of the line in terms of a brittle fault zone can be traced further west. The Engadine Line forms a major NE-SW trending steeply dipping discontinuity affecting the Penninic and Austroalpine nappe stack (fig. 1). It is generally considered as a major sinistral strike-slip fault tentatively active from the late Oligocene to the Oligocene-Miocene boundary, with lateral displacement varying between 3-6 km in the upper Engadine and up to 20 km in the lower Engadine (Trümpy, 1977), and with associated differential throw along-strike highering the Bergell block (Schmid and Froitzheim, 1993). The cataclastic sinistral Engadine Line post-dates both the cooling of the intrusion and its contact aureole (Liniger, 1992; Schmid and Froitzheim, 1993) and ductile structures of the Engadine Line in the brittle-ductile transition area (Ruzicka, 1997). Consequently to this early tectonic evolution, the Bergell pluton was tilted by some 11°E (Rosenberg and Heller, 1997) and an E-W profile across the Bergell pluton exposes 10 kms vertical depth (fig. 1). The country rocks in the structurally deeper western contact area experienced regional high-grade (upper amphibolite to granulite facies) metamorphism at the time of intrusion while along the structurally higher eastern contact country rocks were only at greenschist facies conditions and underwent contact metamorphism. The Permo-Mesozoic cover of the Southern Alps basement was almost unaffected by Tertiary metamorphism, except for the area immediately south of the Insubric Line which was reheated by the hot northern block during the backthrusting event (Hunziker et al., 1997).

South of the Bergell pluton and further east, vertical offset is progressively totally replaced by sub-horizontal dextral strike-slip (Wiedenbeck, 1986; Heitzmann, 1987a; Schmid et al., 1989; Werling, 1992; Meier, 2003) within the 1 km wide greenschist facies mylonite belt (Tonale series) along the southern border of the SSB, that accommodated dextral offset of reasonably 30 to 60 kms over the ductile and brittle displacement (Viola, 2000). The youngest dated event is a cataclastic overprint associated with dextral strike-slip and pseudotachylyte formation on the Tonale master fault (D4, fig. 1b; Fumasoli, 1974; Schmid et al., 1989; Werling, 1992) at 20.6 Ma and 16.4 Ma east and west of the Bergell area, respectively (Müller et al., 2001). In the Bergell region, this shearing event is linked to a major transtensive stress field north of the Tonale fault that kinematically allowed an orogen-parallel stretch (Ciancaleoni et al., 2004), accounting for the previously recognized S-side-up movement along the N-dipping Tonale fault (Fumasoli, 1974) and presumably before sinistral transpression along the Giudicarie Line at ca. 17 Ma (Schönborn, 1992; Viola, 2000).

The Forcola Line located at the top of the Adula nappe (Marquer, 1991) is a major high-angle NE dipping and north-easterly displacing extensional mylonite zone, which accommodates orogen-parallel extension near the eastern border of the Lepontine under greenschist facies to brittle conditions (D4, fig. 1; Meyre et al., 1998). This normal fault is responsible for the disappearance of the Mesozoic sediments of the Misox zone, the suture between the European margin and the Briançonnais domain (Valais trough), leading to a direct contact between the Adula and Tambo nappes towards the south (fig.1). It then reaches the Val Mera, where it is covered by Quaternary alluvial deposits (fig. 1), and splays further south inside the Novate granite which is emplaced syn-kinematically at the southernmost tip of the fault (Ciancaleoni and Marquer, 2004). While an upper age limit of ca. 25 Ma for the onset of faulting is proposed, the fault activity is still only tentatively estimated both in duration and magnitude of vertical displacement terms. According to Meyre et al. (1998), the Forcola fault is responsible pro parte for the dome-like structure in the SE Lepontine zone and might be a good candidate to be an equivalent fault to the Simplon fault (Mancktelow, 1992) in the western Central Alps. However, in map view, the Forcola fault clearly cuts across the Lepontine metamorphic dome at its southernmost termination, and thus doesn't strictly confine the eastern Lepontine dome.

This border is rather found at the Muretto fault (Riklin, 1978; Peretti, 1985; Ring, 1994) that runs parallel to the eastern border of the Bergell intrusion and accommodated normal and dextral oblique-normal faulting associated with minor relative uplift (a few hundred meters) of the western block (D4, fig. 1). Spillmann (1993) proposed that a 10° sinistral rotation along an axis perpendicular to the fault plane leads to a differential vertical motion of 400 m between the northern and southern segments of the fault. Although a discrete main fault plane may be identified in places, intense subsidiary fracturation at the northeastern tip of the Bergell pluton associated with a non-systematic succession of normal, oblique-normal and dextral slip rather characterizes a complex fault zone (Ciancaleoni et al., 2004). The intense hydrothermal alteration of host rocks (Peretti, 1983) pin down the evidence for intensive fluid low and enhanced fluid assisted fracturation soon after the intrusion of the granodiorite and before its solidification. This fault zone post-dates the intrusion and flexuration of the country rocks related to ballooning (Berger and Gieré, 1995; Puschnig, 1996).

In the Tertiary intrusives, a detailed investigation of the brittle tectonics (D4) led to the recognition of a pervasive network of regional faults, ranging from about 400 m to tens of kilometers in length (see insert structural map in fig. 3; Ciancaleoni et al., 2004) with supposed associated throw of ten to hundred of meters. The kinematics of fault families combines generally early normal and oblique-normal faulting mostly pre-dating compressional strike-slip reactivation.

3. Fission-track thermochronology

3.1. Methods

Fission-track dating of zircon and apatite is a powerful tool to constrain the low-temperature thermal history of rocks. Fission-tracks are damage zones in a crystal that are formed by spontaneous fission of 238U (e.g. Wagner, 1968). A fission track age is determined by measuring the density of spontaneous fission tracks and the U concentration of the sample (e.g. Naeser, 1979). Over geological time the annealing rate of fission tracks at surface temperature is very slow but fission tracks anneal with increasing temperature (Naeser and Faul, 1969). Consequently tracks are essentially unstable and undergo significant annealing in a transition zone called the partial annealing zone (PAZ, e.g. Gleadow and Fitzgerald, 1987). For most apatites (fluorapatite) annealing occurs over a temperature range of ca. 60°-120°C (Green et al., 1989) which represents the upper and lower limit of the PAZ, respectively. For zircons annealing temperatures are less constrained and may range from 370 to 190°C according to the annealing model used (Yamada and Tagami, 1995; Tagami et al., 1996; Tagami and Shimada, 1996), but current estimates are ca. 240 ± 60°C (Yamada and Tagami, 1995). Central fission-track ages (i.e. the mean value of the distribution of single grain ages, weighted by the error on each age) have no simple geological meaning and record a complex history of thermal events. For example, when the cooling is rapid, the apatite and zircon fission-track ages (AFT and ZFT, respectively) are interpreted as the approximate time at which the sample cooled down to temperatures of 90°C and 240°C respectively (mean effective "closure" temperature, Dodson, 1973). In cases of episodic or continuous exhumation the pattern of AFT and ZFT ages from elevation profiles documents the preservation of a fossil PAZ or the rate at which exhumation proceeded, respectively (e.g. Wagner et al., 1977; Gleadow and Fitzgerald, 1987). Thus the slope of an age-elevation profile can potentially provide an estimate of the magnitude and timing of exhumation events, provided cooling was fast and continuous. Further information regarding the rate and timing of cooling can be obtained from confined track length distribution in apatites (e.g. Gleadow and Fitzgerald, 1987; Green et al., 1989).

We sampled two sections across the northern and southern part of the Forcola and Muretto faults and one section across the Tonale fault. Sampling to the east of the Muretto was hindered by the lack of suitable material: apatites from meta-arkoses and gneisses from the Margna nappe and South

Sample name	Rock Type	Tectonic Unit	X coordinate	Y coordinate	Elevation (m)	Mineral	Counted Grains	ρ_d x 10^4 (t/cm^2)	ρ_s x 10^4 (t/cm^2)	ρ_I x 10^4 (t/cm^2)	U (ppm)	P(χ^2)	**Central Age (Ma ±1 σ)**	Age dispersion (% var)	MTL (µm) (± 1 SE)	Standard Deviation (µm)
FORC6	Bt Gneiss	Adula nappe	750.525	122.850	390	zircon	20	33.45 (3749)	297.4 (1779)	534.9 (3200)	639.6	0	**15.9 ± 1.0**	24.83		
FORC7	Migmatitic gneiss	Adula nappe	750.400	122.575	530	zircon	20	33.39 (3749)	244.4 (1704)	419.0 (2921)	501.9	0	**16.9 ± 1.1**	24.82		
FORC8	Migmatitic gneiss	Adula nappe	752.575	125.025	220	zircon	3	33.32 (3749)	239.2 (371)	306.9 (476)	368.4	3	**22.6 ± 2.4**	13.65		
FORC9	Migmatitic gneiss	Adula nappe	746.975	126.700	810	zircon	20	33.25 (3749)	214.3 (1577)	517.4 (3807)	622.4	0	**11.9 ± 0.6**	16.85		
FORC10a	Orthogneiss	Adula nappe	747.450	127.225	800	zircon	9	32.32 (3749)	375.9 (841)	571.2 (1278)	706.9	54	**18.0 ± 0.9**	3.28		
FORC10b	Orthogneiss	Adula nappe	747.450	127.225	800	zircon	9	33.19 (3749)	260.5 (619)	425.0 (1010)	512.3	0	**17.4 ± 1.8**	25.81		
FORC 11	Orthogneiss	Adula nappe	747.850	127.875	740	zircon	20	33.12 (3749)	284.6 (1670)	403.7 (2369)	487.6	0	**19.9 ± 1.2**	21.69		
						apatite	*26*	*83.72 (7701)*	*9.269 (295)*	*138.3 (4402)*	*20.7*	*4.1*	***10.5 ± 0.8***	*18.57*	*12.22 ± 0.54 (13) (L.C.)*	*1.95*
															12.72 ± 0.58 (9) (M.R.)	*1.74*
FORC12	Orthogneiss	Tambo nappe	748.850	130.740	790	zircon	21	33.05 (3749)	313.1 (1433)	478.6 (2191)	579.3	0	**18.7 ± 1.0**	18.03		
						apatite	*26*	*80.96 (7701)*	*14.32 (483)*	*173.9 (5866)*	*26.8*	*0.5*	***12.3 ± 0.8***	*22*	*9.46 ± 0.65 (19)*	*2.85*
FORC13	Truzzo granite	Tambo nappe	747.525	129.975	830	*apatite*	*26*	*147.6 (4852)*	*7.517 (268)*	*188.6 (6725)*	*16*	*15.9*	***10.9 ± 0.8***	*11.68*	*12.25 ± 0.51 (21) (L.C.)*	*2.35*
															13.34 ± 0.57 (8) (M.R.)	*1.62*
MU1	Gneiss	Margna nappe	778.800	132.700	2040	zircon	8	32.92 (3749)	246.1 (601)	483.9 (1182)	588	1.2	**14.8 ± 1.2**	15.73		
MU2	Gneiss	Margna nappe	779.000	132.750	2095	zircon	25	32.86 (3749)	128.0 (1220)	216.8 (2066)	263.9	0	**16.7 ± 1.2**	28.11		
						apatite	*13*	*141.5 (4852)*	*1.121 (15)*	*9.941 (133)*	*0.9*	*99.9*	***29.4 ± 8***	*0*	*density loo low*	
MU3	Meta-arkoses	Muretto series	778.725	132.550	2000	zircon	25	32.79 (3749)	291.2 (1837)	268.5 (1694)	327.6	1	**30.1 ± 1.4**	14.6		
						apatite	*9*	*138.5 (4852)*	*0.7059 (9)*	*5.334 (68)*	*0.5*	*100*	***33.7 ± 12***	*0*	*density loo low*	
MU5	Bt-Ms gneiss	Margna nappe	778.450	132.100	2020	zircon	25	32.72 (3749)	291.7 (2848)	340.8 (3328)	416.7	4.1	**23.8 ± 0.8**	8.73		
						apatite	*26*	*135.5 (4852)*	*4.484 (164)*	*108.2 (3958)*	*10*	*0.2*	***10.7 ± 1.2***	*36.48*	*12.14 ± 0.62 (16)*	*2.47*
MU6	Bt-Ms gneiss	Margna nappe	778.450	132.100	2020	zircon	18	32.66 (3749)	132.4 (909)	263.7 (1810)	323	0	**14.3 ± 1.1**	25.44		
						apatite	*16*	*132.5 (4852)*	*0.8309 (17)*	*22.73 (465)*	*2.1*	*99.8*	***8.9 ± 2.2 (7.7 ± 1.6)***	*0*	*density loo low*	
MU7	Bergell granodiorite	Bergell intrusion	774.825	136.900	1995	zircon	21	32.59 (3749)	404.5 (1876)	504.1 (2338)	618.7	0	**23.1 ± 1.4**	23.11		
						apatite	*25*	*129.5 (4852)*	*12.92 (359)*	*270.2 (7509)*	*26.1*	*31.8*	***11.4 ± 0.7***	*7.45*	*11.42 ± 0.37 (40) (L.C.)*	*2.33*
															12.9 ± 0.24 (22) (M.R.)	*1.14*
MU10	Meta-arkoses	Muretto series	775.350	137.950	2030	zircon	7	32.52 (3749)	248.7 (234)	367.8 (346)	452.3	4.9	**18.9 ± 2.2**	20.63		
						apatite	*10*	*126.4 (4852)*	*1.813 (12)*	*5.529 (366)*	*5.5*	*7.6*	***8.5 ± 2.7 (8.3 ± 1.8)***	*28.64*	*density loo low*	
ME1	Bt-Ms gneiss	Southern Alps	765.000	113.575	710	zircon	21	32.39 (3749)	350.9 (1437)	374.8 (1535)	462.9	0.1	**26.0 ± 1.5**	19.16		
						apatite	*24*	*105.9 (7701)*	*4.966 (100)*	*166.3 (3349)*	*19.6*	*7.8*	***6.0 ± 0.7***	*20.01*	*12.92 ± 0.54 (20)*	*2.44*
ME4	Bt Gneiss	Campo-Languard nappe	764.875	114.475	965	*apatite*	*21*	*103.1 (7701)*	*12.34 (288)*	*259.2 (6048)*	*31.4*	*0*	***9.9 ± 1.1***	*41.48*	*12.10 ± 0.32 (35)*	*1.87*

Table 1. Apatite and zircon fission track data. Sample localities are given in Swiss coordinates and are located in fig. 2. All samples have been treated using the external detector method. Number of grains counted is given in column 8. ρd, track density in muscovite detector covering; reported value determined from interpolation of values for detector covering standards at the top and bottom of reactor packages (fluent gradient correction); rs, spontaneous track density; ρi, induced track density; number in parenthesis is the number of tracks counted for ages and fluence calibration or the number of tracks measured for length. All track length measurements have been performed by analyst L.C., unless indicated. P(χ2), chi-squared probability (Galbraith, 1981). P(χ2) is probability for obtaining χ2 value for v degrees of freedom, where v = no. crystals - 1. All ages quoted are central ages (Galbraith and Laslett, 1993), with standard error (SE). Due to low-uranium content, ages in parenthesis for samples MU6 and MU10 have been calculated considering all apatite single grains as one unique apatite grain, for comparison of results ("population method-like" procedure). Apatite ages were calculated with a zeta value of 369 ± 6.12 for dosimeter glass CN5. Zircon ages were calculated with a zeta value of 170 ± 14.53 for dosimeter glass CN1.

Penninic units were so low in uranium (ca. 0.5-2 ppm) that there were insufficient tracks for meaningful age and track lengths statistics (cf. Table 1). Some unrealistic apatite ages or apatite ages with high error margins (e.g. apatite age older than zircon age from the same sample) indicated in Table 1 reflect these practical difficulties and are discussed in paragraph 3.2.2. Apatite and zircon grains were extracted using standard techniques (see e.g. Seward, 1989 for details) and treated with the external detector method (Hurford and Green, 1983). Apatite and zircon ages were determined using the zeta calibration method (Hurford and Green, 1983) with a zeta value of 369 ± 6.12 for dosimeter glass CN5 and a zeta value of 170 ± 14.53 for dosimeter glass CN1, respectively. Fission tracks were counted and track lengths measured on a Zeiss microscope, using a magnification of 1250 under dry objectives for apatites and 1600 with oil immersion for zircons. Ages are quoted as central ages (Galbraith and Laslett, 1993) with standard error at level 1. Whenever possible, 20 or more crystals of each sample were counted for the age determination, but some samples with insufficient apatite or zircons allowed only for no more than 10 grains to be counted (see Table 1). Finally all the results of fission-track age determinations and track length measurements are presented in Table 1, fig. 2 and fig. 3.

3.2. New fission-track ages: results and interpretation of single-grain age distribution

3.2.1. Zircon fission-track ages (ZFT)

In the Forcola area ZFT ages range from 15.9 to 19.9 Ma (numbers 1 to 8 in fig. 3) and document cooling down to below 300°C in the early Miocene, except for sample FORC9 which is significantly younger with a central age of 11.9 ± 0.6 Ma (Table 1 and fig. 3). Only 3 individual zircons grains could be dated in sample FORC8, which the age of 22.6 ± 2.4 Ma is thus very poorly constrained and given here only for comparison of single-grain age distribution with other samples, and no weight will be given to that sample in the further discussion. All but one sample fail the chi-squared test ($P(\chi2) < 5\%$) and show relatively high dispersion (> 10%), a priori suggesting that the grains represent more than one age population (Table 1). Accordingly the common scatter of individual grain ages outside the $\pm 2\sigma$ range around the central age for most samples reflects the $\chi2$ statistics (fig. 3). Both samples from the footwall and the hangingwall of the Forcola fault are characterized by a broad and very similar spread of single-grain ages and large relative error, distributed over ca. 20 Ma time span (fig. 3). Final cooling to below 200°C in the early Upper Miocene is remarkably well defined for most samples. Although there is no internal control on ZFT ages by means of track-length measurements, all these elements better suggest a relative prolonged residence time in the annealing temperature range or in other words a relative slow exhumation event. The resulting apparent ages neither date the time when the samples entered the ZPAZ nor the time when they final-

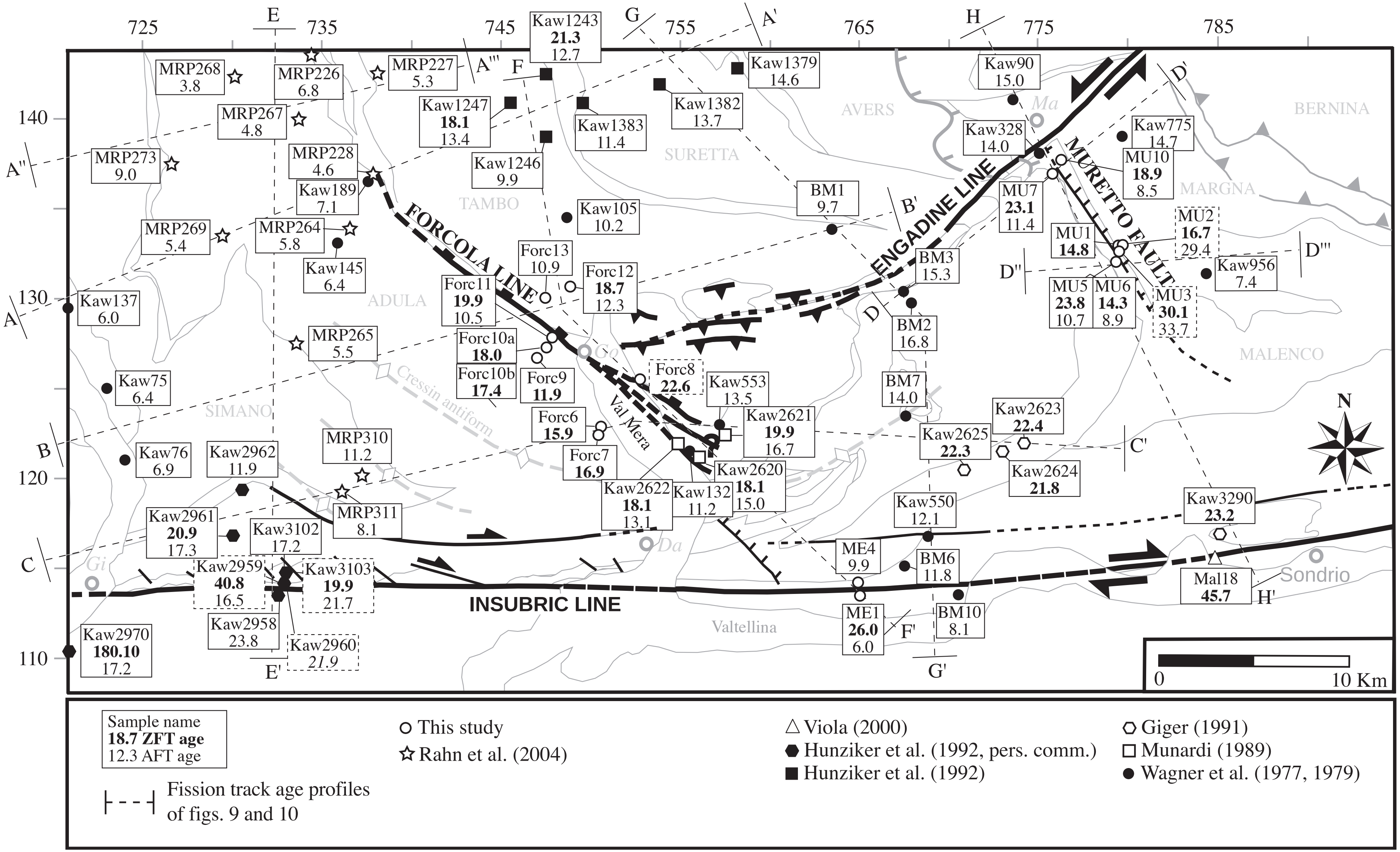

Fig. 2. Structural sketch map with the sample localities, AFT and ZFT central ages. See key at bottom of the figure for explanation of the symbols. Dashed age boxes when corresponding apatite and/or zircon ages are doubtful (see text for discussion). Profile traces refer to figures 9 and 10. Other indications are the same as in figure 1.

ly cooled down below the upper limit of the ZPAZ, but must be interpreted as "mixed" ages not recording a specific cooling event.

Again sample FORC9 departs from this scenario since it entered later in the lower limit of the ZPAZ and remained in there only ca. 10 Ma, assuming that oldest and youngest individual zircon grains date the cooling through both ends of the ZPAZ. Although spatially closed to other samples with a more common single grain age distribution, this sample's central age is similar to ZFT ages encountered regionally further west within the Central Lepontine (see e.g. Hunziker et al., 1992). This might suggest that FORC9 shares a cooling and uplift history similar to the one of deeper nappes in the Lepontine, and that an abrupt transition occurs to the west Bergell area late cooling characteristics. Alternatively the accumulation of relative young single-grain ages in FORC9 is possibly due to late (but pre-Middle Miocene) local heat input (T>200°C), e.g. warm fluid circulations or magmatic events (proximity of dykes not necessarily exposed at the surface). Local effects from unknown intrusions could be possible, considering that numerous ca. 25 Ma old dykes and pegmatites in the SSB (and further north in the Gordona-Chiavenna area, Schmid et al., 1996b) were interpreted to reflect a late thermal pulse akin to considerable fluid and magmatic activity after formation of the SSB in relation to the Novate granite and other virtual granites of the same type not presently outcropping (Gebauer, 1996; Liati et al., 2000). Due to the lack of strong field evidences of major faulting between that sample and other close samples from the Forcola footwall, we prefer at this stage the second alternative.

In the Muretto and Insubric areas (numbers 11 to 16 and 10-11 in fig. 3, respectively), the central ages show more variations and cooling down to below ca. 300°C between 14.3 and 30.1 Ma (Table 1 and fig. 3). All samples fail the chi-squared test ($P(\chi 2) < 5\%$) and show relatively high dispersion (> 10%), again suggesting that the grains represent more than one age population (Table 1). The distribution of single-grain ages is characterized by 3 components (fig. 3): (1) the non-systematic and sparse preservation of partially annealed pre-Oligocene single-grain ages (open circles in radial plots) in some samples from the Bergell country rocks (Margna nappe and Muretto series) and from the South Alpine unit (e.g. samples MU3 and ME1); (2) the starting of the ZFT clock or a scattering of some individual ZFT ages around 28-32 Ma in other samples (grey circles in radial plots) i.e. during the pluton emplacement (indicated by crosses) and extrusion (e.g. samples MU7 and MU5, or MU3 respectively); (3) further cooling over ca. 10 to 20 Ma time interval in the ZPAZ (black circles) before final cooling below 200°C in the middle Miocene. When the single-grain age distribution is bimodal (components 1 and 2 or 3), e.g. those samples which recorded old (pre-intrusion) grains, the resulting ZFT age must be interpreted as a "mixed" age, somewhat older than regionally expected (samples MU3 and ME1. fig. 3). Conversely, those samples with only apparent component

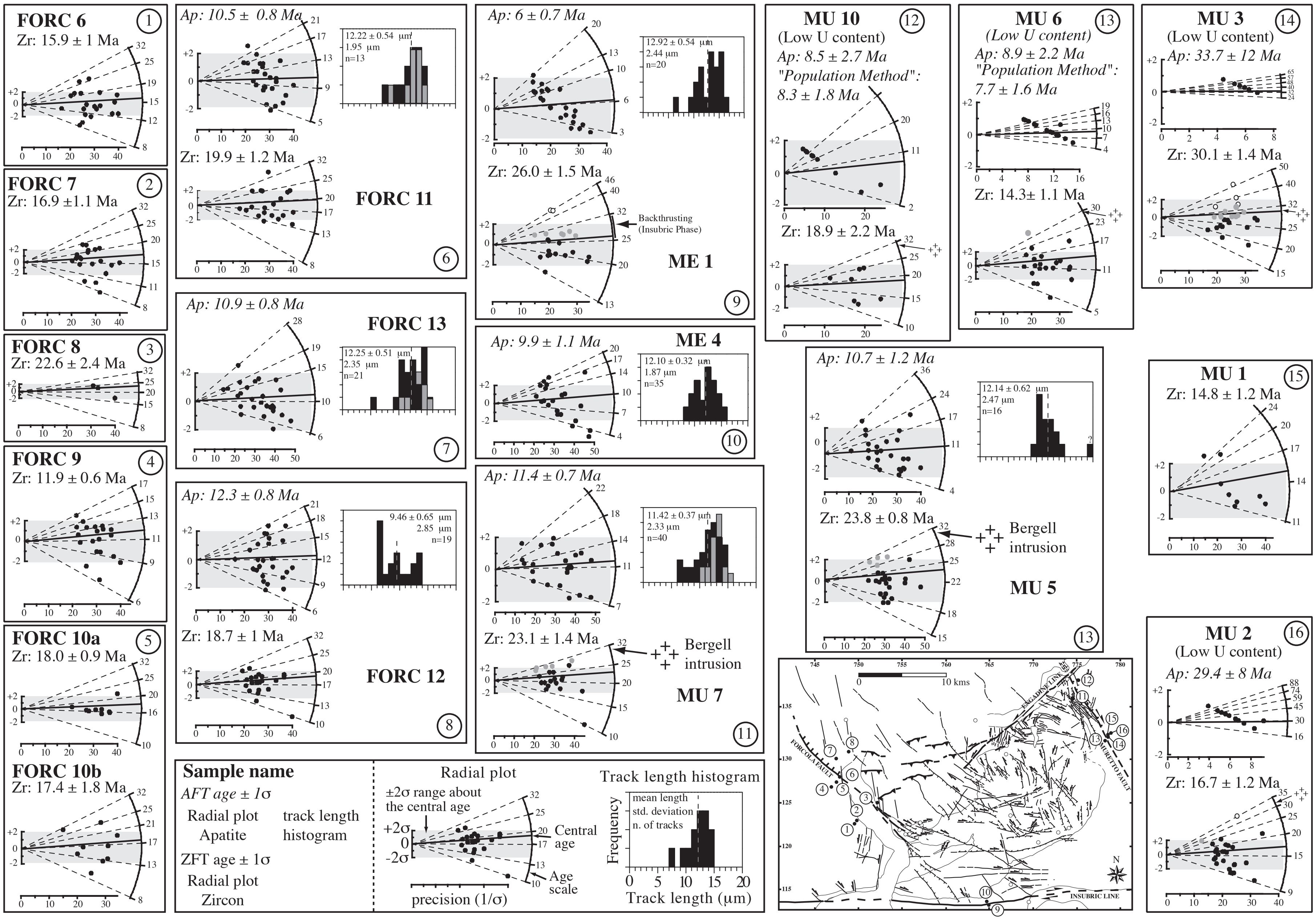
FORC 6
Zr: 15.9 ± 1 Ma
FORC 7
Zr: 16.9 ±1.1 Ma
FORC 8
Zr: 22.6 ± 2.4 Ma
FORC 9
Zr: 11.9 ± 0.6 Ma
FORC 10a
Zr: 18.0 ± 0.9 Ma
FORC 10b
Zr: 17.4 ± 1.8 Ma
FORC 11
Ap: 10.5 ± 0.8 Ma
Zr: 19.9 ± 1.2 Ma
12.22 ± 0.54 µm
1.95 µm
n=13
FORC 13
Ap: 10.9 ± 0.8 Ma
12.25 ± 0.51 µm
2.35 µm
n=21
FORC 12
Ap: 12.3 ± 0.8 Ma
Zr: 18.7 ± 1 Ma
9.46 ± 0.65 µm
2.85 µm
n=19
ME 1
Ap: 6 ± 0.7 Ma
Zr: 26.0 ± 1.5 Ma
12.92 ± 0.54 µm
2.44 µm
n=20
Backthrusting
(Insubric Phase)
ME 4
Ap: 9.9 ± 1.1 Ma
12.10 ± 0.32 µm
1.87 µm
n=35
MU 7
Ap: 11.4 ± 0.7 Ma
Zr: 23.1 ± 1.4 Ma
11.42 ± 0.37 µm
2.33 µm
n=40
Bergell intrusion
MU 10
(Low U content)
Ap: 8.5 ± 2.7 Ma
"Population Method":
8.3 ± 1.8 Ma
Zr: 18.9 ± 2.2 Ma
MU 6
(Low U content)
Ap: 8.9 ± 2.2 Ma
"Population Method":
7.7 ± 1.6 Ma
Zr: 14.3± 1.1 Ma
MU 3
(Low U content)
Ap: 33.7 ± 12 Ma
Zr: 30.1 ± 1.4 Ma
MU 5
Ap: 10.7 ± 1.2 Ma
Zr: 23.8 ± 0.8 Ma
12.14 ± 0.62 µm
2.47 µm
n=16
Bergell intrusion
MU 1
Zr: 14.8 ± 1.2 Ma
MU 2
(Low U content)
Ap: 29.4 ± 8 Ma
Zr: 16.7 ± 1.2 Ma
Sample name
AFT age ± 1σ
Radial plot Apatite
track length histogram
ZFT age ± 1σ
Radial plot Zircon
Radial plot
±2σ range about the central age
+2σ
0
-2σ
Central age
Age scale
precision (1/σ)
Track length histogram
mean length
std. deviation
n. of tracks
Frequency
Track length (µm)
0 5 10 15 20
10 kms
ENGADINE LINE
MURETTO FAULT
FORCOLA FAULT
INSUBRIC LINE
N

Fig.3 (see facing page). Apatite and zircon fission track ages from the Bergell area together with radial plots of single-grain apatite and zircon age variation and confined horizontal track length measurement histograms in apatites. See key at bottom left of the figure for plot and numbers explanation. Each sample is located by a number in the insert structural map of the Bergell and Insubric areas (bottom right of the figure), together with some other literature samples used in this study (see also fig. 2). Track length measurements by analyst M.R. are indicated in grey within length histograms (see also Table 1). In radial plots, the 2√ uncertainty bar on the left side (y-axis) applies to each grain in the diagram. The age is read off by extrapolating a line from the origin through the individual data point to the circular scale. The x-axis denotes precision (normalized values). Precision increases towards the right side. Further annotations are discussed in the text and in Table 1.

3 yield younger ages as compared to other samples (e.g. samples MU1 and MU6). Consequently the high variation in the central ages from samples collected at very similar elevation reflects the annealing characteristics recorded by the combination of components 1 to 3 in the single-grain age distribution (fig. 3).

Pre-intrusive ambient temperatures of 330 to 370°C for pressure in the range 3.5 to 4 kbars (Trommsdorff and Connolly, 1996) prevailed in the pluton country rocks (Forno-Malenco unit and Margna nappe). That upper part of the magmatic body (Berger et al., 1996) thus intruded near the lower limit of the paleo-ZPAZ. Had the roof of the granodiorite been buried above the ZPAZ, i.e. in the ZFT retention zone, then central age of sample MU7 (granodiorite) would preserve the original crystallization age. To the contrary this sample yields a central age of 23.1 ± 1.4 Ma, younger by some 10 Ma than the emplacement age. The single-grain age distribution of that sample combines components 1 and 2, and the sample fails the chi-squared test. The scattering of the oldest single-grain zircon ages around 32-30 Ma, and the tight age grouping of low-temperature geochronologic systems for granodiorite samples (see review in Hansmann, 1996), is in agreement with the concept of fast cooling down to ca. 300°C for the eastern part of the intrusion. The relative large spread in individual grain ages then gives evidence to relatively slow cooling in the ZPAZ for the granodiorite sample.

All samples from the country rocks are situated within 2 kms of the granodiorite in the contact aureole (see Puschnig, 1996 and references therein) and experienced temperatures in excess of the tremolite-isograd (T > 450°C for P=3.5 kbars) or in excess of the talc-isograd (T > 500°C for P=3.5 kbars, Trommsdorff and Connolly, 1996) at the southeastern and eastern border of the pluton, respectively. Even if the ambient pre-intrusive Alpine metamorphism permitted partial annealing of zircons, the subsequent outward heat pulse from the intrusion was a priori largely sufficient to provide a full annealing of the zircon fission-tracks soon after the intrusion. Thermal modeling of the Bergell contact aureole indicates that rocks within 2 kms of the contact have achieved maximum contact metamorphic temperatures and begun cooling less than 0.3 Ma after the intrusion (Trommsdorff and Connolly, 1996). Available radiometric ages from the Bergell aureole indeed further document cooling down to ca. 300°C at 28 Ma (see review in Hansmann, 1996), i.e. only 2 Ma after the emplacement of the granodiorite fission tracks started to accumulate in zircon grains over ca. 10-15 Ma before thermal stability (e.g. samples MU3 and MU5). Thermal modeling however also suggests that the thermal evolution of the contact aureole adjacent to a granite that intruded at 825°C rocks initially at 100°C, i.e. above the ZPAZ, keeps the country rocks 2 kms away from the contact at temperatures in the range 300-350°C until at least 10 Ma after the intrusion (Spear and Peacock, 1989). In the Bergell case, given higher initial ambient temperatures, thermal modeling might consequently support that cooling of the contact aureole, and conversely the granodiorite, occurred both by thermal relaxation and on-going exhumation. It is suggested that the observed various annealing rates and heterogeneous reset among the zircon population within the contact aureole was favoured by on-going exhumation after the intrusion. Concerning those samples with a regional young ZFT age (MU1, MU6 and to less extent MU2), the accumulation of young ages within the single-grain population could alternatively possibly reflect late and local warm fluid circulations (T°>200°C, lower limit of the ZPAZ) associated with the Muretto fault zone fracturation (Peretti, 1983).

The Southern Alps unit south of the Bergell was at very-low grade to unmetamorphic temperatures conditions before the intrusion. We interpret the apparent ZFT age of 26 Ma of sample ME1 as a mixed age due to partial resetting, as shown by the single-grain age distribution combining both scarce but old grains (open circles), Oligocene thermal overprint (grey circles) and Miocene cooling (black circles) (fig. 3). Indeed during the backthrusting event, the hot northern block reheated the already cooled southern block but not sufficiently to completely reset the ZFT system (200°C < T < 350°C). This is also evidenced by the coexistence of pre-Neogene and Neogene ZFT ages south of the Insubric Line (fig. 2) (Hunziker et al., 1997).

In brief, despite complications at the eastern border of the Bergell intrusion, the ZFT ages and the ZFT pattern are very similar for all rocks sampled in the Bergell area, independently of tectonic units and limits. The ZFT parameters suggest a relative slow exhumation event.

3.2.2. Apatite fission-track ages (AFT)

All AFT central ages range between 6 and 12.3 Ma and document cooling down to ca. 100°C in the late Miocene (Fig. 3 and Table 1). At the Bergell eastern contact apatites from meta-arkoses and gneisses of the Muretto series and the Margna gneisses, respectively, have low (<5.5 ppm, samples MU6 and MU10) to very low (<1 ppm, samples MU2 and MU3) uranium concentrations (Table 1), which led to large analytical errors in both individual grain and central ages, and eventually to regionally insignificant AFT ages older than the corresponding ZFT ages (29.4 ± 8 Ma and 33.7 ± 12 Ma, samples MU2 and MU3 respectively). All but three samples fail the chi-squared test ($P(\chi2) < 5\%$) and show relatively high dispersion (> 10%), and the probability that individual grains are consistent with one age population is < 5% (Table 1). Although not investigated in this study, these statistics might reflect chemical heterogeneity of the apatites in the rocks sampled from different units. The single-grain age distribution is remarkably similar for all samples, whatever their tectonic unit position (e.g. samples FORC11 and FORC13 situated in the footwall and the hangingwall of the Forcola Line, respectively, fig. 3). Assuming that the oldest and youngest individual apatite grains date the cooling through both ends of the APAZ and that the closure temperature concept is valid (Dodson, 1973) then all samples likely started to cool down to 120°C at ca. 20 Ma, followed by a long residence time in the APAZ until the Messinian-early Pliocene, when both the North and South Alpine basement were finally exhumed and cooled below 60°C (fig. 3).

The number of confined track lengths measured in the apatites of U-rich samples is relatively low (except for sample MU7, see Table 1) and we don't want to place too much emphasis on these data. For the same reason the track length distribution has not been investigated by forward thermal modeling. The track length distribution of 3 samples has been however cross-checked by two analysts and results compared (Table 1). The mean track lengths (MTL) are comparatively very similar within error margins and vary between 9.46 and 13.34 μm with relative large standard deviation (mostly > 1.6 μm, Table 1). The track length distribution of all samples is relatively broad, slightly negatively skewed and unimodal. For example the broad distribution and low MTL of sample ME4 results from a conspicuous major proportion of very short (< 11 μm) and minor proportion of long (> 14 μm) tracks, in a remarkable opposite fashion to that of sample ME1 from the Southalpine basement. All samples have MTL < 13.5 μm according to both analysts and hence have been partially annealed. The reduced mean track lengths and high standard deviations alone don't yield full inferences on the cooling history but possibly further indicate that the sampled rock column must have resided for a long period of time within the APAZ (110-60°C) before thermal stability. In such a case the AFT ages of corresponding samples do not record specific cooling events. In the absence of forward thermal modeling however, it can not be stated for example whether the sampled rocks experienced significant late reheating that might alternatively explain the short MTL distribution.

As a preliminary conclusion to this section, it can be stated that the apatite fission-track parameters (ages, single-grain ages and track lengths distribution) do not show significant variations across the tectonic boundaries, and so do the zircons. From our AFT and ZFT dating, we infer that the whole Bergell area, i.e. the southeasternmost part of the investigated region, uplifted as a single block and had a very similar thermal history by the early Miocene onwards, as it cooled continuously and relatively slowly through the zircon and apatite PAZ before final near-surface cooling in the Upper Miocene.

3.3. Regional scale age and exhumation pattern

In this section and the followings the new AFT and ZFT ages are integrated in the regional age framework. To unravel the regional scale exhumation pattern at the eastern border of the Lepontine, we first carried out a compilation of AFT and ZFT literature data currently available, including our new dates.

3.3.1. Previous fission-track dating in the eastern Lepontine

The Eastern Central Alps and the Bergell and Insubric areas benefit of an extensive database of fission-track dates, the first campaigns having been initiated in the 70's. In table 2 and figure 2 we present a compilation of currently available AFT and ZFT ages in that part of the Alps, including previously unpublished ages. Wagner et al. (1977) intended to analyse the uplift rates of the Central Alps using this alternative approach to the blocking temperature concept for isotopic systems. Their AFT ages range from 7.4 to 16.8 Ma (fig.2), which represents the oldest AFT ages found in the Central Alps, and show a reasonably good correlation between AFT age and topographic altitude. According to these studies, the Bergell intrusives and surrounding rocks experienced a significant decrease of the uplift rate with time. Regional uplift rates of 0.41 mm/yr from 17 to 13 Ma for the northern Bergell area and 0.26 mm/yr during the last 13 Ma for the southern Bergell and Novate areas were inferred by the AFT dates. More AFT ages for the Novate granite are available from Munardi (1989) who provides apatites in the time range 13.1 to 16.7 Ma and corresponding zircon ages between 18.1 and 19.9 Ma. For the Bergell and Sondrio intrusions, ZFT ages indicate cooling down to ca. 250°C in the early Miocene (21.8 to 23.3 Ma, Giger, 1991). Because no one significant differences are recorded by biotite cooling ages from the Bergell intrusives and from the country rocks east of Val Mera (ca. 23-26 Ma, see review in Hansmann, 1996), the ZFT and AFT ages from these rocks directly documents the exhumation and regional cooling history below 300°C, without interferences from magmatic cooling. In the southern and western parts of the Bergell area, previously unpublished AFT and ZFT ages from the tonalite queue and from the SSB and the Tonale Zone (Hunziker et al., 1992, pers.comm.) indicate cooling below ca. 120 °C and 240°C in the time span 11.9 to 21.9 Ma, and 19.9 to 20.9 Ma respectively. One of these apatite ages is however problematic since the AFT age is older than the corresponding ZFT age (sample KAW 3103, table 2). Another sample, namely KAW 2960, yields a similar apatite age of ca. 22 Ma, and no ZFT age, and reasonably can be considered as tricky. Conversely, the ZFT age of ca. 41 Ma for sample KAW2959, situated in the North Alpine block, is rather similar to the partially annealed zircons characteristics of the South Alpine basement close to the Insubric Line (see hereinafter). North of the Bergell pluton, in the Upper Penninic nappes, AFT and ZFT ages from Hunziker et al. (1992) are in the same range than those further south, namely middle Miocene (9.9 to 14.6 Ma) and early Miocene (18.1 to 21.3 Ma), respectively.

The youngest regional AFT and ZFT ages are found in the Lower Penninic nappes of the Central Alps. Previously published Messinian AFT ages from Wagner et al. (1977) along sections perpendicular to the belt are in good agreement with the overall Late Miocene ages from Rahn et al. (2004) since all together the AFT ages range from 3.8 to 11.2 Ma. From the age data along vertical profiles in the Ticino area, Wagner et al. (1977) determined uplift rates of 0.34 to 0.4 mm/yr over the last 7 Ma for that region of the Central Alps. There is a real lack in ZFT ages currently available in the Lower Penninic nappes of the Eastern Central Alps, which is being fulfilled thanks to both the new ZFT ages presented in this study and a work in progress by Meinert Rahn.

South of the Insubric Line in the Bergell area, the few AFT and ZFT dates currently available from the Southern Alps basement rocks show a great variation according to their distance to the Insubric Line. Indeed a mixed zone of pre-Neogene and Neogene ZFT ages extends until a few kms immediately south of the Insubric line, a transition area in which AFT ages range from early to late Miocene (Hunziker et al., 1997).

We are aware that although AFT and ZFT ages published by the various authors agree within analytical errors, methodological and/or system calibration differences do make absolute comparison of ages between different workers and laboratories quite difficult. Moreover many AFT studies referenced in this manuscript do not provide the track length information and consequently the significance of the reported ages is ambiguous. Accordingly all the AFT and ZFT ages discussed in the following sections are always considered within the uncertainties set by the analyst. All supposed tricky ages as discussed previously, due e.g. to analytical difficulties, are not included in the various plots of following sections (or underlined by dashed symbols).

3.3.2. Regional scale pattern of fission-track data along the transversal transect

The available literature data from the north alpine realm, including our new AFT and ZFT ages, have been plotted on two integrated age-altitude-spatial distribution sections, in order to decipher their regional distribution across the collisional wedge. These integrated traverses run approximatively 65 and 30 kms long in the direction parallel and perpendicular to the belt, respectively, north of the Insubric Line (fig. 4). The regional orogen-perpendicular cooling and exhumation pattern is analysed and discussed first. On the N-S transect the AFT pattern is characterized by 2 main features (fig. 4a):

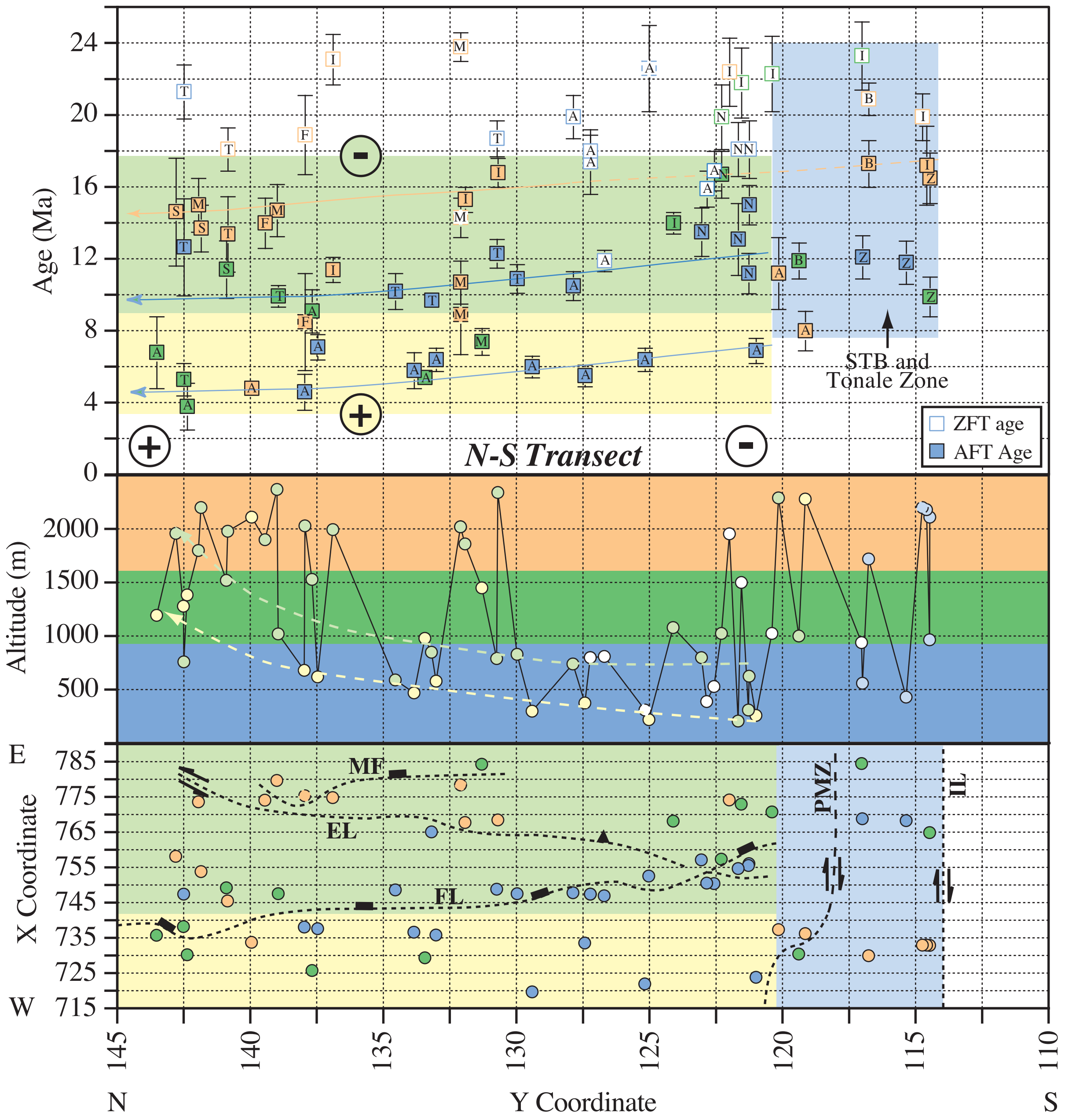

Fig. 4a. Regional scale pattern of all fission-track data along the transversal transect in the age-elevation-location plot. Sample location is given in Swiss coordinates. Open and full squares on top figure are Zircon Fission Track Ages and Apatite Fission Track Ages, respectively. Dashed symbol when sample age is doubtful or tricky. Error bars are ± 1σ. Letters within squares refer to tectonic unit, A: Adula-(Simano)-Grüf Unit; B: Bellinzona-Dascio Zone; F: Forno Unit; I: Periadriatic Intrusives (Bergell, Sondrio); N: Novate granite; S: Suretta Nappe; T: Tambo Nappe; M: Margna Nappe; Z: Tonale Zone. Light color shaded areas in top and bottom plots refer to AFT age distribution only. Plus and minus symbols: relative exhumation along the traverse. Bottom diagram: dashed heavy lines represent major faults. EL: Engadine Line; FL: Forcola Line; IL: Insubric (Tonale) Line; MF: Muretto Fault; PMZ: Paina Marble Zone. Heavy color shaded areas in center diagram deal with elevation range of samples. See text for discussion.

(1) a bimodal distribution of AFT ages between 4 and 9 Ma on the one hand (light yellow shaded area), and between 9 and 22 Ma (light green and blue shaded areas) on the other hand;

(2) a discrete and vaguely discontinuous northward rejuvenation of AFT ages for both age group (arrows in top diagram of fig. 4a), evidenced by the little correlation of ages with altitude (compare age trend arrows with altitude trend arrows in center diagram of fig. 4a). This suggests that the samples along the traverse do not share a single uplift event due to a simple vertical movement. This effect progressively vanishes from the middle part of the transect and moving south until the Novate area latitude, at least for the light green domain.

All but 2 samples (namely MU10 and kaw956, both located in the easternmost field area), concerned with the 4-9 Ma apatite age group are situated within the Lower Penninic unit and within the westernmost part of the Tambo nappe (Upper Penninic unit). Conversely, the 9-22 Ma age group deals with the Upper Penninic nappes (including only the eastern part of the Tambo nappe), the Tertiary intrusives and their country rocks, the SSB and Tonale zone samples. It is also noteworthy that the sampled slopes from the Muretto fault zone (between Y coordinates 132-138, fig. 4a bottom and fig. 2) yield young apatite ages, as compared to altitude, and disturb the N-S horizontal apatite age trend of the more internal domain. Those samples are mostly characterized by U-low content as discussed in section 3.2.2. Alternative explanation to the rejuvenation of ages will be discussed in section 3.4.2. Samples from the western part of the SSB and Tonale zone (light blue area on fig. 4a) but located south of the Adula nappe (between X coordinates 725-740, see fig. 2) are remarkably older than those from the Adula nappe (light yellow) at a similar elevation. Such an age difference is not found between the samples situated in the eastern part of the SSB and Tonale zones (between X coordinates 765-785) and those from north of it in the Tertiary intrusives (light green area). These observations suggest a singular and younger near-surface cooling pattern for the Lower Penninic units and the deeper parts of the Tambo nappe with respect to all other units, as a first approximation independently of tectonic units (fig. 4a, bottom). Conversely the latter units were within 2-4 kms to the surface earlier as compared to the former ones, but no clear horizontal age gradient is relevant to the AFT data in the SSB except for the northern and western parts of it, close to the Paina Marble Zone (PMZ) where young ages clearly show no correlation to altitude (fig. 4a, top and bottom).

Diagrams of fig. 4a enlighten that the AFT ages from the deeper parts of the Lepontine dome (Lower Penninic and western Tambo units) are poorly distributed (narrow age interval) with respect to data from the dome's outside units. Indeed the differences in sample elevation have a greater influence on the age distribution in the eastern parts of the Lepontine dome (fig. 4a, top diagram), which could be explained by a decrease in exhumation rates along-strike of the Lepontine towards the structurally upper domain (circled yellow plus and minus green symbols, respectively, top of fig. 4a and fig. 4b). Accordingly, samples with a similar AFT age (e.g. at circa 13-15 Ma in upper structural levels and ca. 4-7 Ma in lower structural levels) but separated by as much as 1500 m of difference in height at the southern and northern end of the traverse indicates that the northern part of the transect was exhumed faster during the last 14 Ma with respect to the southern one (circled black plus and minus symbols, respectively, top of fig. 4a).

Regarding the ZFT data, the age distribution does not show neither clear trend nor clear age-elevation relationship along the transect. The ZFT ages spread between 16 and 24 Ma. It is however noteworthy that the sampled slopes in the southern portion of the profile were already exhumed at depths consistent with the closure temperature of the AFT system, while they were still at depths corresponding to the closure of the ZFT system in the north in the time span 16-19 Ma (fig. 4a, top). Regarding the bulk northwestward rejuvenation of AFT ages along the transversal profile, a tilt of the paleo-isotherms around a belt-parallel axis during exhumation is proposed. Assuming a geothermal gradient of 30°C.km^{-1}, a closure temperature (Tc) of 240°C and 90°C for the ZFT and AFT systems, respectively, and no or minor tectonic disturbance, the difference in original depth of ca. 5 kms between the northern and southern pieces of the traverse implies a mean value for the tilt angle as high as 9° SE. Assuming that the frontal part of the Suretta nappe is also implied in the tilt (see ZFT and AFT data in table 2), and even the external crystalline Gotthard massif where 16 Ma zircon ages are reported (Michalski and Soom, 1990) but minor tilting of the apatite paleo-isotherms documented (see discussion in paragraph 4) a more realistic average value of 4° SE can be however calculated. Tilting dies out in the Bergell and Insubric areas, and most probably started in the late Lower Miocene to early Middle Miocene and lasted until at least the late Miocene. During the tilt, the southern samples remained in the APAZ, or close to its lower limit, whereas the northern ones cooled down through the APAZ. Accordingly, the AFT parameters in the Bergell area suggest a long time of residence in the APAZ and fail the chi-squared test while the tilted samples pass the test with >5% probability and have longer mean track lengths, suggesting a more rapid cooling (e.g. Adula samples from Rahn et al., 2004, in table 2).

3.3.3. Regional scale pattern of fission-track data along the longitudinal traverse

The most striking characteristics of the orogen-parallel traverse, that strengthen those of the transversal one, are the followings (fig. 4b):

(1) the bimodal distribution of AFT data corresponds to an apparent discrete jump in ages of 3-8 Ma located in the area approximately between the Swiss coordinates 740-745 (grey shaded area in top and bottom diagrams of fig. 4b). In map view the jump in ages area extends across the Forcola Line from the western and central parts of the Tambo nappe in the north to the southeastern part of the Adula nappe in the south;

Table 2. Compilation of available apatite and zircon fission track data in the Eastern Central Alps. Same symbols and units as in Table 1. References given in column 16 are as follows: (1) Wagner et al., 1977, (2) Wagner et al., 1979, (3) Hunziker et al., 1992, (4) Hunziker et al., 1992 (pers. comm.), (5) Giger, 1991, (6) Rahn et al., 2004 (pers. comm.), (7) D. Seward, pers. comm. in Rahn et al., 2004, (8) Hurford, 1986, (9) Viola (2000). Sample data in italics concern data out of map area of fig. 2 but used in this study for discussion. Location of samples from Wagner et al. (1979) are estimated and only given by a coordinate interval. In columns 11 and 15, P.M. and E.D.M. mean apatite analyses by the population method and by the external detector method, respectively.

Sample	locality	x coordinate	y coordinate	altitude (m)	lithology	tectonic unit	**Zircon Age (Ma)**	SE	$P(\chi^2)$	n. of grains	**Apatite age (Ma)**	SE	$P(\chi^2)$	n. of grains	Reference	MTL	SD	n. of tracks
Eastern Central Alps																		
KAW 75	Claro	721.925	125.175	310	gneiss	Leventina nappe					**6.40**	0.65		P.M.	1			
KAW 76	Castione	723.850	121.000	260	bi-ms gneiss	Castione zone (Leventina)					**6.90**	0.70		P.M.	1			
KAW 132	Novate/Mezzola	755.520	121.280	310	pegmatite	Novate granite					**11.20**	1.12		P.M.	1			
KAW 137	Osogna	719.690	129.410	300	gneiss	Leventina nappe					**6.00**	0.60		P.M.	1			
KAW 138	*Pollegio*	*715.570*	*135.400*	*300*	*gneiss ?*	*Leventina nappe*					***5.90***	0.60		P.M.	*1*			
KAW 145	Soazza-1	735.850	133.020	580	bi-gneiss	Adula nappe					**6.40**	0.64		P.M.	1			
KAW 189	Soazza-2	737.630	137.470	620	gneiss	Adula nappe					**7.10**	0.71		P.M.	1			
KAW 328	Lago Di Cavloc	774.080	139.450	1900	gneiss	Forno-Lizun					**14.00**	1.40		P.M.	1			
KAW 550	Ponte Baffo/Val Masino	768.800	117.000	560	gneiss	Tonale Series					**12.10**	1.21		P.M.	1			
KAW 553	Codera	757.150	123.050	800	granite	Novate granite					**13.50**	1.35		P.M.	1			
KAW 775	Fextal	779.700	139.000	2370	phe-augengneiss	Margna nappe					**14.70**	1.47		P.M.	1			
KAW 956	Ca Rotte/Malenco	784.300	131.300	1450	gneiss	Margna nappe					**7.40**	0.74		P.M.	1			
KAW 1237	*Roffla quarry*	*752.260*	*160.800*	*1100*		*Suretta nappe*	***22.10***	*1.4*	*31*	*EDM n=20*	***14.00***	*0.40*		*P.M. 190/200*	*3*	*13.19*	*1.48*	*100*
KAW 1238 a	*Andeer quarry*	*752.100*	*162.430*	*1000*		*Suretta nappe*	***21.80***	*0.15*	*97*	*EDM n=15*	***13.50***	*0.60*		*P.M. 200/200*	*3*	*13.47*	*1.36*	*100*
KAW 1238 b	*Andeer quarry*	*752.100*	*162.430*	*1000*		*Suretta nappe*	***21.80***	*0.15*	*97*	*EDM n=15*	***12.40***	*0.60*		*P.M. 200/200*	*3*	*13.38*	*1.27*	*100*
KAW 1240	*Splügenpass*	*745.400*	*152.150*	*2113*		*Suretta nappe*	***20.30***	*1.3*	*92*	*EDM n=20*	***15.30***	*0.90*		*P.M. 200/200*	*3*	*13.25*	*1.21*	*100*
KAW 1243	Motta	747.450	142.500	760		Suretta nappe	**21.30**	1.5	98	EDM n=20	**12.70**	2.70		P.M. 300/300	3			
KAW 1246	Prestone, lower quarry	747.550	138.950	1020		Suretta nappe					**9.90**	0.60		P.M. 200/200	3	12.90	1.71	100
KAW 1247	Prestone, upper quarry	745.500	140.850	1980		Suretta nappe	**18.10**	1.2	93	EDM n=20	**13.40**	2.10		P.M. 200/200	3			
KAW 1379	Val Madris	758.150	142.800	1960		Suretta nappe					**14.62**	3.22		P.M. 300/300	3			
KAW 1382	Alpe Pian del Nido	753.850	141.850	2200		Suretta nappe					**13.70**	1.30		P.M. 200/200	3	12.90	1.19	8
KAW 1383	Fracisco	749.200	140.900	1520		Suretta nappe					**11.40**	1.60		P.M. 200/200	3			
KAW 2620	E Novate/Val Codera	756.060	121.260	625	leuco-granite	Novate granite	**18.10**	1.6	2.15	EDM n=10	**15.00**	15			5			
KAW 2621	Monticello	757.350	122.300	1025	leuco-granite	Novate granite	**19.90**	1.8	1.25	EDM n=10	**16.70**	16.7			5			
KAW 2622	Riva Novate	754.670	121.670	207	leuco-granite	Novate granite	**18.10**	1.5	2.95	EDM n=10	**13.10**	13.1			5			
KAW 2623	Preda Rossa	774.180	122.000	1955	Tonalite	Bergell intrusion	**22.40**	1.90	0.73	EDM n=10					5			
KAW 2624	Val di Sasso Bissolo	772.950	121.550	1500	Tonalite	Bergell intrusion	**21.80**	1.90	1.39	EDM n=11					5			
KAW 2625	Val Masino	770.750	120.400	1025	Tonalite	Bergell intrusion	**22.30**	2.10	1.16	EDM n=10					5			
KAW 2959	N Passo San Ioro	732.900	114.470	2110	micaschist	Tonale zone	**40.80**	4.40			**16.50**	1.40			4			
KAW 2960	N Passo San Ioro	732.890	114.380	2060	Ms-Bt mylonite	Tonale zone					**21.90**	1.90			4			
KAW 2961	Strasse Cap. Genero-Tunnel	729.960	116.770	1720	Ms-Bt gneiss	Bellinzona-Dascio zone	**20.90**	0.90			**17.30**	1.30			4			
KAW 2962	Val Dei Bu, S Vif	730.440	119.390	1000	Ms-Bt gneiss	Bellinzona-Dascio zone					**11.90**	1.00			4			
KAW 3102	SSW Cima di Cugn, "Biscia"	732.950	114.590	2180	Melirolo augengneiss	Bergell intrusion					**17.20**	2.20			4			
KAW 3103	NNW Cima Di Cugn	732.980	114.750	2200	Ioro Tonalite	Bergell intrusion	**19.90**	1.30			**21.70**	2.40			4			
KAW 3290	E Ruvarti	784.500	117.030	940	leucotonalite	Sondrio intrusion	**23.30**	1.9	1.73	EDM n=11					5			
BM 01	Promontogno	763-764	134-135	850	pre-intrusive rocks	Tambo nappe					**9.70**	0.50		P.M.	2			
BM 02	Val Bondasca-1	767-768	130-131	2340	granodiorite?	Bergell intrusion					**16.80**	0.80		P.M.	2			
BM 03	Val Bondasca-2	767.000	131-132	1860	granodiorite?	Bergell intrusion					**15.30**	0.70		P.M.	2			
BM 06	Val Masino	767-768	115-116	430	pre-intrusive rocks	Tonale Series					**11.80**	1.20		P.M.	2			
BM 07	Bagni del Masino	767-768	123-124	1080	granodiorite	Bergell intrusion					**14.00**	0.60		P.M.	2			
MR P 226	Spina	735.720	143.520	1195	fs-augen paragneiss	Adula nappe					**6.80**	2.00	76	E.D.M. n=15	6	13.60	1.10	11
MR P 227	Pian San Giacomo	738.230	142.510	1280	ms-bt-chl paragneiss	Tambo nappe					**5.30**	0.90	91	E.D.M. n=20	6	13.71	1.73	16
MR P 228	Castello Mesocco	738.060	137.970	680	two mica paragneiss	Adula nappe					**4.60**	1.00	57	E.D.M. n=20	6	13.33	1.53	76
MR P 263	*Splügenpass*	*745.060*	*151.980*	*2120*	*very fine gneiss*	*Tambo nappe*					***16.90***	*1.30*	*18*	*E.D.M. n=20*	*6*	*13.27*	*1.65*	*100*
MR P 264	Soazza	736.610	133.850	470	light ms gneiss	Adula nappe					**5.80**	1.00	60	E.D.M. n=20	6	13.18	1.89	100
MR P 265	Norantola	733.580	127.430	375	two-mica gneiss	Adula nappe					**5.50**	0.60	79	E.D.M. n=20	6	13.95	1.48	100
MR P 266	*Alpe Arami*	*719.390*	*120.970*	*1445*	*migmatitic orthogneiss*	*Adula nappe*					**7.70**	1.30	69	E.D.M. n=20	6	14.03	1.38	46
MR P 267	Trescolmen	733.730	139.950	2110	two-mica orthogneiss	Adula nappe					**4.80**	0.50	76	E.D.M. n=20	6	14.15	1.56	100
MR P 268	Pian d'Asc	730.230	142.370	1385	two-mica orthogneiss	Adula nappe					**3.80**	1.30	13	E.D.M. n=28	6	13.53	1.89	26
MR P 269	Cauco	729.380	133.440	980	two-mica orthogneiss	Adula nappe					**5.40**	0.50	100	E.D.M. n=20	6	13.70	1.46	100
MR P 273	Alp di Lesgiüna	725.720	137.680	1530	two-mica orthogneis	Adula nappe					**9.00**	1.20	98	E.D.M. n=20	6	13.57	1.43	36
MR P 310	Sass del Vacca	737.370	120.155	2290	paragneiss	Adula nappe					**11.20**	2.00	92	E.D.M. n=20	6	13.93	1.34	100
MR P 311	Cima della Stagn	736.200	119.150	2280	orthogneiss	Adula nappe					**8.10**	1.10	89	E.D.M. n=20	6	14.28	1.30	100
Southern Alps																		
DB9018		748.250	111.250	220	gneiss basemet	Southern Alps					**9**	1.40			7			
DB9019		748.250	111.250	200	Basement	Southern Alps					**9.02**	1.48			7			
BM 10	Val Adda	770-771	113-114	265	pre-intrusive rocks	Southern Alps					**8.10**	0.50		P.M.	2			
KAW 2105	*Porto Ronco*	*699.463*	*110.750*	*225*	*bt-ms gneiss*	*Ivrea Zone, Southern Alps*	***48.20***	*3.70*		*EDM n= 11*	***15.20***	*2.10*		*EDM n= 10*	*8*			
KAW 2958	S Passo San Ioro	732.690	113.750	1990	Giumello gneiss	Southern Alps basement					**23.8**	2.10			4			
KAW 2964	Gola Di Lago	718.920	106.960	1090	Ms-Bt gneiss	Southern Alps, Ceneri zone					**19.60**	1.90						
KAW 2970	Cima di Fiori, N Isone	719.780	110.450	1010	Bt-Ms gneiss	Southern Alps, Ceneri zone	**180.10**	15.00			**17.20**	1.50			4			
Ceneri	*Gambarogno*	*711.450*	*111.945*	*210*		Southern Alps, Ceneri zone					***14.6***	*2.20*			*7*			
Mal18	S Triangia Intrusion	784.750	116.250	800		Southern Alps basement	**45.70**	2.55							9			

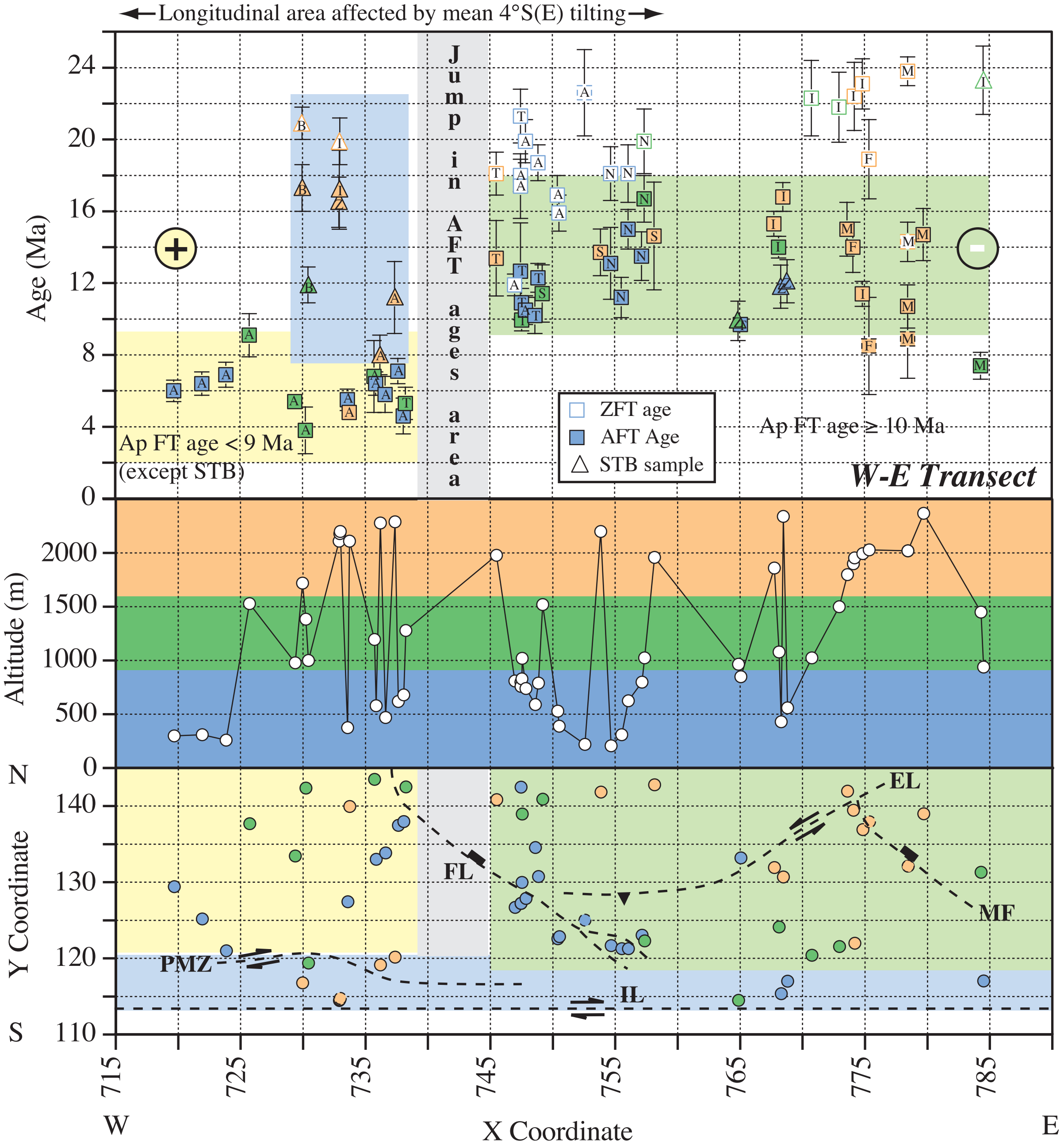

Fig. 4b. Regional scale pattern of all fission-track data along the longitudinal transect. Age-elevation-location plot. Same symbols and units as in fig.4a. Open and full triangles in top diagram refer to STB-Tonale zone samples.

(2) the jump in ages area indeed doesn't affect the samples from the Insubric area (SSB and Tonale zones). The top diagram of fig. 4b clearly points out the previously stated different late cooling history underwent by the Lower Penninic and west Tambo units one the one hand, and the Insubric, Bergell plus country rocks and Upper Penninic terranes on the other hand;

(3) the jump in ages is possibly part of a broader discrete horizontal gradient of increasing apatite ages from W to E, with disregard for altitude dependence;

(4) the mean 4°SE tilting effect on the AFT pattern progressively disappears towards the Lepontine dome's exterior. Indeed east of the Swiss coordinate 760, sampled slopes and valley bottoms yield distinct AFT ages, which is not the case for the tilt implied samples (top diagram of fig. 4b).

At the eastern end of the profile, young ZFT and AFT ages are discussed in section 3.2. and alternatively hereafter in section 3.4.2. The considerable gap in ZFT and AFT data in the apparent jump in ages area makes it actually difficult to decide whether the ages change continuously or discontinuously across this narrow zone. The discontinuous solution would actually imply a faulting event post-dating the 4°SE tilting, and a priori independent of the Forcola Line, while the continuous choice would fit within the dome's outside steady ageing trend. In the latter case, the horizontal along-strike gradient may be due to tilting of the paleo-isotherms clockwise looking N around a belt-perpendicular axis. Yet the AFT ages from the deeper levels (western) of the Adula nappe yield very similar ages of ca. 6 Ma without continuous rejuvenation (fig. 4b), suggesting that the transition to older ages toward the dome's external is quite an abrupt one across the data gap.

Regarding the ZFT data, a breakdown into their orogen-parallel distribution doesn't bring about clear trends but a slight westward migration of cooling below 300°C, that would be similar to the apatite age distribution (fig. 4b). But the considerable lack of ZFT data in the Adula nappe precludes any further inferences regarding the westward distribution of zircon ages within the deeper tectonic level. However the samples from the topographic heights at the eastern and western ends of the traverse provide 20-24 Ma old zircons that are not correlated with altitude (fig. 4b, top). Those from the valley bottoms in the center part of the profile are on the contrary correlated with altitude and provide younger 16-21 Ma old zircon ages. This might suggest a different cooling history between sampled slope and valley bottom.

3.3.4. Thermochronology of faulted blocks and late differential exhumation across the belt

Amounts and rates of denudation in mountain ranges can be constrained, assuming a geothermal gradient, with the help of cooling ages obtained from a single sample by different thermochronological systems. A geothermal gradient of 30°C.km^{-1}, a closure temperature of 240°C and 90°C for the AFT and ZFT systems respectively and a mean surface temperature of 20°C will be assumed for reconstructing the exhumation history of tectonic blocks. An alternative method is provided by the altitude dependence approach, i.e. age-elevation profiles from regional and/or fault-bounded FT data, making any assumption on the geothermal gradient unnecessary. The major assumption underlying the altitude dependence approach is that no tectonic disturbance produced significant differential vertical displacement during exhumation. Moreover Gleadow and Brown (1999) showed that linearity of the age-altitude profiles is verified only at exhumation rates > 30m.Ma^{-1} for a thermal gradient of 25°C.km^{-1}. Finally, the regional pattern of denudation drawn from regional sample arrays yields potential spatial variations in the denudation rates and valuable insights about the mechanisms of denudation (i.e. erosional exhumation and/or tectonic exhumation).

COOLING AND EXHUMATION RATES IN THE 3-8 KMS DEPTH INTERVAL

We investigated six fault-bounded terranes in the Bergell and Insubric areas (fig. 5a), the faults being segments of the PFS. Principally, the ZFT ages of the topographically highest samples (≥ 800 m a.s.l.) do not correlate with altitude (fig.6, blocks 2, 4 and 5 in fig. 7b,d,e), while the ages of samples at lower elevations (< 800 m a.s.l.) closely correlate with elevation (fig. 6, blocks 1 and 3 in fig. 7a,c). This may indicate the presence of a regional break in slope at elevations around 750-1000 m, although the sparse data below the break and the lack of full vertical sections in individual blocks can not verify this unambiguously (fig. 6). Nonetheless, the concordance of ZFT ages for samples above the break in slope, over an altitude range of ca. 1500 m, requires a minimum regional mean exhumation rate of 0.5 mm.yr-1 between 23 and 18 Ma. The mineral pair approach yields mean cooling rates in the range 16-32°C.Ma^{-1}, 11-28°C-Ma^{-1} and 42°C.Ma^{-1} in the interval between the closure temperature of ZFT and AFT systems, for tectonics blocks 2, 4 and 5, respectively (fig. 5b). Such cooling rates indeed correspond to average exhumation rates in the order of 0.53-1.1 km.Ma-1, 0.38-0.92 km.Ma^{-1} and 1.39 km.Ma^{-1}, respectively.

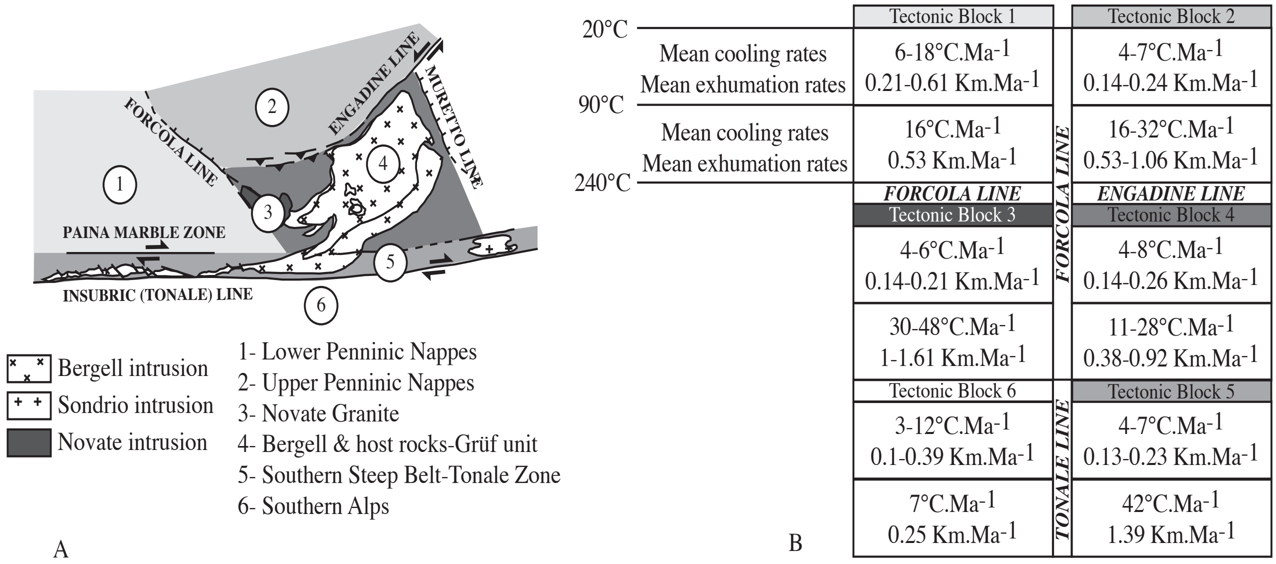

		Tectonic Block 1		Tectonic Block 2
20°C 90°C	Mean cooling rates Mean exhumation rates	6-18°C.Ma^{-1} 0.21-0.61 Km.Ma^{-1}	FORCOLA LINE	4-7°C.Ma^{-1} 0.14-0.24 Km.Ma^{-1}
90°C 240°C	Mean cooling rates Mean exhumation rates	16°C.Ma^{-1} 0.53 Km.Ma^{-1}		16-32°C.Ma^{-1} 0.53-1.06 Km.Ma^{-1}
		FORCOLA LINE		ENGADINE LINE
		Tectonic Block 3		Tectonic Block 4
		4-6°C.Ma^{-1} 0.14-0.21 Km.Ma^{-1}		4-8°C.Ma^{-1} 0.14-0.26 Km.Ma^{-1}
		30-48°C.Ma^{-1} 1-1.61 Km.Ma^{-1}		11-28°C.Ma^{-1} 0.38-0.92 Km.Ma^{-1}
		Tectonic Block 6	TONALE LINE	Tectonic Block 5
		3-12°C.Ma^{-1} 0.1-0.39 Km.Ma^{-1}		4-7°C.Ma^{-1} 0.13-0.23 Km.Ma^{-1}
		7°C.Ma^{-1} 0.25 Km.Ma^{-1}		42°C.Ma^{-1} 1.39 Km.Ma^{-1}

Fig. 5. (A) Structural sketch of tectonic blocks (numbers 1 to 6) separated by major faults. (B) Average cooling and exhumation rates of tectonic blocks at different crustal levels, as deduced by the mineral pair approach.

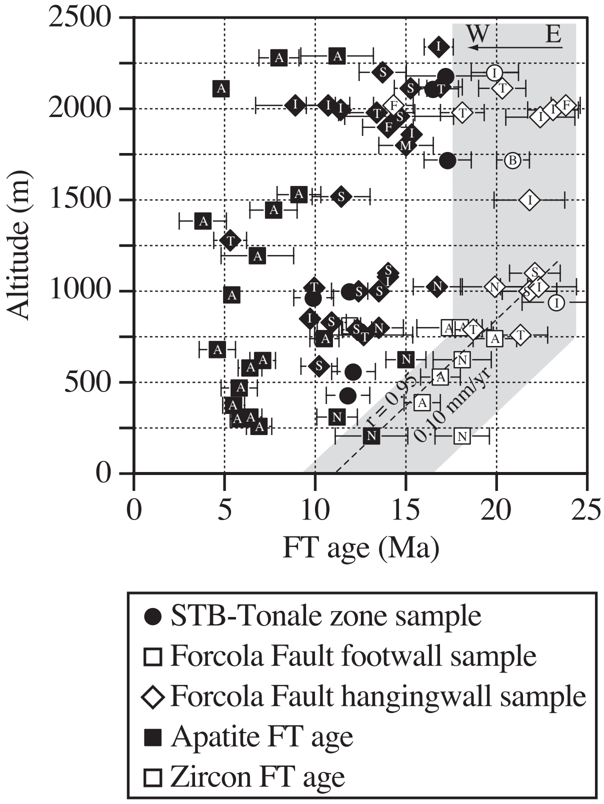

Fig. 6. Age vs. elevation plot of zircon and apatite fission track data from all samples. See key at bottom figure for symbol explanation. Letters within symbols: same as in fig. 4a. Shaded area: age-elevation trend for zircon data. Error bars are ± 1σ.

Below the break in slope exhumation rates of 0.22 to 0.34 mm.yr-1 between 20 and 16 Ma are inferred for tectonic blocks 1 and 3, respectively (fig. 7a,c). Cooling rates in the order of 16°C.Ma-1 and 30-48°C.Ma^{-1}, converted into comparatively higher exhumation rates of 0.53 km.Ma^{-1} and 1-1.61 km-Ma^{-1}, are however calculated for tectonic blocks 1 and 3 respectively, between the closure of zircons and apatites. Alternatively, the broad age-altitude positive correlation for the regional lowest samples yields a relative slow exhumation rate of 0.10 mm.yr-1. The shallower slope defined by the zircon data indicates that the exhumation rate indeed decreased after ca. 20 Ma (fig. 5b). It is also worth mentioning that samples above the break in slope all pass the chi-squared test with probability > 5%, while those below the break fail the test with probability < 5% (Tables 1 and 2). This might indeed suggest a different residence time in the ZPAZ for samples situated above and below the break in slope.

In the regional age-altitude profile, both rocks from the footwall and the hangingwall of the Forcola Line are mixed below and above the break in slope, implying that the changing exhumation rate bears no genetic link to the fault slip rate. Moreover for samples of similar elevation, there is a regional tendency for slightly and gradually younger ZFT ages from the easternmost to the western-

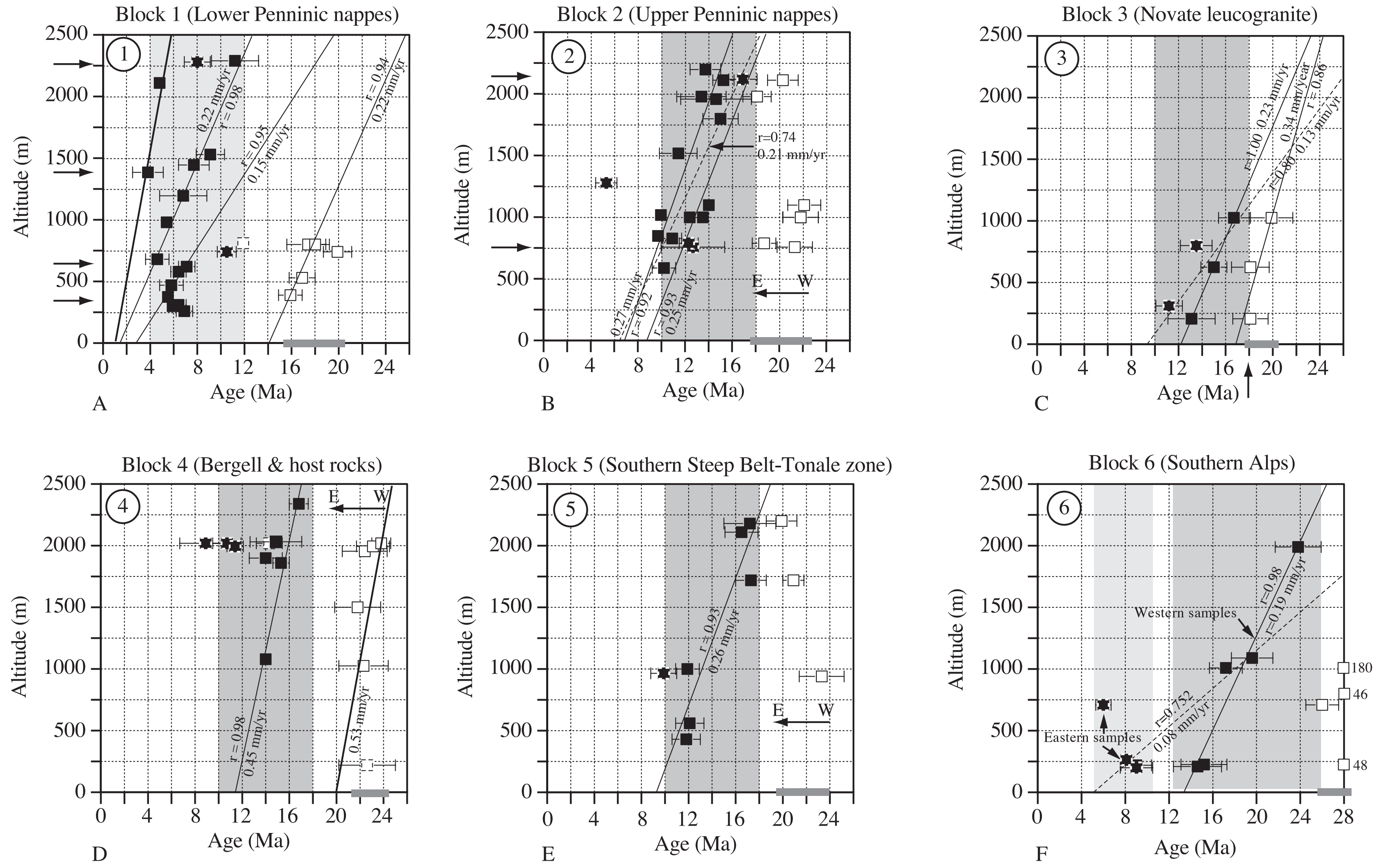

Fig. 7. Age vs. elevation correlation of apatite (full squares) and zircon (open squares) fission track data from individual tectonic blocks. Error bars are ± 1σ. Dashed squares: samples non fitting with calculated best correlation lines, unless discussed in the text. Full and dashed light correlation lines deal with particular groups of samples and all samples, respectively. Heavy correlation line in plots a and d corresponds to minimum estimated 0.5 $mm.yr^{-1}$ exhumation rates. Next to correlation line is indicated both the correlation factor and the exhumation rate given by the slope of the line. Light and medium grey shaded areas: apatite age distribution in each block. Dark grey shaded area next to age scale: zircon age distribution. Squares located at the 28 Ma line in fig. 7f indicate partially annealed zircon samples, with corresponding out of scale age. See text for further discussion.

most samples (fig. 6). The outstanding young ZFT ages not matching the calculated regression line in fig. 7a,d have been discussed in paragraph 3.2.1.

In the Southern Alps block, available ZFT ages are very scarce. However mixed pre-Alpine and Alpine ages coexist in a few kms wide area immediately south of the I.L. (figs. 3 and 7f), which likely evidences a zone where cold rocks of the Southern Alps have been reheated and partially annealed at temperatures above 200°C and below 320°C, during the backthrusting event (Hunziker et al., 1997). One sample (ME1) strongly annealed at the time of backthrusting allowed nonetheless an estimation of a somewhat overestimated mean cooling rate of 7°C.Ma^{-1} akin to a mean exhumation rate of 0.25 km-Ma^{-1} in the time interval 26-6 Ma (fig. 5b), values that are the regionally lowest ones during this time period.

NEAR-SURFACE COOLING AND EXHUMATION RATES

Apatite central ages for the whole data set display only a very broad positive correlation with the topographic altitude and evidence a complex regional age distribution (fig. 6). Bearing in mind that the ages do not fit a model of simple vertical movement (fig. 4a), the subsequent calculated exhumation rates might be meaningless, unless spatially restricted arrays of samples are undertaken.

Typically, the Lower Penninic tectonic block displays the regionally youngest AFT ages (between ca. 6 and 10 Ma) and a complex, disrupted age-altitude pattern (black arrows in fig. 7a). In this block particular groups of samples, as a first approximation spatially distributed over areas of relative limited extent, however show positive linear arrays of age vs. altitude which the slope indicate similar exhumation rates of 0.15 to 0.22 mm.yr^{-1}, for the time ranges 7-5 Ma and 11-5 Ma respectively. However due to (1) the casual linear array for 2 samples not spatially close to others in the latter case and (2) the clustering of data in one group over a narrow range of elevations in the former case, which the slope of the regression line is consequently badly defined, only very broad and quite hazardous exhumation rates can be evaluated by this plot. The lowermost samples, all located in the westernmost part of the investigated area, even produce a slight inverted age-elevation relationship. Other samples show no clear age increase with altitude and even higher exhumation rate in the order of 0.5 mm.yr^{-1v} may be expected. Alternatively, assuming that most ages over 2 kms elevation range are centered around 6 Ma within the error margin, it can be stated that the whole sample array underwent a better bulk exhumation rate of > 0.5 mm.yr^{-1}. By considering the whole AFT data set from the Lower Penninic tectonic block, average cooling rates in the range of 6 to 18°C.Ma^{-1} indeed yield mean exhumation rates of 0.21 to 0.61 km.Ma^{-1} (ca. 0.5 km.Ma^{-1} in average), in the interval between the closure temperature of the AFT system and the surface, i.e. since the late Tortonian (fig. 5b).

AFT ages from all other tectonic blocks are scattered between 10 and 18 Ma for the same elevation range, and are thus significantly older (fig. 7b-e). This evidences the potential discrete jump of ages of minimum 4 Ma between the Lower Penninic tectonic block and those east and south of it. An important point to stress out is that the youngest AFT age from the Upper Penninic nappes block 2 (sample MRP227) has an erratic age compatible with the age pattern of block 1. Similarly the anomalous oldest AFT age at 750m elevation (namely sample FORC11) from the tectonic block 1 matches the age pattern of block 2 (fig. 7a-b). On the basis of those two samples alone, the major tectonic boundary between the Lower and Upper Penninic Units, namely the Forcola Line, doesn't seem to be a good candidate for the discrete jump of AFT ages.

The reasonably good broad positive age-altitude correlation for the whole data set of tectonic block 2 (dashed line, r=0.74) may alternatively be interpreted as a disrupted pattern, yielding better correlations and similar exhumation rates of ca. 0.25 mm.yr^{-1} between 17 and 10 Ma (fig. 7b). The regression line dealing with the oldest ages with regard to altitude in this diagram encompasses mostly the eastern samples from the upper Penninic unit (unless dashed). The mineral-pair approach indicates that rocks originally at 3 kms depth cooled down since the middle Miocene at mean cooling rates of 4 to 7°C.Ma^{-1}. These values correspond to mean exhumation rates of 0.14 to 0.24 km.Ma^{-1} and match the estimations of the altitude-dependence method (fig. 5b).

Tectonic block 3 exhumed near-surface at mean rates of 0.13 mm.yr^{-1} to 0.23 mm.yr^{-1} between 17 and 11 Ma, depending on the interpretation of the linear arrays of age versus altitude (fig. 7c). In the interval between the closure of the apatites and the surface, mean cooling rates in the order of 4 to 6°C.Ma^{-1}, corresponding to very similar exhumation rates of 0.14 to 0.21 km.Ma^{-1} characterize the Novate granite block (fig. 5b). The apatite ages from the Novate granite are however systematically 2 Ma older than the other tectonic blocks 2, 4 and 5.

Similar exhumation rate of 0.26 mm.yr-1 between 17 and 10 Ma is evaluated from the whole samples of tectonic block 5 (fig. 7e), with only one outlier within error margins. Comparable values of 0.13 to 0.23 km.Ma^{-1} are calculated by the mineral-pair approach, as the rocks cooled down at mean rates of 4 to 7°C-Ma^{-1} below 100°C (fig. 5b). Of note is that samples at and above 1000m altitude, situated in the western part of the block and south of the Lower Penninic tectonic block, yield AFT ages older by 4 to 7 Ma as compared with the latter block for the same elevation range, as previously discussed in section 3.3.2 (compare blocks 1 and 5 in fig. 7).

The regional highest exhumation rate of 0.45 mm.yr-1 is obtained from the slope of the regression line in the age-elevation plot of the Bergell tectonic block 4, between 17 and 14 Ma (fig. 7d). Again due to the clustering of data in two groups (no data from the valleys bottom), only a broad exhumation rate can be calculated from this plot. Mean cooling rates of 4-5°C.Ma^{-1} for this block are indeed fairly associated with much lower exhumation rates of 0.14 to 0.17 km.Ma^{-1} in the uppermost crustal levels, as revealed by the mineral pair approach (fig. 5b). The three odd data in this plot all come from the eastern part of the Bergell pluton where perturbation in ages has been previously discussed (see section 3.2.2). Alternatively the whole AFT ages for the tectonic blocks in the southeastern part of the field (blocks 3, 4 and 5), i.e. mainly intrusive rocks all together, correlate closely with sample elevation within error margins and point out a common exhumation rate of ca. 0.25 mm.yr-1.

In the Southern Alps, the AFT ages are split in two groups: the eastern samples (in the Como lake region and east of it, fig. 2) were by some 3-4 kms to the surface at 6-9 Ma, the western ones (west of Como lake) reached the same depth between 14 and 24 Ma and correlate closely with the topographic altitude within 1 σ-error. The latter rocks have been exhumed at a rate of 0.19 mm.yr^{-1} between 24 and 14 Ma (fig. 7f). Due to the discrepancy between western and eastern ages, the age-altitude correlation for all the samples is meaningless. The western basement rocks of the southalpine unit cooled at mean rates of 3 to 5 °C.Ma^{-1} in the early to Middle Miocene and indeed thus reached the surface at mean rates in the order of 0.1 to 0.17 km.Ma^{-1}, while east of Como lake near-surface cooling was achieved at a rate of 8 to 12° C.Ma^{-1} akin to a mean exhumation rate of 0.27 to 0.4 km.Ma^{-1} during the late Miocene (fig. 5b). These data thus suggest a differential cooling along-strike in the Southern Alps during the Miocene, while the eastern samples uplifted to the surface twice faster as compared to the western part.

DISCUSSION

In brief, not all the analysed regions were exhumed at the same time, and potential spatial and temporal variations in the near-surface cooling and exhumation rates at the intra-block level can be recognized from the whole data set of the northernmost tectonic blocks (blocks 1 and 2). Conversely the overall exhumation history of the southeasternmost terranes not readily affected by tilting (blocks 3, 4 and 5) doesn't document such variations. In the depth interval between the closure temperature of the AFT and ZFT systems, i.e. within within 8 to 3 kms of the surface, an homogeneous relatively high regional mean cooling rate of 10 to 30°C.Ma^{-1} prevailed in the Bergell area. Higher estimates up to 40-50°C.Ma^{-1} however have been even calculated for the Novate granite and SSB rocks. In all cases rocks reached the near-surface at mean rates greater than 0.5 km.Ma-1, and values in the range of 1 o 1.9 km.Ma^{-1} are found to be regionally the rule during the early Lower Miocene (fig. 5b). On the whole near-surface rocks in the Eastern Central Alps have been exhumed by the late Lower Miocene to beginning Upper Miocene at a mean rate of ca. 0.20-0.25 km.Ma^{-1}, for mean cooling rates of 4 to 7 °C.Ma^{-1}. These results support that this part of the Alps were not being exhumed at a steady rate during the Miocene.

The Lower Penninic Units and the western part of the Tambo nappe depart somewhat from this scenario since the rocks there were within 3 kms of the surface by late Miocene to early Pliocene, and cooled down at highly varying mean rates in the range of 6 to 18°C.Ma^{-1}, thus up to three times higher estimates as compared to other tectonic blocks (fig. 5b). As the western part of the Tambo nappe is implied in the relative high cooling rates similar to those characteristics of the Adula nappe, tectonically-driven surface uplift at the Forcola Line is not a viable mechanism to explain the marked difference in the mean cooling rates since the late Miocene. Without thermal modeling it is however not possible to decide whether these mean cooling rates are constant over that time or correspond to pulses of exhumation through time. On the basis of the calculated mean cooling rates during the Miocene, no significant tectonic denudation potentially linked to the activity of the Engadine and Tonale Lines during that time is evidenced. The Tonale Line however clearly marks the limit between the highly exhumed north Alpine and the cold south Alpine domains in the early Lower Miocene.

The documented variation in apparent ages and cooling rates may result from a number of processes such as: the variable chemistry of the apatites and associated variability in the annealing characteristics, the long-scale changes in surface morphology and subsequent changes on the geometry of the isotherms, the influence of heat advection and non-steady isotherms, variable erosion rates, diverse small-scale (intra-block) and/or regional tectonic activity at block boundaries, and the methodological and/or system calibration differences set by various analysts. The disrupted pattern in the age-elevation plot of the Novate granite block is most probably related to system calibration differences, since individual linear arrays have been dated by two different analysts and show no systematic relation to major or small-scale tectonics. The chemistry of the apatites has not been investigated therein and both the influence of topography effect and advective heat transfer have proven to be negligible for exhumation rates below 0.5 km.Ma^{-1} and 1 km.Ma^{-1}, respectively (Mancktelow and Grasemann, 1997). In the Lower Penninic basement block, as the vertical relief is greater than 2 kms and local exhumation rates higher than 0.5 km.Ma^{-1} a perturbation of the apatite closure temperature isotherm is made possible, which could potentially make clear the documented variations in cooling rates at the intra-block level.

Alternatively, a breakdown into the structural setting of the five north Alpine fault-bounded terranes might bring about clear trends: all the tectonic units are heavily disrupted by numerous faults and potential tectonic lineaments at the internal level. In the Bergell block for example, a complex and heterogeneous fault pattern is found involving widespread normal and oblique-normal faulting (insert map in fig. 3, Ciancaleoni et al., 2004). But the age pattern there is not significantly disrupted (fig.7d). Due to the steep slope of the regression line in the age-elevation plot in the Bergell unit, this consideration must be however taken into account with caution. Conversely, the higher variation of the ages with respect to the topographic altitude in Lower and Upper Penninic Unit is likely to display some relation to prominent tectonic lineaments (Allanic et al., 2005), provided they displace rocks with a significant vertical displacement component. A systematic investigation of the spatial variation of the cooling rates in relation to the intra-block fault slip would be nevertheless critical to any reconstruction of the late exhumation history of these terranes. Still pulses of exhumation and contrasting exhumation histories from adjoining fault-bounded blocks can be the result of major tectonic boundary activity. Fission-track analysis eventually provides in such cases information on the kinematics and age of slip events on major tectonic contacts. These aspects will be discussed in details in the following section through a series of orogen-parallel and orogen-perpendicular profiles, across the major tectonic contacts and disrupted blocks.

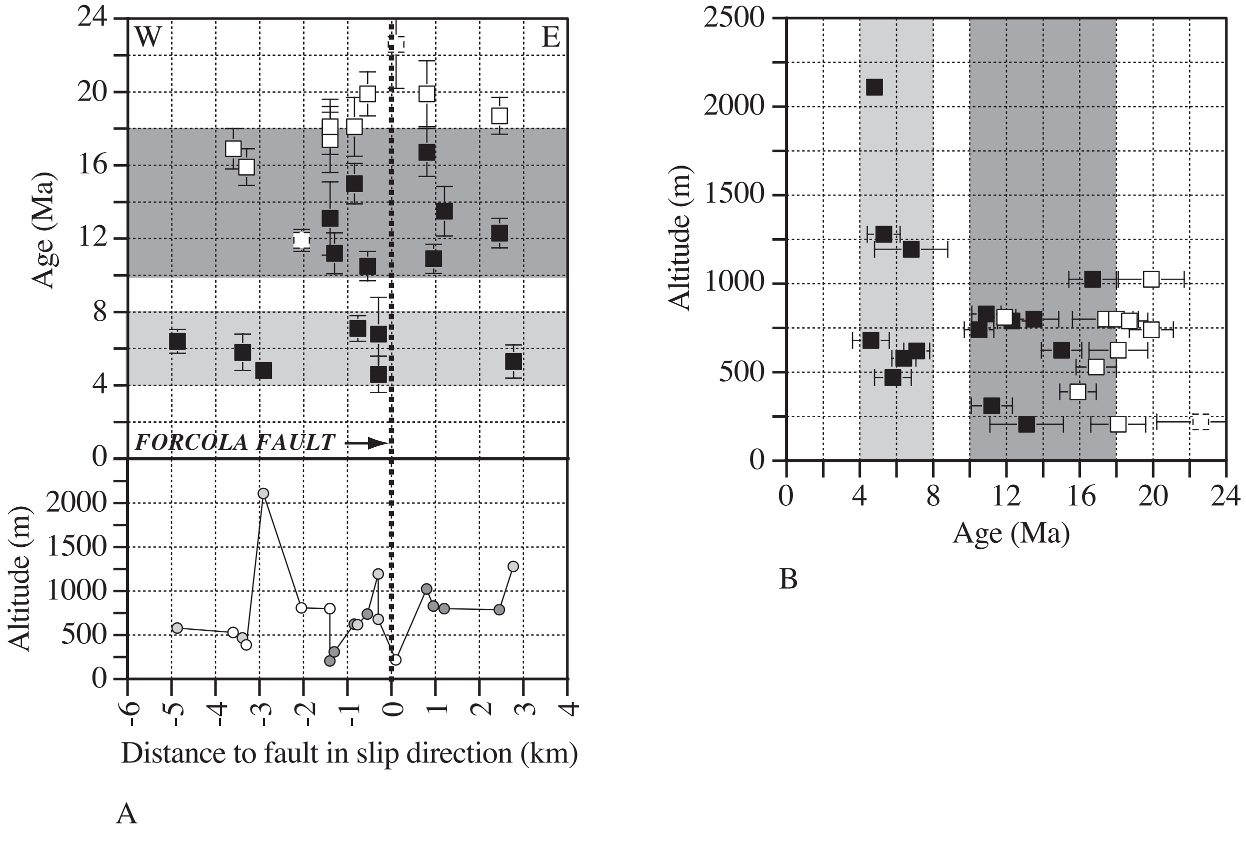

Fig. 8. Age vs. (A) normal distance to the Forcola Line profile, including all samples in the vicinity of the fault and (B) sample elevation. Same symbols as in figure 7. Light and heavy shaded grey areas correspond to the apatite age distribution of northern and southern samples, respectively, along-strike of the fault (compare with fig. 2). Error bars are ± 1σ.

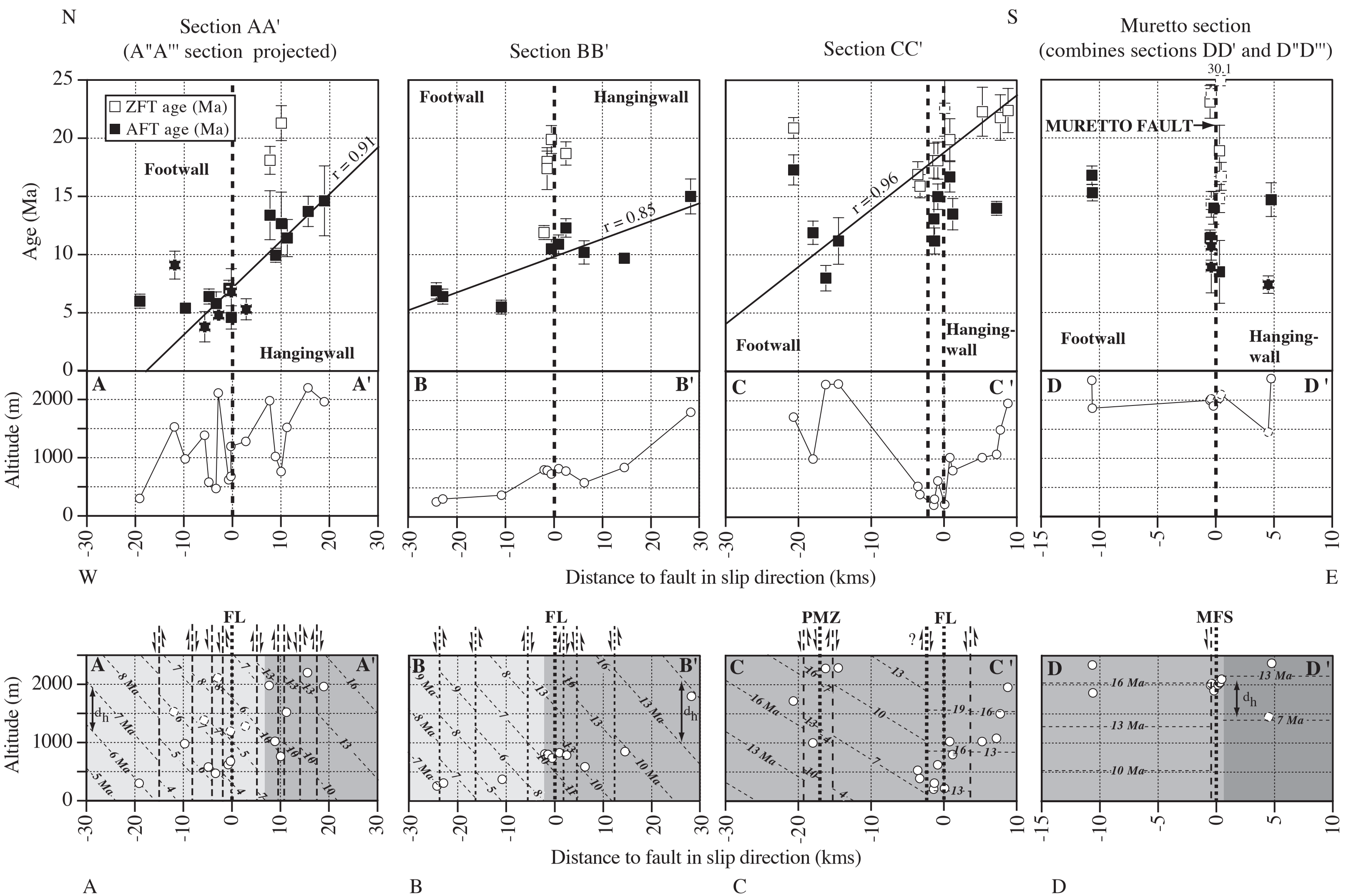

Fig. 9. (A-C) Top: apatite and zircon fission track ages projected on three ENE-WSW-oriented profiles across the Forcola Line and nappe contacts. Same symbols as in figure 7. Error bars are ± 1σ. Bottom: attempt of reconstruction of apatite paleo-isotherms geometry along the profiles. Vertical exaggeration: x12 in plots A and B, x8 in plot C. Light, medium and dark grey shades correspond to mean exhumation rates of 500m.Ma-1, 250m.Ma-1 and 125m.Ma-1, respectively. Exhumation rate is given by dh/dt. Dashed vertical lines indicate potential faults with sense of shear. Dashed samples in (A) top and bottom: projected from profiles A"A"'. (D) Apatite and zircon fission fission track ages from profiles DD' and D"D"' projected on one ENE-WSW-oriented profile across the Muretto Line. Square on 25 Ma line: partially annealed zircon samples with out of scale corresponding age. Dashed samples are from profile D"D"'. Profile traces are indicated in fig. 2. See text for discussion.

3.4. Inferences regarding the tectonic contacts and fault activity at the intra-block level

With the help of the overall AFT and ZFT age database we now propose 8 AFT and ZFT sections (figs. 8, 9 and 10) transverse to the tectonic structures (location on figure 2) in order to discuss the tectonically-driven part of the exhumation pattern across the collisional wedge.

3.4.1. The orogen-parallel sections

THE FORCOLA SECTIONS

A breakdown into the immediate vicinity of the Forcola Line (fig. 8a), with all samples projected on a section at right angle to the fault, definitely evidences: (a) no offset of both the ZFT and AFT ages across the line and (b) the post-Forcola differential exhumation underwent by the northern (light grey) and southern (dark grey) segments of the fault, due to post-16 Ma tilting around an axis perpendicular to it. The similarity of AFT and ZFT ages at ca. 16 Ma across the southern part of the fault is however problematic and is discussed below. The age vs. elevation plot (fig. 8b) clearly evidences that the northern part of the fault uplifted to the near-surface later and faster (between 4-8 Ma at a minimum rate of 0.5 mm.yr^{-1}) as compared to its southern end (between 10 and 17 Ma at slower rate). Accordingly apatites from the southern samples fail the chi-squared test whilst the northern ones don't and thus uplifted faster in the APAZ (see tables 1 and 2).

The sections perpendicular to the Forcola Line further support no abrupt increase of both AFT and ZFT ages at the fault trace (fig. 9a-c, top). Rather the ages are part of a gradient of steadily decreasing AFT ages across the major fault and toward the Lepontine dome's interior and north, i.e. toward more external zones (compare northern and southern sections AA' to CC'). Due to the considerable lack of ZFT ages from the dome's deeper levels, such a gradient can not be clearly demonstrated by the available zircon data, except maybe from section CC' (fig. 9c).

Across the Val Mera however the similar 15-17 Ma old ZFT and AFT ages from the Adula and Novate samples (namely FORC6, FORC7 and Kaw 2620, Kaw 2621, fig. 2, fig. 8a and fig. 9c, top) over less than 5 kms distance is rather problematic and argues in favor of a faulting event because an unrealistic tilt angle would be necessary to accommodate such a differential cooling across such a narrow orogen-parallel distance. Because the Novate granite and the Adula nappe share the same thermal history below 300°C, the slightly youngest zircon ages in the footwall of the Forcola Line (wherever is placed the fault trace in the splay zone, see figs. 1a and 9c), although quite similar within the error margins, might date the very late increments of movements (late Lower Miocene) at the southern tip of the major fault as part of the broader gradient. According to this interpretation, the brittle throw post-17 Ma at the southern tip of the fault is supposed to reach some 3 kms or more in order to account for the similarity in AFT and ZFT ages across the fault (assuming a temperature of 120°C and 200°C for the lower and upper limit of the AFT and ZFT annealing zone, respectively).

Alternatively, moving northward a discrete discontinuity in ages could reasonably occur in the footwall (section BB') then in the hangingwall (section AA') of the Forcola Line (fig. 9a, top), as part of the broader gradient. But the gap of ZFT and AFT data there hamper any definite conclusion to be made. A set of late NNW-SSE-oriented and segmented faults with a dextral component running across the Tambo-Adula-Grüf unit contacts have indeed been described in the Val Mera area and north of it in the Tambo nappe (see insert map in fig. 3) by Marquer et al. (1998) and Huber (1999). On the other hand, the Forcola Line is apparently not significantly displaced despite part of the southern exposure of the Forcola mylonites are covered by quaternary deposits of the Val Mera making blind such a potential offset in this area. This anyway constrains the cumulated displacements on this late fault system to be probably lower than expected.

An attempt of reconstruction of the 90°C paleo-isotherm geometry in space and time, assuming a mean tilt angle of 4° and the estimated various exhumation rates across the collisional wedge, nevertheless provides the basis for the likelihood of cumulated non negligible vertical displacements (up to ca. 2 kms) on faults or sets of faults lowering the eastern block in the vicinity of the Forcola Line (fig. 9a-c, bottom). Other hypothetical young secondary faults or sets of faults (syn to post-tilt) with cumulated lower vertical displacements that might explain the minor dispersion of AFT ages in the longitudinal profiles have been tentatively drawn from such a reconstruction (figs. 9a-c, bottom). We are aware that such inferences however are based on the apatite central ages alone, which are quite similar within the error margins, and assume that all are cooling ages, and thus must be taken with care especially with regard to the estimated quantity of displacement. This reconstruction indeed better provides a qualitative work hypothesis and in all cases structural independent evidences are necessary to validate or not this work hypothesis.

THE MURETTO SECTIONS

Due to unsuitable lithologies and heterogeneous resetting of both AFT and ZFT ages, the Muretto sections are characterized by a big spread in ZFT and AFT ages over a narrow elevation range in the Muretto fault zone. While no sound conclusions can be drawn from ZFT ages, samples from the northern and southern sections nevertheless share very similar AFT ages within error margin both sides of the fault (e.g. ages at ca. 15 Ma and 10 Ma, respectively) and define a continuous pattern across the fault (fig. 9d).

In summary the increase of AFT ages toward the structurally upper units is part of a broad gradient. No abrupt offset of ZFT and AFT ages occurs at the Forcola and Muretto faults, where demonstrable displacements within the resolution of fission-track data did not occur since the Burdigalian. Displacement at the southern tip of the Forcola fault could however outlast (Middle Miocene) the slip event with respect to the northern part of the fault. Additionally this age increase appears to be possibly discontinuous within the resolution of the available data, especially in a few kms wide area located in the immediate hangingwall of the Forcola Line (middle Tambo nappe) in its northern part and possibly in its footwall at its southern termination (Adula nappe). On the basis of structural evidences and well known fault kinematics in the Bergell area (Ciancaleoni et al., 2004) we essentially relate this discrete jump in ages to post-Forcola transverse faulting with a substantial vertical component down-faulting the east.

3.4.2. The transversal sections

In the dome's deeper levels orogen-transversal sections (sections EE' and FF', fig. 10a-b, top), the AFT pattern depicts a steady but wavy gradient of slightly rejuvenating ages toward the north, which can not be simply explained by the altitude dependence but rather is basically the result of the tilting of the isograds around a belt-parallel axis. Toward the dome's periphery where the tilt dies out only the wavy pattern is preserved and essentially due here to differences in sampling elevation (section GG', fig. 10c, top). On the basis of a reconstruction of the 90°C paleo-isotherm geometry in space and time, we relate however the wavy pattern, or part of it, in all sections to be possibly due to late faulting post-dating and/or coeval with the tilt (fig. 10a-c, bottom).

In the more internal section, the increase in AFT ages follows the altitude trend in the Insubric and SSB areas. The difference in elevation between samples with similar AFT age across the Tonale Line and the Paina Marble Zone indicates however a component of north side up offset in the order of 1 to 2 kms, respectively, during the last 18 Ma (fig. 10a, bottom). Toward the dome's outside a discrete 3 to 4 Ma jump in AFT ages within error limits occurs across the Tonale Line east of Val Mera (fig. 10b-c, top). There, an opposite component of north side down displacement, in the km range, is however related to post 12 Ma tectonic activity along the Tonale Line (fig. 10b-c, bottom).

The paleo-isotherm geometry reconstruction also provides the basis for non negligible km range cumulated offset between the Upper Penninic and Grüf-Novate units on the one hand, and between the Novate and SSB-Tonalite queue units on the other hand, lowering the Novate and Grüf units in both cases (fig. 10b, bottom). Potential candidates for slip are the D3 pro-thrusts in the Chiavenna area and a set of E-W running and steeply north dipping brittle faults in the SSB, respectively (see fig. 2 and insert map in fig. 3), which could be reactivated with a normal component coeval with late

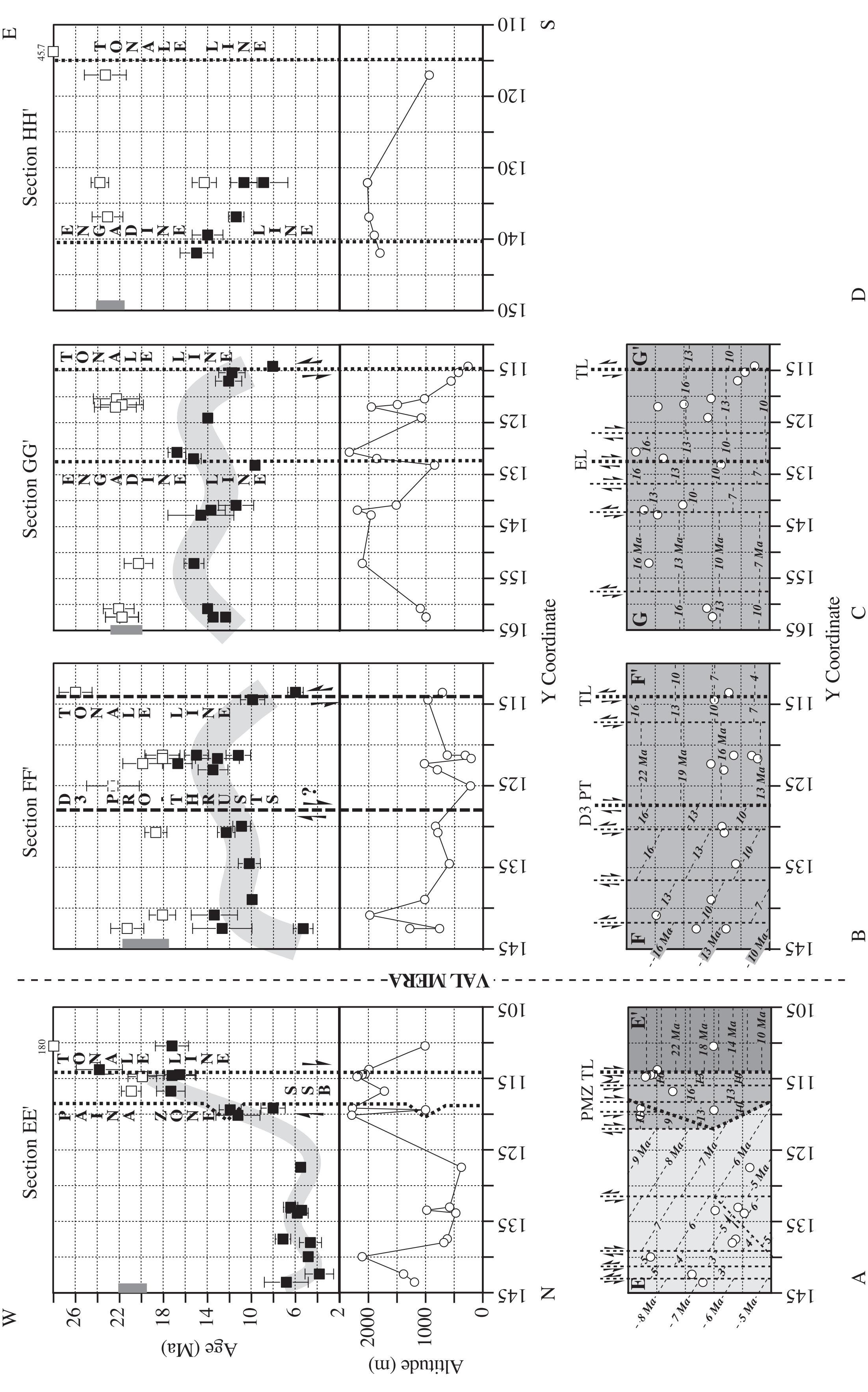

Fig. 10. (A-D) Top: apatite and zircon fission track ages projected on four NNW-SSE-oriented profiles across the major tectonic and nappe contacts. Same symbols as in figure 7. Error bars are ± 1σ. Squares at the 28 Ma line: partially annealed zircon samples with corresponding out of scale age. Light grey shaded area within each plot: age distribution trend (wavy pattern) of apatite data. Dark grey shaded area next to age scale: age distribution of zircon data. Bottom: attempt of reconstruction of apatite paleo-isotherms geometry along the profiles. Vertical exaggeration: x8, x7 and x11 for profiles EE', FF' and GG', respectively. Profile traces are indicated in fig. 2. See text for discussion.

Miocene activity on the Tonale Line. Minor fault population kinematics akin to the latter discontinuities indeed suggests local orogen-perpendicular to orogen-oblique normal slip (Ciancaleoni et al., 2004). This inference regarding the former faults suffers nonetheless independent cross-checking by field evidences since only sinistral but sparse late reactivation of these discontinuities have been documented (Huber, 1999). Further east, the available apatite data from section GG' are actually blind to such late movements across this set of faults in the SSB (fig. 10c).

Addressing the Engadine Line s.s. activity, no discontinuity of the AFT ages occurs across the fault with regard to sections GG' and HH' (fig. 10c-d, top), giving an upper limit (Langhian) for significant vertical movements along the fault. In section HH' running south of the Engadine Line in the footwall of the Muretto fault, a southward 3-4 Ma rejuvenation of AFT ages is documented for samples currently exposed at the same level. The numerous secondary faults in this area provide the opportunity for this relative differential uplift of the southern sector of the Muretto fault's footwall to occur (see insert map in fig. 3). Alternatively the differential uplift could be accommodated by a post-closure of the apatites (i.e. post-Serravallian) differential throw along-strike of the Muretto fault (higher in the south), lower than 1 km between the northern and southern samples (kaw 328 and Mu5, respectively) and compatible with the tilt proposed by Spillmann (1993) on the basis of structural evidences.

Due to the considerable gap in ZFT data in all transversal profiles no sound conclusions akin to the tectonic activity are made possible. North of the Tonale Line however, the profiles exhibit near-invariant ZFT ages over an elevation range of up to 2 kms and across the main tectonic limits (see e.g. profiles FF' and GG', fig. 10b-c, top), suggesting no vertical movement on these structures during the early Miocene in the light of the ZFT data. Additionally a very discrete westward migration of the time of cooling below 300°C may be inferred from the zircon data (22-24 Ma in section HH' down to 18-21 Ma in section FF', grey shaded boxes in fig. 10a-d, top). The Tonale Line moreover clearly marks out the boundary between annealed zircon ages in the North Alpine domain and partially annealed zircons in the South Alpine realm during the Alpine orogeny (fig. 10a, d, top).

In summary, the most striking outcome from the transversal sections is the rapid change in the slip vector orientation on the major faults of the Insubric and SSB areas and along-strike of the belt. While a post-Early Miocene to post-late Middle Miocene thrusting component associated with N-side up displacement on the Tonale Line and Paina Marble Zone is expected within the resolution of the AFT data west of Val Mera, a post-late Middle Miocene normal faulting component on the Tonale and a series of E-W parallel faults down throws the Bergell block east of Val Mera.

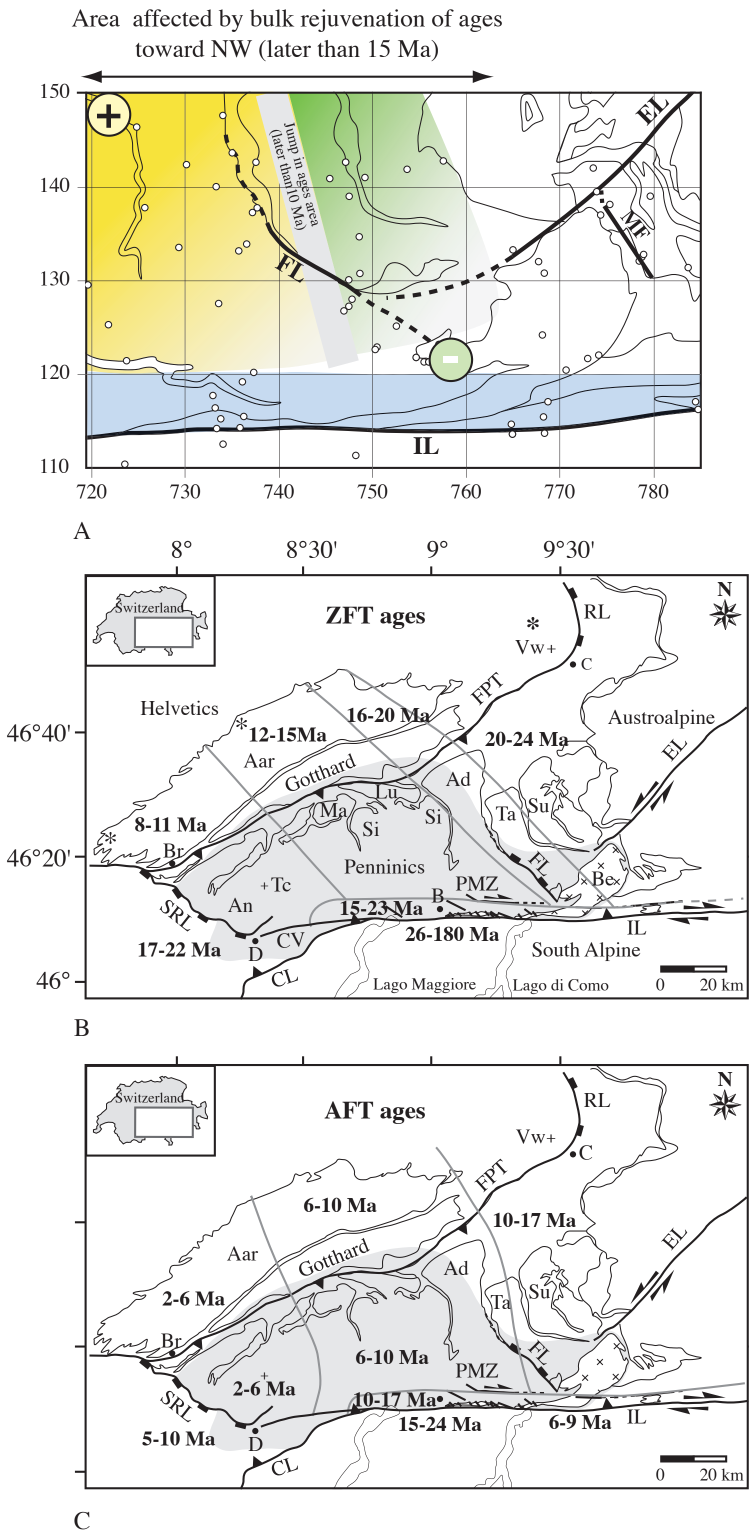

Fig. 11. (A) Bulk NW-directed decreasing apatite age and relative exhumation pattern during the Miocene in the Eastern Lepontine (plus symbol means relative more exhumation). Color code refers to fig. 4a,b. Grid reference in Swiss coordinates. White circles: sampling sites. (B) Simplified tectonic map of the Central Alps and compilation of ZFT ages with age intervals (dark grey lines). Modified from Rosenberg and Heller (1997). Stars indicate location of pre-alpine zircon ages. (C) Idem but with AFT ages. Shaded area in figures B and C: high-grade Lepontine dome. Nappe abbreviations are: Ad, Adula; An, Antigorio; Lu, Lucomagno; Ma, Maggia; Ml, Monte Leone; Si, Simano; Su, Suretta; Ta, Tambo. Other abbreviations are: B, Bellinzona; Be, Bergell pluton; Br, Brig; C, Chur; D, Domodossola; Tc, Toce culmination; CL, Canavese Line, EL, Engadine Line; FL, Forcola Line; FPT, Frontal Penninic Thrust; IL, Insubric Line; PMZ, Paina Marble Zone; RL, Rhine Line; SRL, Simplon-Rhône Line; Vw, Vättis window. Age compilation from Hunziker et al. (1992) and references therein, Rahn et al. (2004), and this study.

4. Discussion

The late cooling pattern at the eastern border of the Lepontine is characterized by a horizontal gradient of decreasing cooling ages from S to N and from E to W, regardless of sampling elevation (fig. 11a). This pattern is part of a broader gradient of decreasing mineral cooling ages from internal (tectonically shallower) toward external (tectonically deeper) units and along-strike in the Central Alps (fig. 11b-c, see e.g. compilation maps in Hunziker et al., 1992 and references therein).

Cooling due to exhumation is likely to have started as soon 35 Ma at relative slow average rates (7-20°C.Ma-1) in the more internal units (Briançonnais domain, Hurford et al., 1989; Marquer et al., 1994), coeval with the activity on the Frontal Penninic Thrust (pre-30 Ma old, fig.12, e.g. Schmid et al., 1997), while the External Crystalline Massif (Aar-Gotthard) was buried and reached peak temperatures (upper greenschist facies) by that time (maximum possible age of climax at 25 Ma; Dempster, 1986). In the early stages of exhumation the cooling pattern of the Central Alps is however strongly dominated by the updoming of the Lepontine. The cooling pattern of the high-grade Lepontine dome is consistent with short periods of rapid tectonic unroofing alternating with slower exhumation rate periods. Higher rates of cooling (> 20-40°C.Ma-1) in the time span 30-20 Ma and the symmetric shape of the cooling anomaly centered on the Lepontine indeed suggest coeval periods of enhanced rates of backthrusting and uplift in the rear of the collision wedge at the Insubric Line and stages of orogen-parallel extension at the dome lateral boundaries (Forcola and Simplon

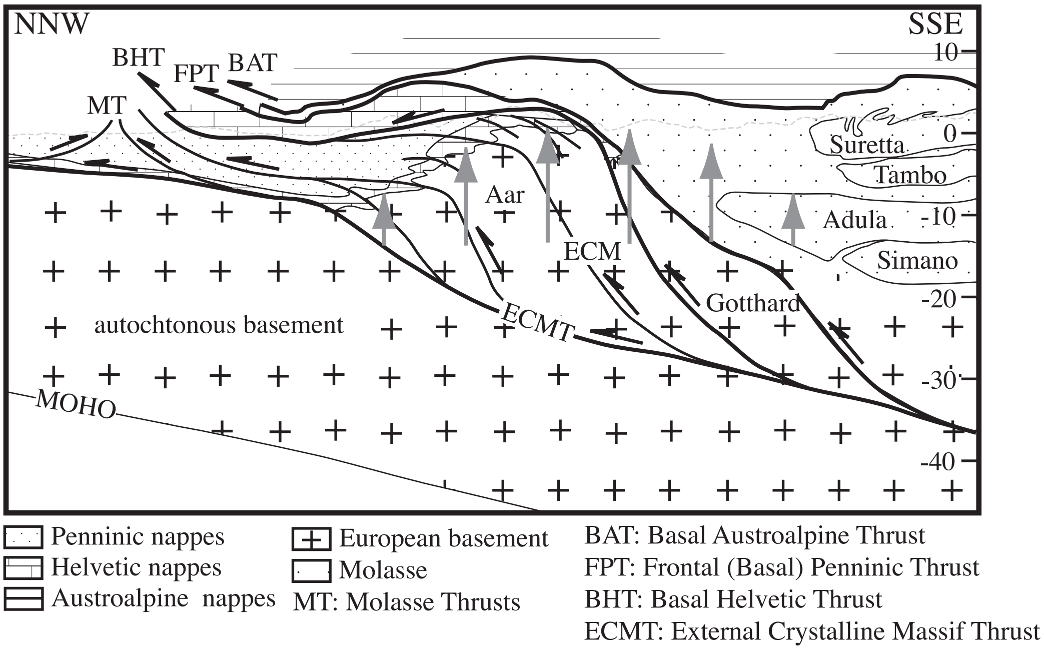

Fig. 12. Crustal scale cross-section along the Eastern Traverse (modified from Schmid et al., 1997, Burkhard, 1999; Badertcher et al, 2002). Vertical grey arrows indicate relative differential uplift within the ECM and in the hinterland by the late early Miocene onwards.

shear-zones, fig. 13; Hurford, 1986; Schmid et al., 1989; Mancktelow, 1992; Schlunegger and Willett, 1999). The enhanced cooling was then shifted westward to the Simplon footwall from the Burdigalian (e.g. Grasemann and Mancktelow, 1993), as the Central Alps were escaping sideways by dextral strike-slip and the peripheral regions of the Alps (including the External Crystalline Massif) progressively undergoing cooling at slow to moderate rates (foreland propagation of the deformation front, e.g. External Crystalline Massif Thrust, fig. 12).

From a geochronological data point of view the uplift history below 300°C (i.e. since the early Miocene) of the External Crystalline Massif (ECM) strongly resembles that of the Lepontine domain (fig. 11b-c). On the whole of the Aar massif the onset of cooling below 300°C started earlier and slower in the northeast (early Miocene) and continued later (Middle Miocene) but at higher rates toward the southwest, implying a full asymmetric updoming sequence which led to a differential exhumation cross and along-strike between the northeastern and southwestern edge of the massif (Michalski and Soom, 1990, plus and minus symbols within open and full circles, respectively, in figs. 13 and 15). Such a cross and along-strike differential cooling sequence by this time is available from the published fission track ages in the Lepontine Dome, leading to an asymmetric dome shape

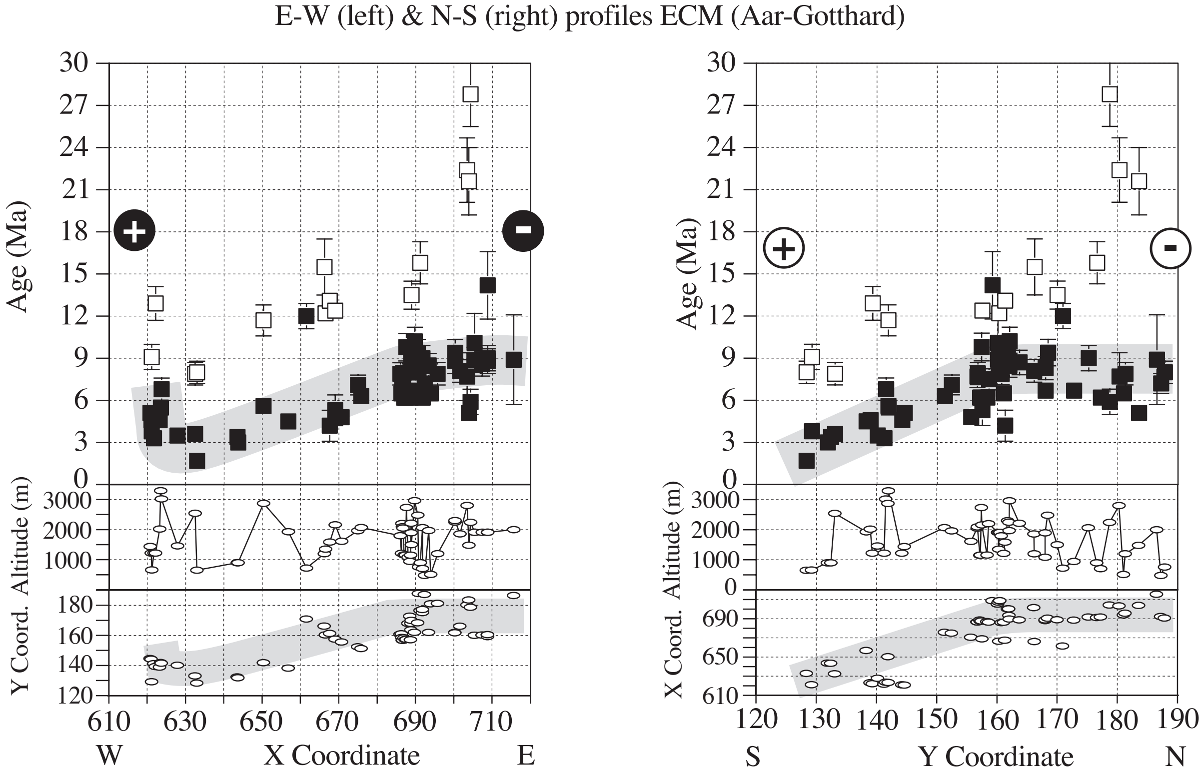

Fig. 13. Zircon and apatite fission-track ages vs. altitude and horizontal distance profiles in the ECM (Aar-Gotthard massif; redrawn from data in Michalski and Soom, 1990; Hunziker et al., 1992 and references therein). Circled plus symbols indicate relatively more and/or younger uplifted regions, as compared to circled minus ones. Open and full circles refer to transversal (right) and longitudinal profiles (left), respectively. Error bars are ± 1σ. Light grey shaded areas mirror the AFT age pattern, as compared to geographic distribution.

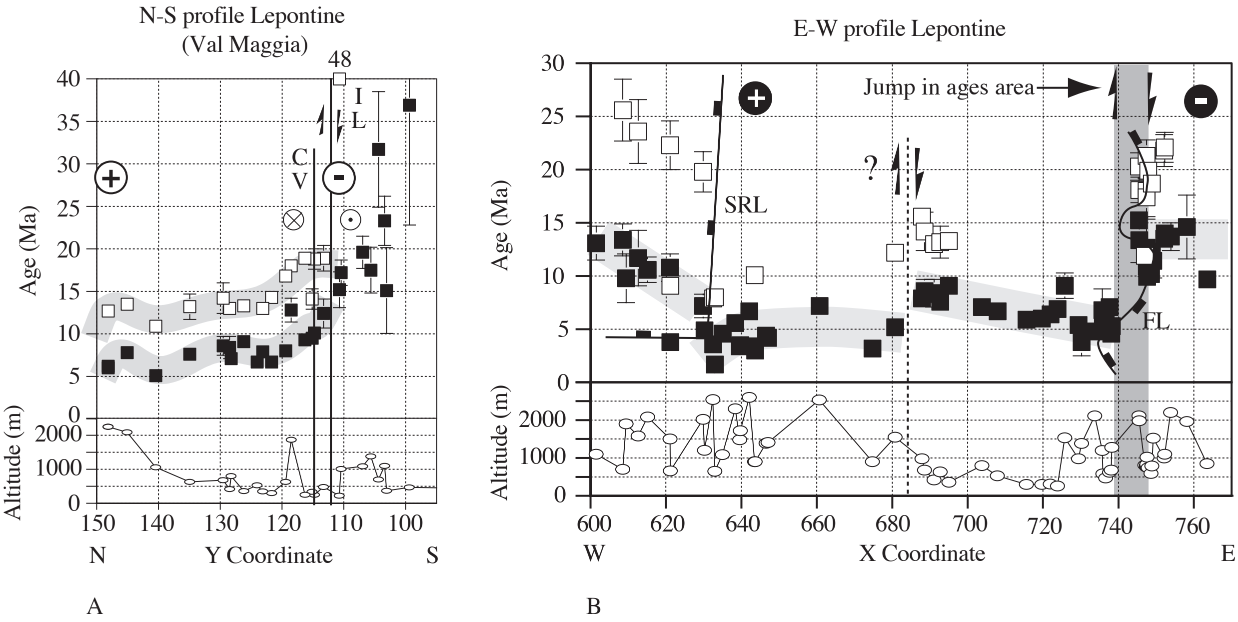

Fig. 14. Zircon and apatite fission-track ages vs. altitude and horizontal distance (A) N-S directed (redrawn from Hurford, 1986 and data in Hunziker et al., 1992, pers. comm.) and (B) E-W directed profiles in the Lepontine (redrawn from data in Hunziker et al., 1992 and references therein, Rahn et al., 2004, and this study). Same symbols and abbreviations as in figs. 11 and 13.

(more exhumation in the W and N; figs. 14 and 15 ; see also fig. 12 in Steck and Hunziker, 1994). Finally in transversal section a typical domal exhumation shape since the early Miocene encompasses the whole Aar external massif and Lepontine domain considered as a "single block", with young ages akin to enhanced uplift in the center and across the Penninic front and the old ages towards the domal rim, i.e. the Insubric Line in the south and the northern Aar massif in the north (figs. 11b-c and 15).

The oldest Alpine ZFT and AFT ages in each segment of the Lepontine are essentially found along the southern parts of the dome in the vicinity of the Insubric Line (Lower Miocene and Middle Miocene zircon and apatite ages, respectively; dark grey shaded area in fig. 15a). The former deal in the Bergell region with moderate to high exhumation rates in the range of 0.50 to 1.6 km.Ma^{-1}, most probably in response to enhanced isostatic adjustment following early and strong differential uplift of the southern study area (D3 regional phase, fig. 1b) and of the Central Alps more generally (Hurford, 1986). Accordingly simple models in which erosion rate is proportional to topographic height generate an asymmetric exhumation pattern characterized by increased uplift and erosion rates toward the retro-direction (e.g. Schlunegger and Willett, 1999). A potential break in slope is documented by the zircon data in the east Lepontine at ca. 20 Ma (fig. 6) associated with a slower and steady mean exhumation rate by the late Lower Miocene onward (fig. 7). These data might mirror a decrease in the erosional unroofing rate after 20 Ma in the highly exhumed core of the collision wedge, a necessary but non unique condition for the orogen to grow outward (e.g. Schlunegger

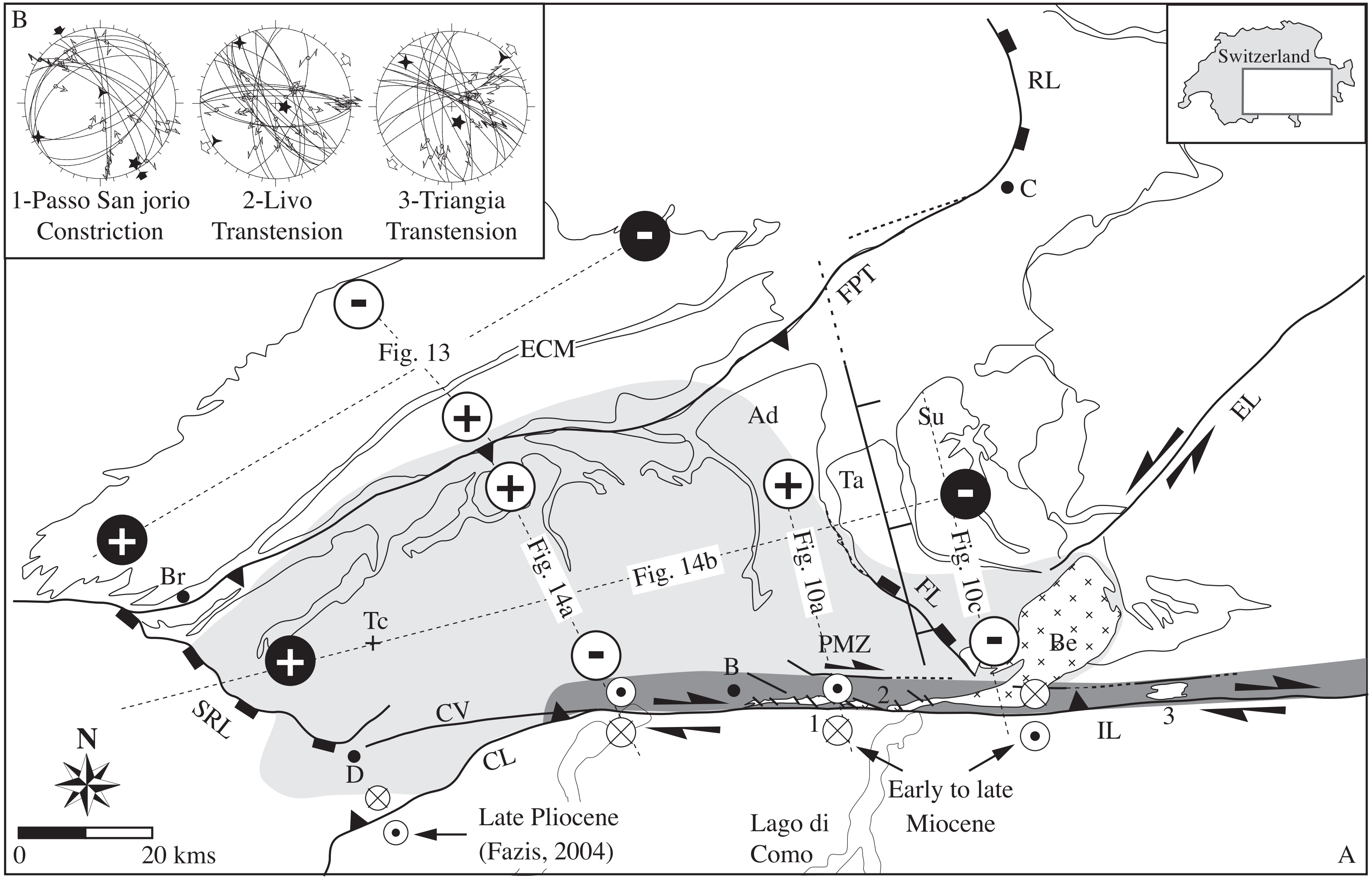

Fig. 15. (A) Cooling and relative exhumation pattern in the Central Alps during the Neogene. Same symbols and abbreviations as in figs. 11 and 13. (B) Representative minor fault population and stress inversion (lower hemisphere projection) along-strike and in the vicinity of the Tonale Fault, located in (A) by numbers 1 to 3. Five, four and three branches star represent the maximum, intermediate and minimum stress axis, respectively. Black and white arrows indicate the direction of shortening and extension, respectively. See text for discussion.

and Willett, 1999), as indicated by the onset of thrusting and uplift of the Aar ECM and shortening in the Southern Alps by this time (e.g. Schönborn, 1992 and Schmid et al., 1996a). Accordingly the high erosion rates before 20 Ma would have kept the orogen in a steady state, the convergence and increased uplift and relief being compensated by surface processes. High erosion rates and rapid exhumation of a thickness of several kilometers of high-grade rocks, in combination with back-thrusting, indeed occurred during the late Oligocene north of the Insubric Line (Giger and Hurford, 1989). Yet the sediment budget in the Alpine flanking basins independently document a drastic relative increase and decrease in the sediment discharge before and after ca. 20 Ma, respectively (Schlunegger et al., 1998; Kuhlemann et al., 2001; Bernet et al., 2001; Schlunegger and Simpson, 2002).

The 20 Ma old zircon ages in the eastern ECM have been interpreted to date the last stages of basement shortening and uplift that started in the Oligocene, as compared to the 8-15 Ma old zircons in the central and western parts of the ECM. Those latter regions conversely uplifted from the late Lower Miocene to the Upper Miocene due to outward thrust propagation also responsible for the relative higher amplitude doming there (fig. 11b, Pfiffner and Heitzmann, 1997a). Amongst tectonic models (Burkhard, 1990, Burkhard, 1999) proposed that the Aar massif was updomed since the Lower Miocene as a stack of several thrust imbricates (Boyer and Elliott, 1982) as it passed over a ramp in the basal thrust, a process coeval with thrusting and folding in the Molasse Basin and Jura mountains (10-12 Ma old), and possibly still on-going today (Persaud and Pfiffner, 2004; fig. 12).

While the 20 Ma old similar ZFT ages from the eastern Aar massif (including the Vättis window) and from the Suretta nappe imply near-horizontal isotherm, the apatite late Miocene to Pliocene paleo-isotherms are actually tilted by 18° NNW around an along-strike axis in front of and within the Aar massif (Schaer et al., 1975; Burkhard, 1999). Such a consequent tilt, 15° NW, rotated as well the Glarus Thrust and the paleo-isotherms that were lying horizontal at ca. 9 Ma (Rahn et al., 1997) above the easternmost part of the massif, but a smaller 2°N tilt was inferred for the Gotthard massif (Burkhard, 1999). In the eastern Lepontine, in the rear of the ECM culmination the herein documented post Lower Miocene mean 4° SE tilting of the apatite paleo-isotherms in the Penninic units nicely fits with the ECM uplift scenario (grey arrows in fig. 12). Yet the tilt doesn't clearly affect the zircon paleo-isotherms since no N-S gradient is relevant to the ZFT data in the tectonically upper Penninic units (figs. 4a and 10). Additionally and with regard to the apatite paleo-isotherms that tilt has been shown to progressively die out toward the Briançonnais and SSB units, i.e. in a more internal position and in the rear of the ECM culmination disappearance (figs. 12 and 15). Conversely zircons and apatites young northward within the Central Lepontine toward the ECM (Hurford et al., 1989, fig. 14a), indicating more rapid and/or more recent uplift in that direction where the Aar crest line is higher and younger as compared to the east (Burkhard, 1990; Pfiffner and Heitzmann, 1997a). This is in turn interpreted to document such a S-directed tilt implying both paleo-isotherms in the central Lepontine domain. Accordingly the age of onset of this tilting matches the estimated onset of enhanced cooling in the external massifs, starting in the early Miocene and proceeding sideways at higher rates by the middle to late Miocene onward (Michalski and Soom, 1990).

Because no major normal fault was active by the late Lower to Middle Miocene in the eastern Lepontine, surface processes achieved unroofing. Because the apatite ages broadly depend on altitude in individual blocks (fig. 7), tilting pre-dates exhumation or alternatively tilting was coeval with erosional unroofing. Low mean exhumation rates of 200 m.Ma^{-1} prevailing in the rear of the wedge since the Middle Miocene support this interpretation (fig. 7). Conversely the mean higher exhumation rates in the deeper Adula nappe and west Tambo nappe (200-600 m.Ma^{-1}) similar to the average erosion rates in the ECM (400-500 m.Ma-1, Schlunegger and Willett, 1999) and Central Alps (400-450 m.Ma^{-1} during the late Neogene to actual, Hurford, 1986; Wagner et al, 1977) might reflect the high rates of crustal uplift toward the deformation front by horizontal shortening and thrusting in the Miocene time (Burkhard, 1990; Pfiffner et al., 1997a).

Additionally the available fission-track data depict an along-strike gradient associated with migration of the time of enhanced cooling and exhumation toward deeper levels of the Lepontine dome. At the eastern border of the Lepontine the change to Lower Miocene zircon ages and to Middle Miocene apatite ages is part of a broader gradient of smoothly increasing ages from the structurally deeper to shallower east dipping units and across the Forcola Line (figs. 7 and 9). Because similar published ZFT and AFT ages at similar elevation are found at both lateral borders of the dome (at ca. 10-14 Ma), and assuming a geothermal gradient of 30°C.km-1 and 150°C temperature difference between the closure of the zircons and the apatites, a mean 4°(N)E tilt around an axis normal to strike can be estimated, in order to take into account ca. 5kms additional uplift in the western Lepontine since the late Middle Miocene (fig. 11 b-c, fig. 14b). Similarly a comparable mean 3°NE tilt deals with the late Miocene FT data at both along-strike extremities of the Aar massif (fig. 13 right).

On the basis of paleomagnetic data, Rosenberg and Heller (1997) proposed that a 15° E tilting of the central Lepontine around an N-S striking axis located in the area of the Como lake and Val Mera (figs. 1a and 15) is due to differential vertical uplift of the western Lepontine as a consequence of increased N-S shortening there. In their model the onset of tilting migrates westward (as old as 30-25 Ma in the Bergell region and post-20 Ma in the Central Lepontine) in line with the shifting of the enhanced N-S shortening across the Swiss Alpine chain, and is accommodated along the major faults of the PFS (Simplon, Insubric and Engadine Lines) in the Swiss Alps. Considering 15 kms of relative vertical displacement of the Simplon fault footwall since ca. 20 Ma (Grasemann and Mancktelow, 1993) the 10 kms additional uplift of the Central Lepontine east of the Toce culmination (western limit of prevailing E dipping foliation in the dome, fig. 15a) within 6-8 Ma correspond to a mean exhumation rate of 1.3-1.6 km.Ma^{-1} between ca. 20 Ma and 12 Ma. This estimation matches the previously documented 1.5 km.Ma^{-1} exhumation rate of the Lepontine core for the period 22-12 Ma, summed up over 1 km.Ma^{-1} of tectonic unroofing and 0.5 km.Ma^{-1} of surface processes (Kuhlemann et al., 2001), and the middle Miocene mean cooling rate of 40°C.Ma-1 deduced for the Lower Penninic nappes (Spiegel et al., 2000). The estimated 4°E tilt since the rocks of the Central Lepontine were by some 8 kms to the surface is thus coherent with the scenario of a broader 15°E tilting process that started in the Oligocene to early Miocene in the eastern Lepontine.

Another issue regarding the tiltings concerns the present day mean 40-50° NE dip of the Forcola mylonites, which have been tilted by some 4 to 15°E and 4°SE, cross and along-strike respectively, after the fault motion (fig. 8). Restoration yields an original shallower dip angle of ca. 34-44°NE, pretty close to the dip angle expected for low-angle normal faults.

The steady nature of the gradient is potentially slightly disrupted in places, leading to the wavy shape (e.g. fig. 10), but more severely in the middle part of the Tambo nappe and possibly in the southeastern part of the Adula nappe, at a prominent set of transversal faults (figs. 4b, 14b and 15). This jump in ages at the transversal faults could be as young as the Tortonian and coincides with the inferred location of the N-S tilt axis as proposed by Rosenberg and Heller (1997). This location further coincides with (fig. 13): (a) the eastern beginning of the ECM height further north and west of the tilt axis, which uplift started in the Oligocene to early Miocene; (b) the progressive vanishing out of both the mean 4°SE and 4°E tilts due to uplift of the ECM and central to western Lepontine; (c) the late Miocene enhanced cooling rates in the Adula and western Tambo nappe, west of the tilt axis; (d) the transitional region of differential throw along the Tonale Line, west and east of the Val Mera-Como lake respectively, during the late Middle Miocene to Upper Miocene (figs 10 and 15).

These considerations suggest a cause and effect relationship. In this block rotation model due to along-strike tilting, oblique slip associated with relative uplift of the Central and Western Lepontine (western block) and downfaulting of the Bergell pluton (eastern block) along-strike of the Tonale Line (pitch W and E for the slickenline, respectively) is expected to accommodate the post-20 Ma westward migration of the time of enhanced cooling and uplift. Accordingly, the westernmost Southern Alps samples in the vicinity of the Insubric Line (assumed to be fully annealed by the backthrusting event) cooled earlier (15-24 Ma) but slower through the APAZ than those situated in the

Como Lake area and east of it, which cooled later (6-9 Ma) but twice faster at the same depth (fig. 11c). This is not difficult to reconcile with a differential movement opposite and akin to the one underwent by the block north of the Tonale Line. Furthermore according to Schmid et al. (1996a) the amount of post early Miocene N-S shortening within the Southern Alps decreases toward the western margin (Canavese region, fig. 15a). Conversely in the North Alpine realm the post early-Miocene maximum total shortening across the belt occurs north of this major bend in the Periadriatic Line i.e. in the western ECM and Lepontine regions (Schmid et al., 1989). But the additional N-S shortening and uplift there is however accommodated by the Simplon detachment that promoted the differential exhumation of the Lepontine (Mancktelow and Pavlis, 1994; Rosenberg and Heller, 1997), a scenario quite different of that of the Southern Alps where no equivalent of such a normal fault of the same age is known. Consequently it is not surprising that rocks that underwent more shortening and exhumation south of the Tonale Line are easternmost ones, exactly in an opposite way to the northern block situation. Such large-scale differential uplift and tilting due to along-strike variation in the total amount of shortening has been recognized as a viable mechanism in the Western Alps (Fügenschuh and Schmid, 2003).

Assuming a brittle dextral offset magnitude of half the estimates of total displacement on the Insubric Line (30 to 60 kms summed up over the ductile and brittle displacement, Heitzmann, 1987a; Schmid et al., 1989; Viola, 2000), a dip angle of 4 to 8° for the slip vector on the Tonale Line would account for the < 2 kms of vertical differential throw during the Neogene (fig. 10a-c). Because reliable outcrops of the brittle Tonale master fault are very scarce, field evidences that might support this interpretation are difficult to establish. Schmid et al. (1989) however describe systematic gently easterly dipping striations for the all extent of the Tonale Line between the Central Lepontine and the eastern Bergell area, thus not readily in line with our interpretation. North of the Como lake, south block up displacement (inferred from drag folding of the sedimentary cover of the South Alpine basement) but sub-horizontal to gently east plunging slickenlines (< 10°E) characterize the exposed fault plane (Fumasoli, 1974), in the supposed tilt axis location (transitional) area. Recent field investigations (Ciancaleoni et al., 2004) regarding the minor faults in the immediate vicinity of the master fault revealed nevertheless a bulk late transtensional strain field in the Sondrio intrusion, while a bulk constrictive one cataclasizes the dextral mylonites at Passo San Jorio (fig. 15b). Further east of Sondrio, Meier (2003) also described late discrete cataclastic N-dipping shear-zones bearing steep slickenlines in the close vicinity to the Tonale Line but associated with a non-systematic south side up movement. Concerning the PMZ, late brittle deformation and cataclasis post-date the calcite mylonites, and fault planes bear both sub-horizontal, eastward and westward dipping striations (Fumasoli, 1974; Heitzmann, 1987a). Thus structural evidences that might support our interpretation of the along-strike differential throw are ambiguous but reasonably provide the basis for the viability of such a mechanism.

Furthermore late transversal faulting associated with downfaulting of the eastern block is also likely to accommodate the differential uplift of the Lepontine and ECM, especially in the area where the tilts progressively die out (less Neogene relative uplift) and the change in vector of movement along the SSB occurs (fig. 15a). Alternatively to tilting of a large rigid block (the Central Alps), a series of discrete late transversal faults with systematic west side-up sense of shear can be envisaged in order to explain the differential uplift. This is not actually documented neither by field investigations in the Bergell area (fig. 3, Ciancaleoni et al., 2004), nor by the breaking up of the AFT pattern possibly due to faulting (figs. 9 and 10), since both approaches show that opposite shear-senses are common. Recent studies in the Central and Western Alps show that transcurrent, transtensive and extensional regimes of deformation, with no or minor compressive ones, dominate in the internal parts of the orogen during the Neogene to actual (Sue and Tricart, 2003; Champagnac et al., 2004; Delacou et al., 2004; Ciancaleoni et al., 2004). These studies in the Western Alps indicate a change in the deformation mode from early (late Oligocene to Miocene) orogen-parallel extrusion over later (Upper Miocene to recent) orogen-perpendicular spreading. Comparatively, such faults with a relative minor vertical component of displacement (figs. 9 and 10), as young as Upper Miocene in the eastern Lepontine, are most probably normal and/or oblique-normal faults that stretch the belt both cross and along-strike. These structures address minor isostatic readjustment and/or strain accommodation issues. Despite the real lack of a sound understanding of the late brittle tectonics in the deeper nappes of the Lepontine including the Adula nappe, normal faulting during closure of the apatites remains a viable mechanism to explain the small-scale spatial variations in exhumation rates and the wavy FT pattern (in both longitudinal and transversal sections) at the intra-block level (figs. 10a and 14a,b). This interpretation is easy to reconcile with the Neogene differential exhumation pattern of both the ECM and Lepontine domains, along and cross-strike of the belt. It is ergo suggested that those faults with a moderate normal component may be of different age in the eastern Lepontine, some of pre-Middle Miocene age contemporaneous with the Forcola extension phase (Ciancaleoni et al., 2004), and some younger ones (re-)activated as isostatic and/or strain accomodation response to the bulk northwestward migration of enhanced uplift in the Central Alps. Eventually this might lead to very young (Pliocene) normal fault movement reactivation of the Insubric Line in the bend region (Fazis, 2004, fig. 15a), south of the area that underwent the maximum amount of transversal shortening during the Neogene.

5. Conclusions

New zircon and apatite fission-track data, together with litterature data, provide new constraints regarding the Neogene activity of the PFS segments in the eastern Lepontine. The sections perpendicular to the Engadine and Forcola Lines, responsible pro parte for the exhumation of the Lepontine dome and Bergell area, respectively, in the late Oligocene, support that significant vertical movements along the faults ceased during the Burdigalian times. Conversely, minor differential throw along-strike of the Muretto fault suggests younger (post-Serravallian) slip increments in this complex fault zone.

Regarding the Tonale fault, the FT data suggest a rapid change in the kinematics of movement, located in the Val Mera-Como lake area, leading to oblique slip and block rotation during the late Middle Miocene to Upper Miocene. Differential throw along-strike resulted in the relative uplift of the Central and Western Lepontine (western block) and downfaulting of the Bergell pluton (eastern block).

The available fission-track data at the eastern border of the Lepontine depict a twofold horizontal gradient of steadily decreasing AFT ages across the major faults and toward the west and north, with disregard for altitude dependence. This late cooling pattern is actually part of a cross and along-strike broader steady gradient associated with migration of the time of enhanced cooling and exhumation toward the ECM and deeper levels of the Lepontine. This pattern is interpreted to be basically due to post-early Miocene S(E)-directed and (N)E-directed tilting of the paleo-isotherms around a strike-parallel and strike-normal axis, respectively. It is suggested that the bulk tilting is related to the post-20 Ma outward migration of the time of enhanced shortening, cooling and uplift in the ECM and Central Lepontine regions.

Tilting post-dates the early Miocene unroofing of the highly exhumed core of the collision wedge at moderate to high exhumation rates in the range of 0.50 to 1.6 km.Ma^{-1}, most probably in response to enhanced isostatic adjustment following early and strong differential uplift toward the retro-direction. In the absence of significant post-early Miocene normal faulting in the eastern Lepontine, tilting was coeval with erosional unroofing, at lower and steady mean rates of ca. 0.20-0.25 km.Ma^{-1} during the late Lower Miocene to beginning Upper Miocene.

The steady nature of the gradient is slightly disrupted in places, leading to a wavy shape of the FT pattern, but more severely in the middle part of the Tambo nappe and across the Forcola Line in the southeastern part of the Adula nappe, at a prominent set of transversal faults lowering the eastern block. Accordingly, block rotation along-strike of the Tonale fault and SSB, as well as brittle normal faulting with a relative small magnitude of displacement at the intra-block level in the hinterland adress strain accomodation and/or minor isostatic readjustement issues in response to the differential Neogene exhumation pattern of the Central Alps.

REFERENCES

Allanic, C., Sue, C., Champagnac, J. D., Delacou, B. and Burkhard, M. (2005). New constraints on the brittle deformation in the Lepontine Alps, from paleostress and pseudotachylites analyses. European Geosciences Union 2005, Vienna, Austria, 24 - 29 April 2005.

Argand, E. (1916). Sur l'arc des Alpes Occidentales. Eclog. Geol. Helv. 14: 145-204.

Berger, A. and Gieré, R. (1995). Structural observations at the eastern contact of the Bergell pluton. Schweiz Miner. Petr. Mitt. 75(241-258).

Berger, A., Rosenberg, C. and Schmid, S. M. (1996). Ascent, emplacement and exhumation of the Bergell pluton within the Southern Steep Belt of the Central Alps. Schweiz Miner. Petr. Mitt. 76: 357-382.

Bernet, M., Zattin, M., Garver, J. L., Brandon, M. T. and Vance, J. A. (2001). Steady-state exhumation of the European Alps. Geology 29(1): 35-38.

Boyer, S. E. and Elliott, D. (1982). The geometry of thrust systems. Bull. Amer. Ass. Petroleum Geol. 66: 1196-11230.

Burkhard, M. (1990). Aspects of the large-scale Miocene deformation in the most external part of the Swiss Alps (Subalpine Molasse to Jura fold belt). Eclogae Geol. Helv. 83(3): 559-583.

Burkhard, M. (1999). Strukturgeologie und tektonik im Bereich Alp Transit. Vorerkundung und Prognose der Basistunnels am Gotthard und am Lötschberg, Zürich, A.A. Balkema.

Champagnac, J. D., Sue, C., Delacou, B. and Burkhard, M. (2004). Brittle deformation in the inner north-western Alps: from early orogen-parallel extrusion to late orogen-perpendicular collapse. Terra Nova 16: 232-242.

Ciancaleoni, L. and Marquer, D. (2004). Syn-extension leucogranite emplacement during convergence in the Eastern Central Alps: case example from the Novate intrusion. Swiss Geoscience Meeting 2004, Université de Lausanne.

Ciancaleoni, L., Marquer, D., Fügenschuh, B., Rahn, M. K. and Sue, C. (2004). Deformation processes during the last stages of the continental collision in the internal part of a mountain belt at the brittle-ductile transition: the Eastern Central Alps case (Bergell and Insubric areas). Swiss Geoscience Meeting 2004, Université de Lausanne.

Delacou, B., Sue, C., Champagnac, J. D. and Burkhard, M. (2004). Present day geodynamics in the bend of the Western and central Alps as constrained by earthquake analysis. Geophys. J. int 158: 753-774.

Dempster, T. (1986). Isotope systematics in minerals: Biotite rejuvenation and exchange during Alpine metamorphism. Earth Planet. Sci. Letters 78: 355-367.

Dodson, M. H. (1973). Closure temperature in cooling geochronological and petrological systems. Contrib. Min. Pet. 40: 259-274.

Fazis, Y. (2004). Finding faults! A normal fault component in the Insubric Line? New apatite fission track ages in the Val d'Ossola / Alps of Italy. Swiss Geoscience Meeting 2004, Université de Lausanne.

Fügenschuh, B. and Schmid, S. M. (2003). Late stages of deformation and exhumation of an orogen constrained by fission-track data: a case study in the Western Alps. GSA Bulletin 115(11): 1425-1440.

Fumasoli, M. W. (1974). Geologie des Gebietes nördlich une südlich der Jorio-Tonale-Linie im westen von Gravedona (Como, Italia). Zürich, Universität Zürich ETH: 230.

Galbraith, R. F. and Laslett, G. M. (1993). Statistical models for mixed fission track ages. Nuclear Tracks and Radiation Measurements 21(4): 459-470.

Gebauer, D. (1996). A P-T-t path for a high pressure ultramafic rock-associations and their felsic country-rocks based on SHRIMP dating of magmatic and metamorphic zircon domains. Example: Alpe Arami (Central Swiss Alps). Earth Processes: Reading the Isotopic Code. A. Basu and S. R. Hart, Geophys. Monogr. Ser. 95: 307-328.

Gebauer, D. (1999). Alpine geochronology of the Central and Western Alps: new constraints for a complex geodynamic evolution. Schweiz. Mineral. Petrogr. Mitt. 79: 191-208.

Giger, M. and Hurford, A. J. (1989). Tertiary intrusives of the Central Alps: their Tertiary uplift, erosion, redeposition and burial in the south-alpine foreland. Eclog. Geol. Helv. 82: 857-866.

Giger, M. (1991). Geochronologische und petrographische studien an Geröllen und Sedimenten der Gonfolite-Lombarda Gruppe (Südschweiz und Norditalien) und hir Vergleich mit dem alpinen Hinterland. Bern, Universität Bern: 227.

Gleadow, A. J. W. and Fitzgerald, P. G. (1987). Uplift history and structure of the Transantartic Mountains: new evidence from fission track dating of basement apatites in the Dry Valleys area, southern Victoria Land. Earth Planet. Sci. Letters 82: 1-14.

Gleadow, A. J. W. and Brown, R. W. (1999). Fission track thermochronology and the long-term denudational response to tectonics. Geomorphology and Global Tectonics. M. A. Summerfield, John Wiley and Sons Ltd, Chichester: 57-75.

Grasemann, B. and Mancktelow, N. (1993). Two-dimensional thermal modelling of normal faulting: the Simplon Fault Zone, Central Alps, Switzerland. Tectonophysics 225: 155-165.

Green, P. F., Duddy, I. R., Laslett, G. M., Hegarty, K. A., Gleadow, A. J. W. and Lovering, J. F. (1989). Thermal annealing of fission tracks in apatite

4. quantitative modelling techniques and extension to geological timescales. Chem. Geol. 79: 155-182.

Hansmann, W. (1996). Age determination on the Tertiary Masino-Bregaglia (Bergell) intrusives (Italy, Switzerland): a review. Schweiz. Mineral. Petrogr. Mitt. 76: 421-451.

Heitzmann, P. (1987a). Evidence of late oligocene/early miocene backthrusting in the central alpine "root zone". Geodinamica Acta 1(3): 183-192.

Huber, R. K. and Marquer, D. (1996). Tertiary deformation and kinematics of the southern part of the Tambo and the Suretta nappes (Val Bregaglia, Eastern Swiss Alps). Schweiz. Mineral. Petrogr. Mitt. 76: 383-397.

Huber, R. K. (1999). Tectonometamorphic evolution of the Eastern Pennine Alps during Tertiary continental collision: Structural and petrological relationships between Suretta-, Tambo-, Chiavenna and Gruf units (Switzerland/Italy). Neuchâtel, University of Neuchâtel.

Hunziker, J. C., Desmons, J. and Martinotti, G. (1992). Thirty-two years of geochronological work in the Central and Western Alps: a review on seven maps. Mémoires de Géologie (Lausanne) 13.

Hunziker, J. C., Hurford, A. J. and Calmbach, L. (1997). Apine cooling and uplift. Deep Structures Of The Swiss Alps: Results Of NRP 20. O. A. Pfiffner, Lehner P., Heitzmann P., Mueller S., Steck A. Basel, Birkhäuser: 260-263.

Hurford, A., Flisch, M. and Jäger, E. (1989). Unravelling the thermo-tectonic evolution of the Alps: a contribution from fission track analysis and mica dating. Alpine tectonics. M. P. Coward, Dietrich, D., Park, R.G. London, Geological Society Special Publication. 45: 369-398.

Hurford, A. J. and Green, P. F. (1983). The Zeta age calibration of fission-track dating. Isotope Geoscience 1: 285-317.

Hurford, A. J. (1986). Cooling and uplift patterns in the Lepontine Alps, South Central Switzerland and an age of vertical movement on the Insubric fault line. Contrib. Mineral. Petrol. 92(4): 413-427.

Kuhlemann, J., Frisch, W., Dunkl, I. and Székely, B. (2001). Quantifying tectonic versus erosive denudation by the sediment budget: the Miocene core complexes of the Alps. Tectonophysics 330: 1-23.

Liati, A., Gebauer, D. and Fanning, M. (2000). U-Pb SHRIMP dating of zircon from the Novate granite (Bergell, Central Alps): evidence for Oligocene-Miocene magmatism, Jurassic/Cretaceous continental rifting and opening of the Valais trough. Schweiz Miner. Petr. Mitt. 80: 305-316.

Liniger, M. H. (1992). Der ostalpin-penninische Grenzbereich im Gebiet der nördlichen Margna-Decke (Graubünden, Schweiz). Zürich, ETH Zürich.

Mancktelow, N. (1992). Neogene lateral extension during convergence in the Central Alps: evidence from inter-related faulting and backfolding around the Simplonpass (Switzerland). Tectonophysics 215: 295-317.

Mancktelow, N. and Grasemann, B. (1997). Time-dependent effects of heat advection and topography on cooling histories during erosion. Tectonophysics 270: 167-195.

Mancktelow, N. S. and Pavlis, T. L. (1994). Fold-fault relationships in low-angle detachment systems. Tectonics 13(2): 668-685.

Marquer, D. (1991). Structures et cinématique des déformations alpines dans le granite de Truzzo (Nappe de Tambo: Alpes centrales suisses). Eclogae geol. Helv. 84(1): 107-123.

Marquer, D., Baudin, T., Peucat, J. J. and Persoz, F. (1994). Rb-Sr mica ages in the Alpine shear zones of the Truzzo granite: Timing of the Tertiary alpine P-T-deformations in the Tambo nappe (Central Alps, Switzerland). Eclogae geol. Helv. 85(3): 1-61.

Marquer, D., Challandes, N. and Schaltegger, V. (1998). Early Permian magmatism in Briançonnais terranes: Truzzo granite and Roffna rhyolite (Eastern Pennine nappes, Swiss and Italian Alps). Schweiz Miner. Petr. Mitt. 78: 397-415.

Meier, A. (2003). The Periadriatic Fault System in Valtellina (N-Italy) and evolution of the southwestern segment of the Eastern Alps. Zurïch, ETH Zurïch: 190.

Merle, O., Cobbold, P. R. and Schmid, S. (1989). Tertiary kinematics in the Lepontine Dome. Alpine tectonics. M. P. Coward, Dietrich, D., Park, R.G. London, Geol. Soc. London Spec. Publ. 45: 113-134.

Meyre, C., Marquer, D., Schmid, S. M. and Ciancaleoni, L. (1998). Syn-orogenic extension along the Forcola fault: correlation of Alpine deformations in the Tambo and Adula nappes (Eastern Pennine Alps). Eclogae Geol. Helv. 91: 409-420.

Michalski, I. and Soom, M. (1990). The Alpine thermo-tectonic evolution of the Aar and Gotthard massifs, Central Switzerland: Fission Track ages on zircon and apatite and K-Ar mica ages. Schweiz. mineral. petrogr. Mitt. 70: 373-387.

Milnes, A. G. (1974). Post-nappe folding in the western Lepontine Alps. Eclog. Geol. Helv. 67: 333-348.

Müller, W., Prosser, G., Mancktelow, N., Villa, I. M., Kelley, S. P., Viola, G. and Oberli, F. (2001). Geochronological constraints on the evolution of the Periadriatic Fault System (Alps). Int. J. Earth Sci. (Geol Rundsch) 90: 623-653.

Munardi, W. (1989). Der Osthang des Valle della Mera zwischen Samolaco und Dubino: Petrographische, geochemische und geochronologische Bearbeitung der gesteine unter besonderer Berücksichtigung des Novät-Granits. Bern, Universität Bern: 161.

Naeser, C. W. and Faul, H. (1969). Fission track annealing in apatite and sphene. J. Geophys. Res. 74: 705-710.

Naeser, C. W. (1979). Fission track dating and geological annealing of fission tracks. Lectures In isotope Geology. E. Jäger, Hunziker, J. C. New York, Springer-Verlag: 154-169.

Nievergelt, P., Liniger, M., Froitzheim, N. and Mählmann, R. F. (1996). Early to mid Tertiary crustal extension in the Central Alps: the Turba mylonite zone (Eastern Switzerland). Tectonics 15(2): 329-340.

Niggli, E. (1970). Alpine metamorphose und Alpine Gebirgsbildung. Fortschritte der Mineralogie 47: 16-26.

Oberli, F., Meier, M., Berger, A., Rosenberg, C. and Gieré, R. (1996). 230Th/238U disequilibrium systematics in U-Th-Pb dating: nuisance or powerful tool in geochronometry ? 6th V.M. Goldschmidt Conference, Heidelberg.

Peretti, A. (1983). Geologie und Petrographie der Forno-Serie. Piz Dei Rossi. Zürich, ETH Zürich.

Peretti, A. (1985). Der Monte-del-Forno-Komplex am Bergell-Ostrand: Seine Lithostratigraphie, alpine tektonik und metamorphose. Eclog. Geol. Helv. 78: 23-48.

Persaud, M. and Pfiffner, O. A. (2004). Active deformation in the eastern Swiss Alps: post-glacial faults, seismicity and surface uplift. Tectonophysics 385: 59-84.

Pfiffner, O. A. and Heitzmann, P. (1997a). Geologic interpretation of the seismic profiles of the Central Traverse (lines C1, C2, C3-north). Deep Structures Of The Swiss Alps: Results Of NRP 20. O. A. Pfiffner, Lehner P., Heitzmann P., Mueller S., Steck A. Basel, Birkhäuser: 115-122.

Puschnig, A. R. (1996). Regional and emplacement-related structures at the northeastern border of the Bergell intrusion (Monte Del Forno, Rhetic Alps). Schweiz Miner. Petr. Mitt. 76: 399-420.

Rahn, M. K., Hurford, A. J. and Frey, M. (1997). Rotation and exhumation of a thrust plane: Apatite fission-track data from the Glarus thrust, Switzerland. Geology 25(7): 599-602.

Rahn, M. K., Ciancaleoni, L., Fügenschuh B. and Marquer, D. (2004). FT data between Lepontine dome and Bergell intrusion: key area for the late exhumation of the Central Alps ? Swiss Geoscience Meeting 2004, Université de Lausanne.

Riklin, K. (1978). Strukturen und Metamorphose im Bereich der südlichen Muretto-Linie. Schweiz Miner. Petr. Mitt. 58: 345-356.

Ring, U. (1994). The kinematics of the late Alpine Muretto fault and its relation to dextral transpression across the Periadriatic Line. Eclog. Geol. Helv. 87: 811-831.

Rosenberg, C., Berger, A. and Schmid, S. M. (1995). Observation from the floor of a granitoid pluton: Inferences on the driving force of final emplacement. Geology 23: 443-446.

Rosenberg, C. L. and Heller, F. (1997). Tilting of the Bergell pluton and Central Lepontine area: combined evidence from paleomagnetic, structural and petrological data. Eclogae Geol. Helv. 90: 345-356.

Ruzicka, J. W. (1997). Der Nordland des Grüf-Komplexes und seine Beziehung zur Engadiner Linie. Basel, Universität Basel.

Schaer, J. P., Reimer, G. M. and Wagner, G. A. (1975). Actual and ancient uplift rate in the Gotthard region, Swiss Alps: A comparison between precise levelling and fission-track age. Tectonophysics 29: 293-300.

Schlunegger, F., Jordan, T. E. and Klaper, E. M. (1998). Controls of erosional denudation in the orogen on foreland basin evolution: the Oligocene central Swiss Molasse basin as an example. Tectonics 16: 823-840.

Schlunegger, F. and Willett, S. (1999). Spatial and temporal variations in exhumation of the central Swiss Alps and implications for exhumation mechanisms. Exhumation processes: Normal Faulting, Ductile Flow and Erosion. U. Ring, M. T. Brandon, G. S. Lister and S. D. Willett. London, Geological Society Special Publication. 154: 157-179.

Schlunegger, F. and Simpson, G. (2002). Possible erosional control on lateral growth of the European Central Alps. Geology 30(10): 907-910.

Schmid, S. M., Aebli, H. R., Heller, F. and Zingg, A. (1989). The role of the Periadriatic Line in the tectonic evolution of the Alps. Alpine Tectonics. M. P. Coward, D. Dietrich and R. G. Park. London, Geological Society Special Publication. 45: 153-171.

Schmid, S. M. and Froitzheim, N. (1993). Oblique slip and block rotation along the Engadine line. Eclogae geol. Helv. 86(2): 569-593.

Schmid, S. M., Pfiffner, O. A., Froitzheim, N., Schönborn, G. and Kissling, E. (1996a). Geophysical-geological transect and tectonic evolution of the Swiss-Italian Alps. Tectonics 15(5): 1036-1064.

Schmid, S. M., Berger, A., Davidson, C., Gieré, R., Hermann, J., Nievergelt, P., Puschnig, A. R. and Rosenberg, C. (1996b). The Bergell pluton (Southern Switzerland, Northern Italy): Overview accompanying a geological-tectonic map of the intrusion and surrounding country rocks. Schweiz. Mineral. Petrogr. Mitt. 76: 329-355.

Schmid, S. M., Pfiffner, O. A. and Schreurs, G. (1997). Integrated cross-section and tectonic evolution of the Alps along the Eastern Traverse. Deep Structures Of The Swiss Alps: Results Of NRP 20. O. A. Pfiffner, Lehner P., Heitzmann P., Mueller S., Steck A. Basel, Birkhäuser Verlag: 289-304.

Schönborn, G. (1992). Alpine tectonics and kinematic models of the central Southern Alps. Mem. Sci. Geol. XLIV: 229-393.

Seward, D. (1989). Cenozoic basin histories determined by fission track dating of basement granites, South Island, New Zealand. Chem. Geol. (Isotope Geoscience Section) 79: 31-48.

Sue, C. and Tricart, P. (2003). Neogene ongoing normal faulting in the inner western Alps: a major evolution of the late alpine tectonics. Tectonics 22(5): 1050.

Spear, F. S. and Peacock, S. M. (1989). Metamorphic Pressure-temperature-time paths. Washington D.C., American Geophysical union.

Spiegel, C., Kuhlemann, J., Dunkl, I., Frisch, W., von Eynatten, H. and Balogh, K. (2000). The erosion history of the Central Alps: evidence from zircon fission track data of the foreland basin sediments. Terra Nova 12: 163-170.

Spillmann, P. (1993). Die Geologie des penninisch-ostalpinen Grenzbereichs im südlichen Bernina-Gebirge. Zürich, ETH Zürich.

Steck, A. and Hunziker, J. C. (1994). The Tertiary structural and thermal evolution of the Central Alps: compressional and extensional structures in an orogenic belt. Tectonophysics 238: 229-254.

Tagami, T., Carter, A. and Hurford, A. J. (1996). Natural long-term annealing of the zircon fission-track system in Vienna Basin deep borehole samples: constraints upon the partial annealing zone and closure temperature. Chem. Geol. 130: 147-157.

Tagami, T. and Shimada, C. (1996). Natural long-term annealing of the zircon fission track system araound a granitic pluton. Journal of Geophysical Research 101(B4): 8245-8255.

Trommsdorff, V. and Connolly, J. A. D. (1996). The ultramafic contact aureole about the Bregaglia (Bergell) tonalite: isograds and a thermal model. Schweiz Miner. Petr. Mitt. 76: 537-547.

Trümpy, R. (1977). The Engadine Line: a sinistral wrench fault in the Central Alps. Mem. Geol. Soc. China 2: 1-17.

Viola, G. (2000). Kinematics and timing of the Periadriatic fault system in the Giudicarie region (Central-Eastern Alps). Zürich, ETH Zürich.

von Blanckenburg, F. (1992). Combined high precision chronometry and geochemical tracing using accessory minerals applied to the Central-Alpine Bergell intrusion. Chemical Geology 100: 19-40.

von Blanckenburg, F. and Davies, J. H. (1995). Slab breakoff: A model for syncollisional magmatism and tectonics in the Alps. Tectonics 14/1: 120-131.

Wagner, G. A. (1968). Fission track dating of apatites. EPSL 4: 411-415.

Wagner, G. A., Reimer, G. M. and]äger, E. (1977). Cooling ages drived by apatite fission-track, mica Rb-Sr and K-Ar dating: The uplift and cooling history of the Central Alps. Memorie degli Instituti di Geologia e Mineralogia dell'Universita di Padova. S. C. Tipograf. Padova. XXX: 27.

Wagner, G. A., Miller, D. S. and Jäger, E. (1979). Fission track ages on apatite of Bergell rocks from Central Alps and Bergell boulders in Oligocene sediments. Earth and Planetary Science Letters 45: 355-360.

Wenk, E. (1984). Brittle-ductile transition zone in the northern Bergell Alps. Geol. Rdsch. 73: 419-431.

Werling, E. (1992). Tonale-, Pejo- une Judicarien-Linie: Kinematik, Mikrostrukturen und Metamorphose von tektoniken aus räumlich interferierenden, aber verschiedenaltrigen Verwerfungszonen. Zürich, ETH Zürich.

Wiedenbeck, M. (1986). Structural and isotopic age profile across the Insubric Line, Mello, Valtellina, N. Italy. Schweiz. mineral. petrogr. Mitt. 66: 211-227.

Yamada, R. and Tagami, T. N., S.; Ito, H. (1995). Annealing kinetics of fission tracks in zircon: an experimental study. Chemical Geology (Isotope Geoscience Section) 122: 249-258.

Chapter 6

Conclusions

Conclusions

In this comprehensive study, the late deformation processes under brittle-ductile and brittle conditions in the Bergell region of the Eastern Central Alps have been characterized using a combination of structural and analytical methods. The arising picture indicates that the late Alpine fault pattern in the Bergell and Insubric areas of the Central Alps encompasses at all scales normal, oblique-slip and strike-slip faults. The tectonic regime associated with these faults is distributed in space and time into extensional and transcurrent displacements. Major sets of transversal and longitudinal fault systems are the result of one major extensive to transtensive tectonic event. The tectonic regime in the Bergell region, however, evolved from this state of stress to a more transcurrent and eventually transpressive one. The fault-slip data analysis of the minor fault population is coherent for both the extensive and strike-slip tectonic regimes, and yields a consistent orientation of the extension axes in the ENE-WSW direction (orogen-parallel). The shortening direction related to the transcurrent regime is conversely oriented in the NNW-SSE direction. The intraplate stress recorded in the Bergell area (European plate) is considered to be transmitted across the plate boundary from the interplate slip vector of Adria.

In the Bergell region, conjugated sets of map-scale strike-slip faults define sets of triangular wedges that lead to eastward escape of the Eastern Central Alps. The far-field kinematic framework of the collision between the Adriatic and European plates and gravity failure in the core of the belt determine the direction of escape. The combination of strike-slip and normal faulting displacement is typical of a model of eatsward lateral extrusion of the Eastern Central Alps, in response to the ongoing convergence between the Adria and European plates.

Within this process, widespread normal faulting is a major long-lived event which led to the orogen-parallel extension. In particular, a major late Alpine normal fault outcrops at the contact between the Adula and Tambo nappes. This prominent shear zone consists of greenschist facies mylonites and cataclasites that accommodated a relative vertical displacement of about 3 kms associated with down-faulting of the eastern block in the orogen-parallel direction. The ca. 25 Ma old Novate leucogranite was emplaced syn-extension under mid-crustal conditions at the southern tip of the Forcola fault. The deformation inside the magmatic body is highly heterogeneous and characterized by strongly localized and anastomozed ductile shear zones surrounding lenses of weakly deformed granite and later faults formed at the brittle-ductile transition. The mylonitisation occured soon after the intrusion, under conditions of the amphibolite-greenschist facies transition. These structures developed progressively during cooling of the intrusion. The fault kinematic analysis of the conjugated shear-zones indicates a non-coaxial deformation associated with an orogen-parallel extension strongly compatible with that at the Forcola mylonites. A model of extensional jog opening by vertical shearing along the Forcola shear zone provided the space available for magma ascent and emplacement. This provides new upper timing constraints on the activity of the Forcola Line that must definitively have been active at 25 Ma.

This age is compatible with the late Oligocene age (28-25 Ma) for the conjugated dextral strike-slip at the Tonale Line and sinistral strike-slip at the Engadine Line, as well as normal faulting at the Muretto fault. The onset of Forcola orogen-parallel extension is therefore in good temporal and kinematic agreement with conjugated dextral strike-slip faulting under brittle-ductile conditions at the Tonale and Engadine Lines. These prominent faults accommodated the onset of eastward-directed extrusion of the Eastern Central Alps in the late Oligocene.

New zircon and apatite fission-track data across the Forcola fault provide additional constraints regarding the Neogene activity of the fault. No abrupt offset of zircon and apatite fission-track ages occurs at the fault trace, giving an upper age limit (Langhian) for significant vertical displacement. A similar maximum upper age limit (Langhian) for the end of the vertical displacement on the Muretto normal fault and on the Engadine Line is demonstrated by zircon and apatite fission-track age profiles across these faults. Regarding the Tonale Line, the fission track data suggest the likelihood of vertical displacements along the fault from the Middle Miocene onwards.

Lateral extrusion in the core of the Alpine belt during the last stages of the continental collision is therefore an outstanding deformation process that predominates everywhere along the strike of the belt. Clearly established in the Eastern Alps and proposed in the Western Central Alps, this mechanism is now demonstrated by this study as a viable deformation process at the eastern border of the Lepontine dome. Questions remain, e.g. whether the brittle-ductile tectonics within the central Lepontine core fit with this scenario. In the affirmative lateral extrusion and orogen-parallel extension must be definitely considered as a tectonic process characteristic of the late Alpine geodynamics since the Neogene.

Annex

Published article in Terra Nova, 2006, Vol 18, No. 3, 170-180

Syn-extension leucogranite deformation during convergence in the Eastern Central Alps: example of the Novate intrusion.

Laurent Ciancaleoni, Didier Marquer

doi: 10.1111/j.1365-3121.2006.00677.x

Syn-extension leucogranite deformation during convergence in the Eastern Central Alps: example of the Novate intrusion

Laurent Ciancaleoni[1] and Didier Marquer[2]

[1]*Institut de Géologie, Université de Neuchâtel, Rue Emile Argand, 11, CH-2007 Neuchâtel, Switzerland;* [2]*EA2642 Géosciences, Université de Franche-Comté Géosciences, 16 route de Gray, F25030 Besançon Cedex, France*

ABSTRACT

The Novate intrusion is a Late Alpine leucogranite that intruded the structures related to dextral back-thrusting along the Periadriatic Fault System in the Eastern Central Alps. The Novate granite was heterogeneously deformed from amphibolite to greenschist facies conditions during cooling of the intrusion. The deformation inside the granite is characterized by strongly localized and anastomosed ductile shear zones surrounding lenses of weakly deformed granite and by late faults formed at the brittle–ductile transition. The fault kinematic analysis of conjugated shear zones suggests that the Novate leucogranite was emplaced at 25 Ma in an extensional regime along the southern tip of the Forcola Fault. A model of extensional jog opening by vertical shearing along the Forcola Fault provided the space for magma accommodation. The Novate granite is the first evidence for orogen-parallel syn-extensional leucogranite emplacement during the Oligocene collision in the Alps.

Terra Nova, 18, 170–180, 2006

Introduction

Over the last decades pluton emplacement in the crust has been described in a wide range of tectonic settings, either contractional (D'lemos *et al.*, 1992; Hutton and Ingram, 1992; Tikoff and De Saint-Blanquat, 1997; Brown and Solar, 1998; De Saint-Blanquat *et al.*, 1998), transcurrent (Hutton and Reavy, 1992; Vauchez *et al.*, 1997) or extensional (Hutton *et al.*, 1990; Scaillet *et al.*, 1995; Acocella and Rossetti, 2002). Common to these studies is the general spatial and temporal relationships between magmatic bodies and crustal shear zones and the resolution of the 'space problem', i.e. space needed to accommodate magma (e.g. Brown, 1994; Tikoff *et al.*, 1999). According to some authors, regional tectonic structures are believed to exert some control on the ascent and emplacement of plutons (e.g. Strong and Hanmer, 1981; Hutton *et al.*, 1990; Paterson *et al.*, 1990; D'lemos *et al.*, 1992; Clemens *et al.*, 1997; Roman-Berdiel *et al.*, 1997; Vauchez *et al.*, 1997).

In the case of the calcalkaline magmatism in the Alps, such a relationship between deformation and magma emplacement has been reviewed (Rosenberg, 2004). This magmatism is spatially and temporally associated with transpressive deformation along the Periadriatic Fault System (PFS) during convergence between the Adria and Europe (e.g. Schmid *et al.*, 1989; Berger *et al.*, 1996). In this paper we address the syn-tectonic emplacement of a Late Alpine leucogranite, the Novate intrusion. We propose that this granite was intruded along an extensional segment of the PFS, the Forcola Fault.

Geological setting

In the studied area, after the Eocene nappe emplacement and exhumation (D1 and D2 regional phases, Meyre *et al.*, 1998 and references therein), the PFS is a major Alpine tectonic feature related to the collisional history of the Alps (Schmid *et al.*, 1989 and references therein). In the Bergell region of the Eastern Central Alps (Fig. 1a), the post-nappe deformation history is constrained by the ages of three Oligocene intrusions (Schmid *et al.*, 1996b): the Bergell tonalite and granodiorite (32 and 30 Ma; Von Blanckenburg, 1992), the Sondrio tonalite (Biotite K/Ar cooling ages of 30–32 Ma; Giger, 1991) and the Novate leucogranite (24–26 Ma; Liati *et al.*, 2000 and references therein). The Late Oligocene post-collisional dextral transpression across the Insubric Mylonites belt (D3, Milnes, 1974; Schmid *et al.*, 1996a) has led to: (1) back-folding and back-thrusting of the Central Alps over the Southern Alps, providing a rapid exhumation of the Bergell area (Giger and Hurford, 1989; Berger *et al.*, 1996); and (2) a dextral offset of 30–100 km (Heitzmann, 1987; Schmid *et al.*, 1996a; Viola *et al.*, 2001).

Late Oligocene–Early Miocene orogen-parallel extension along the brittle–ductile Forcola normal fault post-dates back-thrusting and is coeval with purely dextral slip on the Insubric Line (D4, Fig. 1b, Schmid *et al.*, 1989; Meyre *et al.*, 1998). Exposed in the northwestern end of the Novate granite, this normal fault reaches Val Mera, where it is covered by Quaternary deposits, and is thought to splay further south inside the Novate granite on the basis of foliation maps (Meyre *et al.*, 1998).

The fine-grained Novate granite is a garnet-bearing S-type two-mica leucogranite derived from partial melting of crustal rocks during the Late Alpine decompression (e.g. Oschidari and Ziegler, 1992; Von Blanckenburg *et al.*, 1992). The Novate granite and the associated dike swarms cross-cut the late back-folding structures and Bergell Pluton fabrics (Fig. 1b, Wenk, 1973; Berger *et al.*, 1996). The structural trends in the wall rocks are undisturbed by the granite intrusion (Fig. 1b). The southeastern contact

Correspondence: Dr L. Ciancaleoni, Laboratoire de géodynamique des rifts et des marges passives, UFR Sciences et Techniques, Av. Olivier Messiaen, 72085 Le Mans Cedex 09, France. Tel.: 00 41 32 718 26 57; fax: 00 41 32 718 26 00; e-mail: laurent.ciancaleoni@unine.ch

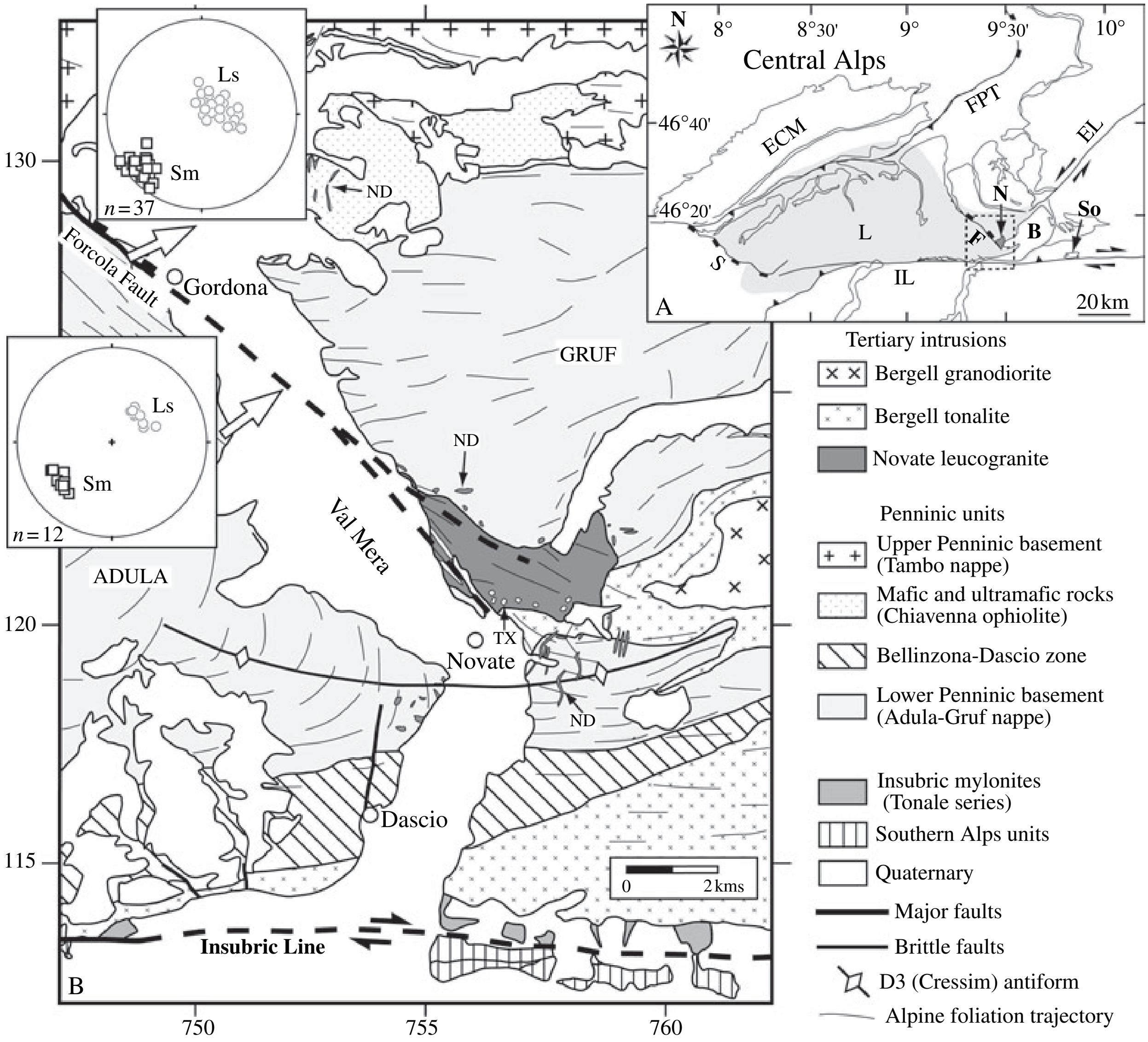

Fig. 1 (A) Location of the study area (dashed rectangle) with respect to the Central Alps framework (ECM, external crystalline massif; FPT, Frontal Penninic Thrust; L, Lepontine dome (shaded area); S, Simplon Line; IL, Insubric Line; EL, Engadine Line; F, Forcola Fault; B, Bergell Pluton; N, Novate pluton; So, Sondrio pluton). Modified from Rosenberg and Heller (1997). (B) Geological and tectonic settings of the western Bergell region. Modified from Berger *et al.* (1996), Schmid *et al.* (1996b) and Meyre *et al.* (1998). Latitudes and longitudes are given in Swiss coordinates. ND, Novate dykes; TX, Bergell tonalite xenoliths. Foliation trajectory from Meyre *et al.* (1998) and Wenk (1973). Stereoplots (lower hemisphere projection): structural data (Sm, mylonitic foliation; Ls, stretching lineation) from the Forcola normal fault extension phase. Open arrows indicate the direction of faulting (top to NE) according to Forcola stretching lineation.

trends northeast and contains numerous Bergell tonalite blocks showing no preferred orientation within the enclosing granitic magma. The western and northern contacts, albeit partly covered by Quaternary alluvial deposits, show a northwest trending orientation, i.e. parallel to the Forcola Fault trend. In this part of the granite, large gneissic xenoliths from the adjacent wall rocks are stretched parallel to the northeast-dipping foliation (Schmid *et al.*, 1996b).

Heterogeneous deformation and strain distribution in the Novate granite

In plutonic rocks heterogeneous deformation is essentially localized into arrays of anastomosing shear zones. These shear zones surround lens-shaped domains of weakly deformed rocks (e.g. Mitra, 1979; Ramsay and Allison, 1979; Bell, 1981; Choukroune and Gapais, 1983; Gapais *et al.*, 1987; Marquer, 1991; Marquer *et al.*, 1996). Shear zone patterns are described as slip surfaces that accommodate most of the bulk deformation. Therefore, they have been used as reliable shear criteria and strain markers (e.g. Gapais *et al.*, 1987).

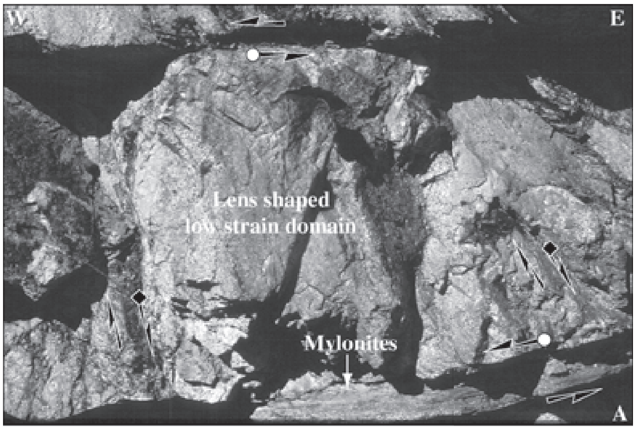

Fig. 2 Field examples of the heterogeneous deformation pattern in the Novate: small-scale conjugated shear zones surrounding lenses of weakly deformed granite. For symbols explanation, see Fig. 3. Arrows show sense of shear on slip surfaces.

Ductile shear zones pattern

In the Novate granite, heterogeneous deformation is present at all scales of observation (Figs 2 and 3). Ductile shear zones are underlined by mylonites and ultramylonites. Large volumes of granite with a weak magmatic foliation are preserved (e.g. local subhorizontal schlieren).

In this paper we focus on the retrograde solid state deformation of the granite during low-grade country rocks D4 regional deformation phase. A weakly marked schistosity and stretching lineation occur in the core of the lenses and become pronounced close to and inside the high-strain zones. Shear zone patterns have been analysed at different elevations within the granite on a vertical profile (Fig. 3a,c). The bulk shear zone pattern is described in terms of a shear zone plane, stretching lineation and associated shear sense. The schistosity (*XY* plane of deformation) measured in the core of weakly deformed lenses shows a consistent average N150° strike (parallel to the *Y* direction) and ENE steep dip (great circle S in stereograms, Fig. 3c) and bears a nearly down-dip stretching lineation (L, black triangles in stereograms, Fig. 3c). The shear zone pattern is

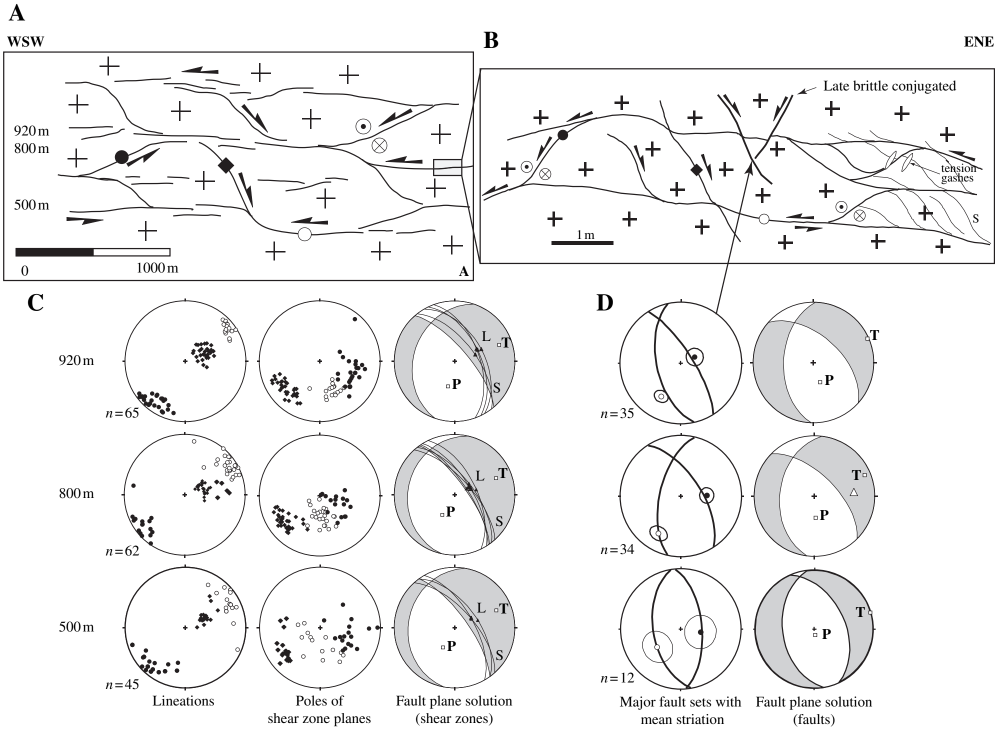

Fig. 3 Shear zone pattern and strain analysis in the Novate granite. (A) Vertical cross-section showing the strain distribution. Open and full circles, shear zones with a westward shear sense; black squares, shear zones with an eastward shear sense. See text for more explanations. (B) Illustration of the shear zone pattern at 800 m. (C) Shear zone pattern analysis. Same symbols as in (A). Stereonets: Wulff lower hemisphere projection of lineations, poles of shear zones and kinematic analysis using Faultkin (Allmendinger *et al.*, 1989). White- and grey-shaded areas are the pression and tension quadrants, respectively, *P* and *T*, best-fit compression and tension axes respectively. Great circles (S) and black triangles (L) are the schistosity and lineation measured in the field in low strain domains. (D) Kinematic analysis of brittle–ductile faults. Left side stereonets: mean east- and west-dipping brittle–ductile fault planes with corresponding mean striation (99% confidence cone). White triangle symbol on the right side stereonet at site 800 m: mean pole to tension gashes (incremental extension direction).

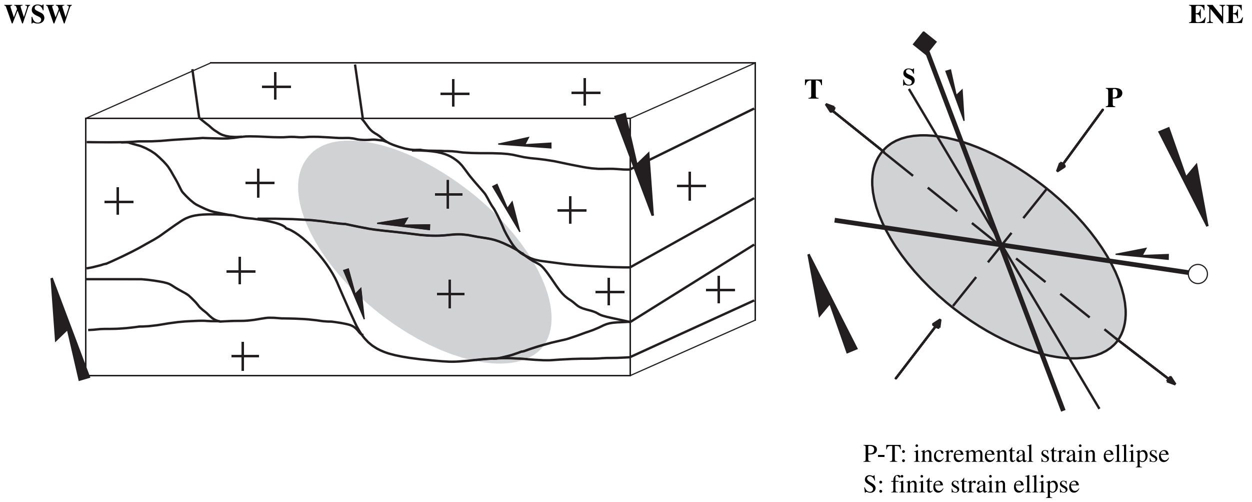

Fig. 4 Kinematic interpretation of the deformation in the Novate granite. The large arrows correspond to the dominant shear system. *P* and *T* are the resolved compression and tension axes respectively. S is the average of the schistosity and lineation measured in the field and represents the finite strain ellipse. Light grey-shaded ellipse corresponds to the incremental strain ellipse constructed from the resolved *P*–*T* axes. The obliquity between the incremental and finite strain ellipses indicate an eastward sense of shear. Symbols are the same as in Fig. 3.

illustrated by conjugated shear zones intersecting close to the *Y* direction. The first set consists of shallowly N-dipping shear zones with a NE–SW stretching lineation and a sinistral–reverse (top-to-the SW) shear sense (open circles in Fig. 3). The second set is represented by NNE–SSW moderately W-dipping shear zones bearing a NE–SW lineation associated with a sinistral–normal shear sense (full circles in Fig. 3). The third set deals with NW–SE shear zones steeply to moderately dipping toward the NE and bearing a nearly down-dip lineation associated to a normal (top-to-the NE) movement (full squares in Fig. 3). Locally this set appears to have been reactivated under cooler conditions and to have underwent oblique–normal shearing. Both sets of shear zones are equally expressed.

Ductile–brittle faults pattern

The strain is also concentrated in a major set of steep brittle–ductile narrow E-dipping normal faults (typically less than 1 cm in width), with

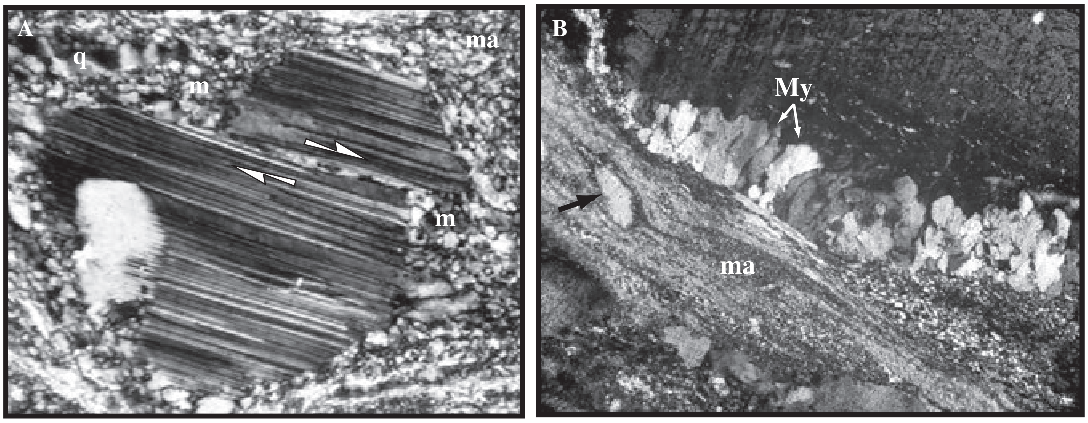

Fig. 5 Examples of microstructures in the Novate mylonites. (A) Plagioclase porphyroclast with a mantle (m) of dynamically recrystallized feldspar and transected by a shear band, in a fine-grained matrix of feldspar–quartz aggregates (ma). Note that pure quartz layers are coarser grained (q). Field of view is 3.5 mm. (B) Myrmekite (My) lobes fringing a large porphyroclast of K-feldspar. The myrmekites have sharp and generally rounded boundaries against the K-feldspar. The myrmekite passes into fine-grained and recrystallized aggregates of quartz and plagioclase (dominantly oligoclase) in the matrix (ma). In the fine-grained matrix, a feldspar (σ-type) is dynamically recrystallized and shows a core and mantle structure (black arrow). Field of view is 3.5 mm.

Table 1 Representative electron microprobe analyses and mineral formulae of sample VC5 (high-angle mylonites) at the orthogneissic and mylonitic stages.

	Oligoclase				K-feldspar				Phengite			
Label	**VC5-ls-2 (core)**	**VC5-ls-5 (rim)**	**VC5-ls-68 (core)**	**VC5-ls-77 rim (albite)**	**VC5-ls-121 (core)**	**VC5-ls-123 rim (oligoclase)**	**VC5-ls-143 (core)**	**VC5-ls-148 rim (oligoclase)**	**VC4-ls33**	**VC4-ls40**	**VC4-ls87**	**VC4-ls133**
Weakly deformed rock												
SiO_2	62.65	63.53	63.01	66.53	64.38	65.54	64.27	65.82	45.70	46.28	46.53	45.86
TiO_2	0.00	0.00	0.00	0.00	0.00	0.00	0.00	0.00	0.97	0.18	0.85	0.24
Al_2O_3	23.37	22.98	23.32	20.39	18.69	21.46	18.47	21.24	32.88	34.11	32.63	33.29
FeO	0.00	0.10	0.03	0.00	0.04	0.03	0.06	0.08	3.50	1.88	2.39	2.89
MnO	0.00	0.00	0.00	0.00	0.00	0.00	0.00	0.00	0.02	0.06	0.11	0.04
MgO	0.00	0.00	0.00	0.00	0.00	0.00	0.00	0.00	0.94	1.23	1.32	1.20
CaO	4.62	4.26	4.55	1.54	0.03	2.47	0.05	2.17	0.01	0.00	0.00	0.00
Na_2O	9.08	9.28	9.00	10.84	1.33	10.09	1.48	10.67	0.49	0.30	0.27	0.37
K_2O	0.23	0.24	0.28	0.18	14.74	0.14	14.69	0.18	10.96	11.08	11.15	11.21
Total Wt%	99.94	100.38	100.19	99.47	99.22	99.73	99.01	100.16	95.47	95.12	95.24	95.12
Number of cations												
Si	2.777	2.800	2.784	2.934	2.985	2.888	2.987	2.892	3.088	3.105	3.131	3.101
Ti	0.000	0.000	0.000	0.000	0.000	0.000	0.000	0.000	0.049	0.009	0.043	0.012
Al	1.221	1.194	1.214	1.060	1.021	1.114	1.012	1.100	2.618	2.697	2.588	2.653
Fe	0.000	0.003	0.001	0.000	0.001	0.001	0.002	0.003	0.198	0.105	0.135	0.163
Mn	0.000	0.000	0.000	0.000	0.000	0.000	0.000	0.000	0.001	0.003	0.006	0.002
Mg	0.000	0.000	0.000	0.000	0.000	0.000	0.000	0.000	0.095	0.123	0.132	0.121
Ca	0.219	0.201	0.215	0.073	0.002	0.117	0.002	0.102	0.001	0.000	0.000	0.000
Na	0.780	0.793	0.771	0.927	0.120	0.862	0.134	0.909	0.064	0.039	0.035	0.049
K	0.013	0.014	0.016	0.010	0.871	0.008	0.871	0.010	0.945	0.948	0.957	0.967
Total cations	5.010	5.004	5.001	5.004	5.000	4.989	5.008	5.016	7.058	7.031	7.028	7.068
Ab%	77.053	78.686	76.931	91.786	12.070	87.385	13.267	89.031				
An%	21.649	19.951	21.507	7.201	0.166	11.829	0.232	9.995				
Or%	1.298	1.362	1.562	1.012	87.763	0.787	86.501	0.974				

	Oligoclase				Albite				K-feldspar				Phengite			
Label	**VC5-hs-210**	**VC5-hs-220**	**VC5-hs-192**	**VC5-hs-214**	**VC5-hs-178**	**VC5-hs-179**	**VC5-hs-183**	**VC5-hs-189**	**VC5-hs-185**	**VC5-hs-209**	**VC5-hs-212**	**VC5-hs-217**	**VC4-hs196**	**VC4-hs198**	**VC4-hs199**	**VC4-hs201**
Mylonites																
SiO_2	68.56	68.62	65.14	69.33	66.70	66.88	67.50	67.23	65.35	65.49	67.01	66.66	45.93	46.17	45.76	45.61
TiO_2	0.00	0.00	0.00	0.00	0.00	0.00	0.00	0.00	0.00	0.00	0.00	0.00	0.19	0.33	0.14	0.20
Al_2O_3	19.42	19.59	22.11	19.16	20.77	20.75	20.45	20.61	18.42	18.41	18.88	18.76	34.07	34.00	34.81	33.88
FeO	0.07	0.04	0.07	0.05	0.07	0.02	0.02	0.00	0.04	0.08	0.00	0.00	2.80	1.96	1.67	2.74
MnO	0.00	0.00	0.00	0.00	0.00	0.00	0.00	0.00	0.00	0.00	0.00	0.00	0.03	0.03	0.03	0.05
MgO	0.00	0.00	0.00	0.00	0.00	0.00	0.00	0.00	0.00	0.00	0.00	0.00	0.62	0.93	0.69	0.70
CaO	3.35	4.05	3.05	3.22	1.48	1.68	1.22	1.41	0.09	0.19	1.42	0.33	0.01	0.00	0.00	0.00
Na_2O	7.24	7.68	10.12	7.14	11.00	10.87	10.83	10.82	1.08	2.65	4.81	4.94	0.39	0.26	0.30	0.36
K_2O	1.42	0.32	0.14	1.88	0.11	0.12	0.23	0.18	15.37	13.17	7.78	9.52	10.88	11.31	11.25	11.09
Total Wt%	100.06	100.31	100.63	100.77	100.13	100.32	100.25	100.26	100.36	99.98	99.90	100.21	94.93	94.98	94.64	94.64
Number of cations																
Si	2.997	2.985	2.853	3.012	2.923	2.926	2.949	2.939	3.000	2.998	3.002	3.001	3.100	3.107	3.085	3.093

Table 1 Continued

	Oligoclase				Albite				K-feldspar				Phengite			
Label	**VC5-hs-210**	**VC5-hs-220**	**VC5-hs-192**	**VC5-hs-214**	**VC5-hs-178**	**VC5-hs-179**	**VC5-hs-183**	**VC5-hs-189**	**VC5-hs-185**	**VC5-hs-209**	**VC5-hs-212**	**VC5-hs-217**	**VC4-hs196**	**VC4-hs198**	**VC4-hs199**	**VC4-hs201**
Ti	0.000	0.000	0.000	0.000	0.000	0.000	0.000	0.000	0.000	0.000	0.000	0.000	0.010	0.017	0.007	0.010
Al	1.000	1.004	1.142	0.981	1.073	1.070	1.053	1.062	0.997	0.993	0.997	0.996	2.710	2.697	2.765	2.708
Fe	0.002	0.001	0.002	0.002	0.002	0.001	0.001	0.000	0.001	0.003	0.000	0.000	0.158	0.110	0.094	0.155
Mn	0.000	0.000	0.000	0.000	0.000	0.000	0.000	0.000	0.000	0.000	0.000	0.000	0.002	0.002	0.002	0.003
Mg	0.000	0.000	0.000	0.000	0.000	0.000	0.000	0.000	0.000	0.000	0.000	0.000	0.062	0.093	0.069	0.071
Ca	0.157	0.189	0.143	0.150	0.070	0.079	0.057	0.066	0.004	0.009	0.068	0.016	0.001	0.000	0.000	0.000
Na	0.613	0.648	0.860	0.601	0.935	0.922	0.917	0.917	0.096	0.235	0.418	0.432	0.051	0.034	0.039	0.047
K	0.079	0.018	0.008	0.104	0.006	0.007	0.013	0.010	0.900	0.769	0.444	0.546	0.937	0.971	0.967	0.959
Total cations	4.848	4.845	5.008	4.849	5.010	5.004	4.989	4.994	4.999	5.007	4.930	4.990	7.030	7.030	7.029	7.046
Ab%	72.202	75.812	85.051	70.323	92.517	91.530	92.918	92.315	9.569	23.198	44.909	43.417				
An%	18.463	22.090	14.180	17.509	6.887	7.821	5.795	6.655	0.446	0.904	7.327	1.612				
Or%	9.335	2.098	0.769	12.168	0.596	0.649	1.287	1.030	89.985	75.897	47.765	54.970				

Mineral formulae are calculated based on eight oxygen (plagioclase and K-feldspar) and 11 oxygen (phengites). Fe is assumed to be divalent. Analyses were performed on a CAMECA SX50 electron microprobe at the Mineralogical Institute, University of Lausanne, with natural minerals as standards and a beam diameter of around 2 μm; acceleration voltage, 15 kV; beam current, 15 nA; counting time, 8 s; correction procedure: PAP.

low amounts of penetrative deformation to purely brittle deformation. They are conjugated with a pure brittle-conjugated set of W-dipping normal faults (Fig. 3b,d). The E-dipping ones commonly show down-dip to oblique–normal dextral striations on the slip surfaces and lie in a subparallel orientation to the steep ductile shear zone. They anastomose with or cross-cut the flat-lying shear zones. Locally, however, they are also cross-cut by the flat lying shear zones, which suggests that both slip systems are coeval and grew during progressive deformation. On the other hand, the W-dipping major set of faults generally offsets the ductile flat lying shear zones and must be somewhat younger during the progressive development of this ductile–brittle pattern (Fig. 3b). The sense of shear for this set is oblique–normal sinistral.

Kinematic interpretation

The orientation of the resolved *P* and *T* axes resulting from the fault kinematic analysis of the brittle and ductile shear zones are thought to be close to the principal axes of the incremental strain ellipsoid (light grey ellipse in Fig. 4, Wotjal and Pershing, 1991; Srivastava *et al.*, 1995; Marquer *et al.*, 1996; Twiss and Unruh, 1998). The resolved incremental strain axes orientation is compared to the orientation of the principal axes of the finite strain ellipsoid deduced from the schistosity–stretching lineation couples measured in the lens-shaped domains of low strain. The schistosity lies close to a great circle bounding the tension and compression quadrants, and is at low angle to the steep set of ductile and brittle–ductile shear zones. Additionally, it is placed in an asymmetric position with respect to the calculated extension field. The lineation dips slightly oblique with respect to the resolved *T* axis (Fig. 3c). The fault kinematic analysis of the conjugate shear zones and the bulk asymmetry between the resolved *T* axis and the average of schistosity–stretching lineation orientations indicates a noncoaxial deformation associated with an ENE–WSW-directed extension (Fig. 4).

Table 2 Representative electron microprobe analyses and mineral formulae of sample VC4 (low-angle mylonites).

	Oligoclase				Albite				K-feldspar					Phengite			
Label	VC4-hs-16	VC4-hs-27	VC4-hs-36	VC4-hs-100	VC4-hs-66	VC4-hs79	VC4-hs106	VC4-hs111	VC4-hs19	VC4-hs60	VC4-hs67	VC4-hs58 (core)	VC4-hs69 rim (oligoclase)	VC4-hs88	VC4-hs91	VC4-hs93 (core)	VC4-hs94 (tail)
SiO_2	64.97	63.82	64.02	63.80	65.84	65.73	66.19	65.72	65.08	64.89	67.37	65.47	65.76	46.14	46.26	45.23	45.92
TiO_2	0.00	0.00	0.00	0.00	0.00	0.00	0.00	0.00	0.00	0.00	0.00	0.00	0.00	0.28	0.21	0.64	0.32
Al_2O_3	22.02	22.51	22.68	22.39	20.97	20.88	20.96	20.98	18.37	18.19	17.90	18.22	21.66	34.15	34.35	34.18	34.88
FeO	0.05	0.03	0.00	0.01	0.04	0.05	0.02	0.01	0.01	0.13	0.03	0.06	0.05	1.98	2.00	2.83	1.93
MnO	0.00	0.00	0.00	0.00	0.00	0.00	0.00	0.00	0.00	0.00	0.00	0.00	0.00	0.02	0.08	0.06	0.01
MgO	0.00	0.00	0.00	0.00	0.00	0.00	0.00	0.00	0.00	0.00	0.00	0.00	0.00	0.99	0.80	0.60	0.60
CaO	3.33	3.75	3.90	3.44	1.80	1.86	1.80	2.06	0.01	0.00	0.31	0.04	2.53	0.00	0.04	0.00	0.02
Na_2O	9.41	9.69	9.52	10.14	10.55	11.00	10.80	10.69	1.50	0.67	5.83	1.37	10.23	0.28	0.25	0.54	0.28
K_2O	0.19	0.19	0.14	0.13	0.49	0.13	0.16	0.13	14.74	15.79	8.36	14.98	0.11	10.94	11.08	10.86	10.67
Total Wt%	99.97	99.99	100.26	99.91	99.69	99.65	99.93	99.59	99.71	99.67	99.8	100.14	100.34	94.79	95.07	94.96	94.63
Number of cations																	
Si	2.860	2.821	2.820	2.823	2.820	2.903	2.910	2.902	3.001	3.004	3.032	3.008	2.882	3.105	3.106	3.060	3.088
Ti	0.000	0.000	0.000	0.000	0.000	0.000	0.000	0.000	0.000	0.000	0.000	0.000	0.000	0.014	0.011	0.033	0.016
Al	1.142	1.172	1.177	1.167	1.177	1.087	1.086	1.092	0.998	0.993	0.949	0.986	1.119	2.708	2.718	2.725	2.764
Fe	0.002	0.001	0.000	0.000	0.000	0.002	0.001	0.000	0.000	0.004	0.001	0.002	0.002	0.111	0.112	0.160	0.109
Mn	0.000	0.000	0.000	0.000	0.000	0.000	0.000	0.000	0.000	0.000	0.000	0.000	0.000	0.001	0.005	0.003	0.001
Mg	0.000	0.000	0.000	0.000	0.000	0.000	0.000	0.000	0.000	0.000	0.000	0.000	0.000	0.099	0.080	0.060	0.060
Ca	0.157	0.178	0.184	0.163	0.184	0.088	0.085	0.098	0.000	0.000	0.015	0.002	0.119	0.000	0.003	0.000	0.001
Na	0.803	0.831	0.813	0.870	0.813	0.942	0.920	0.915	0.134	0.060	0.509	0.122	0.869	0.037	0.033	0.071	0.037
K	0.011	0.011	0.008	0.007	0.008	0.007	0.009	0.007	0.867	0.933	0.480	0.878	0.006	0.939	0.949	0.937	0.915
Total cations	4.975	5.013	5.002	5.032	5.002	5.028	5.011	5.014	5.001	4.994	4.987	4.998	4.998	7.014	7.017	7.049	6.991
Ab%	82.716	81.517	80.932	83.626	88.940	90.818	90.769	89.718	13.408	6.027	50.677	12.214	87.456				
An%	16.191	17.421	18.297	15.682	8.369	8.487	8.343	9.576	0.038	0.001	1.481	0.184	11.934				
Or%	1.092	1.063	0.770	0.692	2.691	0.695	0.888	0.707	86.553	93.972	47.842	87.602	0.610				

Mineral formulae are calculated based on eight oxygen (plagioclase and K-feldspar) and 11 oxygen (phengites). Fe is assumed to be divalent. Analyses were performed on a CAMECA SX50 electron microprobe at the Mineralogical Institute, University of Lausanne, with natural minerals as standards and a beam diameter of around 2 μm; acceleration voltage, 15 kV; beam current, 15 nA; counting time, 8 s; correction procedure: PAP.

Regarding the fault kinematic analysis of the major sets of brittle and brittle–ductile faults, the resolved *P*- and *T*-axes orientation is consistent with that of the ductile shear zone pattern. The bulk displacement pattern along faults and the orientation of the bulk strain field akin to the penetrative deformation in the Novate granite are therefore strongly compatible. This suggests that all slip surfaces encompassing ductile and brittle structures acted together to accommodate the bulk of the deformation. Thus, ductile and brittle structures might have developed during cooling of the intrusion. Moreover, the geometry and kinematics of deformation inside the Novate granite are strongly compatible with extensional structures described along the brittle–ductile Forcola mylonites north of Val Mera (compare with Fig. 5 in Meyre *et al.*, 1998).

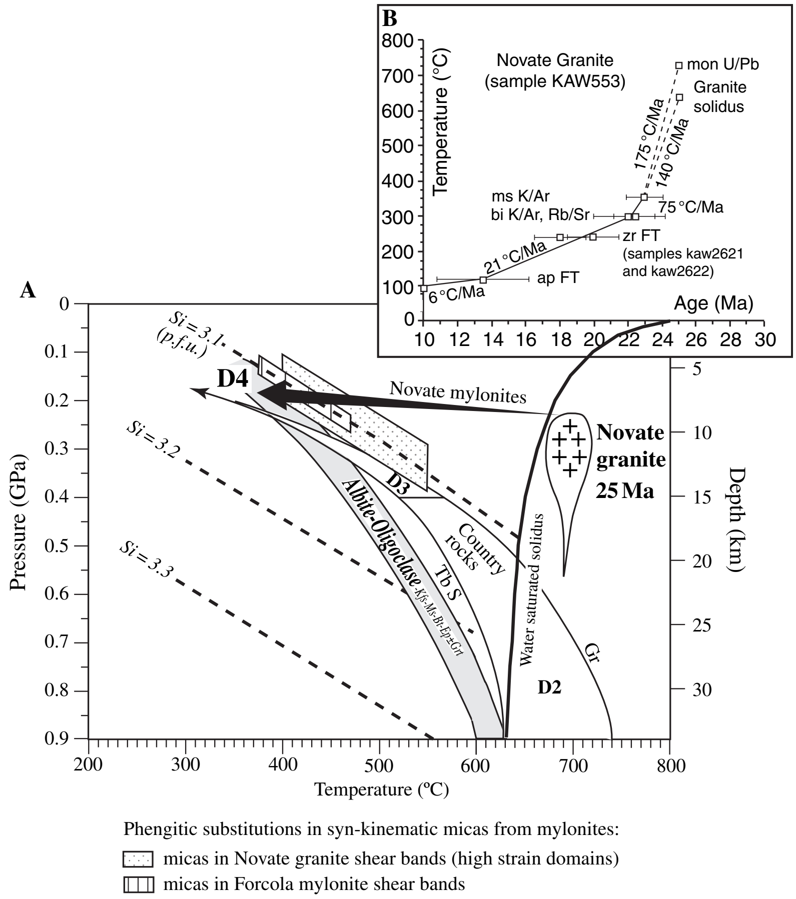

Fig. 6 (A) *P–T* conditions for the Novate granite shear zones and regional *P–T* path for the country rocks. Phengite barometry with Si content (p.f.u.) (shaded boxes) is based on Massone and Schreyer (1987) and Massone and Szpurka (1997). Stability field for plagioclase is from Maruyama *et al.* (1983). *P–T* path for the southern Tambo (Tb) and Suretta (S) nappes, and Gruf unit (Gr), is taken from Huber (1999). Water-saturated solidus is from Whitney (1988). (B) Cooling curve for the Novate granite (sample kaw 553). Modified from Hansmann (1996). Error bars are 2σ. Abbreviations: ap FT, apatite fission track; bi, biotite; mon, monazite; ms, muscovite; zr FT, zircon fission track. Zircon fission track ages are from Novate granite samples kaw 2621 and kaw 2622 (Giger, 1991).

P–T conditions of mylonitization

Deformation microstructures from weakly deformed rocks to highly strained ones are expressed by: (1) a strong decrease in grain size at the onset of deformation by transgranular fracturing of the feldspar phase; (2) the plastic behaviour of quartz through all stages of progressive deformation, while both K-feldspar (Kfs) and plagioclase (Pl) primarily fractured and recrystallized along microshear bands and at grain margins (incipient and marginal recrystallization) in association with chemical changes (Data Repository item, Tables 1 and 2; Fig. 5a); (3) the destabilization of the feldspar phase, in the presence of a water-rich fluid phase and the growth and neocrystallization of new minerals, leading to an assemblage quartz + oligoclase + albite + K-feldspar + phengite + biotite ± epidote ± grenat in the highly strained zones (mylonites and ultramylonites); and (4) the non-cataclastic granular flow of oligoclase-rich polyphase aggregates in the high-strain domains (Stünitz and Fitzgerald, 1993).

The composition of newly formed plagioclase (typically less than 10 μm in grain size) shows a lower An content (*c.* An 6–12) that the parent plagioclase (*c.* An 20), but is dominated by oligoclase and less albite. The recrystallized K-feldspar (*c.* Or 89–86) is stable in low to intermediate deformation stages but is relictual and progressively replaced by new grains of more albitic feldspar composition (*c.* Or 76–55) in the fine grain matrix. The common occurrence of deformation-induced myrmekites (An 10–15, Fig. 5b) with increasing strain indicates that the Ca-bearing plagioclase (oligoclase) was stable. Deformation-induced myrmekites have been commonly described in upper greenschist facies to lower amphibolite facies (see a review in Fitzgerald and Stünitz, 1993).

A *P–T* path for cooling of the Novate granite and conditions of mylonite formation is presented with respect to the *P–T* evolution of the surrounding tectonic units (Fig. 6a). The microstructural observations suggest that deformation leading to mylonites in the Novate intrusion proceeded over a temperature range from amphibolite conditions down to greenschist facies metamorphic conditions, at the regional tectonic phase D4 pressure recorded by the host rocks. The phengitic substitutions in the Novate syn-kinematic white mica (Data Repository item, Tables 1 and 2) (phengite barometry, Massone and Schreyer, 1987) have

Table 3 Representative electron microprobe analyses and mineral formulae of phengites from Forcola mylonites (sample G5).

	Phengite				
Label	**G5–0**	**G5–3**	**G5–7**	**G5–51 (core)**	**G5–53 (rim)**
SiO_2	46.82	46.38	45.95	47.35	46.55
TiO_2	0.48	1.07	1.21	0.42	0.53
Al_2O_3	33.19	33.85	31.57	32.87	33.83
FeO	0.99	0.91	1.79	0.95	0.95
MnO	0.01	0.00	0.04	0.04	0.03
MgO	2.01	1.50	3.14	2.02	1.81
CaO	0.00	0.01	0.07	0.00	0.01
Na_2O	0.57	0.52	0.21	0.42	0.41
K_2O	10.95	10.87	10.22	11.11	10.95
Total Wt%	95.03	95.11	94.20	95.18	95.06
Number of cations					
Si	3.133	3.098	3.110	3.161	3.111
Ti	0.024	0.054	0.062	0.021	0.027
Al	2.617	2.665	2.518	2.586	2.664
Fe	0.055	0.051	0.101	0.053	0.053
Mn	0.001	0.000	0.002	0.002	0.002
Mg	0.200	0.149	0.317	0.201	0.180
Ca	0.000	0.001	0.005	0.000	0.001
Na	0.074	0.067	0.028	0.054	0.053
K	0.935	0.926	0.882	0.946	0.933
Total cations	7.039	7.011	7.025	7.024	7.024

Mineral formulae are calculated based on 11 oxygen. Fe is assumed to be divalent. Analyses were performed on a CAMECA SX50 electron microprobe at the Mineralogical Institute, University of Lausanne, with natural minerals as standards and a beam diameter of around 2 μm; acceleration voltage, 15 kV; beam current, 15 nA; counting time, 8 s; correction procedure: PAP.

low Si-contents of *c.* 3.1 (Fig. 6a). These values are roughly similar to the Si content of phengites from shear bands of the Forcola mylonites (Data Repository item, Table 3) and correspond to the pressure conditions of about 0.2 GPa of the D4 deformation in the country rocks.

Discussion and conclusions

Geochronological data (e.g. Hansmann, 1996 and references therein; Liati *et al.*, 2000) indicate that the Novate granite intruded at 24–25 Ma and cooled down to temperature conditions of 300–350 °C during the Early Miocene (23–21 Ma age interval, Fig. 6b) according to biotite and muscovite K–Ar and Rb–Sr ages. Further cooling across the brittle–ductile transition occurred during the Burdigalian onwards (zircon fission track ages at *c.* 18-20 Ma; Hansmann, 1996). These radiometric ages indicate that the shear zone pattern inside the Novate intrusion was active during the fast isobaric cooling of the intrusion, reaching D4 country rocks *P–T* conditions at *c.* 0.2 GPa-400 °C soon after emplacement (Fig. 6a,b). We therefore suggest that the shear zone pattern represents the end of a progressive extensional deformation that might have begun before or during the pluton construction. Therefore, the shear zone pattern gives insight into the kinematics of pluton emplacement.

The conjugated shear zone pattern indicates a non-coaxial deformation in an extensional setting compatible with the kinematics of deformation along the Forcola mylonites, i.e. associated with an orogen-parallel extension (Meyre *et al.*, 1998). Another indication of this tectonic environment is the NW–SE elongated shape of the Novate pluton in map view at its northwestern side, which further corroborates a spatial and temporal relationship between the magmatic body and the crustal-scale extensional shear zone. The structures of the host rocks are mainly not deflected by the intrusion of the Novate granite. The host rocks were therefore principally passive during emplacement of the magma, excluding ductile diapiric uprise as a possible intrusion mechanism. Host rock xenoliths incorporated into the magma essentially at the southern border of the granite (Fig. 1a) indicate limited magmatic stopping effects during emplacement. This implies that a plausible emplacement mechanism may be that of the intrusion of magma surges into a tectonically generated space (permitted intrusion in the sense of Hutton, 1988).

We propose therefore that the Novate leucogranite was emplaced at 25 Ma under upper crustal conditions, at the southern tip of a crustal-scale extensional shear zone, the Forcola mylonites. Indeed, the shear zone pattern geometry inside the magmatic body might suggest a simple releasing bend opening emplacement (Fig. 7, steps 1–3). The extensional jog opened by vertical shearing along the Forcola shear zone provided the space available for magma ascent and emplacement. During cooling of the granite, secondary shear zones and solid state schistosity developed within the intrusion in response to the extensional shearing environment. This emplacement model along an active extensional shear zone solves the space problem for magma accommodation in a simple manner (Hutton *et al.*, 1990). These results yield important new issues about Alpine tectonics, giving the first evidence for Oligocene leucogranite intrusion during syn-collisional extension in the internal Alps.

Acknowledgements

This research project was supported by grant nos 20-45405.9 and 2000-52'218.97 from the Swiss National Science Foundation. F. Bussy is thanked for microprobe facilities in Lausanne and for the advices on the microprobe-running techniques. Constructive criticisms from A. Kalt, S. Schmid, M. Burkhard and B. Fügenschuh were of great help. We thank the referees, Michel De Saint-Blanquat and an anonymous reviewer, for their helpful comments in improving this manuscript.

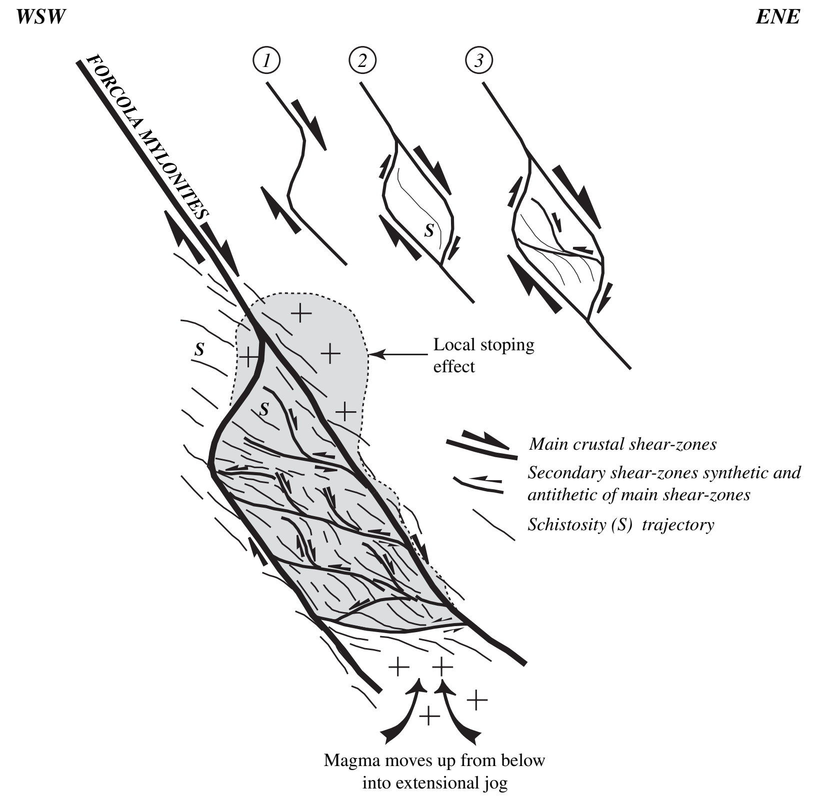

Fig. 7 Pull-apart model in cross-section for Novate granite emplacement and cooling within an active extensional crustal shear zone. High to low-temperature solid state deformation (secondary shear zones synthetic and antithetic of main shear zones) develops progressively within the dilatant site after magma transfer by on-going shearing (stages 1–3). Upward transfer is sustained by the buoyancy of the magma. Local minor stopping effect may modify the granite contacts as the granite spread laterally and/or upward during and after the main magma stock was passively emplaced (dashed line).

References

Acocella, V. and Rossetti, F., 2002. The role of extensional tectonics at different crustal levels on granite ascent and emplacement: an example from Tuscany (Italy). *Tectonophysics*, **354**, 71–83.

Allmendinger, R.W., Marrett, R.A. and Cladouhos, T., 1989. *FAULTKIN-Program*. Dep. of Geol. Sc., Cornell University, Ithaca, NY.

Bell, T.H., 1981. Foliation development: the contribution, geometry and significance of progressive bulk, inhomegeneous shortening. *Tectonophysics*, **75**, 273–296.

Berger, A., Rosenberg, C. and Schmid, S.M., 1996. Ascent, emplacement and exhumation of the Bergell pluton within the Southern Steep Belt of the Central Alps. *Schweiz. Mineral. Petrogr. Mitt.*, **76**, 357–382.

Brown, M., 1994. The generation, segregation, ascent and emplacement of granite magma: the migmatite-to-crustally-derived granite connection in thickened orogens. *Earth-Sci. Rev.*, **36**, 83–130.

Brown, M. and Solar, G.S., 1998. Granite ascent and emplacement during contractional deformation in convergent orogens. *J. Struct. Geol.*, **20**, 1365–1393.

Choukroune, P. and Gapais, D., 1983. Strain pattern in the Aar granite (Central Alps): orthogneiss developed by bulk inhomeogeneous flattening. *J. Struct. Geol.*, **5**, 411–418.

Clemens, J.D., Petford, N. and Mawer, C.K., 1997. Ascent mechanisms of granitic magmas: causes and consequences. In: *Deformation-enhanced Fluid Transport in the Earth's Crust and Mantle. Mineral. Soc. Ser.* (M.B. Holness, ed.), pp. 145–172. Chapman and Hall, London.

D'lemos, R.S., Brown, M. and Strachan, R.A., 1992. Granite magma generation, ascent and emplacement within a transpressional orogen. *J. Geol. Soc. London*, **149**, 487–490.

De Saint-Blanquat, M., Tikoff, B., Teyssier, C. and Vigneresse, J.L., 1998. Transpressional kinematics & magmatic arcs. In: *Continental Transpressional and Transtensional Tectonics* (R.E. Holdsworth, R.A. Strachan and J.F. Dewey, eds), pp. 327–340. Geological Society Special Publication, London.

Fitzgerald, P.G. and Stünitz, H., 1993. Deformation of granitoïds at low metamorphic grade. Part I: reactions and grain size reduction. *Tectonophysics*, **221**, 269–297.

Gapais, D., Bale, P., Choukroune, P., Cobbold, P., Mahdjoub, Y. and Marquer, D., 1987. Bulk kinematics from shear zone patterns: some field examples. *J. Struct. Geol.*, **9**, 635–646.

Giger, M., 1991. Geochronologische und petrographische studien an Geröllen und Sedimenten der Gonfolite-Lombarda Gruppe (Südschweiz und Norditalien) und hir Vergleich mit dem alpinen Hinterland. PhD dissertation, Universität Bern, Bern, 227 pp.

Giger, M. and Hurford, A.J., 1989. Tertiary intrusives of the Central Alps: their Tertiary uplift, erosion, redeposition and burial in the south-alpine foreland. *Eclogae Geol. Helv.*, **82**, 857–866.

Hansmann, W., 1996. Age determination on the Tertiary Masino-Bregaglia (Bergell) intrusives (Italy, Switzerland): a review. *Schweiz. Mineral. Petrogr. Mitt.*, **76**, 421–451.

Heitzmann, P., 1987. Evidence of Late Oligocene/Early Miocene backthrusting in the central alpine 'root zone'. *Geodin. Acta*, **1**, 183–192.

Huber, R.K., 1999. Tectonometamorphic evolution of the Eastern Pennine Alps during Tertiary continental collision: structural and petrological relationships between Suretta-, Tambo-, Chiavenna and Gruf units (Switzerland/Italy). PhD dissertation, University of Neuchâtel, Neuchâtel, 125 pp.

Hutton, D.H.W., 1988. Granite emplacement mechanisms and tectonic controls: inferences from deformation studies. *Trans. R. Soc. Edinb. Earth Sci.*, **79**, 245–255.

Hutton, D.H.W. and Ingram, G.M., 1992. The Great Tonalite Sill of Southeastern Alaska and British Columbia: emplacement into an active contractional high angle reverse shear zone. *Trans. R. Soc. Edinb. Earth Sci.*, **83**, 383–386.

Hutton, D.H.W. and Reavy, R.S., 1992. Strike–slip tectonics and granite petrogenesis. *Tectonics*, **11**, 960–967.

Hutton, D.H.W., Dempster, T., Brown, P.E. and Becker, S.D., 1990. A new mechanism of granite emplacement: intrusion in active extensional shear zones. *Nature*, **343**, 452–455.

Liati, A., Gebauer, D. and Fanning, M., 2000. U–Pb SHRIMP dating of zircon from the Novate granite (Bergell, Central Alps): evidence for Oligocene–Miocene magmatism, Jurassic/Cretaceous continental rifting and opening of the Valais trough. *Schweiz. Mineral. Petrogr. Mitt.*, **80**, 305–316.

Marquer, D., 1991. Structures et cinématique des déformations alpines dans le granite de Truzzo (Nappe de Tambo: Alpes centrales suisses). *Eclogae Geol. Helv.*, **84**, 107–123.

Marquer, D., Challandes, N. and Baudin, T., 1996. Shear zone patterns and strain partitioning at the scale of a Penninic nappe: the Suretta nappe (Eastern Swiss Alps). *J. Struct. Geol.*, **18**, 753–764.

Maruyama, S., Susuki, K. and Liou, J.G., 1983. Greenschist-amphibolite transition equilibria at low pressures. *J. Petrol.*, **24**, 583–604.

Massone, H.J. and Schreyer, W., 1987. Phengite geobarometry based on the limiting assemblage with K-feldspar, phologopite and quartz. *Contrib. Mineral. Petrol.*, **96**, 212–224.

Massone, H.J. and Szpurka, Z., 1997. Thermodynamic properties of white micas on the basis of high-pressure experiments in the systems K2O-MgO-Al2O3-SiO2 and K2O-FeO-Al2O3-SiO2-H2O. *Lithos*, **41**, 229–250.

Meyre, C., Marquer, D., Schmid, S.M. and Ciancaleoni, L., 1998. Syn-orogenic extension along the Forcola fault: correlation of Alpine deformations in the Tambo and Adula nappes (Eastern Pennine Alps). *Eclogae Geol. Helv.*, **91**, 409–420.

Milnes, A.G., 1974. Post-nappe folding in the western Lepontine Alps. *Eclogae Geol. Helv.*, **67**, 333–348.

Mitra, G., 1979. Ductile deformation zones in Blue Ridge basement rocks and estimation of finite strains. *Bull. Geol. Soc. Am.*, **90**, 935–951.

Oschidari, H. and Ziegler, U.R.F., 1992. Vergleichende Sm-Nd und Rb-Sr Untersuchungen an Bergeller Geröllen aus der Gonfolite Lombarda ('Südalpine Molasse') und an Bergeller und Novate-Granitoiden des Ursprungsgebietes. *Eclogae Geol. Helv.*, **85**, 375–384.

Paterson, S.R., Tobisch, O.T. and Morand, V.J., 1990. The influence of large ductile shear zones on the emplacement and deformation of the Wyangala Batholith, SE Australia. *J. Struct. Geol.*, **12**, 639–650.

Ramsay, J.G. and Allison, I., 1979. Structural analysis of shear zones in an Alpinised Hercynian granite (Maggia Lappen, Pennine zone, Central Alps). *Schweiz. Mineral. Petrogr. Mitt.*, **59**, 251–279.

Roman-Berdiel, T.D., Gapais, D. and Brun, J.P., 1997. Granite intrusion along strike–slip zones in experiment and nature. *Am. J. Sci.*, **297**, 651–678.

Rosenberg, C.L., 2004. Shear zones and magma ascent: a model based on a review of the Tertiary magmatism in the Alps. *Tectonics*, **23**, TC3002, doi: 10.1029/2003TC001526.

Rosenberg, C.L. and Heller, F., 1997. Tilting of the Bergell Pluton and Central Lepontine area: combined evidence from paleomagnetic, structural and petrological data. *Eclogae Geol. Helv.*, **90**, 345–356.

Scaillet, B., Pêcher, A., Rochette, P. and Champenois, M., 1995. The Gangotri granite (Garhwal Himalaya): laccolithic emplacement in an extending collision belt. *J. Geophys. Res.*, **100**, 585–607.

Schmid, S.M., Aebli, H.R., Heller, F. and Zingg, A., 1989. The role of the Periadriatic Line in the tectonic evolution of the Alps. In: *Alpine Tectonics* (M.P. Coward, D. Dietrich and R.G. Park eds), pp. 153–171. Geological Society Special Publication, London.

Schmid, S.M., Pfiffner, O.A., Froitzheim, N., Schönborn, G. and Kissling, E., 1996a. Geophysical–geological transect and tectonic evolution of the Swiss–Italian Alps. *Tectonics*, **15**, 1036–1064.

Schmid, S.M., Berger, A., Davidson, C., Gieré, R., Hermann, J., Nievergelt, P., Puschnig, A.R. and Rosenberg, C., 1996b. The Bergell Pluton (Southern Switzerland, Northern Italy): overview accompanying a geological-tectonic map of the intrusion and surrounding country rocks. *Schweiz. Mineral. Petrogr. Mitt.*, **76**, 329–355.

Srivastava, D.C., Lisle, R.J. and Vandycke, S., 1995. Shear zones as a new type of paleostress indicator. *J. Struct. Geol.*, **17**, 663–676.

Strong, D.F. and Hanmer, S.K., 1981. The leucogranites of southern Britanny: origin by faulting, frictional heating, fluid flux and fractional melting. *Can. Miner.*, **19**, 163–176.

Stünitz, H. and Fitzgerald, P.G., 1993. Deformation of granitoïds at low metamorphic grade. Part II: granular flow in albite-rich mylonites. *Tectonophysics*, **221**, 299–324.

Tikoff, B. and De Saint-Blanquat, M., 1997. Transpressional shearing and changing kinematics in the late Cretaceous Sierra Nevada magmatic arc, California. *Tectonics*, **16**, 442–459.

Tikoff, B., De Saint-Blanquat, M. and Teyssier, C., 1999. Translation and the resolution of the space problem. *J. Struct. Geol.*, **21**, 1109–1118.

Twiss, R.J. and Unruh, J.R., 1998. Analysis of fault slip inversion: do they constrain stress or strain rate? *J. Geophys. Res. B Solid Earth*, **103**, 12205–12222.

Vauchez, A., Pacheco Neves, S. and Tommasi, A., 1997. Transcurrent shear zones and magma emplacement in neoproterozoic belts of Brazil. In: *Granite: From Segregation of Melt to Emplacement Fabrics* (J.L. Bouchez, D.H.W. Hutton and W.E. Stephens, eds), pp. 275–293. Kluwer Academic, Norwell, MA.

Viola, G., Mancktelow, N. and Seward, D., 2001. Late Oligocene–Neogene evolution of the Europe–Adria collision: new structural and geochronological evidence from the Giudicarie Fault System (Italian Eastern Alps). *Tectonics*, **20**, 999–1020.

Von Blanckenburg, F., 1992. Combined high precision chronometry and geochemical tracing using accessory minerals applied to the Central-Alpine Bergell intrusion. *Chem. Geol.*, **100**, 19–40.

Von Blanckenburg, F., Früh-Green, G., Diethelm, K.H. and Stille, P., 1992. Nd-, Sr-, O-isotopic and chemical evidence for a two stage contamination history of mantle magma in the Central Alpine Bergell intrusion. *Contrib. Mineral. Petrol.*, **110**, 33–45.

Wenk, H.R., 1973. The structure of the Bergell Alps. Part III. *Eclogae Geol. Helv.*, **66**, 255–291.

Whitney, J.A., 1988. The origin of granite: the role and source of water in the evolution of granitic magmas. *Geol. Soc. Am. Bull.*, **100**, 1886–1897.

Wotjal, S. and Pershing, J., 1991. Paleostresses associated with faults of large offset. *J. Struct. Geol.*, **13**, 49–62.

Received 1 October 2005; revised version accepted 28 February 2006